Improvements in spectral modeling of sea states : numerical and physical aspects and contributions of space remote sensing

Matías Alday Gonzalez

COLLEGE SCIENCES DOCTORAL DE LA MER BRETAGNE ET DU LITTORAL

UBO Université de Bretagne Occidentale

THESE DE DOCTORAT DE

L'UNIVERSITE
DE BRETAGNE OCCIDENTALE

ECOLE DOCTORALE N° 598
Sciences de la Mer et du Littoral
Spécialité : *Océanographie, physique et environnement*

Par

Matías ALDAY GONZALEZ

Améliorations de la modélisation spectrale des états de mer

Aspects numériques et physiques et apports de la télédétection spatiale

Thèse présentée et soutenue à Brest, le 3 mai 2023
Unité de recherche : Laboratoire d'Océanographie Physique et Spatiale (LOPS)

Rapporteurs avant soutenance :

Xavier BERTIN	Directeur de Recherche, CNRS-Université de La Rochelle
Joanna STANEVA	Hydrodynamics and Data Assimilation group leader, Helmholtz-Zentrum Geesthacht - ALLEMAGNE

Composition du Jury :

Président :	Xavier CARTON	Professeur, Université de Bretagne Occidentale, LOPS
Examinateurs :	Xavier BERTIN	Directeur de Recherche, CNRS - Université de La Rochelle
	Joanna STANEVA	Directrice du département Hydrodynamique et assimilation de données Institute for Coastal Systems, Helmholtz-Zentrum Hereon-Allemagne
	Jean-Raymond BIDLOT	Chercheur au Centre Européen de Prévision à Moyen Terme (CEPMMT / ECMWF) – Royaume-Uni
	Mélissa MENENDEZ	Chercheuse au IH-Cantabria, Universidad de Cantabria - Espagne
Dir. de thèse :	Fabrice ARDHUIN	Chercheur au Laboratoire d'Océanographie Physique et Spatiale

Acknowledgement

First and foremost thanks to my parents, Ximena and Herman, for their efforts and sacrifices along the way. It takes distance and perspective to fully process and appreciate what seems to be trivial when you are a kid. To my sisters Karla, Constanza and Macarena, thanks for your love and company in the distance, and for understanding the moments of absence when I was fully submerged in this "process".

To my fiancé and best friend Delphine, special thanks to you, for your patience, for bringing balance and strength, and for the everyday life. This effort is also yours in many levels. I love you.

To my very good Brestois friends (most of them partners in crime). The ones who are there Sophia, Greace, Esther, Dani, Ramón, Christian, Pierre, Marine, and the little turtles Noa and Helí. The ones who left, Guillaume, Heather, Pauline ...(I am obviously forgetting many others). My time/life in France would not have been half as special without you.

To the Utrecht gang, Karla, Allix, Jane, and André, you certainly made the country change easier. Thanks for being who you are.

I am not forgetting any of my colleagues in LOPS (all of you!, the list is long). Since my internship days, to my engineer days, to my PhD candidate days, there was always someone to count on. Abderrahim, I miss our morning talks before starting the day.

I want to particularly thank what I consider to be my close "team" in this whole story, my thesis supervisor Fabrice Ardhuin. and Mickael Accensi. Fabrice, thanks for the support, help, advice, for the random talks in the middle of our meetings (those are always funny), and most of all, for giving me a chance on first place. Mick, we had a great run, thanks for being such a good team player, for showing me all the "cool tricks", and of course for teaching me mushroom hunting inside Ifremer. In my experience, having a good team dynamic is the exception, not the trend. You both are one of the main reasons why I stayed in France for so long.

Table of Contents

I Introduction **19**

I.1 General context . . . 19

I.1.1 About the spectral representation of waves and numerical models . 19

I.1.2 Importance of the sea sates characterization . . . 24

I.1.3 Satellite altimetry and measurement of waves . . . 26

I.1.4 Scientific questions . . . 31

I.2 Objectives . . . 31

I.3 General methods . . . 32

I.4 The WAVEWATCH III model . . . 33

1 Effects of improved forcing and spectral resolution at global scale **37**

1.1 Introduction . . . 37

1.2 Method . . . 38

1.3 Global model setup . . . 39

1.3.1 Forcing fields . . . 39

1.3.2 Adjusted parametrizations and parameters . . . 40

1.3.3 Spectral and spatial discretization . . . 42

1.3.4 Model adjustments . . . 42

1.4 Influence of forcing field choices . . . 52

1.4.1 Choice of forcing wind field . . . 52

1.4.2 Effects of wave-ice parametrizations and forcing fields . . . 54

1.4.3 Effect of currents . . . 56

1.5 Model discretization . . . 59

1.5.1 Spatial resolution . . . 60

1.5.2 Spectral grid resolution . . . 61

1.6 Wave directionality and alternative dissipation parameterizations . . . 62

1.7 Validation . . . 66

1.7.1 Validation with altimeter data . . . 66

1.7.2 Comparison to ERA5 wave heights . . . 66

1.7.3 Validation with buoy data 69
1.8 Conclusions 72

2 Accuracy of spectral wave models in coastal environments: Application to the Atlantic coasts of Europe 75
2.1 Introduction 75
2.2 Method 76
2.3 Model set-up and sensitivity tests 77
2.3.1 Mesh construction 77
2.3.2 Bottom sediment map 78
2.3.3 Source terms and numerical choices 79
2.3.4 Boundary conditions and forcing fields improvements 80
2.3.5 Spectral discretization and time steps 81
2.4 Wave data sources 82
2.4.1 Buoy data 82
2.4.2 Satellite altimetry data 83
2.5 Model Performance 84
2.5.1 Influence of high spatial resolution 84
2.5.2 Adjustments in wind-wave generation and swell dissipation 86
2.5.3 Wave-Current Interactions 90
2.5.4 Effects of spectral directional resolution 97
2.5.5 Bottom friction effects 103
2.6 Model validation with altimetry data 110
2.7 Conclusions 113

3 Alternative parameterizations and their effect on spectral energy directionality 117
3.1 Introduction 117
3.2 Model parameterizations 121
3.2.1 Nonlinear wave interactions 121
3.2.2 Wave breaking parameterizations 126
3.2.3 Model configurations 133
3.3 Wave data 134
3.4 T700 dissipation effects on energy directionality and the tail of the spectrum 135
3.5 Global impact of alternative dissipation parameterizations 143

3.5.1 Wave heights . . . 143
3.5.2 Spectral shapes . . . 148
3.6 Underwater acoustic data and directional spectral tail properties . . . 151
3.7 Conclusions . . . 156

4 Conclusion **159**
4.1 Reminder of the main scientific questions and objectives . . . 159
4.2 Main outcomes of the study . . . 160
4.3 Findings . . . 161
4.4 Perspectives . . . 163
4.5 Future work . . . 167

Appendix **169**
A Global model implementation . . . 169
B Regional model implementation . . . 170
C Parameters used with T700 implementations . . . 171
C.1 Namelist details for T707-QGM . . . 171
C.2 Namelist details for T702 . . . 171

Bibliography **173**

FIGURES

I.1 (a) Relations between frequency-domain and time-domain representation of waves when Fourier analysis is applied to a 1-dimensional elevation time series. Adapted from figure 5.4 in Bai and Jin (2016). (b) Reconstruction of a given sea state from the superposition of several waves' planes with different directions and wavelength. Adapted from Pierson et al. (1955b). . 22

I.2 Mixed swell and wind sea conditions simulated at buoy 46246. (a) Directional wave spectrum from simulation. (b) Frequency wave spectrum computed from directional spectrum. Simulation result from January 23 of 2011, 03:00:00 UTC. Arrows in (a) indicate overall mean direction D_m (white), mean wind sea direction (magenta) and the swell mean direction (gray), very similar to the overall peak direction. Direction notation is "waves travelling to". 23

I.3 Schematic view of the influence of waves on air–sea exchanges. Adapted from figure 1.A in Cavaleri et al. (2012) 25

I.4 Storm surge event in the coasts of Valparaíso, Chile (August 8, 2015). Photograph provided by Patricio Winckler (senior researcher at Universidad de Valparaíso). 26

I.5 (a) Time line of completed, on going, and future satellite missions. (b) Example of 1 day altimeter coverage of Jason-2, Cryosat-2 and SARAL. In (a) continuous lines show missions with altimeter instrument. In (a) Ka and Ku bands in black and blue respectively. Red rectangles represent instruments with SAR mode. 27

I.6 H_s JFM global trends (1993-2018) computed with (a) Sea State CCI V1 altimeter data (Piollé et al., 2020) and (b) with WAVEWATCH III generated hindcast (Alday et al., 2021). Trend estimations provided by Antoine Hochet. 28

I.7 (a) Principle of radar altimetry measurement (adapted from Frappart et al., 1999). (b) Scheme of the change of illuminated area in time (adapted from http://sar.kangwon.ac.kr/etc/rs_note/rsnote/cp4/cp410.htm). (c) Scheme of the theoretical ocean waveform from the Brown model (Brown, 1977). (d) Examples of measured waveforms for small wave heights (blue) to large wave heights (green) recorded by SARAL-AltiKa. 30

1.1 Sub-Grids nesting layout for multi-grid tests. Colors indicate areas where computations are performed and grids' rank in the nesting scheme: Blue is rank 2, Green is rank 3, and Red is rank 4. 43

1.2 Error statistics for H_s for the $\beta_{\max}$ sensitivity runs (a) Normalized mean difference between model runs – with parameters given in Table 1.2 – and the Jason-2 altimeter data, (b) normalized root mean square difference. . . 45

1.3 Error statistics for H_s for the wind correction sensitivity runs (a) Normalized mean difference between model runs – with parameters given in Table 1.2 – and the Jason-2 altimeter data, and (b) scatter index. 46

1.4 (a) Histogram of H_s values in the Jason-2 and co-located model simulations. (b) Differences between the model and altimeter histograms. Plots shown are from wind correction tests only. (c) Same as (a) but with a logarithmic scale. (d) Difference of logarithm of the modeled and measured H_s histograms. 47

1.5 (a) Histogram of H_s values in the Jason-2 and model simulations absolute frequency of occurrence difference (WW3 - alitmetry data). (b) Normalized mean bias. Plots shown are from s_7 and Re_c sensitivity tests. 48

1.6 H_s absolute frequency of occurrence difference (WW3 - altimetry data) from Atlantic and Pacific basins. 49

1.7 H_s NMD within Atlantic and Pacific basins as a function of observed wave heights. H_s bins' range is 0.25 m. 50

1.8 NMB for 1-year averaged H_s using ERA5 winds. Modelled year: 2011. Parameter settings from test T475. Colorbar indicates NMD values in %. Black lines represent positive 10 % contours. 51

1.9 Scatter plot of wind speed for the months of January to July 2011. ERA5 intensity bins along x-axis. Top panels: ECMWF operational product vs ERA5, Middle panels: Ifremer vs ERA5. Bottom panels: CFSR vs ERA5. Colors give the logarithm of the number of data points in each 0.25 m/s×0.25 m/s wind speed bin. 53

1.10 Normalized Mean Difference of modelled H_s minus Sea State CCI Altimeter data, averaged over the year 2011, using (a) ERA5, (b) CFSR, (c) ECMWF operational deterministic products and (d) Ifremer winds. The model was run with the set of parameters T475 as given in Table 1.2. Colorbar indicates NMD in percent. Black and yelow lines mark the +10 and +20 % contours. 54

1.11 Scatter Index of modelled H_s minus Sea State CCI Altimeter data, averaged over the year 2011, using (a) ERA5, (b) CFSR, (c) ECMWF operational deterministic products and (d) Ifremer winds. The model was run with the set of parameters T475 as given in Table 1.2. Colorbar indicates SI in percent. Black and yelow lines mark the +10 and +20 % contours. 55

1.12 Differences in NMB and SI in percentage points for the T475 parameterization variations when using: (a,b) using dissipation, scattering and ice break-up (IC2, IS2) or partial ice blocking (IC0), (c,d) iceberg forcing or no iceberg forcing. 57

1.13 Root mean square current velocity (a) at 15 m depth using in situ drifter data from the Surface Velocity Program (SVP) processed by Elipot et al. (2016) with rms velocity computed over 30-day long trajectories and attributed to the center of that trajectory and white ocean pixels corresponding to 1 by 1 degree squares in which no data was available, (b) as given by the CMEMS GLORYS reanalysis, (c) as given by the CMEMS-Globcurrent product based on altimeter sea level anomalies, mean dynamic topography inferred from satellite gravimeters and ocean drifters, and “Ekman currents” estimated from ECMWF wind analyses. 58

1.14 Left: Change in Normalized Mean Difference (NMD in percentage points) for H_s with currents and the T475 parameterization versus the same simulation without current. For both simulatons the reference is the Sea State CCI H_s for the year 2011. Right: same for difference in SI, with the dark blue corresponding to a reduction of 4 percentage points (e.g. from 14% to 10%) when TSCV forcing is used. 59

1.15 NMD and SI variations in percentage points for the year 2011: values for Multi-grid minus values for Single grid setup, both using the same T475 parameters. Left panel: Difference in NMD values, in this case red values represent a reduction of the negative NMD. 60

1.16 (a)NMD for 1 year averaged H_s using T475 with 36 directions and (b) differences in NMD for T475 with 36 directions with respect to 24 directions (Fig. 1.10.a). Black lines mark the positive 10 % contours. (c) SI for 1 year averaged H_s using T475 with 36 directions and (d) SI difference for T475 with 36 directions with respect to 24 directions. Analyzed year: 2011. Black and yellow lines mark the positive 10 and 20 % contours respectively. 62

1.17 Modeled mean direction (a,b) and spread (c,d) for low frequencies ($f <$ 0.4 Hz) and high frequencies ($f > 0.4$ Hz) at buoy 46246 for the year 2018. Colors show the number of 3 hour records for which the model-buoy pair falls in one bin, as normalized by the maximum value nmax. The solid lines gives the mean modeled value for each observation bin. 63

1.18 Differences in model results for an academic case considering a uniform ocean and a constant wind speed of 10 m/s starting from no waves. The WAM4.5 parameterization is close to the one used in the ERA5 reanalysis, and the T700NL2 corresponds to the parameterization of Romero (2019) with the non-linear interactions computed with the exact Webb-Resio-Tracy method (van Vledder, 2006). 65

1.19 Change in NB and SI from the T471 to T700 change in parameterization for the year 2018. These simulations did not include ocean currents. 65

1.20 Performance parameters for 22 years hindcast using T475. (a) H_s NMD curves and (b) SI curves, the reference year (2011) used for model tuning has been highlighted with a black star. (c) and (d) are the NMD and SI time series of 1.5 to 10 m H_s bins. Bin size is 0.25 m. Altimeters used for validation: Topex (1997-2002), Envisat (2003-2010), Jason-2 (2011-2012), Saral (2013-2018). 67

1.21 Performance parameters curves for test T475 and ERA5 wave product with respect to Jason-3 altimeter data. (a) H_s NMD, and (b) NRMSD. Analyzed year: 2018. H_s bin size is 0.25 m. 68

1.22 (a) Scatter Index for 1 year (2018) averaged ERA5 H_s with respect to Jason-3 altimeter data. (b) Difference in scatter index between T475 and ERA5 waves product (T475 - ERA5). 69

1.23 Modeled and measured mean spectra, scatter plots for H_s, and mean periods $T_{m-1,0}$, $T_{m0,2}$ at selected buoys listed in Table 1.4. 71

2.1 (a) Refinement polygons in red. (b) Final mesh elements size distribution, coastlines polygons in black, in grey mesh nodes where boundary conditions are prescribed from the global model. (c) Bathymetry reconstruction with mesh. Colorbar in (c) represents depths with respect to MSL in meters. Map data in (a) are from ©Google Landast / Copernicus. 78

2.2 Bottom sediment size map. D_{50} values assigned to each mesh node for: (a) Full domain, (b) Bay of Biscay and the English Channel and (c) UK. Colorbar represents D_{50} in mm. Gray dashed lines represent 200 m depth contours, continuous gray lines represent 50 m depth contours. 79

2.3 (a) Spatial coverage from selected tidal models. Blue and green rectangles have a 250 m resolution, and the orange and yellow area have resolutions of 700 m and 2000 m respectively. (b)Example of merged tidal harmonics from Ifremer's tidal atlas and FES2014. Colorbar in (b) represents M2 amplitude values in meters; black lines show the boundary and coastline polygons. 81

2.4 Buoys location and bathymetry features.(a) Buoys along French coast. (b), (c), (d) and (e) details of French buoys locations. (f) detail of Belgian buoys location. Colorbar shows depths in meters with respect to MSL. Maximum depth on each panel has been selected to enhance bathymetry details. . . . 83

2.5 Mean H_s fields from global and regional model, and H_s normalized mean differences (Global - Regional). Dashed black lines represent the 400 m depth contours. Areas where no wave data are available from the global grid are highlighted with a gray background in left and right panels. Results for February 2011. 85

2.6 NMD and SI for tests leading to T475 (Table 2.3). Results for January 2014. In (a) and (b) modelled results compared with buoys 62074 and 62069 respectively. H_s bin size is 0.25 m, periods bin size is 0.2 s. 88

2.7 Performance parameters for energy levels at each discrete frequency of the spectrum, for tests leading to T475 (Table 2.3). Results for January 2014 at buoys 62066, 62078, 62074 and 62069. In panels (a) to (d) modelled results compared with buoy data. Time series of modelled and measured H_{20} for buoys 62078 in (e) and 62074 in (f). 89

2.8 Normalized mean bias of H_s for the North Atlantic (WW3 - altimeter SWH). Wave height bins are 0.25 m. 1-year tests for 2011 and 2014 are identified with black and fuchsia lines respectively. Altimtetry significant wave heights (SWH) from Jason-2. 91

2.9 Global currents effects over (a) H_s, (b) D_p and (c) directional spreading. In left panel, model output for test using BC generated with global currents at 2011-02-16 00:00:00 UTM. NMD results in middle and right panels are for test with BC obtained without global surface currents with respect to test with BC from global grid forced with global currents. Colorbars in middle and left panels represent NMD in [%]. Full simulation duration of tests is 1 month. 93

2.10 Tidal currents effects over (a) H_s, (b) D_p and (c) directional spreading. NMD results obtained with respect to test using tidal currents. In left panel, NMD with respect to model output at 2011-02-16 00:00:00 UTM presented in left panel of Fig. 2.9. Colorbars represent NMD in [%]. Full simulation duration of tests is 1 month. 94

2.11 Tidal currents effects over T_p. NMD results obtained with respect to test using tidal currents. (a) T_p field at 2011-02-16 00:00:00 UTM, (b) NMD calculated at 2011-02-16 00:00:00 UTM, (c) NMD detail computed for the full simulation duration. Colorbar in (b) and (C) represent NMD in [%]. Full simulation duration of tests is 1 month. 95

2.12 Evaluation of tidal currents effects on wave energy distribution (a) , H_s and T_{m01} at buoy 62059 (Cherbourg Exterieur). Parameteres NMD and time series in (b) and (c) respectively. Results for January 2014. H_s bin size is 0.25 m, T_{m01} bin size is 0.2 s 96

2.13 Effects of boundary conditions with lower directional resolution at different output locations. (a) Boundary node W12N56 (Lon.: 12°, Lat.: 56°) (b) 62074 (Belle Ile), (c) 62069 (Pierres Noires), (d) 62059 (Cherbourg). Differences and NMD (36D24BC-36D36BC) computed for January 2014. White contours marking energy levels on left panels are the same plotted in black on the corresponding right panels for energy difference and NMD. Direction convention is towards energy is traveling to. 99

2.14 (a) Normalized mean differences (NMD) and (b) normalized root mean squared differences (NRMSD) between tests 36D24BC - 36D36BC and 48D24BC - 48D48BC. Analyzed period : February 2011. Colorbars represent changes in quantities between tests in [%] units. 101

2.15 (a) H_s field at 2011-02-01 13:00:00 UTM for different directional resolution tests specified in Table 2.4. (b) Differences in H_s fields presented in (a). Offshore swell conditions at 2011-02-01 13:00:00 UTM (to west of the Orkney and Shetland Islands): $T_p = \sim$14 s, $D_m = \sim$260°. 102

2.16 H_s bias (WW3-altimeter) computed with (a) Saral year 2014 and (b) Envisat year 2011. Dashed black lines show 200 m depth contour, green lines the 50 m depth contours, and gray lines depth contours from 100 to 150 m depth. Magenta ovals in (b) highlight areas with mayor bias reduction. . 106

2.17 Bottom friction effects at buoy 62078 (year 2014). Performance analysis using (a) complete time series and (b) extreme events ($H_s > 3.5$ m). (c) H_s time series for cases with and without SHOWEX parameterization. Time series of (d) Shields number ψ and (e) dissipation term $f_e u_{\mathrm{b,rms}}$. In (a) and (b) green line shows the modelled averaged values at each 0.15 m wave height bin. Colorbars represent the wave heights frequency of occurrence normalized by the total amount of analyzed data N. Time series in (d) and (e) computed with WW3's frequency spectrum following eq. 2.4 to 2.12. D_{50} taken from bottom sediment map (Fig. 2.2). Blue dashed line in (d) represents the critical Shields number. 108

2.18 WW3-Buoy H_{10} comparison for tests without bottom friction, using default JONSWAP and with SHOWEX parameterization including the implemented bottom sediment map. Results for (a) Westhinder and (b) Scheur Wielingen buoy location for year 2014. Green line shows the modelled averaged values at each 0.02 m wave height bin. Colorbars represent the wave heights occurrences normalized by the total amount of analyzed data N. . . 109

2.19 (a) NMD and (b) SI of H_s as function of distance to the coast (WW3-altimeter SWH). Bins' width is 1 km 112

3.1 Typical shape of source terms and specturm evolution, both integrated over directions. This simulation is the result of the integration of $dE/dt = S$, which corresponds to spatially uniform sea state, only involving in time, here with a constant wind speed of 15 m/s starting from zero energy at $t = 0$. The similar magnitude of $S_{\rm tot}$ and $E \times 10^{-3}$ in the top panel means that the spectrum evolves on a time scale of 1000 s after 3 hours. This time scale grows to a day after 48 hours, which corresponds to a "fully developed" sea state which does not grow much. Reproduced from Ardhuin (2019). . . 119

3.2 Geometrical arrangement of the wavenumbers that satisfy the 4-wave interaction rule. Each line corresponds to a different value of $f_1 + f_2$. 123

3.3 Direction integrated nonlinear transfer terms $S_{\rm nl}(f)$ computed with various methods: EXACT-NL (SWAMP Group et al., 1985), DIA (blue line), GQM-fine (thick black line), GQM-rough (red dotted line) for the spectrum of case 3 in Hasselmann and Hasselmann (1981). The frequency spectrum E(f) is superimposed (in green). Adapted from Fig. 1 in (Gagnaire-Renou et al., 2010). 125

3.4 Numerical mask used for North Pacific simulations using the WRT method for nonlinear interactions. Active (wet) grid nodes in light blue, land grid nodes in dark blue and excluded nodes in yellow. Longitudes in plot are presented from 0 to 360° but actual WW3 grid is from -180 to 180°. 134

3.5 Evolution of (a) wave height (b) cross-wind over down-wind mean square slopes ratio, for a uniform ocean starting from rest with 10 m/s wind, and spectral distribution of (c) saturation level and (d) overlap integral after 30 hours of integration. Results with existing parameterizations based on Ardhuin et al. (2010) (T475, T475b), Rogers et al. (2010) (ST6) are shown for reference, together with Romero (2019) with several proposed adjustments (see Table 3.1). 137

3.6 Inverse dissipation time scale S_{ds}/E and directional spectrum shape $E(f,\theta)$ for frequencies 0.5 Hz (in top panels) and 1 Hz (bottom panels). These are obtained after 100 hours of simulation for a uniform ocean with a constant wind speed of 10 m/s blowing in direction 90°. 139

3.7 Same as Fig. 3.5, for simulations using exact methods for the non-linear 4-wave interactions. 140

3.8 Same as Fig. 3.6, for simulations using exact methods for the non-linear 4-wave interactions, with the addition of directional spreads σ_1, defined from a_1 and b_1 directional moments, and σ_2, defined from a_2 and b_2 directional moments following (Kuik et al., 1988). 142

3.9 Model global performance with different parameterizations as a function of the wave height: T475, T702-Bm1.7, T702-Bm1.7b and T707-GQM. Wave heights performance parameters for year 2011 (WW3 - Jason-2). (a) H_s NMD, (b) scatter index, (c) H_s occurrences differences (to better observe changes for wave heights < 5 m) and (d) H_s occurrences in log scale. . . . 145

3.10 Normalized mean differences (NMD on left panel) and scatter index (SI on right panel) for H_s. Black and yellow lines represent the 10% and 20% contours respectively. Colorbars represent NMD and SI in % points. 146

3.11 Oceanographic parameters at buoy 46246 and Ocean Station Papa for 27 to 28 January 2011: (a) Wind speed, wind direction, (b) significant wave height over a wind event recorded at Ocean Station Papa and current at 15 m depth (projected on the wind direction) nearby buoy 46246 (CDIP station 166), (d) evolution of the mean wave direction and (e) the evolution of the wave spectrum $E(f)$, with contours for the check ratio equal to 0.8 overlaid in black. 149

3.12 H_s field evolution between 27 and 28 of January 2011. Colorbars indicate H_s values in meters, and the cross indicates the location of buoy 46246. Longitude coordinates are from 0 to 360° in these plots. 150
3.13 Modeled and measured spectrum, multiplied by f^5 (top panels), first mean spread $\sigma_1(f)$ (middle panels), and second mean spread $\sigma_2(f)$ (bottom panels). 151
3.14 Time series of 3-hourly wind speed and direction and 10-minute averaged measurements (panels a,d) and noise level over a few weeks of summer (a,b,c) and winter (d,e,f) in 2007 at the ALOHA Cabled Observatory, north of Ohahu Hawaii, using data provided by Duennebier et al. (2012) and model runs T475, T702 and T700-GQM. In order to give results comparable to T700, results for T475 are multiplied by 10 for 1 Hz and 15 for 20 Hz. . 153
3.15 Correlation of modeled acoustic noise at the ALOHA observatory, north of Ohahu Hawaii, for the year 2007 using data provided by Duennebier et al., 2012 and model runs T475, T700, T702 and T700-GQM. 155

4.1 Distribution of drag coefficients for 4 different model runs over the month of January 2007, taking all model output every 3 hours. In each panel the red line is the Edson et al. (2013) COARE3.5 value of C_d in neutral conditions, the solid black line is the mean value for each wind speed and the dashed lines bracket 95% of the values. 166

Chapter I

Introduction

I.1 General context

The observation, understanding, and later the necessity to predict ocean waves have been constantly evolving for over a century. The availability of measurements gathered with in situ and remote sensing techniques have allowed to extend our knowledge on wind generated waves. There is an intrinsic feedback between these and numerical models, which in the end are used to reproduce (hindcast) or predict (forecast) wave conditions. Typically the analysis of gathered data allows to progress towards better simulations, as new details on physical processes are unveiled and then included in models. Sometimes it is the other way around, and we look for specific capabilities from measuring devices in order to verify something first noticed in simulations and that is anticipated by logical deduction of a physical process. The present thesis aims to find the elements, in spectral wave models, that will lead to improvements in different aspects of the simulated sea states, taking into account the used forcing fields, physical parameterizations and numerical aspects.

I.1.1 About the spectral representation of waves and numerical models

First documented measurement of the sea states were made after the second half of the 1800s (e.g. Abercromby, 1887; Cornish, 1904; Cornish, 1910; Schott, 1893). In particular, Cornish (1904), also attempted to relate the sea state to meteorological conditions and the local geography (Bretschneider, 1965). The early linear and higher order theories by Airy (1845) and Stokes (1847), and later the long waves theory by Boussinesq (1872) mainly focused on their mechanical properties, but the effect of winds were not considered. By all means, this does not imply that these authors were not aware of the fact that when wind blows over water, surface waves are formed. Most likely, a clear explanation of this

phenomenon was still being developed. It is probably later, with the works of L. Kelvin and H. Helmholtz around 1888 that the basis for the study of wind waves generation are set (Kelvin-Helmholtz theory in Lamb, 1945).

Several years after, with a series of scientific advances and in the middle of the Second World War, great progress is made into predicting the wave fields' characteristics based on atmospheric conditions (e.g. Suthons, 1945). With special attention to wave generation due to winds, the transformation mechanisms present throughout propagation, to shoaling and breaking processes in shallow waters at the coast (Dean and Dalrymple, 1991). The gained scientific momentum and the continuous increase of offshore oil drilling in the mid 1950s with its consequent engineering challenges, and with an overall recovering economy, many subsequent studies followed. Most of them not only looking for improvements in the physics behind forecasting techniques in deep waters (e.g. Bretschneider, 1952; Pierson et al., 1955a; Sverdrup and Munk, 1947), but also trying to understand the complex properties of the sea states spectra and their effect in coastal areas (e.g. Bretschneider and Reid, 1954; Caldwell and Williams, 1961; Munk, 1949).

It was already common for sailors in past times to relate the characteristics of the blowing wind to the sea state, and how this could be favourable or dangerous for navigation. The concept of a "representative" wave height that came from experienced observers can easily be thought as the first way to characterize the sea state. In fact, the idea of the "significant wave height" derives from the perception of this characteristic observed wave height. Concept that is first defined by Sverdrup and Munk (1946) as the average of the highest third from a group of observed waves ($H_{1/3}$) to describe the random waves from a statistical approach. This last point is of great importance for the characterization of the sea states. Clearly, a mean wave height ($\overline{H}$) and estimated wave period (T) from a recorded time series can be a simple way to describe the wave conditions, and might be of use for a very narrow set of applications. On the other hand, extremely detailed raw information by itself often increases confusion. It is thus more efficient to analyze the evolution and characteristics of certain properties over time scales much larger than a single wave period or distances much larger than a wavelength. In order to do this, it is preferable to follow the statistical and moreover the spectral approach.

The spectral analysis of waves is based on the Fourier method. A time series of recorded sea surface elevations can be considered as the discrete sum of many sinusoidal wave components, each of them with their particular frequency (f_i), and where their phases are commonly considered as random and uniformly distributed between 0 and 2π.

The randomness of phases implies that the phase of a particular recorded wave component i is completely uncorrelated to any other component j. Normally a long elevations' time series is divided into M realizations thus, a realization m of the recorded time series is expressed in terms of the Fourier series as follows,

$$\eta_m(t) = \sum_{i=1}^{N} a_{m,i} \cos\left(2\pi f_i t + \Theta_{m,i}\right) \tag{I.1}$$

with $\eta_m(t)$ the elevation time series of the realization m and where, for the Fourier mode i, $a_{m,i}$, f_i, and $\Theta_{m,i}$ are the amplitudes, frequencies and phases.

Then, with the average of all Fourier amplitudes as function of the frequencies one obtain the amplitudes spectrum: $A(f_i) = \langle a_{m,i} \rangle$. Finally, for a given length of the recorded time series (e.g. 30 min) the sea state is considered stationary, which allows the application of the ergodicity theorem and the previously computed mean of m realizations can be considered as a temporal mean. Since the mechanical wave energy (the sum of potential and kinetic) per unit surface of the ocean, for a sinusoidal wave of amplitude a is $E_m = \rho_w g a^2/2$, then the energy at each frequency f_i can be expressed as:

$$\rho_w g \left\langle \frac{1}{2} a_{m,i}^2 \right\rangle = \rho_w g \frac{1}{M} \sum_{m=1}^{M} \frac{1}{2} a_{m,i}^2 \tag{I.2}$$

although normally the $\rho_w g$ term is dropped and the power density spectrum is preferred to avoid dependency on the record length:

$$E(f_i) = \frac{1}{\Delta f} \left\langle \frac{1}{2} a_{m,i}^2 \right\rangle \tag{I.3}$$

In very long records, the frequency interval Δf tends to zero, hence, it is possible to estimate the continuous form of the spectrum $E(f)$.

This derivation, here briefly explained, can be generalized to include wave directionality (Fig. I.1.b). From a 3 dimensional record $\eta(x, y, t)$, the decomposition of wave components can be done in frequency, wavelength and propagation direction. Then the Fourier series to represent the sea surface elevation becomes:

$$\eta_m(x, y, t) = \sum_{i=1}^{P} \sum_{j=1}^{Q} a_{m,i,j} \cos\left(2\pi f_i t + k_i \cos(\theta_j) x - k_i \sin(\theta_j) y + \Theta_{m,i,j}\right) \tag{I.4}$$

where changes in the wave number k_i and frequency f_i are related by the linear dispersion

relation (eq. I.19) and θ_J is the wave propagation direction of the Fourier mode (i,j). Analog to the procedure to obtain the frequency spectrum, the continuous directional spectrum of wave energy density can be expressed as:

$$E(f,\theta) = \lim_{\Delta f \to 0} \lim_{\Delta \theta \to 0} \frac{1}{\Delta f \Delta \theta} \left\langle \frac{1}{2} a_{i,j}^2 \right\rangle \tag{I.5}$$

The frequency spectrum can be obtained by integrating the directional spectrum along the directions dimension:

$$E(f) = \int_0^{2\pi} E(f,\theta) d\theta \tag{I.6}$$

Notice that when the Fourier analysis is applied to a time series, the phases are lost, thus from the wave spectrum it is only possible to reconstruct a "sinthetic" time series of elevations that is statistically similar to the original one.

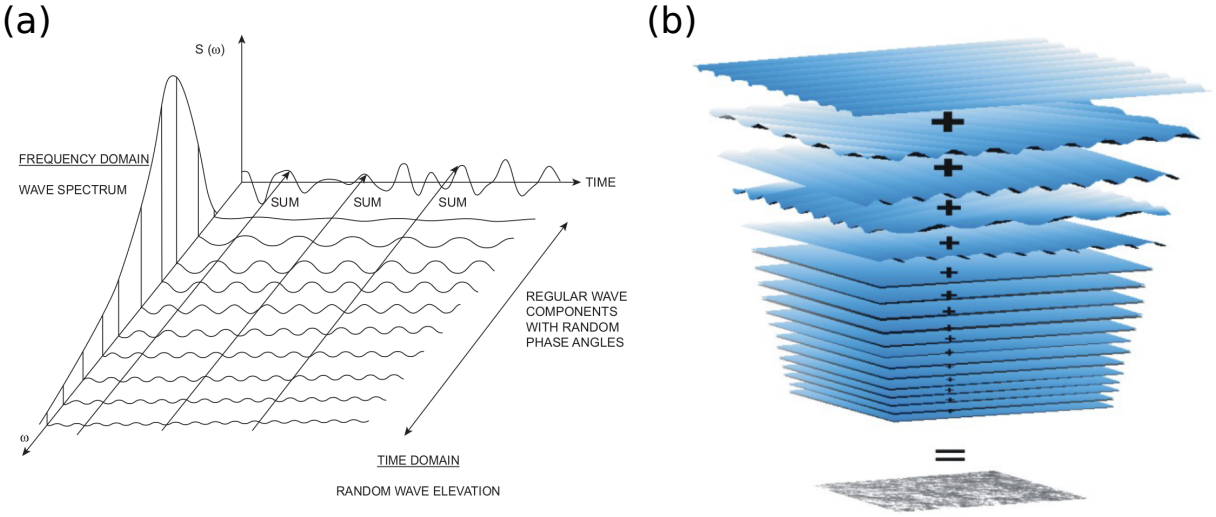

Figure I.1 – (a) Relations between frequency-domain and time-domain representation of waves when Fourier analysis is applied to a 1-dimensional elevation time series. Adapted from figure 5.4 in Bai and Jin (2016). (b) Reconstruction of a given sea state from the superposition of several waves' planes with different directions and wavelength. Adapted from Pierson et al. (1955b).

From the spectral representation of waves, different characteristics of the sea state can be retrieved. First inferred by simple observation, like the presence of swells coming from different directions, a developing wind sea, or the peak period (T_p) and peak wave direction (D_p) indicating where the highest spectral energy is (Fig. I.2). Other general parameters that characterize average quantities like the significant wave height (eq. I.7),

mean periods (eq. I.8) or mean direction (eq. I.9) can be computed by integrating along the frequencies and direction dimensions,

$$H_s = 4\sqrt{\int_0^{\infty}\int_0^{2\pi} E(f,\theta)d\theta df} \tag{I.7}$$

$$T_{m0,p} = \left[\frac{\int_0^{2\pi}\int_0^{\infty} f^n E(f,\theta)df\,d\theta}{\int_0^{2\pi}\int_0^{\infty} E(f,\theta)df\,d\theta}\right]^{-1/n}, \quad n=-1,1,2 \tag{I.8}$$

$$D_m = \arctan\left(\frac{\int_0^{2\pi}\int_0^{\infty}\sin(\theta)E(f,\theta)df\,d\theta}{\int_0^{2\pi}\int_0^{\infty}\cos(\theta)E(f,\theta)df\,d\theta}\right) \tag{I.9}$$

in practice, for integration along the frequencies dimension, the upper limit of the integral is taken as the maximum frequency of the instrument when data comes from measurements, or the maximum frequency considered in a numerical model. For a narrow frequency band spectrum, H_s (also named H_{m0}) computed from eq. I.7 is approximately equal to $H_{1/3}$ (Longuet-Higgins, 1952). Since the spectral approach to analyze the wave fields has been widely adopted, it is common to use H_s as the "representative" wave height of the sea state, and it is normally the first parameter used to characterize it.

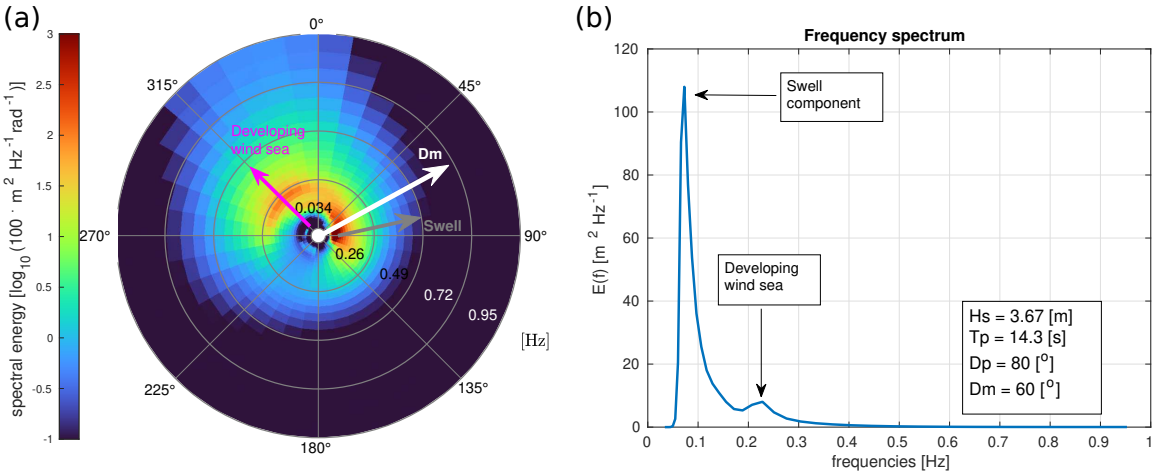

Figure I.2 – Mixed swell and wind sea conditions simulated at buoy 46246. (a) Directional wave spectrum from simulation. (b) Frequency wave spectrum computed from directional spectrum. Simulation result from January 23 of 2011, 03:00:00 UTC. Arrows in (a) indicate overall mean direction D_m (white), mean wind sea direction (magenta) and the swell mean direction (gray), very similar to the overall peak direction. Direction notation is "waves travelling to".

Two important assumptions have been made to this point. First considering the sea

states stationary within a specific time window, and second, the fact that k_i and f_i are related following the linear wave theory. In fact, compared to the evolution of a single wave, the evolution of the wave spectrum (or wave action, as explained in I.4) is slow, and it is one of the main features that allow for wave modelling. The use of linear wave theory implies that spectral models predict well wave (or energy) propagation phenomena like refraction and shoaling, but since the assumption of slowly varying depths is employed, they do not resolve highly non linear effects like depth induced wave breaking. These elements are typically added as "parameterizations", numerical expressions developed to represent physical processes. In general, in spectral models, all processes related to the balance of generation, growth and dissipation are included as separate terms. This separation is also needed when working with coupled models (e.g. wave-atmospheric) since each of these elements correspond to a flux of energy and momentum between models in the coupled system. These terms are further discussed in section I.4, and specific parameterizations to account for wave growth, deep waters wave breaking, bottom friction and nonlinear wave interactions are analyzed throughout this document.

Progress in wave modeling capabilities for open ocean applications have allowed to reduce overall errors of parameters describing mean properties of the sea states like H_s, $T_{m0,1}$ or D_m obtained from the full integration of the spectral energy. Most of these improvements are due to the constant development of the physical parameterizations and the empirical adjustments to fit observations. Although this latter approach has helped to simulate wave parameters that are highly correlated with measurements in some regions, the wave spectra shape and evolution can still largely differ (Resio et al., 2016). Differences that, to a large extent, are attributed to inaccuracies in the representation of the energy balance in wave generation, evolution and dissipation processes.

In general the quality of numerical wave model output is a function of at least three factors, in decreasing order of importance. First, the accuracy of forcing fields (e.g. Cavaleri and Bertotti, 1997), second, the realism of parameterization of processes representing spectral wave evolution (e.g. Ardhuin et al., 2010) and third, the numerical choices made to integrate the Wave Action Equation (WAE), namely discretization and numerical schemes (e.g. Roland and Ardhuin, 2014; Tolman, 1995a).

I.1.2 Importance of the sea sates characterization

Spectral wave models have largely evolved since they were first introduced in the 1950s (e.g. Gelci, 1957), in the present days they are routinely used for many applications in

Earth sciences and engineering. Global and regional wave datasets generated through models such as WAM (Bidlot, 2005; WAMDI, 1988) or WAVEWATCH III®(The WAVEWATCH III ® Development Group, 2019) have helped to improve our knowledge of the wind-generated wave dynamics. Improvements on the modeled sea states are largely related to the progressive understanding of the feedback between ocean and atmospheric processes and their effect on the weather/climate system (Cavaleri et al., 2012). The estimation of ocean-atmosphere interactions (e.g. surface drift and air-sea fluxes, sea surface albedo) are highly dependant on the sea states characteristics and are key to predict and understand the global climate trends and variability (Fig. I.3).

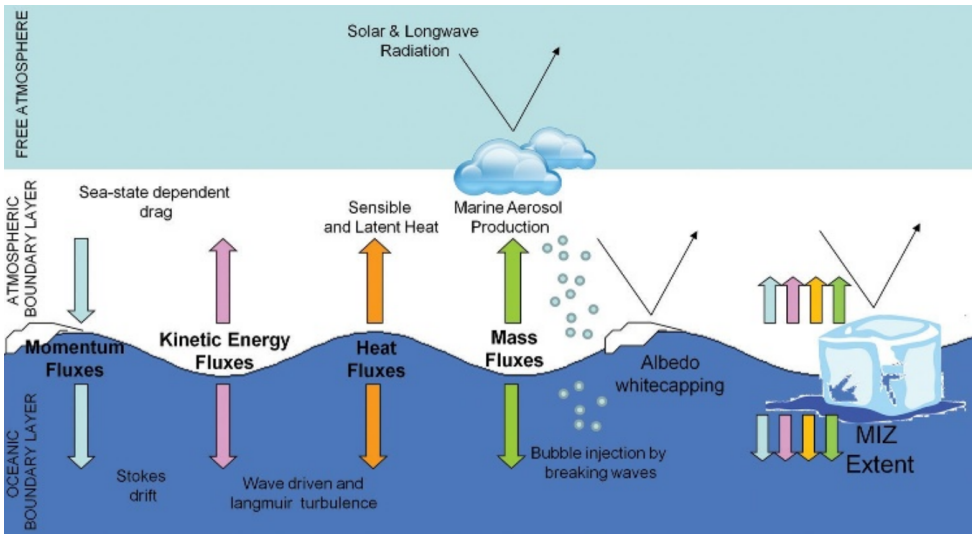

Figure I.3 – Schematic view of the influence of waves on air–sea exchanges. Adapted from figure 1.A in Cavaleri et al. (2012)

Traditional structural studies in ocean and port engineering relies on the quality of large wave datasets to estimate operation and design conditions. Studies of nearshore dynamics like littoral currents, the generation of infra-gravity waves and their effect on sediment transport (e.g. Franz et al., 2017) or the beach profile changes, directly depend on the characteristics of the directional spectra (Baldock et al., 2010), especially during the evolution of extreme events (Delpey, 2012). Moreover, an accurate characterization and prediction of these latter events, like the storm surge presented in Fig. I.4, are key for hazard assessments and management in coastal communities (e.g. Samaras et al., 2016). In the last 2 decades, and in the context of climate change counter measures, larger efforts have been directed towards reducing the uncertainties in wave energy resource assessments, which requires higher temporal and spatial resolution, and a proper

representation of complex wave interactions in coastal environments (e.g. García-Medina et al., 2021; Wu et al., 2020).

In more recent years, new applications of the models, for example in seismology (e.g. Lecocq et al., 2019) or infrasound monitoring (De Carlo et al., 2021) have made possible by the ever increasing quality of modeled wave spectra and associated parameters.

Figure I.4 – Storm surge event in the coasts of Valparaíso, Chile (August 8, 2015). Photograph provided by Patricio Winckler (senior researcher at Universidad de Valparaíso).

I.1.3 Satellite altimetry and measurement of waves

The significant wave height (SWH) was first measured from space with Skylab in 1974 and became a routine measurement with the GEOSAT (Geodetic/Geophysical Satellite) altimeter in 1985 (McConathy and Kilgus, 1987). The satellite mission lasted only a few years due to the degradation of the altimeter's output power (Shapiro, 1988), but it marked the start of an unprecedented source of oceanographic and geodesic data. It is only after 1990 that measurements from space became more frequent after the launch of the European Remote-Sensing Satellite (ERS-1) in 1991, with a continuously growing satellite constellation to date (Fig. I.5.a). The combined missions of satellite radar altimeters since the early 90's have allowed to drastically increase the spatial and temporal coverage of many ocean parameters, including wind speed, significant wave height (Fig. I.5.b) or the mean dynamic sea surface topography. At the same time, these growing datasets have been used in many applications like numerical models validation, data assimilation (e.g.

Aarnes et al., 2015), estimation of global geostrophic currents, wind and wave climatology or estimation of long term trends of these parameters (e.g. Stopa et al., 2019; Young et al., 2011) (see Fig. I.6).

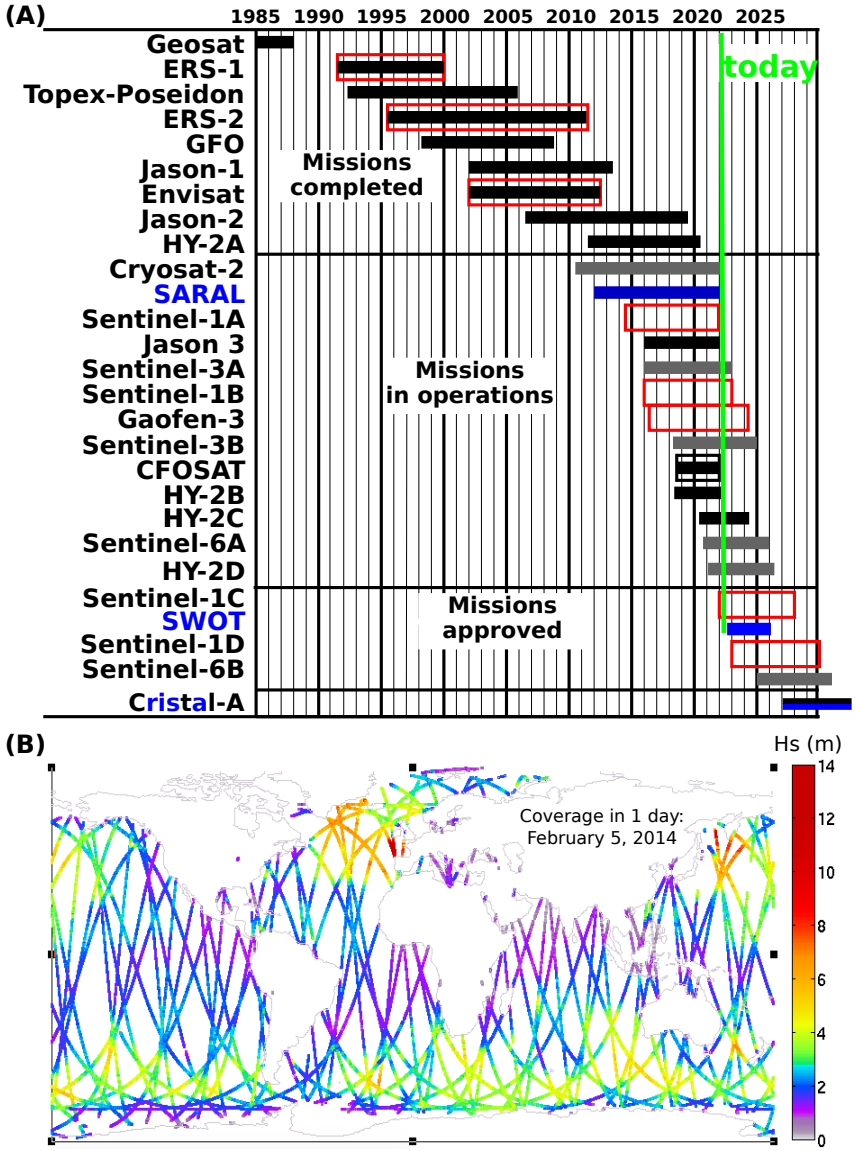

Figure I.5 – (a) Time line of completed, on going, and future satellite missions. (b) Example of 1 day altimeter coverage of Jason-2, Cryosat-2 and SARAL. In (a) continuous lines show missions with altimeter instrument. In (a) Ka and Ku bands in black and blue respectively. Red rectangles represent instruments with SAR mode.

The altimeter is a nadir-looking instrument, which means that it points almost directly below the satellite tracing a ground track pattern that depends on the selected orbit

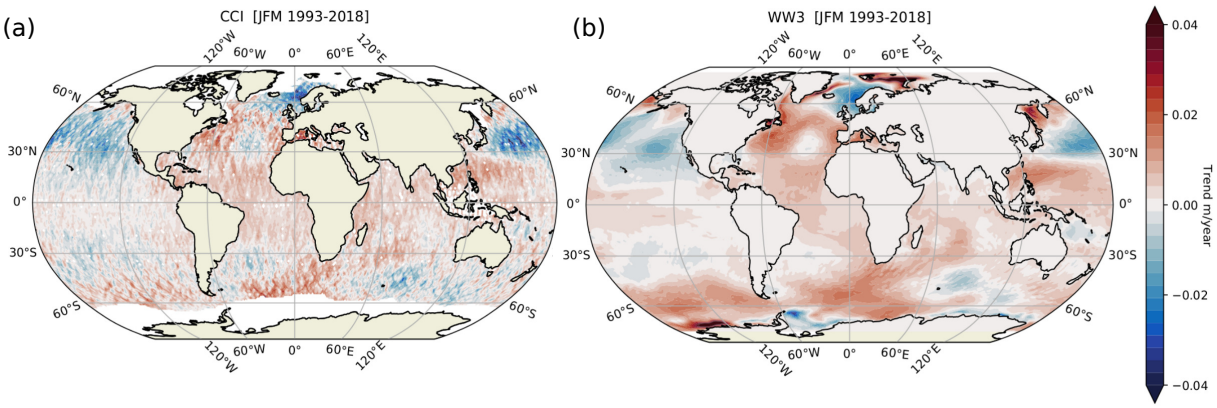

Figure I.6 – H_s JFM global trends (1993-2018) computed with (a) Sea State CCI V1 altimeter data (Piollé et al., 2020) and (b) with WAVEWATCH III generated hindcast (Alday et al., 2021). Trend estimations provided by Antoine Hochet.

geometry. The repetition cycle of this ground track, typically between 3 to 10 days, also depends on the orbit characteristics, namely inclination and altitude. The footprint of the instrument's (pencil-like) beam on the ground (A_f) as defined in Chelton et al. (2001) is "the area on the sea surface within the field of view subtended by the beam width (full width at half power) of the antenna gain pattern". The area depends on the flight height and the radars frequency band, commonly Ku (10.9-22.0 GHz) or Ka (like SARAL), with diameters ranging from 4 to 10 km. In general it is desired a footprint area small enough so that the wave field or sea surface roughness can be considered homogeneous.

The basic concept of altimetry is to measure the return time of a pulse sent by the active radar towards the ocean surface, with celerity c at a distance R of the sea surface (also called range; Fig.I.7.a). In essence, the return time of a pulse of short duration τ is $t = 2R/c$ (with $\tau \ll t$ and c the speed of light). The electromagnetic radiation power received back to the instrument (P_r) is:

$$P_r = T^2 P_e \frac{\lambda_0^2}{(4\pi)^3 R^4} G^2 \sigma \tag{I.10}$$

where λ_0 is the pulse wavelength, G the antenna gain, P_e the emitted power from the radar, T^2 the two-way atmospheric transmittance, and σ the backscatter coefficient.

Given its shape, the emitted pulse progressively intersects the sea surface, a process that is analyzed as a series of "iluminated" fractions of the same area, of the total radar footprint area at equidistant times (range gate, see Fig. I.7.b). The echo waveform of a sent pulse has a characteristic form described by the Brown model (Brown, 1977), which

is related to the radiation power detected at each range gate. As schematized in Fig. I.7.c, 5 basic parameters can be defined:

- Epoch at mid-height: Gives the time delay of the expected return of the radar pulse (estimated by the tracker algorithm) and thus the time the radar pulse took to travel the range (R) and back again.
- The amplitude of the useful signal (P): P with respect to the emission amplitude gives the backscatter coefficient σ_0.
- The thermal noise P_o.
- The leading edge slope, which is used to relate the echo signal to the significant wave height (SWH).
- The trailing edge slope, which, depending on the radar system is linked to a mis-pointing of the antenna or the beam-width of the antenna pattern.

Ocean waves information is derived from the shape of the return waveform, SWH are proportional to the slope of the leading edge, with a flatter slope related to larger wave heights. If we imagine an ideal "flat" ocean surface, the return signal of a pulse is almost non scattered, thus each of the illuminated areas are smooth at each range gate (as schematized in Fig. I.7.b) inducing a sharp increase of the leading edge. On the other hand, in the presence of rough seas or large swells, the return signal of a pulse becomes scattered with different illuminated areas, which causes the amplitude of the wave form to increase more gradually over time (Fig. I.7.d).

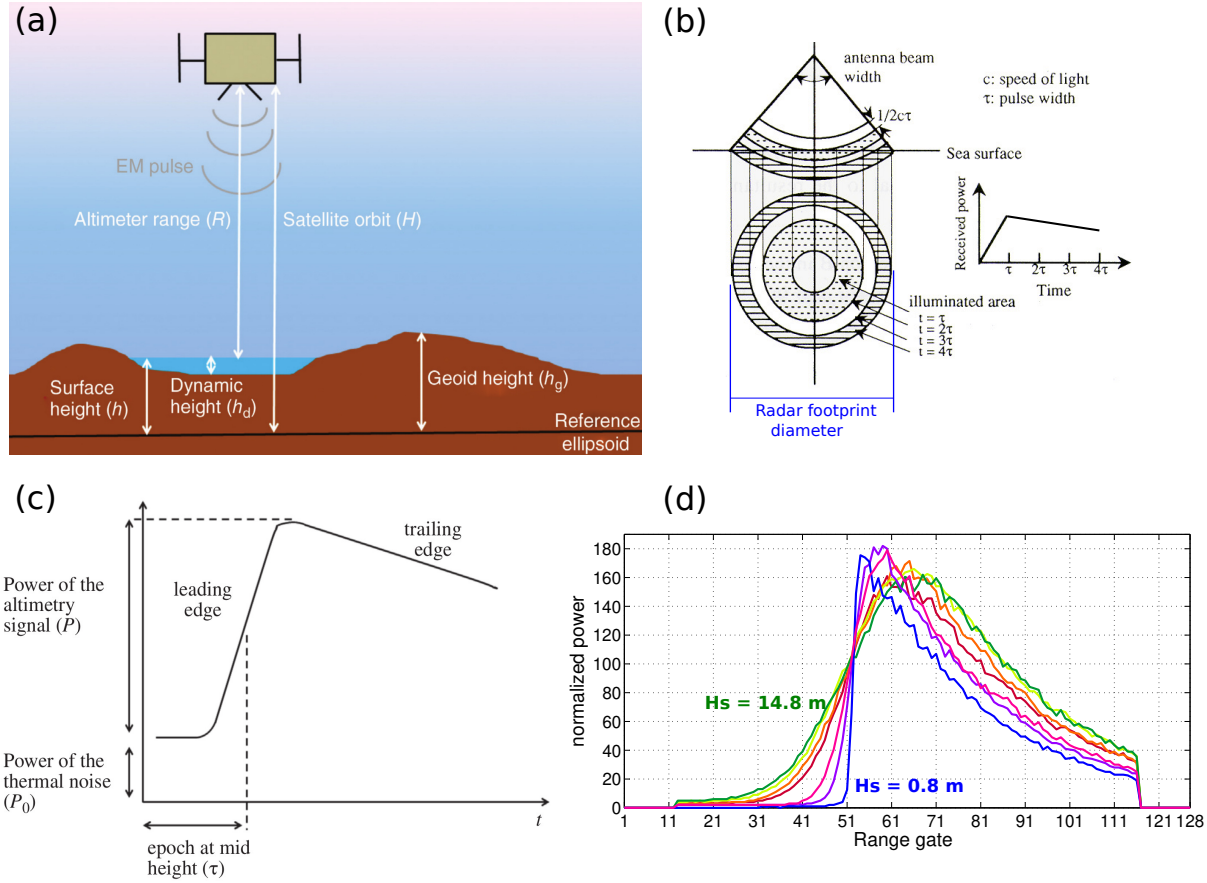

Figure I.7 – (a) Principle of radar altimetry measurement (adapted from Frappart et al., 1999). (b) Scheme of the change of illuminated area in time (adapted from http://sar.kangwon.ac.kr/etc/rs_note/rsnote/cp4/cp410.htm). (c) Scheme of the theoretical ocean waveform from the Brown model (Brown, 1977). (d) Examples of measured waveforms for small wave heights (blue) to large wave heights (green) recorded by SARAL-AltiKa.

I.1.4 Scientific questions

It is clear that there have been many advances in wave models in the last 60 years since Gelci (1957), with constant efforts to optimize numerical aspects and the parameterizations included to represent physical processes (e.g. Ardhuin et al., 2010; Hasselmann and Hasselmann, 1985; Janssen, 1991; Leckler, 2013; Romero, 2019). Additionally the advent of the satellite altimetry era has played a large role in the improvement of the forcing fields used in wave models. At global scale namely surface winds and currents. The increasing amount of assimilated data from altimeters in atmospheric and ocean models has helped to reduce the errors in these forcing fields.

As mentioned in I.1.1 the quality of the numerical models' output depends mainly on the accuracy of the forcing fields, the used physical parameterizations and the numerical aspects like spatial and spectral discretization. It is thus of interest to analyze and quantify how these choices influence the simulated sea states characteristics at global scale and in coastal environments. In this context, the present study evolves around 3 main questions:

— What is the effect of combined improved forcing fields and increased resolution in the model setup and how do they affect the simulated sea states?
— How sensitive are the wave parameters and the spectral shape to different parameterizations and to their adjustments?
— What are the main drivers of errors?

I.2 Objectives

The main objective of this thesis is to analyze and improve the characteristics of the simulated sea states. This is done through the study of the effects on wave generation, propagation and dissipation, introduced by changes/adjustments in physical parameterizations, spectral and spatial resolution, and the forcing fields considered. Through the analysis of several model configurations, this work aims to identify those elements that have the most important repercussions in the model output. From the exposed core objective, 3 related specific objectives can be unfolded:

— Improve the model performance at global scale mainly in terms of wave heights distributions and reduction of differences with respect to altimeter data.
— Verify in coastal regions (Atlantic coast of Europe) the effects of the model adjustments done at global scale , and identify other potential sources of errors in intermediate to shallow water depth environments using both in situ and altimeter

measurements.

— Analyze changes in the energy directional distribution of the wave spectrum, due to the implementation of different wave dissipation parameterizations and methods to account for nonlinear wave interactions.

I.3 General methods

Most of the analyses carried out in this document are based on comparisons of different modeled quantities with respect to remote sensing (altimeter), in situ data from buoys, and in some cases with respect to output from models with a different setup. These comparisons are aimed to help identifying the changes introduced in the simulated sea states, that are consequence of modifications applied to the formulations included to account mainly for wave generation, propagation and dissipation processes. The statistical expressions used throughout the document are the Mean Differences (MDIFF, eq. I.11), Normalized Mean Differences (NMD, eq. I.12), Root Mean Squared Differences (RMSD, eq. I.13), Normalized Root Mean Squared Differences (NRMSD, eq. I.14), the Scatter Index (SI, eq. I.15) and the sample Pearson correlation coefficient (CORR, eq. I.16).

$$\mathrm{MDIFF} = \frac{1}{N}\sum(X_{\mathrm{mod}} - X_{\mathrm{obs}}) \tag{I.11}$$

$$\mathrm{NMD} = \frac{\sum(X_{\mathrm{mod}} - X_{\mathrm{obs}})}{\sum(X_{\mathrm{obs}})} \tag{I.12}$$

$$\mathrm{RMSD} = \sqrt{\frac{\sum(X_{\mathrm{mod}} - X_{\mathrm{obs}})^2}{N}} \tag{I.13}$$

$$\mathrm{NRMSD} = \sqrt{\frac{\sum(X_{\mathrm{mod}} - X_{\mathrm{obs}})^2}{\sum X_{\mathrm{obs}}^2}} \tag{I.14}$$

$$\mathrm{SI} = \sqrt{\frac{\sum\left[(X_{\mathrm{mod}} - \overline{X_{\mathrm{mod}}}) - (X_{\mathrm{obs}} - \overline{X_{\mathrm{obs}}})\right]^2}{\sum X_{\mathrm{obs}}^2}} \tag{I.15}$$

$$\mathrm{CORR} = \frac{\sum(X_{\mathrm{mod}} - \overline{X_{\mathrm{mod}}})(X_{\mathrm{obs}} - \overline{X_{\mathrm{obs}}})}{\sqrt{\sum(X_{\mathrm{mod}} - \overline{X_{\mathrm{mod}}})^2}\sqrt{\sum(X_{\mathrm{obs}} - \overline{X_{\mathrm{obs}}})^2}} \tag{I.16}$$

where X_{mod} is a modeled quantity and X_{obs} the reference value of that quantity from observations.

Notice that in the previous expressions the term “difference” is employed instead of

for example, bias or errors. This is done in the spirit of assuming that observations or measurements have limitations and/or intrinsic errors in the data collection and post-process, an thus, they are considered as a reference point instead of an "absolute truth".

Values from CORR and SI should be interpreted carefully. In particular, CORR can be misleading when too many outliers are present in the analyzed sample (Huber, 2004), while a large SI doesn't always relate to a poorer model performance, for example in the presence of slight time shifts, between simulations' results and observations, of highly oscillating quantities. CORR is mainly used in Chapter 2 to compare time series of modeled wave parameters with buoy data and in Chapter 3 to compare modelled acoustic noise with underwater acoustic noise measurements.

Application of these statistical indicators to the bulk of data, for example a complete wave heights' time series from a buoy or a particular location of the model domain, helps to gain an idea of the mean overall performance of the model for the analyzed time window. A more detailed performance assessment can be obtained by applying parameters like the NMD, NRMSD or SI to binned groups of the analyzed variables, and have more insight on the behavior of the simulations' results at specific ranges. The latter approach is extensively used in Chapter 1 to compare model wave heights collocated in time and space to match altimeter measurements (along-track analysis).

I.4 The WAVEWATCH III model

A brief description of the wave numerical model employed throughout this documents is included in the present section. For further details refer to the user manual (The WAVEWATCH III® Development Group, 2019).

WAVEWATCH III (from hereon WW3) is a third generation wave model originally developed at the US National Centers for Environmental Prediction (NOAA/NCEP), based on the work from Tolman (1991) and Tolman (1992). Nowadays it is the core of a community wave modelling framework that aims to include the latest developments in the field of wind-wave modeling dynamics, including processes of generation, propagation and different sources of dissipation.

The model solves the spectral action density balance equation, with the assumption that water depth, currents, as well as the wave field vary on time and space scales that are much larger than variations of a single wave. Physical processes in the governing equation are incorporated as "source terms" which include parameterizations for: Wave growth due

to the action of the wind, different forms to account for nonlinear wave to wave interactions and wave evolution, scattering caused by wave-bottom interactions, bottom friction, triad wave interactions, and dissipation effects due to whitecapping, depth induced breaking, and interactions with mud and ice.

The governing equation is solved in terms of the wave action ($N(k,\theta)$) instead of the energy spectrum ($E(k,\theta)$) because, in general, the wave action is conserved (e.g. Bretherton and Garret, 1970). Wave propagation then is expressed as follows:

$$\frac{DN(k,\theta)}{Dt} = \frac{S}{\sigma} \tag{I.17}$$

$$\sigma = 2\pi/T \tag{I.18}$$

In eq. I.17, the quasi-uniform linear wave theory is applied considering slowly varying depth and currents, which gives the following expressions for the dispersion relation (eq. I.19) and Doppler shift effect that interrelate the phase parameters σ and ω:

$$\sigma^2 = gk\tanh(kd) \tag{I.19}$$

$$\omega = \sigma + \boldsymbol{k}\cdot\boldsymbol{U} \tag{I.20}$$

where DN/Dt represents the total wave action derivative moving with a wave component, and S the net effects of the combined source terms. σ is the relative (or intrinsic) radian frequency observed from a reference frame that moves with the mean current, ω is the absolute wave frequency observed from a fixed frame of reference. T is the wave period, d the mean depth, $\boldsymbol{k}$ is the wave number vector, and $\boldsymbol{U}$ the mean current vector depth and time averaged over the scale of individual waves.

Notice that assuming that depths and currents have small gradients (slowly varying), implies that diffraction can generally be ignored, although this effect can be added later as a source term.

In WW3 wave propagation is done using the conservative Eulerian form of the balance equation (eq. I.17), which conserves the total wave action/energy. The balance equation in Cartesian coordinates used in WW3 is:

$$\frac{\partial N}{\partial t} + \nabla_x \cdot \dot{\boldsymbol{x}} N + \frac{\partial \dot{k} N}{\partial k} + \frac{\partial \dot{\theta} N}{\partial \theta} = \frac{S}{\sigma} \tag{I.21}$$

$$N(k, \theta, \boldsymbol{x}, t) = N \tag{I.22}$$

$$\dot{\boldsymbol{x}} = \boldsymbol{c}_g + \boldsymbol{U} \tag{I.23}$$

$$\dot{k} = -\frac{\partial \sigma}{\partial d}\frac{\partial d}{\partial s} - \boldsymbol{k} \cdot \frac{\partial \boldsymbol{U}}{\partial s} \tag{I.24}$$

$$\dot{\theta} = -\frac{1}{k}\left[\frac{\partial \sigma}{\partial d}\frac{\partial d}{\partial m} + \boldsymbol{k} \cdot \frac{\partial \boldsymbol{U}}{\partial m}\right] \tag{I.25}$$

where $\boldsymbol{c_g} = (c_g \cos(\theta), c_g \sin(\theta))$, s a a coordinate in the direction of θ and m a coordinate perpendicular to s.

For large scale applications eq. I.21 is expressed in spherical coordinates. With longitude λ, latitude ϕ and maintaining the local variance, the balance equation takes the following form:

$$\frac{\partial N}{\partial t} + \frac{1}{\cos\phi}\frac{\partial}{\partial \phi}\dot{\phi} N \cos\theta + \frac{\partial}{\partial \lambda}\dot{\lambda} N + \frac{\partial}{\partial k}\dot{k} N + \frac{\partial}{\partial \theta}\dot{\theta} N = \frac{S}{\sigma} \tag{I.26}$$

$$\dot{\phi} = \frac{C_g \cos\theta + U_\phi}{R} \tag{I.27}$$

$$\dot{\lambda} = \frac{C_g \sin\theta + U_\lambda}{R\cos\phi} \tag{I.28}$$

where R is Earth's radius, and U_ϕ and U_λ are the projected current components.

The net source term S includes all the parameterizations included to account for energy input, evolution of the spectrum and sink terms. In deep waters there are 3 main elements considered. First, the (wind) input term S_{in} for atmosphere-wave interaction, which is typically positive during the development of wind seas, but can be negative in the case of swells travelling faster than the wind. Second, the nonlinear interactions term S_{nl} to account for the wave-wave resonant mechanism key in the transfer of energy from high frequencies (short waves) to the low frequencies of the spectrum. And third, the wave-ocean interactions term dominated by wave breaking dissipation S_{ds}.

S_{in} describes better the dominant exponential wind-wave growth process, which is why for model initialization a linear input term S_{ln} can be added to provide a more realistic initial wave growth. An in-depth analysis of the changes introduced to the seas states through adjustments applied to S_{in} is presented in Chapter 1. Effects due to changes and

different formulations employed for S_{nl} and S_{ds} are discussed in Chapter 3.

Processes affecting wave propagation in intermediate to shallow waters, like triads interactions, energy dissipation due to bottom friction or, in very shallow conditions, depth induced wave breaking, can be added with S_{tr}, S_{bot} and S_{db} respectively. A detailed analysis on the effects of bottom friction parameterizations is included in Chapter 2. Other source terms available in WW3 are wave-ice interactions (S_{ice}), scattering of waves (S_{sc}), wave reflection in shorelines (S_{ref}). Thus, the net source term expression can be expressed as:

$$S = S_{\mathrm{ln}} + S_{\mathrm{in}} + S_{\mathrm{nl}} + S_{\mathrm{ds}} + S_{\mathrm{bot}} + S_{\mathrm{db}} + S_{\mathrm{tr}} + S_{\mathrm{sc}} + S_{\mathrm{ice}} + S_{\mathrm{ref}} \tag{I.29}$$

Chapter 1

Effects of improved forcing and spectral resolution at global scale

1.1 Introduction

The global hindcasts presented in Rascle et al. (2008) and Rascle and Ardhuin (2013), and the Arctic hindcast of Stopa et al. (2016b) are unique in providing wave parameters in an "Earth System" context, including wave-related fluxes of momentum and energy between the ocean, atmosphere and sea ice. These hindcasts have been used in a wide range of applications, including as a source of boundary conditions for coastal models (Boudière et al., 2013; Roland and Ardhuin, 2014), air-sea fluxes and upper ocean mixing (Wunsch and Ferrari, 2009), surface drift of kelp or plastics (Dobler et al., 2019; Fraser et al., 2018; Onink et al., 2019), and the investigation of microseisms (e.g. Nishida and Takagi, 2016; Retailleau et al., 2017). For most open ocean regions, the accuracy of significant wave height (H_s) estimates is typically better than 10%, with great benefits for the safety of life at sea, but for some regions, in enclosed seas, regions of strong currents, and near the sea ice, H_s errors typically exceed 20%, and other parameters can be much less accurate, in particular the shape of the frequency spectrum, the height of swells or the directional spreading (Stopa et al., 2016b). The reasons for these errors, and some first steps to reduce them, are the main topic of the present chapter.

A set of performance analyses are carried out at global scale using mainly wave heights retrieved from altimeter measurements. The proposed analyses are aimed to identify the influences of the changes in the wind-wave generation and swell damping, forcing fields and spectral resolution over the simulated H_s. Additionally, a brief first discussion on alternative parameterizations that can lead to improvements for some parameters most sensitive to the higher frequencies of the wave spectrum but that, so far, have not led to

improvements in H_s estimates is included.

The chapter is organized as follows: Expressions used to assess the model's performance are described in section 1.2, the effect of adjustment to model parameterizations is presented in section 1.3, the impact of forcing field choices in section 1.4, and the influence of model discretization in section 1.5. In section 1.6, a first discussion on alternative parameterizations and their effect in wave directionality. The global validation presented in section 1.7 shows a clear improvement compared to sea state parameters produced by Rascle and Ardhuin (2013) and, for specific conditions, also an improvement on the H_s estimates in the ERA5 reanalysis. Conclusions follow in section 1.8.

The content of this chapter has been published in Alday et al. (2021).

1.2 Method

The normalized root mean square difference (NRMSD), scatter index (SI) and normalized mean difference (NMD) were employed to assess the model - satellite or model - buoy discrepancies and its change when model parameterizations, forcing or discretization are modified. These statistical parameters were calculated for the entire domain and over a set of specific ocean regions (defined in table 1.3), for each 1-year test in table 1.2. They are defined as follows,

$$\mathrm{NRMSD}(X) = \sqrt{\frac{\sum(X_{\mathrm{mod}} - X_{\mathrm{obs}})^2}{\sum X_{\mathrm{obs}}^2}} \tag{1.1}$$

$$\mathrm{SI}(X) = \sqrt{\frac{\sum\left[(X_{\mathrm{mod}} - \overline{X_{\mathrm{mod}}}) - (X_{\mathrm{obs}} - \overline{X_{\mathrm{obs}}})\right]^2}{\sum X_{\mathrm{obs}}^2}} \tag{1.2}$$

$$\mathrm{NMD}(X) = \frac{\sum(X_{\mathrm{mod}} - X_{\mathrm{obs}})}{\sum X_{\mathrm{obs}}} \tag{1.3}$$

where $\mathrm{X_{obs}}$ and $\mathrm{X_{mod}}$ are the altimeter significant wave heights (denoised) and the modelled H_s respectively. For the tuning process, $\mathrm{X_{obs}}$ is the along-track data from the altimeter, and $\mathrm{X_{mod}}$ is obtained by interpolating the model output in space and time from the closest 4 grid points, into the position of the altimeter measurement. For analysis of the spatial distribution of NMD and SI (global map), satellite tracks are re-gridded to match the model spatial discretization, hence $\mathrm{X_{obs}}$ and $\mathrm{X_{mod}}$ are the observed and modelled H_s at a given spatial point (longitude, latitude) of the modelled domain.

Note that other normalizations could be used (Mentaschi et al., 2015), and in particular a larger scatter index is not always the indication of a poorer model performance, in particular in the presence of large biases or large fluctuations.

We particularly looked at differences for different ranges of observed values of H_s, binning all the model output as a function of the satellite values. In general, for the model's performance assessment, attention was only paid to H_s larger than 1.0 m because H_s smaller than 0.75 m is not very accurate due to limited sampling of the signal associated with the radar bandwidth (Ardhuin et al., 2019b; Smith and Scharroo, 2015). All along-track performance analyses were done with wave heights bins of 0.25 m width.

1.3 Global model setup

1.3.1 Forcing fields

Because waves are forced by the wind, are damped by sea ice, and are strongly modified by currents, any improvement in the knowledge of these three forcing fields should result in better wave model results.

One of the main features in the generation of the wave hindcast analyzed in the present chapter, is the utilization of the wind fields from the fifth generation ECMWF atmospheric reanalyses of the global atmosphere, ERA5 (Hersbach et al., 2020), and the introduction of satellite-derived merged surface current product that combines geostrophic and Ekman currents, as produced by the Copernicus Marine Environment Monitoring System (CMEMS). The ERA5 reanalysis was developed using 4D-Var data assimilation from the Integrated Forecast System (IFS) model cycle 41r2. The number of observations assimilated from different measurement sources goes from 0.75 million per day in 1979 to approximately 24 million in 2018. The hourly output wind fields with a 31 km horizontal grid resolution, represents a clear increase in detail compared with some of its predecessors, like ERA-Interim (Dee et al., 2011). Still, the limited horizontal resolution makes the ERA5 wind fields less well resolved than those of recent ECMWF operational analyses Tco1279 Gaussian grid with an equivalent resolution of 9 km. Rivas and Stoffelen (2019) showed that ERA5 winds have a root mean square difference with the ASCAT winds that is 20% lower compared to ERA-Interim. Still, at wind speeds above 20 m/s, ERA5 biases may be as large as -5 m/s (Pineau-Guillou et al., 2018), which should have a very important impact on waves modeled with ERA5 winds.

The surface current fields were taken from the CMEMS-Globcurrent product (Global Ocean Multi Observation Product, MULTIOBS_GLO_PHY_REP_015_004), with a resolution of 3 hour in time, and 0.25 degrees in latitude and longitude. This current field is the sum of geostrophic and Ekman components based on the method of Rio et al. (2014), using an updated mean dynamic topography (MDT) from CNES-CLS (Mulet et al., 2021), which is key for the reconstruction of the ocean absolute dynamic topography from altimetry data. With the geostrophic approximation, the MDT is used to estimate surface currents.

Finally, the ice concentration is taken from the Ifremer SSMI-derived daily product (Girard-Ardhuin and Ezraty, 2012). For ice thickness, that matters most near the ice edge where it is poorly known, a constant 1 m ice thickness was used. Partial blocking of waves by icebergs is represented following Ardhuin et al. (2011) using the Ifremer-Altiberg icebergs distribution database (Tournadre et al., 2015).

1.3.2 Adjusted parametrizations and parameters

Atmosphere-wave interactions include both, wave generation as parametrized by Janssen (1991) with modifications by Bidlot et al. (2005) and Bidlot et al. (2007), and swell damping caused by the air-sea friction effect described by Ardhuin et al. (2009). The details and adjustments of these parametrizations are described in Ardhuin et al. (2010), and Leckler (2013), here a brief description of only those parameters adjusted in the present work is included. A more comprehensive description can be found in The WAVEWATCH III ® Development Group (2019).

In particular, the wind input source term was reduced by using a modified friction velocity u_* with a frequency dependent term u'_*, similar to what was done by Chen and Belcher (2000). Eqs. (20) in Ardhuin et al. (2010) is:

$$S_{\rm atm}(f,\theta) = S_{\rm out}(f,\theta) + \frac{\rho_a}{\rho_w}\frac{\beta_{\rm max}}{\kappa^2}\exp(Z)Z^4\left(\frac{u_*}{C}\right)^2 \tag{1.4}$$

$$\times \max\{\cos(\theta-\theta_u),0\}^p \sigma F(f,\theta) \tag{1.5}$$

where: $S_{\rm out}$ is the energy flux from the ocean to the atmosphere (swell dissipation term), Z= $\log(\mu)$, with μ the dimensionless critical height as given by Janssen (1991, eq. 16). $\rho_{\rm a}$ is the air density, $\rho_{\rm w}$ the water density and κ is von Kármán's constant. C is the wave phase speed, θ the wave direction, $\theta_{\rm u}$ the wind direction, and σ the wave relative

frequency ($2\pi/f_r$, observed from a reference frame moving with the mean current).

In eq. (1.4) $\beta_{\max}$ is a non-dimensional wind-wave growth coefficient that has been used as a tuning parameter to calibrate for wind strength biases (e.g. Stopa et al., 2019). The tuning of this parameter will be revisited for ERA5 winds in the present study.

The swell dissipation parameterization is based on observations of ocean swell evolution from satellite data (Ardhuin et al., 2009). It includes expressions to take into account the effects of the transitions from (linear) viscous boundary layer to (non-linear) turbulent boundary layer. The smoothing between these two regimes accounts for the Rayleigh distribution of wave heights (Perignon et al., 2014). The negative part of the wave-atmosphere interaction, is thus parameterized as follows,

$$S_{\rm out}(k,\theta) = \quad r_{\rm vis} S_{\rm out,vis}(k,\theta) + r_{tur} S_{\rm out,tur}(k,\theta), \tag{1.6}$$

where the two weights give the relative importance of viscous and turbulent attenuation, and are controlled by the ratio of the significant Reynolds number $\mathrm{Re} = 2u_{\rm orb,s}H_s/\nu_a$ and its critical value $\mathrm{Re_c}$.

$$r_{\rm vis} = \quad 0.5\left[1 - \tanh\left((\mathrm{Re} - \mathrm{Re_c})/s_7\right)\right] \tag{1.7}$$

$$r_{\rm tur} = \quad 0.5\left[1 + \tanh\left((\mathrm{Re} - \mathrm{Re_c})/s_7\right)\right]. \tag{1.8}$$

Based on the analogy with oscillatory bottom boundary layers, $\mathrm{Re_c}$ was initially set to 1.5×10^5.

Wave energy loss to the ocean is dominated by wave breaking, and parameterized following the saturation-based breaking ideas of Phillips (1985). An ad hoc "cumulative term" was added to enhance the dissipation of relatively short waves (Ardhuin et al., 2010; Banner and Morison, 2006). Alternatives are discussed in section 5.

Finally, to reduce computational costs, the Discrete Interaction Approximation (DIA, Hasselmann and Hasselmann, 1985) is employed to represent the 4-wave nonlinear interactions. This rather crude parameterization induces errors that are partly corrected by the other adjusted source terms in the Wave Action Equation (Banner and Young, 1994).

1.3.3 Spectral and spatial discretization

The wave spectrum is discretized in 24 directions, equivalent to a 15° directional resolution, and 36 exponentially spaced frequencies from 0.034 to 0.95 Hz, with a 1.1 increment factor from one frequency to the next. The selected frequency range represents a departure from previous hindcasts (e.g. Rascle and Ardhuin, 2013), in which a narrower frequency range was employed, from 0.037 to 0.71 Hz. Although the parameterizations used here are not very accurate for frequencies above 3 times the wind sea peak (e.g. Peureux et al., 2018), the extension to higher frequencies allows to better capture the variability of the wave spectrum for very low wind speeds or very short fetches. The lower frequencies are there to let the spectrum develop for the most severe storm cases (Hanafin et al., 2012). The third order Upwind Quickest advection schemes (Leonard, 1991) was used for both spatial and spectral advection, and the correction for the Garden Sprinkler Effect proposed by Tolman (2002).

All the model testing and tuning presented in section 1.3.4 was performed over a near-global grid with a spatial resolution of 0.5°, from 78° S to 83° N in latitude. However, all the other results, including the final hindcast, use a multi-grid system (Chawla et al., 2013; Tolman, 2008) in which regional grids provide a refinement near the coasts, the ice edge, and in regions of strong currents. A total of 7 nested grids were placed within the global grid, 6 regular grids and 1 curvilinear grid for the Arctic region. Details of the nested grids are provided in table 1.1 and Fig. 1.1. As shown in Fig. 1.1, the boundaries of the high resolution domains (in color) generally follow the coast at 500 km distance, including regions around Hawaii and the Tuamotus for the East Pacific grid, and the Azores for the North-East Atlantic grid. The regions in white are only covered with the global 0.5 degree resolution. The boundary conditions from a lower rank grid are taken at the edges of the colored regions in Fig. 1.1, and the higher rank grid results are spatially averaged to give the lower rank grid solution where these overlap (Tolman, 2008).

The benefits of the multi-grid system are particularly discussed in section 1.5.1. Compared to Rascle and Ardhuin (2013), including the Arctic grid allowed to provide a truly global wave hindcast.

1.3.4 Model adjustments

The value of $\beta_{\max}$ in eq. (1.4), s_7 and Re_c in eqs. (1.7) and (1.8) have been adjusted to minimize the model differences against satellite altimeter measurements of H_s by the

Table 1.1 – Nested grids characteristics. Global grid is defined as rank 1.

Sub-Grid Name	**Region**	**Grid type**	**Spatial resolution**	**Rank**
ATNE-10M	North-East Atlantic	regular	1/6°	2
ATNW-10M	North-West Pacific	regular	1/6°	3
AFRICA-10M	Africa	regular	1/6°	3
PACE-10M	East Pacific	regular	1/6°	2
CRB-3M	Carribean Sea	regular	1/20°	3
NC-3M	New Caledonia and Vanuatu	regular	1/20°	3
ARC-12K	Arctic Ocean	curvilinear	12 km	4

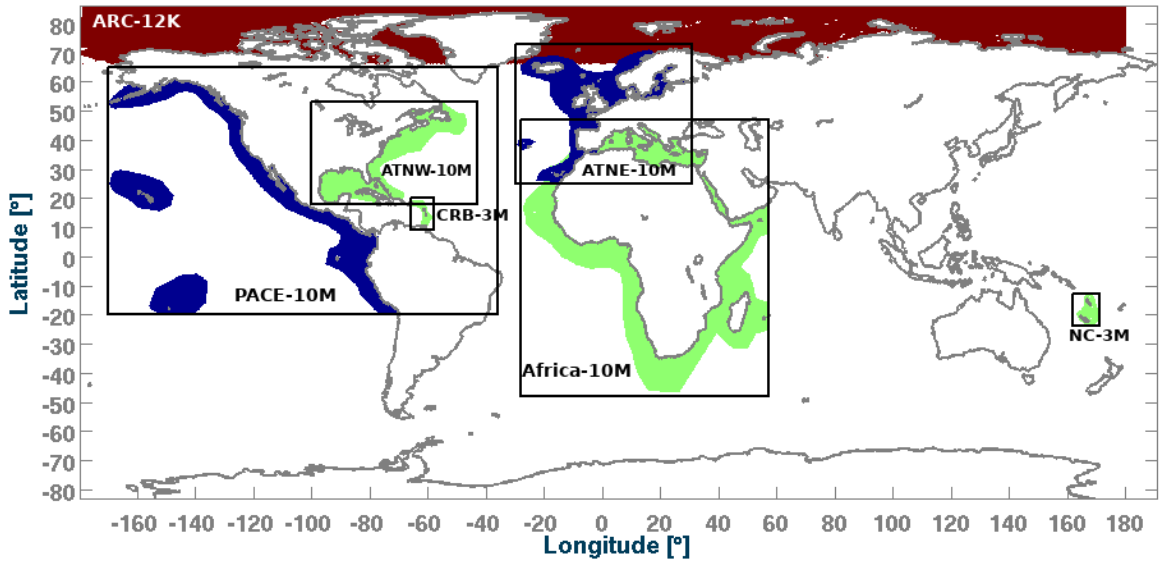

Figure 1.1 – Sub-Grids nesting layout for multi-grid tests. Colors indicate areas where computations are performed and grids' rank in the nesting scheme: Blue is rank 2, Green is rank 3, and Red is rank 4.

Jason-2 mission for the year 2011, using the European Space Agency Climate Change Initiative data set (Dodet et al., 2020). A full year simulation is used for calibration to properly sample all types of sea states in all seasons, and the year 2011 has been chosen because it had the highest wave heights ever recorded (Hanafin et al., 2012), which allows a sampling of the most extreme conditions. The variable used is the "denoised" significant wave height, at 1 Hz (approximately 7 km) resolution. The model tests performed and associated parameter values are listed in table 1.2. All test simulations are 1-year hindcasts with data output frequency of 3 hours. These tests also include some wind bias correction.

This correction is defined as a piece-wise linear correction, with modeled wind speeds above U_c multiplied by a factor x_c as follows,

$$U_{10,\mathrm{corr}} = U_{10,\mathrm{raw}} + x_c \max\left\{U_{10,\mathrm{raw}} - U_c, 0\right\}. \tag{1.9}$$

Table 1.2 – Models parameters and their adjustments, in bold, leading to run T475. All parameters not specified here correspond to the default T471 parameterization (Rascle and Ardhuin, 2013; The WAVEWATCH III ® Development Group, 2019). Variables $\beta_{\max}$, s_7, Re_c, U_c and x_c correspond to namelist parameters BETAMAX, SWELLF7, SWELLF4, WCOR1 and WCOR2 in the WW3 input files (see Appendix A for the full set of parameters).

Name for set of parameters	$\beta_{\max}$	$\mathbf{s_7}$	$\mathbf{Re_c}$	$\mathbf{U_c}$ (m/s)	$\mathbf{x_c}$
T471f	1.33	3.60×10^5	1.50×10^5	–	–
T471	1.43	3.60×10^5	1.50×10^5	–	–
Bm1.5	1.50	3.60×10^5	1.50×10^5	–	–
Bm1.65	1.65	3.60×10^5	1.50×10^5	–	–
Bm1.7	1.70	3.60×10^5	1.50×10^5	–	–
Bm1.75	**1.75**	3.60×10^5	1.50×10^5	–	–
Bm1.65-W01	1.65	3.60×10^5	1.50×10^5	20	1.05
Bm1.65-W02	1.65	3.60×10^5	1.50×10^5	21	1.05
Bm1.65-W03	1.65	3.60×10^5	1.50×10^5	23	1.08
Bm1.65-W04	1.65	3.60×10^5	1.50×10^5	22	1.05
Bm1.7-W02	1.70	3.60×10^5	1.50×10^5	21	1.05
Bm1.7-W03	1.70	3.60×10^5	1.50×10^5	23	1.08
Bm1.7-W04	1.70	3.60×10^5	1.50×10^5	22	1.05
Bm1.75-W02	**1.75**	3.60×10^5	1.50×10^5	21	1.05
Bm1.75-W03	**1.75**	3.60×10^5	1.50×10^5	23	1.08
Bm1.75-W04	**1.75**	3.60×10^5	1.50×10^5	22	1.05
Bm1.75-W02-s7-01	**1.75**	3.96×10^5	1.50×10^5	21	1.05
Bm1.75-W02-s7-02	**1.75**	4.14×10^5	1.50×10^5	21	1.05
Bm1.75-W02-s7-03	**1.75**	$\mathbf{4.32 \times 10^5}$	1.50×10^5	21	1.05
Bm1.75-W02-s7-03-s4-01	**1.75**	$\mathbf{4.32 \times 10^5}$	1.35×10^5	21	1.05
Bm1.75-W02-s7-03-s4-02	**1.75**	$\mathbf{4.32 \times 10^5}$	1.20×10^5	21	1.05
T475	**1.75**	$\mathbf{4.32 \times 10^5}$	$\mathbf{1.15 \times 10^5}$	21	1.05

Previous parameter settings defined as "T471" were used as a starting point. After gradual increases of $\beta_{\max}$ without changing the other parameters (sets T471f to Bm1.75 as defined in table 1.2), a persistent negative NMD for H_s values larger than 7 m is found, as illustrated in Fig. 1.2. This behavior is expected to be related to an underestimation

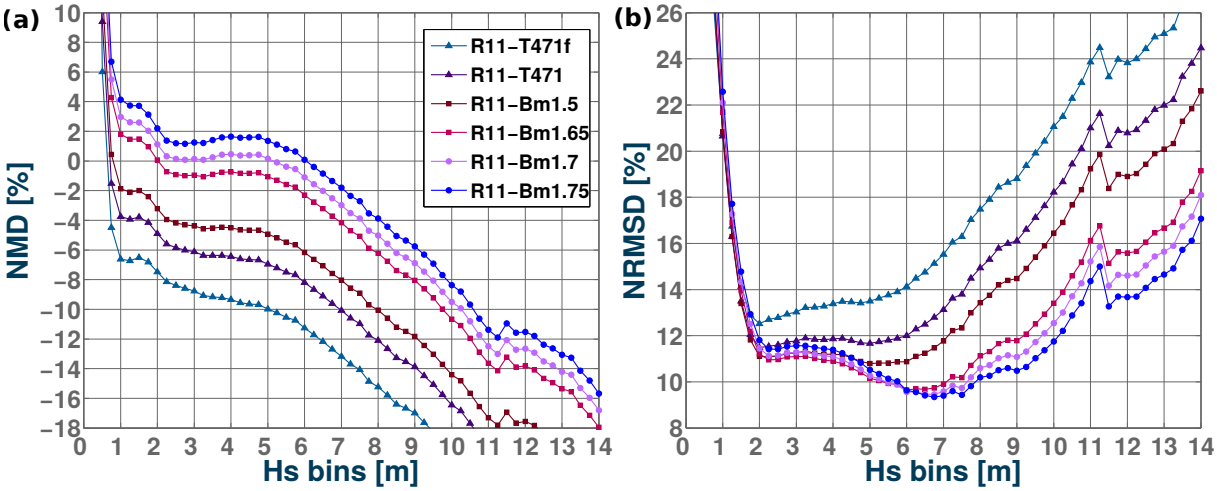

Figure 1.2 – Error statistics for H_s for the $\beta_{\max}$ sensitivity runs (a) Normalized mean difference between model runs – with parameters given in Table 1.2 – and the Jason-2 altimeter data, (b) normalized root mean square difference.

of wind speeds in excess of 25 m/s in ECMWF IFS model results, including the ERA5 data set, as analyzed by (Pineau-Guillou et al., 2018). This wind-speed dependent bias, which is not found with CFSR winds, was the main motivation for introducing the wind speed correction in eq. (1.9).

After setting $\beta_{\max} = 1.75$, wind speed corrections with the parameters Bm1.75-W02 helped to reduce the wave heights underestimation in the 8–14 m range (Fig. 1.3).

The wind speed U_c at which the correction kicks in is consistent with the analysis of models and in situ wind data by Pineau-Guillou et al. (2018), where it was demonstrated that typically strong winds above 20 m/s are underestimated by the ECMWF models.

Once the NMD and NRMSD were reduced, particular attention was paid to the distribution of H_s. The applied changes in $\beta_{\max}$ and wind correction lead to more intense waves in storms and swells radiated from these storms. As a result the swell dissipation necessarily needs further tuning, which is done here by adjusting s_7 and Re_c. This adjustment can be done using wave spectra measurements from buoys, but also using the distribution of H_s. Indeed, the smoothing of swell dissipation was introduced in eq. (1.6) by Leckler et al. (2013) to correct the sharp jump around 2 m in the distribution of modeled H_s that was first noted by D. Vandemark (personal communication, 2012). It was only later rationalized as an effect of the Rayleigh distribution of wave heights with turbulent boundary layers over the largest waves in a group and viscous boundary layers over the lowest waves in a group (Perignon et al., 2014; Stopa et al., 2016b). Fig. 1.4 shows the distribution of

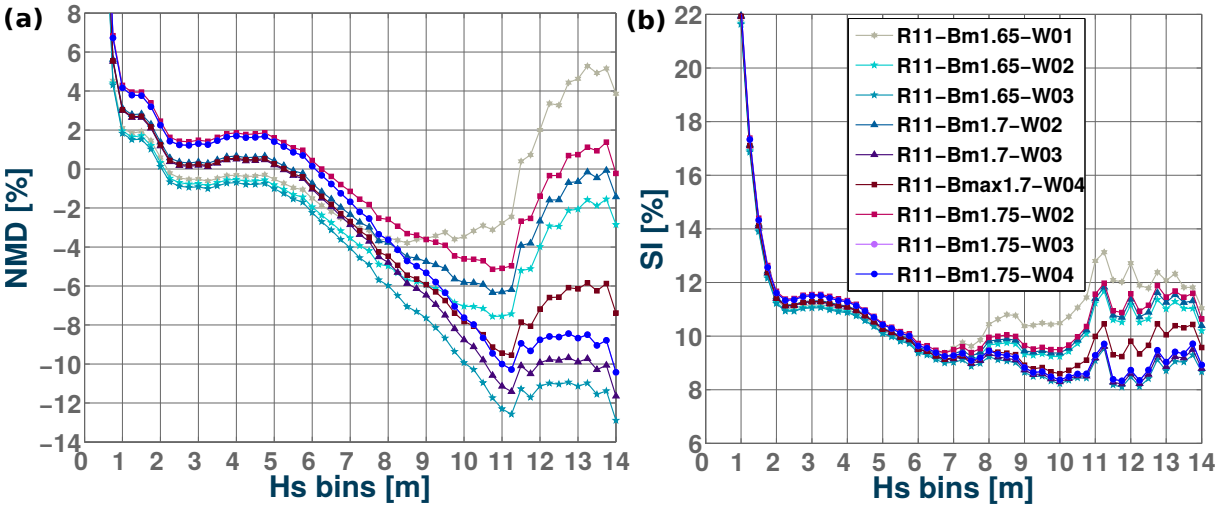

Figure 1.3 – Error statistics for H_s for the wind correction sensitivity runs (a) Normalized mean difference between model runs – with parameters given in Table 1.2 – and the Jason-2 altimeter data, and (b) scatter index.

H_s in the model and observations. With panel b showing the difference between model and observation to make the discrepancies more visible for wave heights smaller than 8 m, and in panel d the difference of the log of frequency of occurrence to see the deviations for larger H_s. Augmenting s_7 from 3.6×10^5 with the parameters s7-01 to 4.32×10^5 with s7-03 spreads the transition from viscous to turbulent dissipation over a wider range of H_s and tends to smooth the histogram of wave heights. This corrects the bias in the distribution around $H_s = 2.0$ m but makes things worse around 1.5 m. To correct those errors requires also shifting the transition Reynolds number Re_c to lower values in runs s4-01, s4-02 and s4-03 as shown in Fig. 1.5.a. These later adjustments made it possible to match the occurrence of the highest values of H_s, up to 14 m, as shown in Fig. 1.5.b.

Although H_s gives a very limited description of the sea state, the great benefit of H_s altimeter data is their global coverage, and the differences between model and observation over different regions of the world ocean can also be revealing due to the different types of sea states found in these regions (Chen et al., 2002), but also due to different forcing by winds, currents and sea ice. Table 1.3 defines the different ocean regions for which we have looked at regional H_s statistics. Further analyses on effects over the directional spreading and other wave parameters based on in-situ measurements, are presented in section 1.6 and 1.7.3 respectively.

The adjustments of $\beta_{\max}$ and wind intensities corrections showed particularly good improvements in the North and South Pacific. By only augmenting the $\beta_{\max}$ value (for

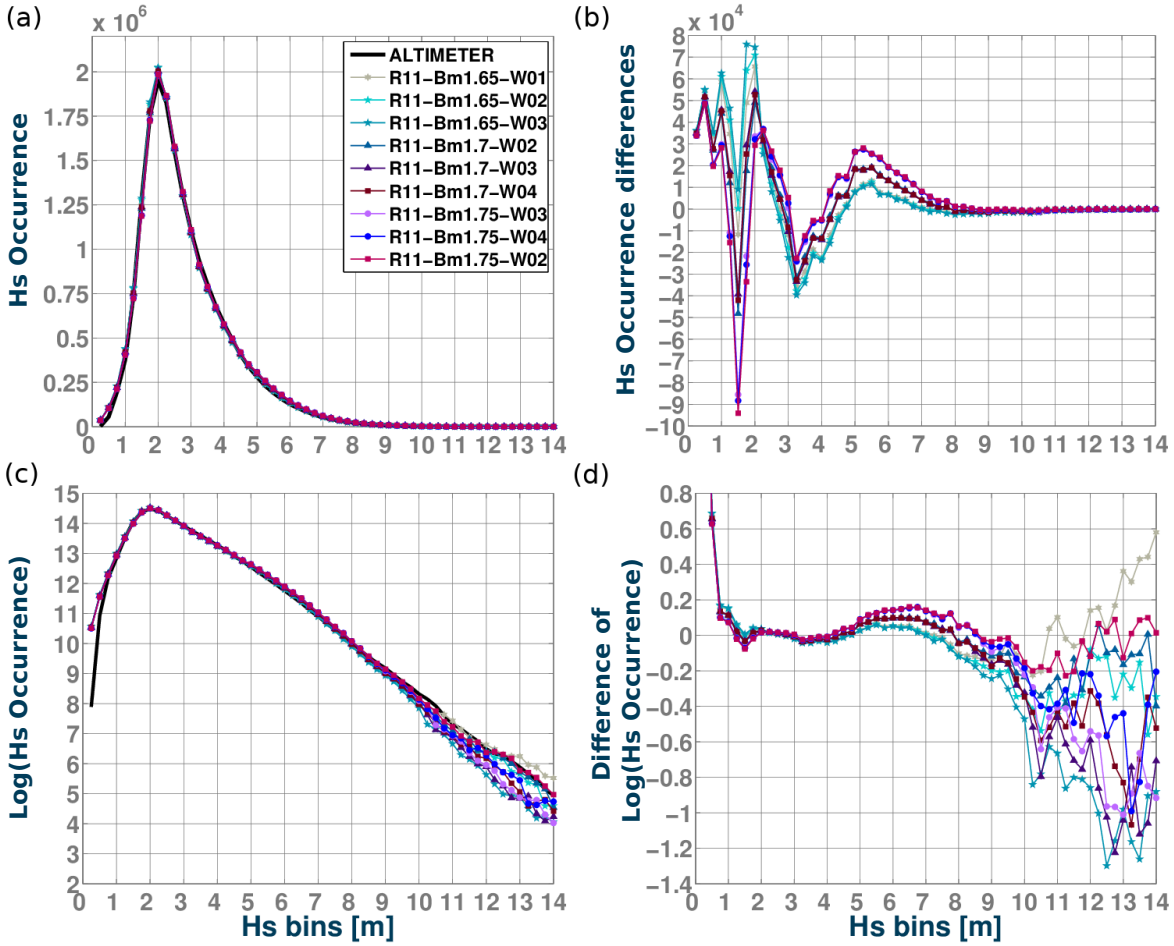

Figure 1.4 – (a) Histogram of H_s values in the Jason-2 and co-located model simulations. (b) Differences between the model and altimeter histograms. Plots shown are from wind correction tests only. (c) Same as (a) but with a logarithmic scale. (d) Difference of logarithm of the modeled and measured H_s histograms.

Table 1.3 – Regions definition for performance analysis.

Region (basin)	**Minimum Longitude** [°]	**Maximum Longitude** [°]	**Minimum Latitude** [°]	**Maximum Latitude** [°]
North Atlantic	-80	-5	10	50
South Atlantic	-68	20	-54	-2
North Pacific	125	-100	5	60
South Pacific	150	-73	-54	-2
Indian Ocean	50	100	-30	25
Southern Ocean	-179.98	180	-70	-55
NO SOUTH	-179.98	180	-55	66

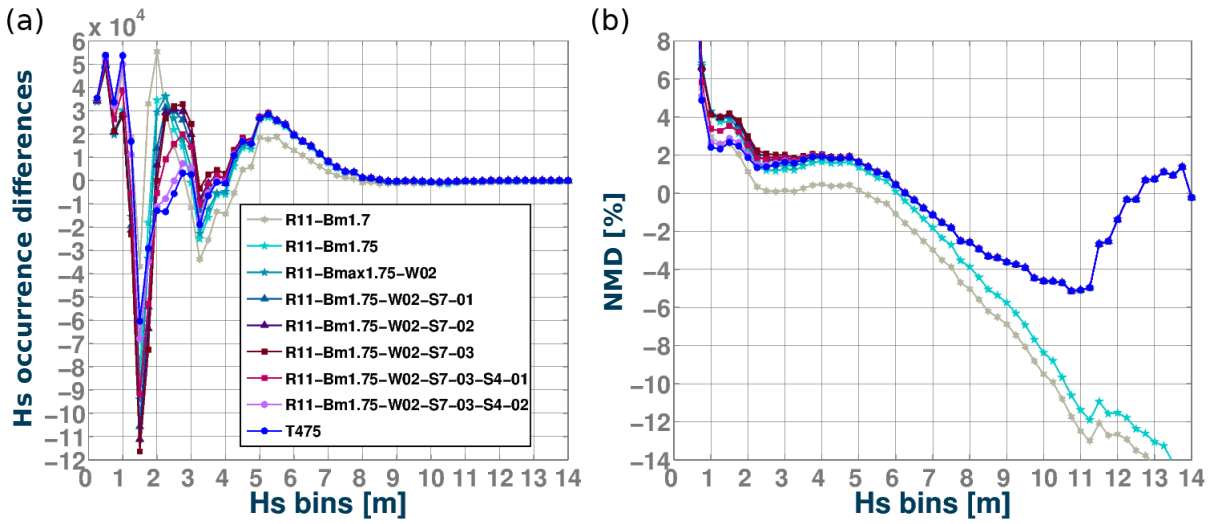

Figure 1.5 – (a) Histogram of H_s values in the Jason-2 and model simulations absolute frequency of occurrence difference (WW3 - alitmetry data). (b) Normalized mean bias. Plots shown are from s_7 and Re_c sensitivity tests.

example in tests R11-Bm1.7 and R11-Bm1.75), an important decrease of the H_s occurrences is obtained around 2 m, especially in the South Pacific, but this comes at the price of an excess of H_s values in the 1–1.5 m range (Fig. 1.6).

Higher values of $\beta_{\max}$ also reduced the overall negative bias in wave heights within the range of 1.5–7 m, with a further reduction of the negative NMD when the selected wind correction is applied. This specially improves the NMD for H_s of 7 to 11 m in the North Atlantic and South Pacific (Fig. 1.7). The South Pacific stands out as a region of high positive bias (Fig. 1.8).

Although it is possible that winds in the Southern Ocean may have specific biases due to a limited set of data used for assimilation, the state of the atmosphere is very much controlled by remote sensing data, including radiometers and scatterometers that are assimilated globally (Hersbach et al., 2020).

Another peculiarity of the Southern Ocean is the importance of the circumpolar current that generally flows from West to East. Not taking it into account is known to produce a large positive bias of the order of 20 cm in wave heights due to the relative wind effect (Rapizo et al., 2018; Rascle et al., 2008), and large gradients in H_s associated to refraction (Quilfen and Chapron, 2019). Indeed, the relevant wind speed for wave generation is the wind velocity minus the surface current velocity. However, these previous estimates use numerical models that are not very reliable for surface current assessments

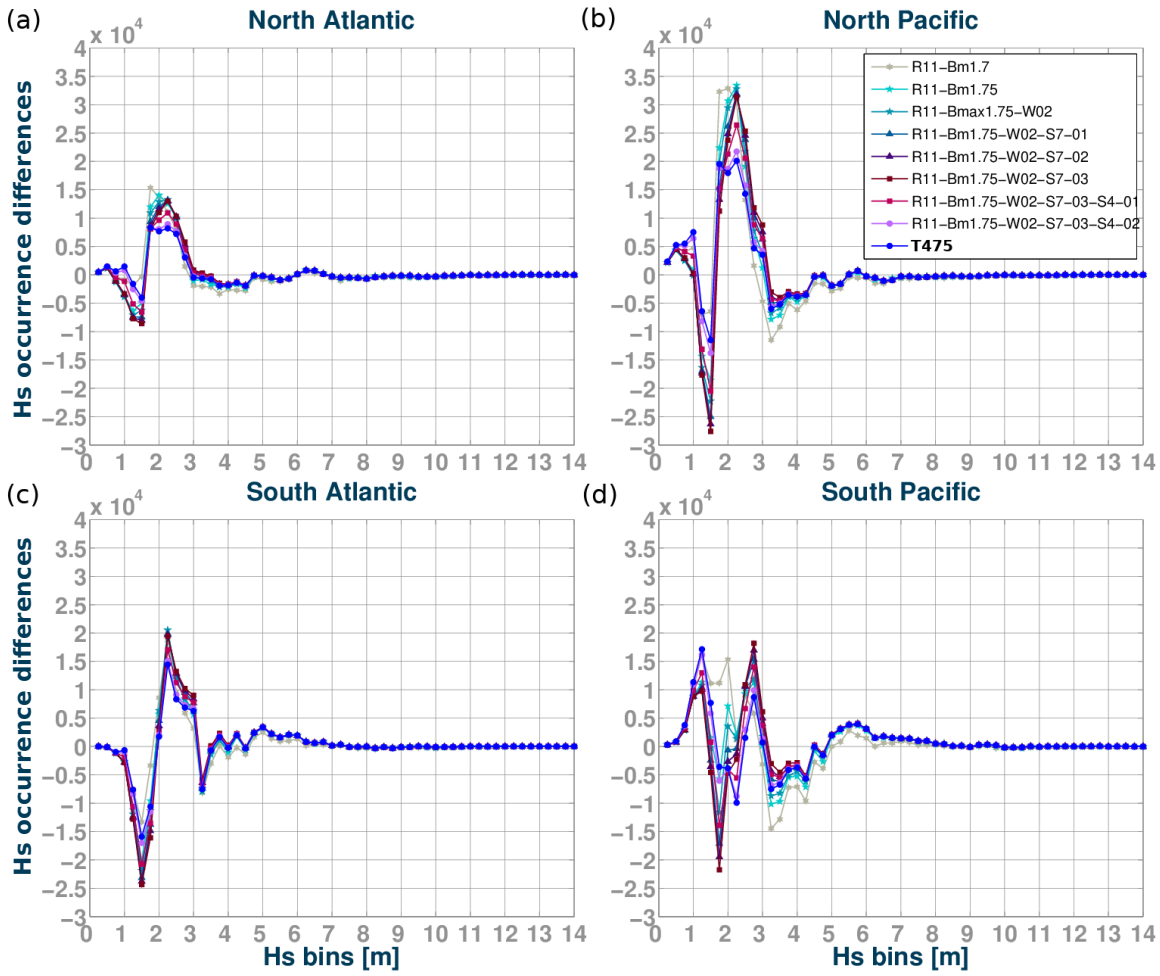

Figure 1.6 – H_s absolute frequency of occurrence difference (WW3 - altimetry data) from Atlantic and Pacific basins.

(ESA, 2019). Another effect specific to the Southern Ocean is the presence of both sea ice and icebergs, with a very large impact on wave heights (Ardhuin et al., 2011). The year 2011 has a rather large anomaly in iceberg numbers, although not as large as in 2009 (Tournadre et al., 2016). Finally, the details in sea ice concentration near the ice edge and the parameterizations of wave-ice interactions are another important source of uncertainties at latitudes south of 55°S (Ardhuin et al., 2020; Doble and Bidlot, 2013). For these reasons, alternative forcing fields for winds, ice and currents, and their impact on the model results are further investigated.

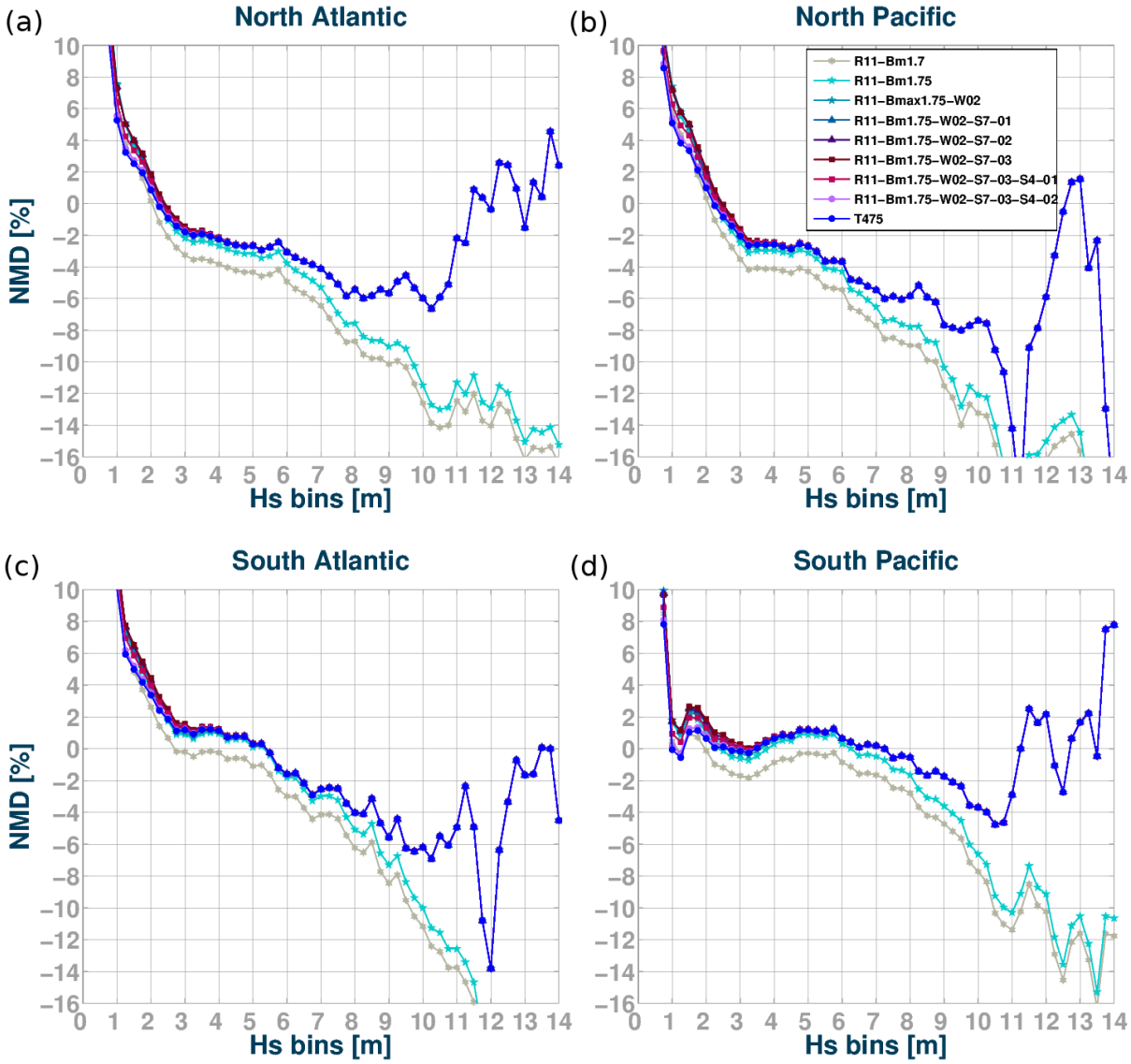

Figure 1.7 – H_s NMD within Atlantic and Pacific basins as a function of observed wave heights. H_s bins' range is 0.25 m.

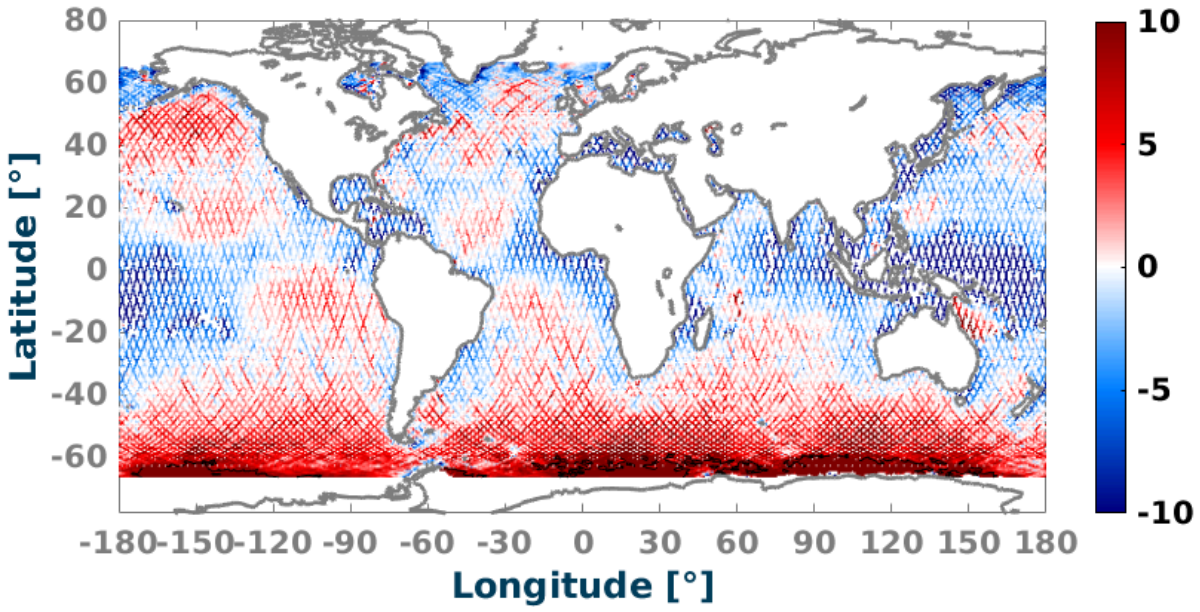

Figure 1.8 – NMB for 1-year averaged H_s using ERA5 winds. Modelled year: 2011. Parameter settings from test T475. Colorbar indicates NMD values in %. Black lines represent positive 10 % contours.

1.4 Influence of forcing field choices

As it was done for the choice of model parameters, forcing set-up and related model perfomance was done over the year 2011, with a complete validation on other years described in section 1.7. Whereas only Jason-2 data was used for the model calibration, now the full ESA Sea State Climate Change Initiative merged altimeter data set is employed, using the denoised 1-Hz data for the significant wave height (Dodet et al., 2020). For the year 2011 this includes data from the following satellite missions: Jason-1, Envisat, Jason-2 and Cryosat-2. Using the model with parameters T475, the "baseline" model setup run uses ERA5 winds, Ifremer sea ice and iceberg concentrations, and CMES-Globcurrent surface currents.

1.4.1 Choice of forcing wind field

Now, results using three alternative wind fields are compared. These include the operational ECMWF IFS winds which, for the year 2011, was obtained with IFS cycle 37r2, an earlier and less accurate version of IFS compared to the 41r2 used for ERA5. The CFSR winds (Saha et al., 2010) used by Rascle and Ardhuin (2013) were also considered. Finally the Ifremer CERSAT Global Blended Mean Wind Fields (Bentamy et al., 2018) were also tested (from here on just named "Ifremer"). Other wind fields like ERA-Interim and MERRA2 (Gelaro et al., 2017) have also been considered in other hindcasts such as Sharmar et al. (2021), with analyses focused on inconsistencies and trends of the different atmospheric forcing.

The main difference between the Ifremer winds and the 2 other data sets, is that the Ifremer 6-hourly surface wind fields are estimated mainly from scatterometer wind vector observations, merged with wind magnitude measurements from radiometer data (SSM/I, SSMIS, WindSat) and the ERA-Interim atmospheric wind reanalyzes. Further details on the product and methods can be found in Bentamy et al. (2012) and Bentamy et al. (2013).

As discussed by Rascle and Ardhuin (2013) and Stopa et al. (2019), different wind fields are biased relative to one another. This is true for the average values around 7 m/s, and biases are even larger for high speeds over 20 m/s (Pineau-Guillou et al., 2018). This is shown again here in Fig. 1.9. The NCEP operational GFS model (not shown here) and CFSR hindcast both have wind speeds higher than those produced by the ECMWF models (operational IFS results and ERA5 results), leading to higher wave heights when

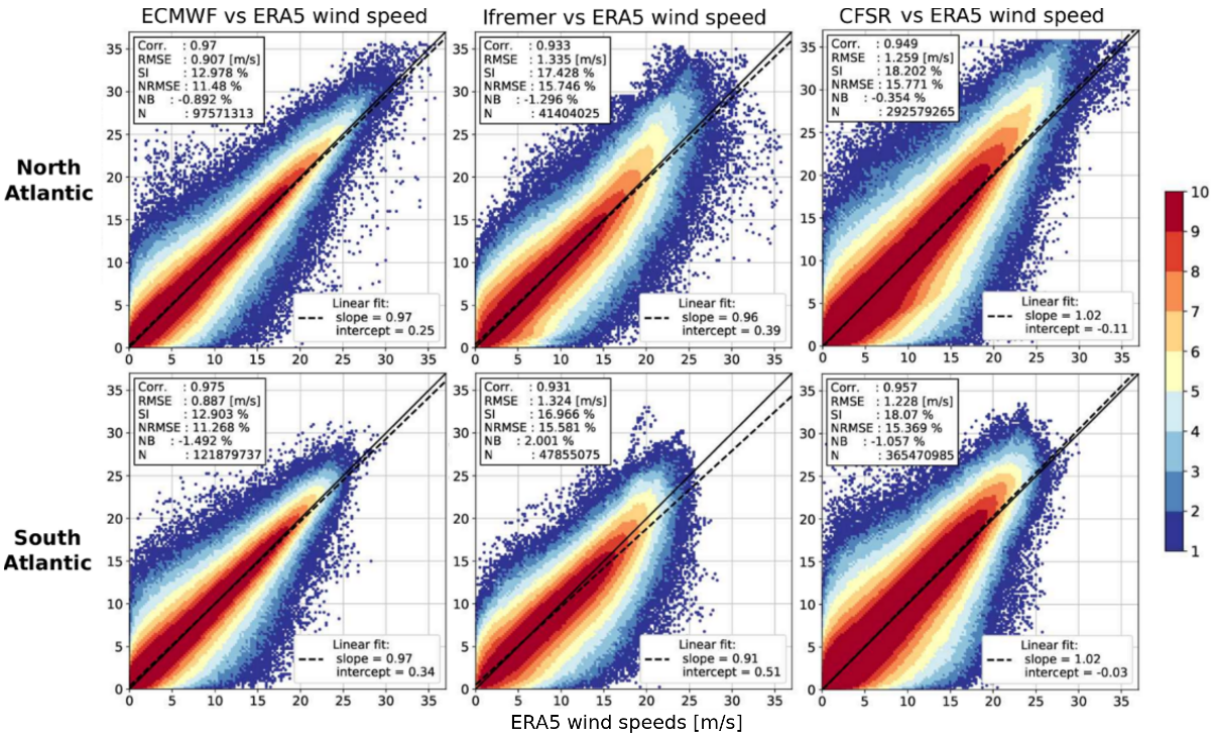

Figure 1.9 – Scatter plot of wind speed for the months of January to July 2011. ERA5 intensity bins along x-axis. Top panels: ECMWF operational product vs ERA5, Middle panels: Ifremer vs ERA5. Bottom panels: CFSR vs ERA5. Colors give the logarithm of the number of data points in each 0.25 m/s×0.25 m/s wind speed bin.

using NCEP winds. Because the Ifremer blended wind product uses ERA-Interim as a background "filler" when and where observations are too far in space or time, these data sets where homogenized to have the same low bias for average conditions (slope of 0.91 for the Ifremer wind vs the ERA5 winds in the South Atlantic) but higher values for wind speeds above 20 m/s that are more frequent in the North Atlantic.

There is also a clear indication that ECMWF operational winds give higher values for wind speeds above 20 m/s compared to ERA5, probably due to the higher resolution of the operational IFS model (25 km approx. and hourly output for 2011). The consequences of these wind field properties on the wave height biases are shown in Fig. 1.10.

Given the relative biases of the different wind datasets, it is not surprising that, without any retuning, the T475 set of parameters gives large H_s biases when used with other wind forcing than ERA-5. In particular the CFSR winds give positive biases larger than 15% over most of the oceans.

The Ifremer winds have interesting properties and are probably more realistic in some

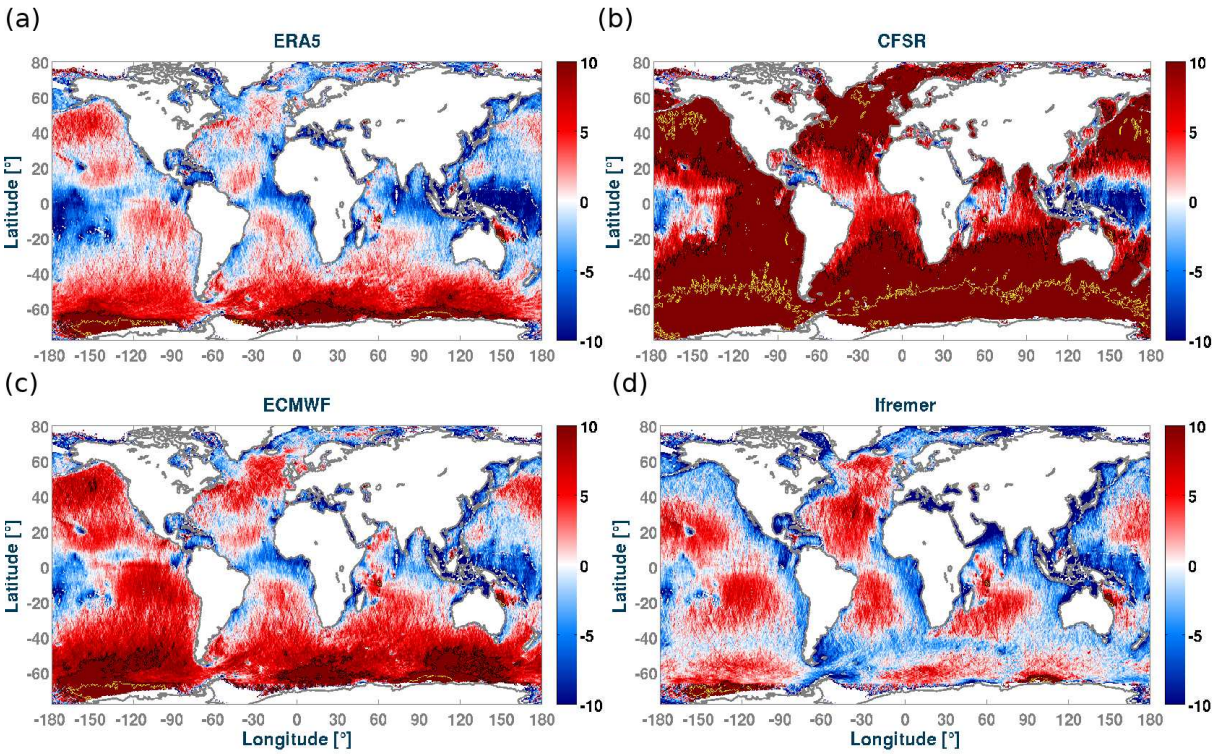

Figure 1.10 – Normalized Mean Difference of modelled H_s minus Sea State CCI Altimeter data, averaged over the year 2011, using (a) ERA5, (b) CFSR, (c) ECMWF operational deterministic products and (d) Ifremer winds. The model was run with the set of parameters T475 as given in Table 1.2. Colorbar indicates NMD in percent. Black and yelow lines mark the +10 and +20 % contours.

regions, where they give lower scatter index (Fig 1.11.d), including the southern ocean where the bias is also lower and significantly different (Fig. 1.10.d). This difference between Ifremer and ERA5 winds is possibly due to the fact that the remote sensing data used in the Ifremer product generally measures a wind that is relative to the current and not an absolute wind (Quilfen et al., 2004). There is also probably a contribution to the generally low bias of the ERA-Iterim product that is used to fill in between the different satellite passes.

1.4.2 Effects of wave-ice parametrizations and forcing fields

Much work has been done on the interactions of waves and sea ice in the recent years, with a large emphasis on pancake ice (Thomson et al., 2018), that is particularly relevant near the ice edge and during the freeze-up period (Doble et al., 2003). Here,

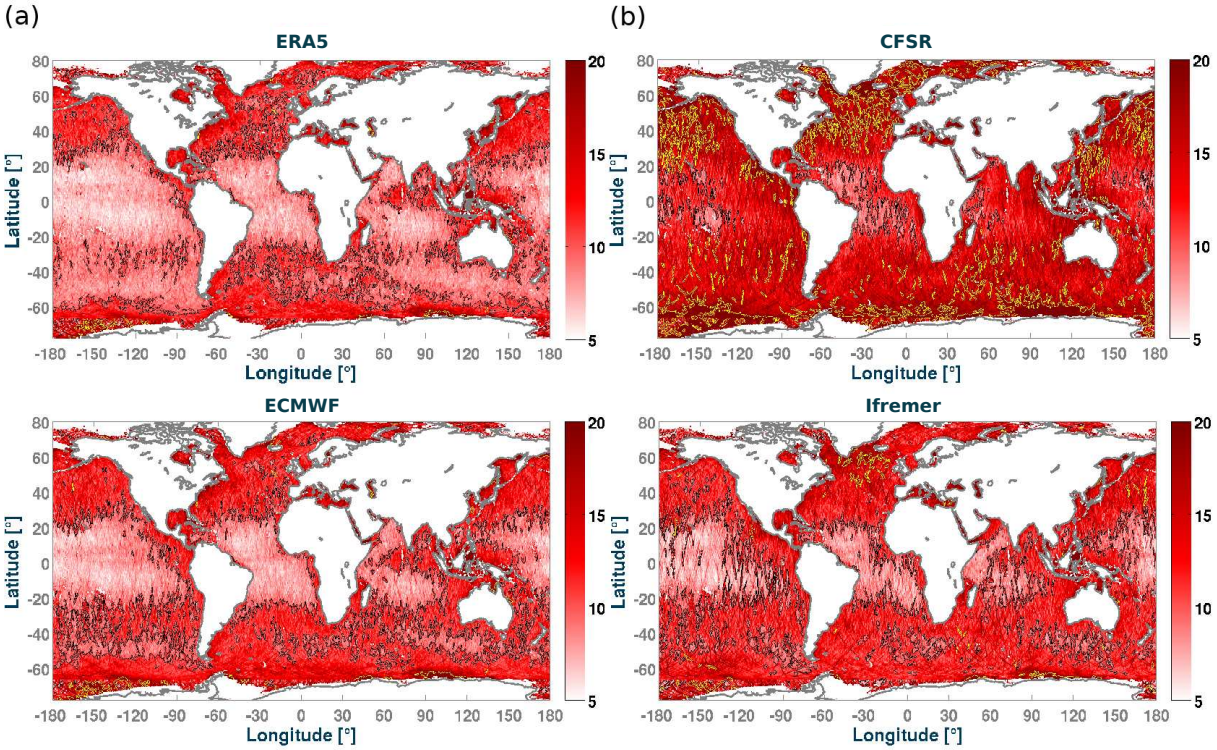

Figure 1.11 – Scatter Index of modelled H_s minus Sea State CCI Altimeter data, averaged over the year 2011, using (a) ERA5, (b) CFSR, (c) ECMWF operational deterministic products and (d) Ifremer winds. The model was run with the set of parameters T475 as given in Table 1.2. Colorbar indicates SI in percent. Black and yelow lines mark the +10 and +20 % contours.

a parameterization associated to the presence of larger floes and their possible break-up induced by waves is included. In particular the formulation used in the baseline simulation was developed by Boutin et al. (2018) and adjusted by Ardhuin et al. (2020) to 2 months of waves measured in the sea ice of the Ross sea. That parameterization combines both wave scattering in sea ice with a wave-induced ice break-up (IS2) and dissipation below ice plates including a smooth laminar to rough turbulent flow as a function of the boundary layer Reynolds number (IC2, Stopa et al., 2016b). Given uncertainties on ice thickness, in particular in the Southern Ocean (Williams et al., 2014) and around the ice edge where it matters for wave-ice interactions, a crude and simple constant thickness of 1 m was chosen. This parameterization is compared to the old default WW3 parameterization that is a 40 km exponential decay of wave energy proportional to the ice concentration (IC0 parameterization). The new IC2+IS2 parameterization gives a much weaker attenuation near the ice edge, and thus a larger value of H_s in the open

ocean where data for validation is available (Fig. 1.12.a,b). It was noticed that the scatter index is generally reduced around the ice, especially around Greenland and in the Ross sea. These areas typically require more validation, and the model resolution (0.5°) is probably marginal for the Southern Ocean, whereas the 12 km resolution in the Arctic allows a more detailed investigation of wave-ice interactions. A validation of the predicted wave parameters and maximum floe size in the ice-covered regions is out of the scope of the present analysis.

Much less work has been devoted to the effect of icebergs, so here the parameterization proposed by Ardhuin et al. (2011) is used. It was verified that including icebergs has a clear effect on reducing the bias and scatter index where the icebergs are present. For the year 2011, a large concentration of icebergs was found in both the South-East of the Pacific and the South of the Indian ocean, giving a bias reduction up to 10 percentage points and, locally, a very large reduction in scatter index up to 6 percentage points (Fig. 1.12.c,d). The concentration of icebergs in the South Pacific in 2011 is associated with two large icebergs, C19a and B15j, that drifted northward and eastward within the Antarctic Circumpolar Current (Tournadre et al., 2016; Tournadre et al., 2015), later breaking up into hundreds of smaller icebergs. These small icebergs are much more effective in reducing the wave energy flux, compared to a single parent iceberg, as they have a much larger cross section.

1.4.3 Effect of currents

Ocean surface currents can have large influences on the wave field either locally through the relative wind effect and advection, or down-wave of current gradients, due to refraction, with larger effects associated to larger current magnitude (Ardhuin et al., 2012). An important difficulty for properly taking currents into account at global scales is that there are no global observations of the Total Surface Current Velocity (TSCV) that matters for wind waves, and the only proper surface measurements are made with High Frequency radar near the coasts (Barrick et al., 1974; Roarty et al., 2019). Instead, the closest global proxy is given by the drift velocity around 15 m depth provided by instruments of the Surface Velocity Program (Elipot et al., 2016; Lumpkin et al., 2017), with only about 1500 drifters globally giving a 500 km resolution. It has been observed that at the Equator and a few other places of interest, the 15-m depth drift is often in the opposite direction of the surface drift. Most importantly, finer spatial resolution is needed, typically down to 30 km, to represent most of the refraction effects (Ardhuin et al., 2017a; Marechal and

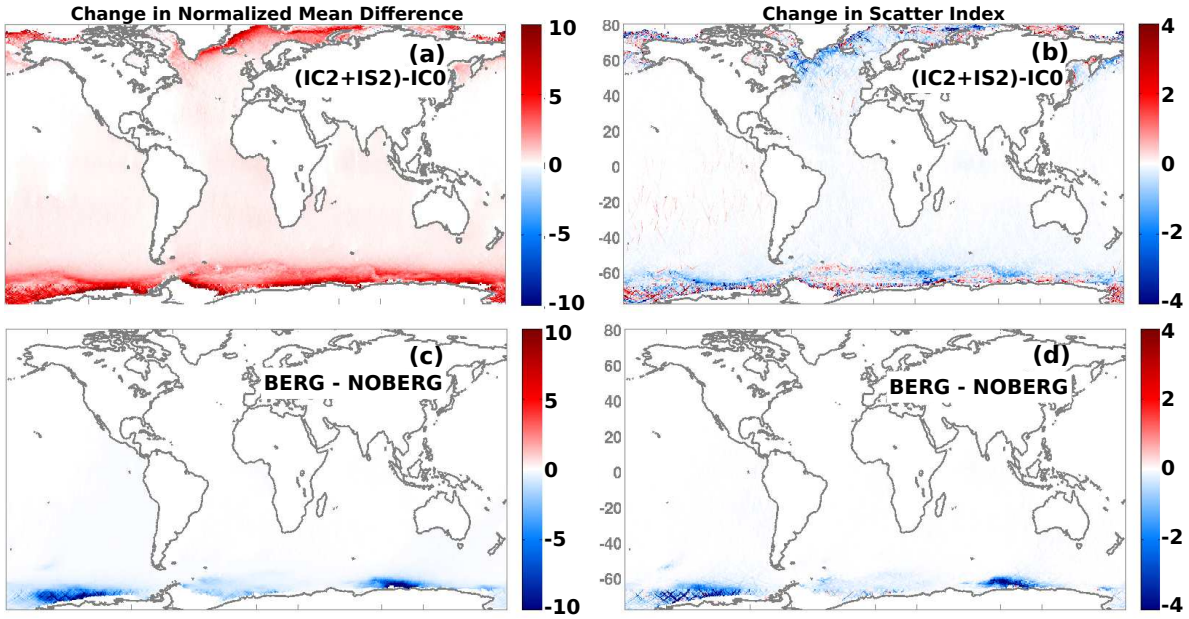

Figure 1.12 – Differences in NMB and SI in percentage points for the T475 parameterization variations when using: (a,b) using dissipation, scattering and ice break-up (IC2, IS2) or partial ice blocking (IC0), (c,d) iceberg forcing or no iceberg forcing.

Ardhuin, 2021). As a result, surface current estimates are often taken from numerical models, or, which is the case of the CMEMS Globcurrent product used here, derived from combined observations of sea surface height anomaly, mean dynamic topography and surface winds, assuming a quasi-geostrophic equilibrium of the Coriolis force associated to the surface current with the combination of the wind stress and the pressure gradient associated to sea surface height. Except possibly for western boundary currents such as the Gulf Stream or the Agulhas, this approach does not work very well, in particular around the equator and in mid-latitudes where currents are dominated by near-inertial currents as illustrated in Fig. 1.13. The CMEMS Global Ocean Multi Observation Products (MULTIOBS_GLO_PHY_REP_015_004) has an average current that is closer to the SVP drifter climatology than the CMEMS Global Ocean Reanalysis (GLORYS) product GLOBAL-REANALYSIS-PHY-001-031, in particular around the Equator, which is why the former product was chosen as the TSCV forcing.

Given all these limitations it is not specially surprising that the TSCV is seldom used at global scale. Including the TSCV forcing can indeed increase errors in some regions due to errors in the forcing field, but it generally corrects part of the bias and gives lower scatter index for wave heights compared to altimeter data, as illustrated in Fig. 1.14.

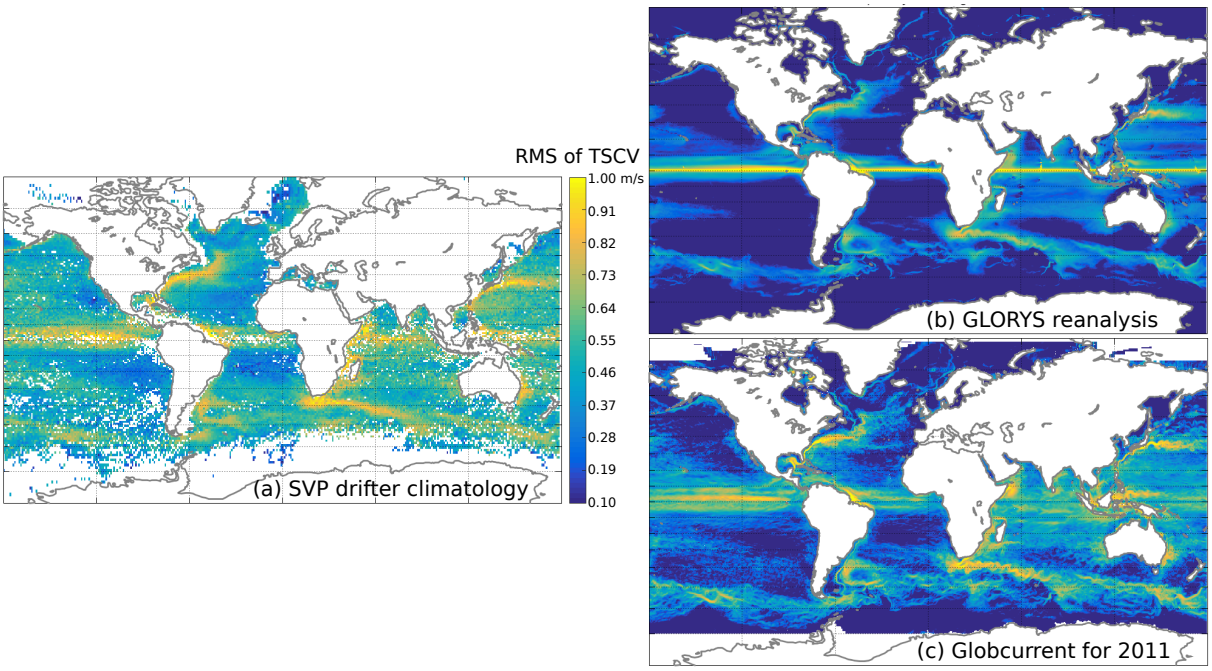

Figure 1.13 – Root mean square current velocity (a) at 15 m depth using in situ drifter data from the Surface Velocity Program (SVP) processed by Elipot et al. (2016) with rms velocity computed over 30-day long trajectories and attributed to the center of that trajectory and white ocean pixels corresponding to 1 by 1 degree squares in which no data was available, (b) as given by the CMEMS GLORYS reanalysis, (c) as given by the CMEMS-Globcurrent product based on altimeter sea level anomalies, mean dynamic topography inferred from satellite gravimeters and ocean drifters, and "Ekman currents" estimated from ECMWF wind analyses.

Comparing the 1-year simulation with parameters T475 with and without currents, a clear lower bias is found along the Equator and in the Southern ocean when currents are used, as already reported by Rascle et al., 2008. This is probably associated with the relative wind effect, with wave generation given by the difference between the wind vector and the TSCV and not the wind vector alone. It must be noticed that this approach can overestimate the current effect when the atmosphere model is not coupled with an ocean model (Hersbach and Bidlot, 2008; Renault et al., 2016), however, it is also expected that the TSCV is generally underestimated by the CMEMS-Globcurrent product.

The reduction of the scatter index against altimeter H_s that is brought by the current (blue regions in Fig. 1.14.b) clearly corresponds to the regions of strong currents where their spatial variability can cause a large variability of the heights of incoming waves around the current: this is the case in the Agulhas current, in the Gulf Stream, the

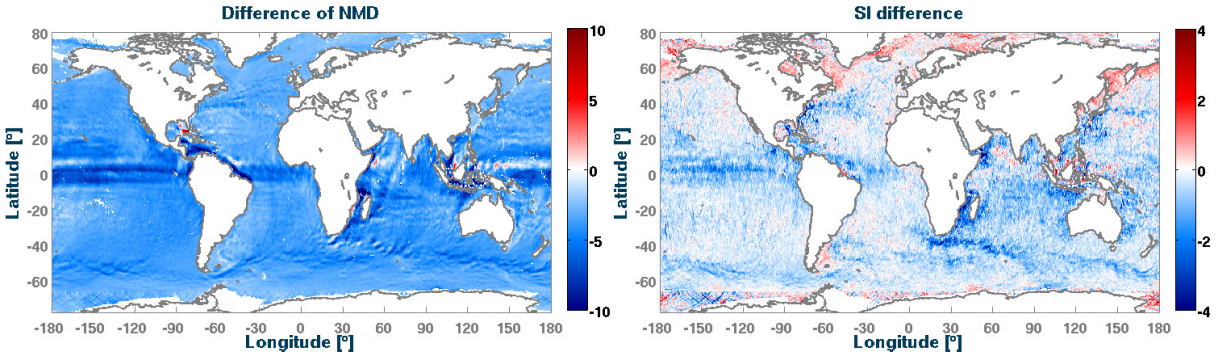

Figure 1.14 – Left: Change in Normalized Mean Difference (NMD in percentage points) for H_s with currents and the T475 parameterization versus the same simulation without current. For both simulatons the reference is the Sea State CCI H_s for the year 2011. Right: same for difference in SI, with the dark blue corresponding to a reduction of 4 percentage points (e.g. from 14% to 10%) when TSCV forcing is used.

Kuroshio, the Mozambique channel, and the Somali current. However, as shown in Fig. 1.11, these regions are still places where the model's error are relatively large, possibly due to a combination of factors, including errors in the TSCV fields, insufficient directional resolution of the wave model (Marechal and Ardhuin, 2021), and insufficient spatial resolution in the TSCV field and/or the wave model. It is noticed that the scatter index is generally increased for latitudes above 50° N, probably due to an insufficient resolution of the altimetry where the Rossby radius of deformation is less than 50 km (Ballarotta et al., 2019). Given the importance of the spectral and spatial discretizations, these aspects are discussed in the following section.

1.5 Model discretization

The choice of spatial and spectral discretizations can have a large impact on the model solutions, and it also has a direct and clear impact on the cost of the model, the time needed to perform the simulations. As a result, the particular choices made for the discretizations are a compromise between the computational cost, range of expected applications, and the accuracy benefits. The 28-years hindcast used around 500,000 cpu hours distributed over 504 processors, distributed in 18 nodes that each hold 28 CPUs and 75Gb of memory.

1.5.1 Spatial resolution

Using higher resolution grids is critical for resolving smaller scale variations in the sea state that are caused by the time-varying forcing fields (wind, current, sea ice) or fixed features (shoreline, water depth, bottom sediment type and grain size). In practice, small scale gradients in wave heights are dominated by the distance to the coast and the presence of strong currents (Quilfen and Chapron, 2019). Because some important current systems are located close to coasts, it was chosen to define nested grids that cover the relatively shallow waters of the coastal regions and, where possible, extend over strong current regions (Fig. 1.1). As a result, the North-West Atlantic grid covers the Grand Banks and the Gulf Stream, as well as the entire gulf of Mexico. In a similar fashion, the Africa grid was extended to the south to cover the Agulhas current retroflexion. Using different grids also allows to adjust the model parameters locally.

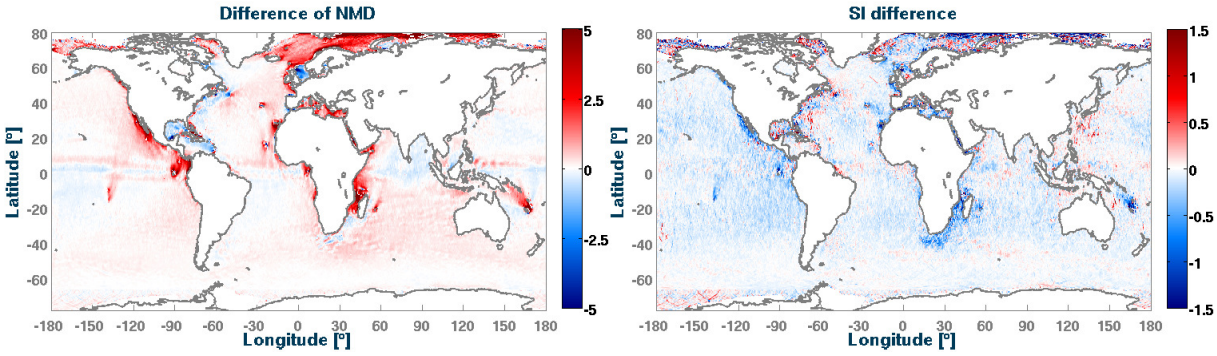

Figure 1.15 – NMD and SI variations in percentage points for the year 2011: values for Multi-grid minus values for Single grid setup, both using the same T475 parameters. Left panel: Difference in NMD values, in this case red values represent a reduction of the negative NMD.

Because the wind-wave growth tuning that corresponds to T475 is very similar to T471, it tends to give an underestimation of the wave height for short fetches (Stopa et al., 2016a). This effect is more pronounced with higher resolution grids, which explains the general reduction in wave height for enclosed seas and eastern coasts (stronger negative bias, in blue in Fig. 1.15.a). It was also found that the explicit higher resolution of shorelines and islands gives larger H_s values compared to the subgrid treatment of complex shorelines and islands in a coarser grid (Chawla and Tolman, 2008), explaining the more positive bias around 140°E 10°S, downwave of the Tuamotus, or around the Galapagos, Azores etc. The presence of the full Arctic ocean thanks to the Arctic grid also adds wave

energy that was otherwise missing in the near-global grid that stopped at 83°N. Further details on the effects of spatial resolution are addressed in section 2.5.1 of Chapter 2.

Overall, the scatter index is reduced over most of the ocean with the strongest reduction in regions of strong currents like the Agulhas current, or along complex coastlines such as the Baja California peninsula (blue regions in Fig. 1.15.b).

1.5.2 Spectral grid resolution

However, to converge to the true solution of the wave action equation, increasing only the spatial resolution is not enough, and a finer spectral resolution is also needed, in particular for parameters sensitive to numerical diffusion like the directional spread (Ardhuin and Herbers, 2005). Although it is known that current effects on wave heights would be better resolved with 48 directions instead of only 24 (Ardhuin et al., 2017b; Marechal and Ardhuin, 2021), for the present hindcast only 24 directions have been used because of the much lower CPU cost, and because differences in wave heights when using 24 or 36 directions were fairly limited. Fig. 1.16.b shows a change in the Normalized Mean Difference that is mostly limited to the tropical regions, especially around coasts and islands for which the finer directional resolution must have an impact on swell propagation, but the change in scatter index is typically much less than 1 percentage point (Fig. 1.16.d).

Compared to the costly increase of directional resolution, a higher benefit in terms of H_s accuracy is found in increasing the spectral range with a maximum frequency of 0.95 Hz instead of the 0.72 Hz used by Rascle and Ardhuin, 2013. This higher frequency gives a better response, in particular for the short fetch and low wind conditions in which the peak of the wind sea would otherwise not be well resolved.

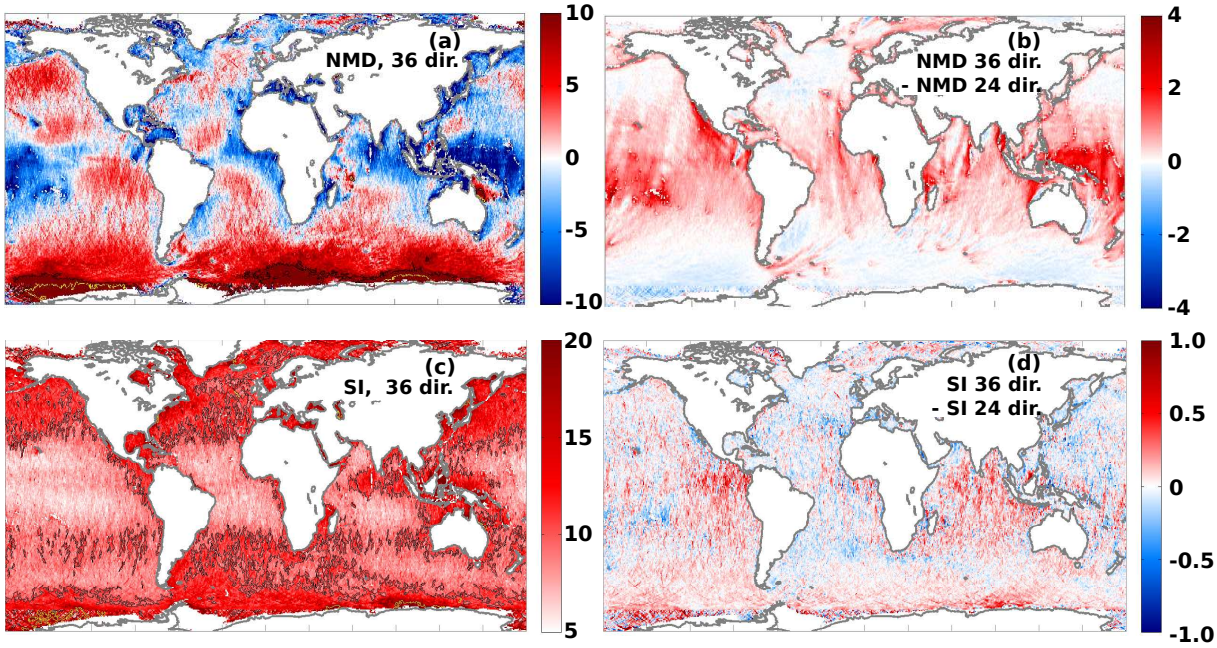

Figure 1.16 – (a)NMD for 1 year averaged H_s using T475 with 36 directions and (b) differences in NMD for T475 with 36 directions with respect to 24 directions (Fig. 1.10.a). Black lines mark the positive 10 % contours. (c) SI for 1 year averaged H_s using T475 with 36 directions and (d) SI difference for T475 with 36 directions with respect to 24 directions. Analyzed year: 2011. Black and yellow lines mark the positive 10 and 20 % contours respectively.

1.6 Wave directionality and alternative dissipation parameterizations

As noted by Stopa et al. (2016b), the directional spread (Kuik et al., 1988) is the least well predicted parameter among the most common metrics used to define the shape of the wave spectrum. Whereas the mean direction is well controlled by the wind evolution and the time scale of adjustment of the wave field, the directional spread is probably influenced by details of the wave generation and dissipation parameterizations. In this section, 3-hour averaged data from WMO buoy 46246 in the North East Pacific is used as an example (see table 1.4 and Fig. 1.17), which is the station 166 of the Coastal Data Information Program and is maintained by Thomson et al. (2013). The correlation coefficient for $\sigma_\theta(f)$ falls below 0.7 for frequency above 0.3 Hz. Indeed, the model has no skill in predicting $\sigma_\theta(f)$ for frequencies > 0.5 Hz, and the shape of the modeled spectral tail is given by the shape at frequency f_m with an energy level decreasing like $(f_m/f)^5$,

where f_m is a dynamically adjusted maximum prognostic frequency, set to 2.5 times the mean frequency of the wind sea part of the spectrum.

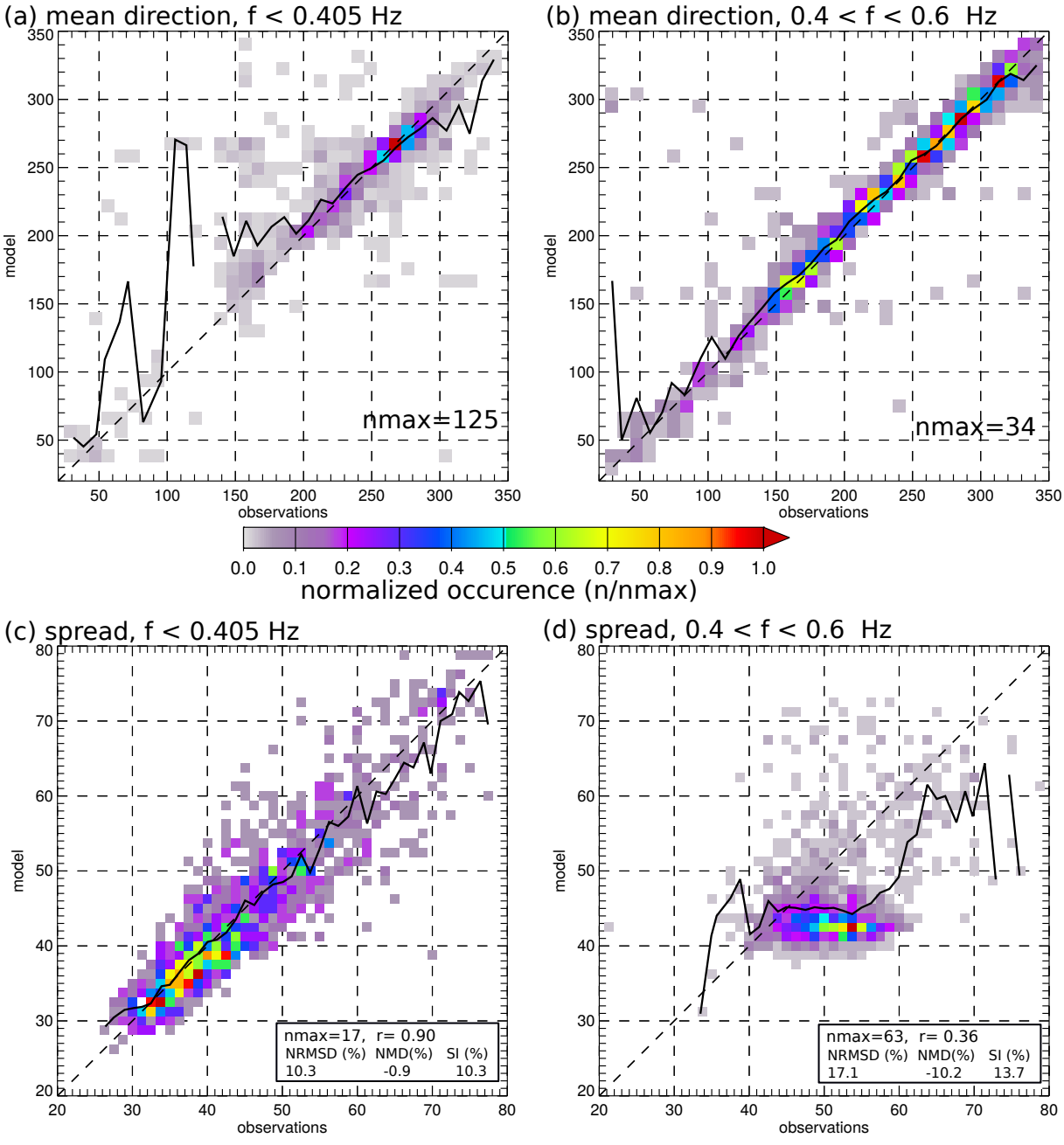

Figure 1.17 – Modeled mean direction (a,b) and spread (c,d) for low frequencies ($f < 0.4$ Hz) and high frequencies ($f > 0.4$ Hz) at buoy 46246 for the year 2018. Colors show the number of 3 hour records for which the model-buoy pair falls in one bin, as normalized by the maximum value nmax. The solid lines gives the mean modeled value for each observation bin.

Note that the directional spread at low frequencies is, close to coasts, very sensitive to shoreline reflections (Ardhuin and Roland, 2012). Whereas this has a limited impact on most wave parameters, it is a critical contribution to microseism and microbarom sources (De Carlo et al., 2021; Stutzmann et al., 2012). In the present hindcast, the slope-based reflection coefficient proposed by Ardhuin and Roland (2012) has not been used because of the difficulty of defining the proper slope and mixed results when validating modeled microseisms. Instead, constant reflexion coefficients of 5%, 10% and 20% were defined for the resolved shorelines, subgrid shorelines and icebergs, respectively. Clearly that parameterization will have to be tested and further improved upon using buoy directional spreads together with microseism and microbarom data.

The T475 parameterization is thus still fairly poor for the frequency range 0.4 to 1 Hz when the waves are developed (when the wind sea peak frequency is below 0.15 Hz), in particular for the directional distribution (Fig. 1.17.d), which is critical for the ratio of crosswind to downwind mean square slope (Munk, 2009), wave breaking statistics (Romero et al., 2017) and the sources of microseisms and microbaroms at seismic or acoustic frequencies above 0.8 Hz (De Carlo et al., 2020; Farrell and Munk, 2010; Peureux and Ardhuin, 2016). Recent work have suggested that the shape of the dissipation function could be better described by Romero (2019), giving the T700 set of parameters in the WAVEWATCH III model, available in versions 7.0 and above. In T700, the ad hoc and not very effective cumulative term of Ardhuin et al. (2010) is replaced with a cumulative term that could be explained by the straining of short waves caused by long waves (Peureux et al., 2021). Preliminary tests reveal an interesting behavior for the shape of the high frequency spectrum (Fig. 1.18), which allows to remove the imposed diagnostic tail for $f > f_m$ thanks to a completely local (in the spectral sense) parameterization of the breaking probability, and the added cosine-squared angular dependence in the parameterization of the cumulative effect. Possibly this imposed shape of the cumulative term will have to be revised, as for example an isotropic spectrum of long waves should produce an isotropic effect unless it is a joint effect of the long and short waves. However, Romero (2019) has produced the first parameterization that is able to produce larger cross-wind slopes than down-wind slopes for wavelengths around 1 m (after 7 hours in Fig. 1.18.d, the dominant direction for mss1 in T700NL2 is indeed the cross-wind direction), which are critical to explain the first of the inconvenient sea truths highlighted by Munk (2009).

Taken "out of the box" without the present retuning, the Romero (2019) parameterization performs similarly to T471 in terms of scatter index but has a 2 to 6% higher value

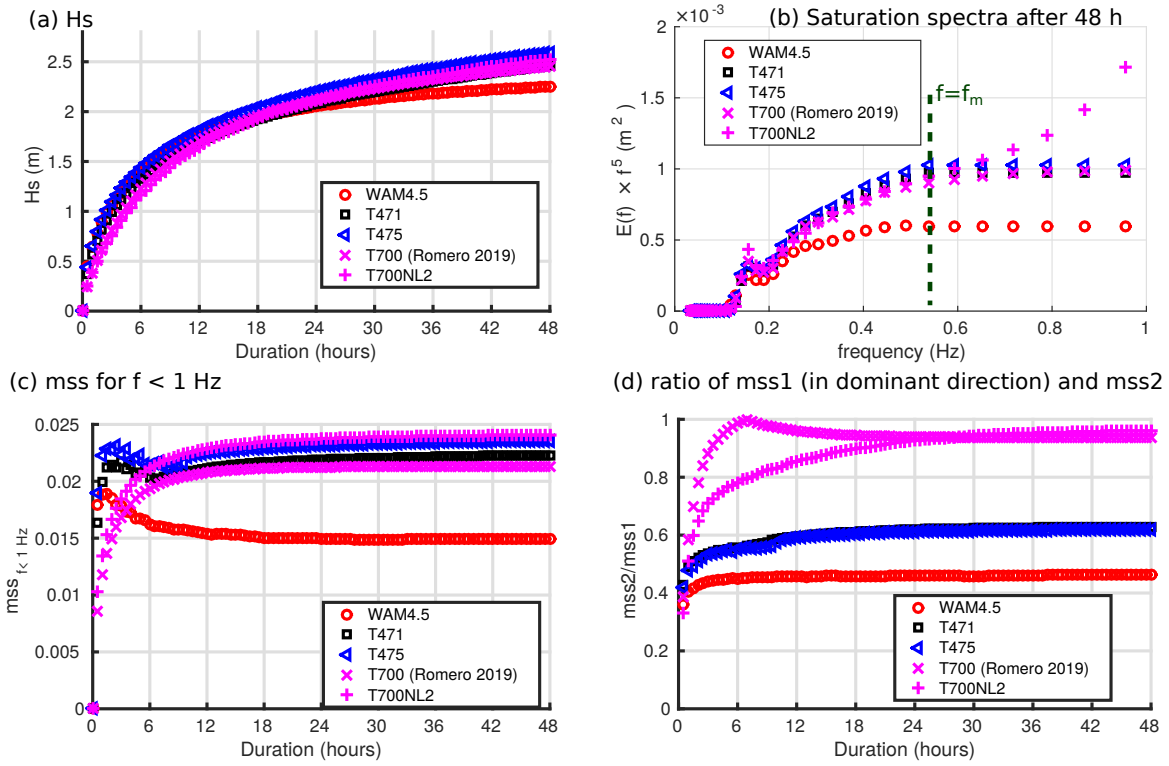

Figure 1.18 – Differences in model results for an academic case considering a uniform ocean and a constant wind speed of 10 m/s starting from no waves. The WAM4.5 parameterization is close to the one used in the ERA5 reanalysis, and the T700NL2 corresponds to the parameterization of Romero (2019) with the non-linear interactions computed with the exact Webb-Resio-Tracy method (van Vledder, 2006).

of wave height (Fig. 1.19) that will also require an adjustment of the swell dissipation. The benefits of such a parameterization will probably be most important for the model

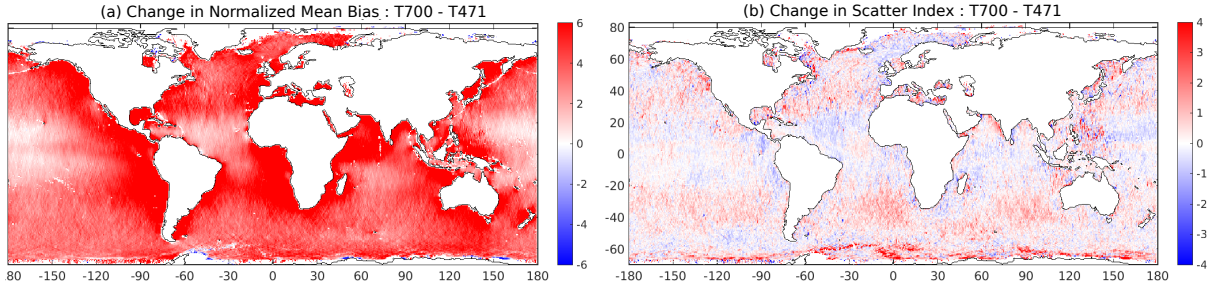

Figure 1.19 – Change in NB and SI from the T471 to T700 change in parameterization for the year 2018. These simulations did not include ocean currents.

parameters that are most sensitive to the high frequencies, including the mean square

slope, and will require an important upgrade of the wave model in the way these shorter wave components are treated, so that its results can be validated with radar back-scatter data (e.g. Nouguier et al., 2016).

1.7 Validation

1.7.1 Validation with altimeter data

An important concern about numerical wave model hindcasts for all applications is their consistency in time which can be compromised by the time-evolving error statistics of the forcing fields (winds, currents, sea ice) and/or of the assimilated data which may both introduce time varying biases and jumps, possibly requiring the statistical adjustment of the forcing fields (e.g. Stopa et al., 2019) or the correction of the model results. It is thus necessary to verify the consistency of the model output over time. This requires validation data that are stable in time. The satellite altimeter H_s measurements of Dodet et al. (2020) were especially designed for this purpose are used to look at the evolution of the NMB and SI over the years 1997 to 2018 (Fig. 1.20).

A general agreement is found over the years, with lower variations of the mean difference than was found by Rascle and Ardhuin (2013) when using CFSR winds, and which had to be corrected in later hindcasts (Stopa et al., 2019). Still, the changes from -1 to 2% for the bulk of the data ($1.5 < H_s < 4$ m) suggest a systematic drift in either the ERA5 wind speeds or the altimeter data, with relatively flatter biases as a function of H_s for the years 2011-2018 (but still a decrease in the mean model values or an increase in the altimeter values), and steeper H_s-dependent biases for the years 1997-2010. The scatter index shows a general reduction of the random differences that can be caused by a reduction in the random noise of satellite altimeter data for the more recent missions and an improvement in the quality of the ERA5 wind fields thanks to the assimilation of a richer set of mesaurements (Hersbach et al., 2020).

1.7.2 Comparison to ERA5 wave heights

Because the ERA5 reanalysis also included a wave product it is questionable that the efforts made to adjust the implemented model have any added value, especially because the ERA5 wave model assimilates altimeter wave heights and uses a wind forcing at the 10 minutes time step of the atmospheric circulation model to which it is coupled.

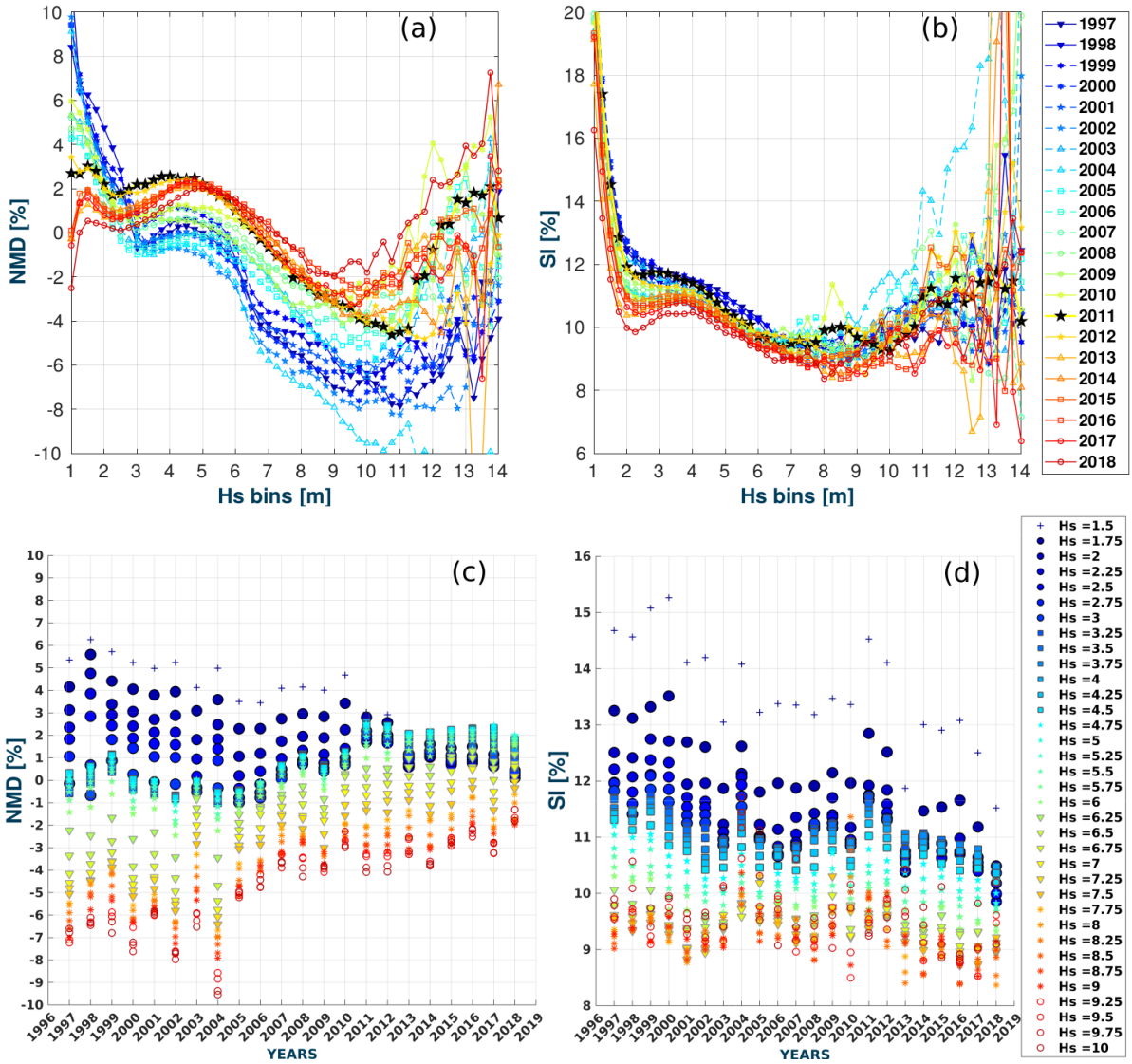

Figure 1.20 – Performance parameters for 22 years hindcast using T475. (a) H_s NMD curves and (b) SI curves, the reference year (2011) used for model tuning has been highlighted with a black star. (c) and (d) are the NMD and SI time series of 1.5 to 10 m H_s bins. Bin size is 0.25 m. Altimeters used for validation: Topex (1997-2002), Envisat (2003-2010), Jason-2 (2011-2012), Saral (2013-2018).

However, it is known (J.R. Bidlot, personal communication) that the same ECMWF wave model that uses improved wave generation and dissipation parameterization in the IFS cycle 46R1 that is operational as of June 6, 2019 (ECMWF, 2019) and is similar to T471, already gives better results than the ERA5 wave heights at buoy locations. It

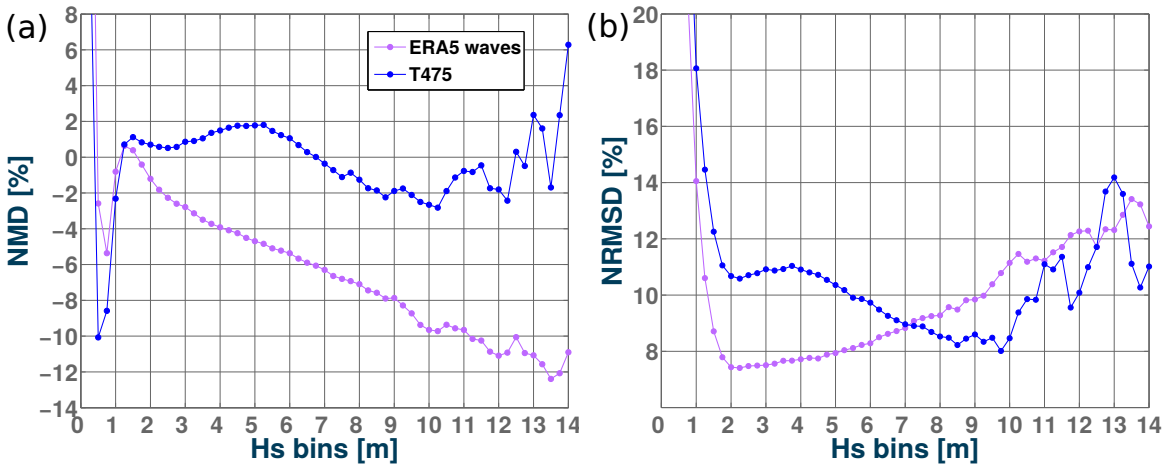

Figure 1.21 – Performance parameters curves for test T475 and ERA5 wave product with respect to Jason-3 altimeter data. (a) H_s NMD, and (b) NRMSD. Analyzed year: 2018. H_s bin size is 0.25 m.

is thus interesting to look at the differences between the ERA5 wave heights and the results of the present hindcast. It is important to highlight that the model adjusted in the present study uses different forcing, in particular for currents, sea ice and icebergs, and as previously descrived, it also includes some shoreline and iceberg reflexion. It also produces different output parameters, including fluxes of energy between the ocean and atmosphere, in addition to the parameters that can be derived from the wave spectrum. Here, the two simulations are compared using the Jason-3 data for 2018, which has not been assimilated in ERA5.

Fig. 1.21 shows a very strong negative bias in the ERA5 wave heights that, combined with a much lower random errors, gives larger rms differences for $H_s > 7$ m. Looking at the spatial distribution of these errors, larger random errors are typically found in the Southern ocean with T475 compared to ERA5 wave heights (Fig. 1.22), possibly a benefit of the assimilation of the other satellite missions where the satellite tracks are most dense, and lower random error are found in a few specific areas with T475, including in the Agulhas current, which shows again the benefit of properly including ocean surface currents in a wave model.

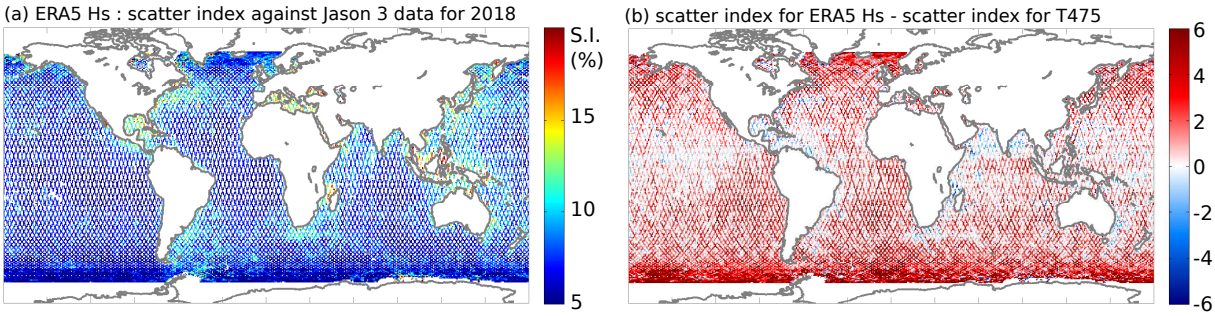

Figure 1.22 – (a) Scatter Index for 1 year (2018) averaged ERA5 H_s with respect to Jason-3 altimeter data. (b) Difference in scatter index between T475 and ERA5 waves product (T475 - ERA5).

1.7.3 Validation with buoy data

So far all the presented analysis, except for a brief discussion of mean direction and directional spread, has been based on wave heights alone, whereas the generated hindcast is based on the simulation of ocean wave spectra and produces a wide range of spatially gridded parameters as well as spectra at selected locations: around 10,000 points all along the world coastline plus the locations of moored buoys and a few additional offshore points. Even though the model was only marginally changed compared to the version validated by Stopa et al. (2016a), it is interesting to look at errors on the shape of spectra and wave period and directions parameters.

These comparisons are not simple because of the large response differences of different buoy types for wavelengths shorter than 10 m ($f \simeq 0.4$ Hz) in particular 3 m diameter discus buoys tend to filter frequencies above 0.4 Hz which are well reproduced, up to 0.6 Hz by 0.8 m diameter Waverider buoys (e.g. Ardhuin et al., 2019b). The present analysis is thus focus on the 0.05 to 0.4 Hz frequency band. Another difficulty is that most Waverider buoys are located in coastal areas, here a total of 5 buoys that are representative of different wave climates have been selected, as listed in Table 1.4. The buoy heave spectra were averaged over 3 h intervals matching the output frequecny of the model.

Fig. 1.23 shows different validations of the spectral content of the wave spectrum. Away from the coasts, at station Papa (buoy 46246), the average wave spectra in Fig. 1.23.a reveals a general good behavior of the model compared to Datawell buoy measurements with mean differences under 10% in the frequency range 0.05 to 0.4 Hz. The deviation at low frequencies can be due to the presence of infragravity waves in the buoy

Table 1.4 – List of buoys selected for detailed validation over the years 2018 and 2019. Note that data was missing before July 6, 2019 for buoy 46246.

WMO code	latitude	longitude	depth	shore distance	buoy type
46246	50.0 N	145.20 W	4252 m	900 km	Datawell WR
51208	22.285 N	159.574 W	200 m	5 km	Datawell WR
51004	17.53 N	152.25 W	5183 m	300 km	3-m discus
42097	25.70 N	83.65 W	81 m	130 km	Datawell WR
44098	42.80 N	70.17 W	77 m	37 km	Datawell WR

measurements which were not included in the model simulation, but could have been added and have a typical height of 1 cm in the open ocean (Ardhuin et al., 2014). That deviation could also be the result of mooring line effects. At high frequencies, the model understimation for $f > 0.5$ Hz may be due to the buoy heave resonance (Datawell, 2014).

The variability of the energy content at different frequencies is generally well captured by the parameters H_s and mean periods $T_{m0,2}$ (which is more sensitive to the high frequencies) and $T_{m-1,0}$ (more sensitive to the low frequencies). With a bias for the mean periods at buoy 46246 under 1% and a scatter index around 5%, the model is particularly accurate for the shape of the wave spectrum.

For other buoys, differences between the model and the observations can reveal errors in buoy measurements (e.g. the spectrum roll-off for $f > 0.52$ Hz at 51004 is typical of 3-m discus buoys) and difficulties for the model to resolve coastal sea state variability and growth for relatively short fetches. In particular, the energy for low frequencies ($f < 0.06$ Hz) is strongly underestimated in the Gulf of Mexico and the Gulf of Maine.

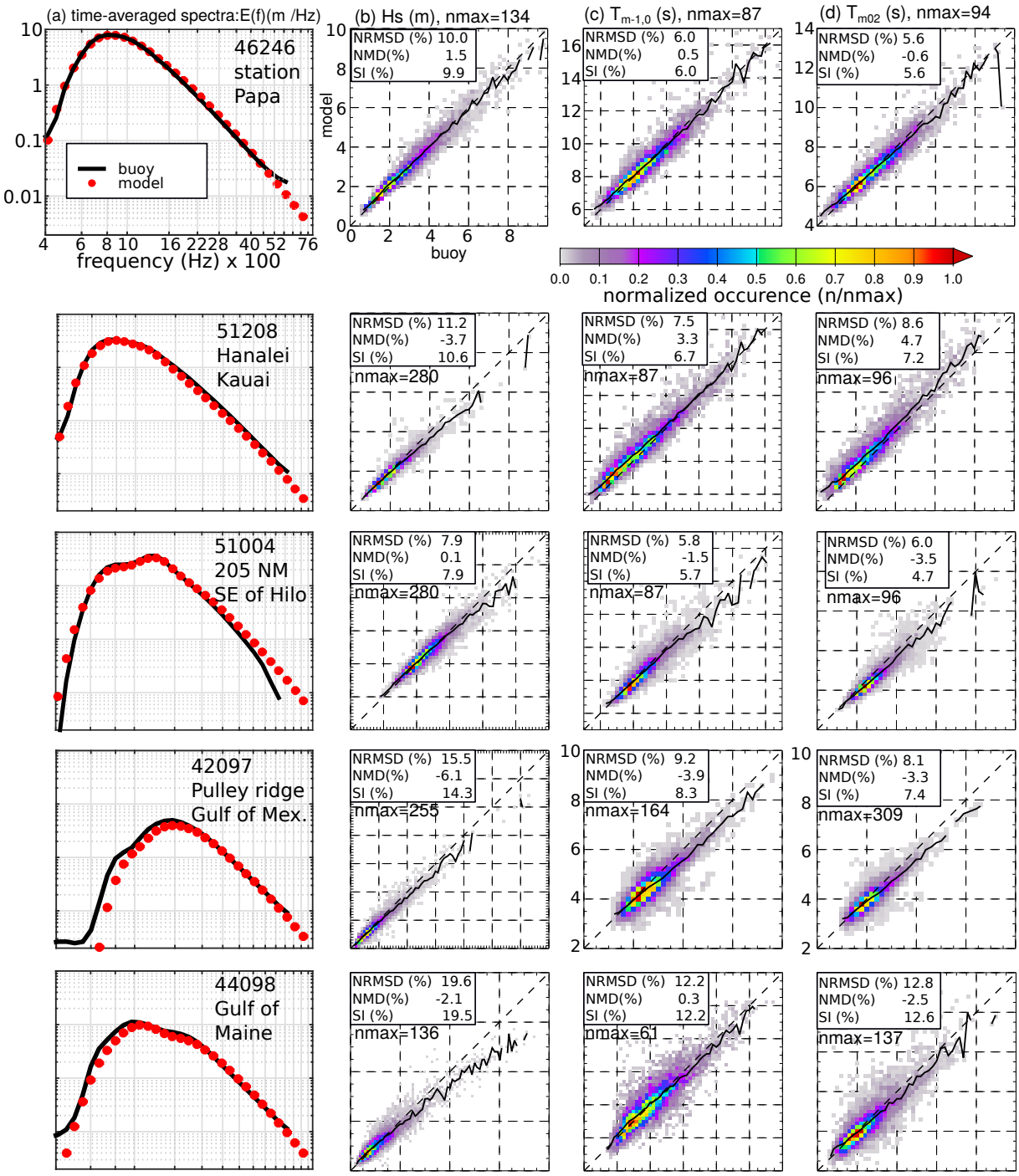

Figure 1.23 – Modeled and measured mean spectra, scatter plots for H_s, and mean periods $T_{m-1,0}$, $T_{m0,2}$ at selected buoys listed in Table 1.4.

1.8 Conclusions

The present section discusses the influence of forcing fields (winds, surface current, sea ice concentration, iceberg concentration), parameterizations (wind-wave generation and swell damping) and resolution (in physical and spectral space) on the wave heights produced by a wave model global hindcast, using the WAVEWATCH III modelling framework and satellite-derived wave heights. It is unfortunately not practical to test all the possible combinations of model settings, but it is expected that the choice of forcing fields and adjustment of parameters is generally robust, and the measurements shows that the present hindcast, in the context of the Integrated Ocean Waves for Geophysical and other Applications (IOWAGA) project, is generally superior to the previous version described by Rascle and Ardhuin (2013), and in some regions, for large wave heights, is superior to the ERA5 reanalysis wave product.

For the forcing, it was found that ERA5 winds, once corrected for a low bias at wind speeds above 21 m/s, gave more accurate results than operational ECMWF analyses or the CFSR reanalysis. The Bentamy et al. (2018) merged satellite-model product gave interesting results specially in the Southern Ocean where lower over estimation of wave heights is obtained. It was also found that the use of currents provided by CMEMS-Globcurrent generally improved the model results. Probably because these current estimates are missing a significant part of the Total Surface Current Velocity, they degraded the model results at latitudes larger than 50° N. Finally, the importance of both sea ice and icebergs for Southern Ocean and Arctic wave heights was confirmed.

For the model parameterizations of air-sea interactions, it was shown that the distribution of H_s around the global maximum of 2 m, could be used to adjust the transition from a laminar to a turbulent boundary layer above the waves, that is very important for the attenuation of swells, and is probably the most sensitive part of the model parameterizations.

Regarding model discretizations, a great benefit in including the 0.7 to 1 Hz frequency range was verified, even though the directionality in that range is not yet well described by the model when waves are developed.

For all these tests at global scale, only limited validation was performed for other parameters besides the significant wave height. Additional analysis on parameters like the directional spreading, peak direction and mean periods are presented in Chapter 2. It is expected that future adjustments will particularly focus on the high frequencies

($f > 0.4$ Hz) with more validation of the variables that are most sensitive to that frequency range, starting with the mean square slope and its directional components. These elements are partially discussed in Chapter 3 where the effects of the weave breaking parameterization by Romero (2019) are analyzed.

Chapter 2

Accuracy of spectral wave models in coastal environments: Application to the Atlantic coasts of Europe

2.1 Introduction

The progressive improvement of parameterizations in spectral wave models based on the wave action equation (WAE), like SWAN (Booij et al., 1999) or WAVEWATCH III®(The WAVEWATCH III ® Development Group, 2019), has helped to continuously extend their use into coastal regions and areas with shallower water depths. With the introduction of currents, bottom friction related to different sediment types and coastal reflection, errors in the main wave parameters have dropped to levels similar to open ocean simulations (Ardhuin et al., 2012; Roland and Ardhuin, 2014; Salmon et al., 2015). High resolution modeling has also become more efficient with the implementation of unstructured grids (mesh), providing flexible spatial resolution taking into account wave characteristics and bathymetry features (Alves et al., 2013; Benoit et al., 1996; Dietrich et al., 2011; Roland, 2008). In particular, previous works by Boudière et al. (2013) and Wu et al. (2020) present the implementation and validation of high resolution hindcasts for wave resource assessments along French waters and the U.S. West Coast respectively.

As mentioned initially, the accuracy of spectral models is a function of at least 3 main factors. First, the accuracy of forcing fields, second, the realism of the parameterizations of processes representing spectral wave evolution and third, the numerical choices made to integrate the WAE, namely discretization and numerical schemes. For example, in the hindcast presented in Chapter 1 (Alday et al., 2021), more accurate wave height distributions were obtained at global scale by adjusting parameterizations and discretizations.

When it comes to nested models, the characteristics of the boundary conditions should also be taken into account.

In the present chapter the analysis is extended to intermediate and shallow water depths. To this end, a high resolution wave hindcast for European Atlantic waters is presented, using boundary conditions from the global model adjusted in Chapter 1. Particular attention is paid to the effects of tidal currents, directional resolution and bottom friction over the simulated wave fields. Performance analysis of the results is also extended to other wave parameters and conducted in terms of the significant wave heights, directional spreading, peak direction, and mean periods. Additionally, analyses on the energy distribution as a function of frequency were conducted to further explore the changes introduced through modifications in the forcing, resolution or the boundary conditions.

Details on the model setup, source terms and numerical choices are presented in section 2.3. Wave measurements used for sensitivity analyses and validation in 2.4. The model performance analysis is described in section 2.5 followed by its validation and conclusions in sections 2.6 and 2.7.

The content of this chapter has been published in Alday et al. (2022).

2.2 Method

In additon to the statistical parameters presented section in 1.2, the Root Mean Squared Differences (RMSD) and the Mean Differences (MDIFF) are included to assess the accuracy of the coastal model.

$$\mathrm{RMSD}(X) = \sqrt{\frac{\sum(X_{\mathrm{mod}} - X_{\mathrm{obs}})^2}{N}} \tag{2.1}$$

$$\mathrm{MDIFF}(X) = \frac{1}{N}\sum(X_{\mathrm{mod}} - X_{\mathrm{obs}}) \tag{2.2}$$

$$\tag{2.3}$$

where X_{obs} are the observed quantities from in-situ or satellite measurements, X_{mod} are the modelled quantities (spectral values or integrated wave parameters), and N the total amount of analyzed data.

The RMSD and NMD are used mainly to put in context changes of the analyzed quantities (wave parameters or spectral energy), otherwise perceived as large variations

when analyzed only with NRMSD or NMD.

2.3 Model set-up and sensitivity tests

2.3.1 Mesh construction

The triangle grid used for the simulations was created using an interface developed at BGS IT&E (Polymesh 2-D Mesh Generator). The main data sources employed for the mesh construction were coastline polygons from OpenStreetMap (last update of used data set: 2018-06-10 09:33), bathymetric information from EMODnet (2016 version) and HOMONIM digital terrain models (DTM). The DTM sources have gridded resolutions of ∼210 and ∼110 m respectively, with depths defined with respect to the mean sea level (MSL). Although the coastline is generally located at high water levels with an exact definition that varies from country to country, a constant 2 m minimum depth value was imposed at the coastline to preserve the shoreline geometry and avoid unrealistic wave height gradients at the nearshore that could be triggered by the combination of large tidal sea level variations (wet and dry effect) with inadequate spatial resolution in very shallow areas close to the shore.

Previous to the triangulation, a nodes' homogenization of the coastlines was applied to ensure a minimum segment length of 400 m in the polygons. An extra segment coarsening (up to 1200 m) and trimming was applied along the Norwegian fjords to reduce the final amount of nodes. This action facilitated obtaining a more relaxed CFL restriction, which implies a larger minimum time step for wave propagation, 13 s in this case, but it also implies that details of the Norwegian coastline are not as well resolved. In addition, nodes from an existing mesh (Boudière et al., 2013) with the exception of those placed less than 800 m from the coastlines, were included in the generation of the new mesh fixing their previous position. This was done to facilitate the use of the new results by users of the previous hindcast.

Finally, the resolution was increased in 14 zones of interest for marine energy users, (Fig. 2.1.a). The generated mesh has a total of 328,030 nodes (Fig. 2.1.b), with a resolution (triangle side) ranging from ∼200 m at the coast and refined zones to, approximately 15 km in deep offshore areas.

An alternative to this careful editing of the mesh is the use of implicit schemes. However, using implicit schemes with CFL values much larger than 1 opens the door to both

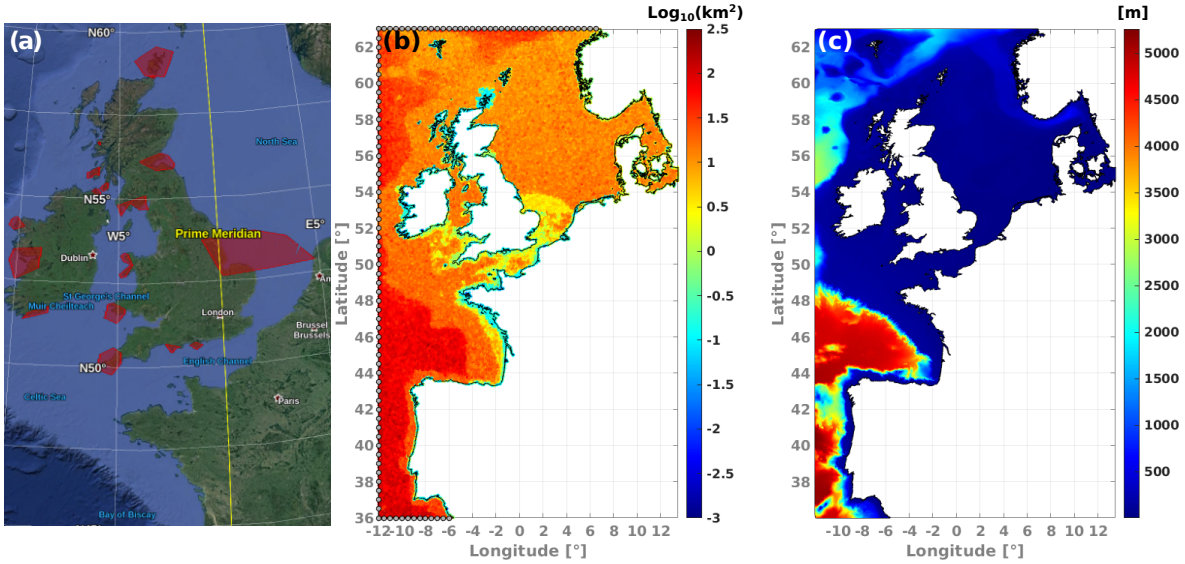

Figure 2.1 – (a) Refinement polygons in red. (b) Final mesh elements size distribution, coastlines polygons in black, in grey mesh nodes where boundary conditions are prescribed from the global model. (c) Bathymetry reconstruction with mesh. Colorbar in (c) represents depths with respect to MSL in meters. Map data in (a) are from ©Google Landast / Copernicus.

larger advection errors (stability does not imply accuracy) and larger splitting errors as the time steps for advection can be much smaller than the refraction and source term time step (Roland and Ardhuin, 2014). It was preferred to stick to the explicit N-scheme because numerical efficiency is not central in the study, and it simplifies comparisons with global model results that also use explicit schemes. Implicit schemes are probably necessary when resolving regional scales and surf zones in the same mesh when CFL constraints require prohibitively small time steps in explicit schemes.

2.3.2 Bottom sediment map

The construction of a sediment grain size map was included to properly represent wave energy dissipation due to bottom friction (see section 2.5.5 for results). In the model, the grain size is characterized by its median diameter D_{50}, defined at each node of the mesh. The D_{50} values where estimated from the EMODnet harmonized seabed substrate charts. The minimum grain size was set to 0.02 mm, while zones characterized as pebbles or larger elements (boulders and bedrock) were represented with a D_{50}=150 mm. By default, the

minimum grain size was applied to all regions where no substrate was specified. Since most areas with no bottom characterization are in deep waters (e.g. $>$ 400 m), this assumption does not have any relevant effect on the wave fields evolution. The bottom sediment diameter map is presented in Fig. 2.2.

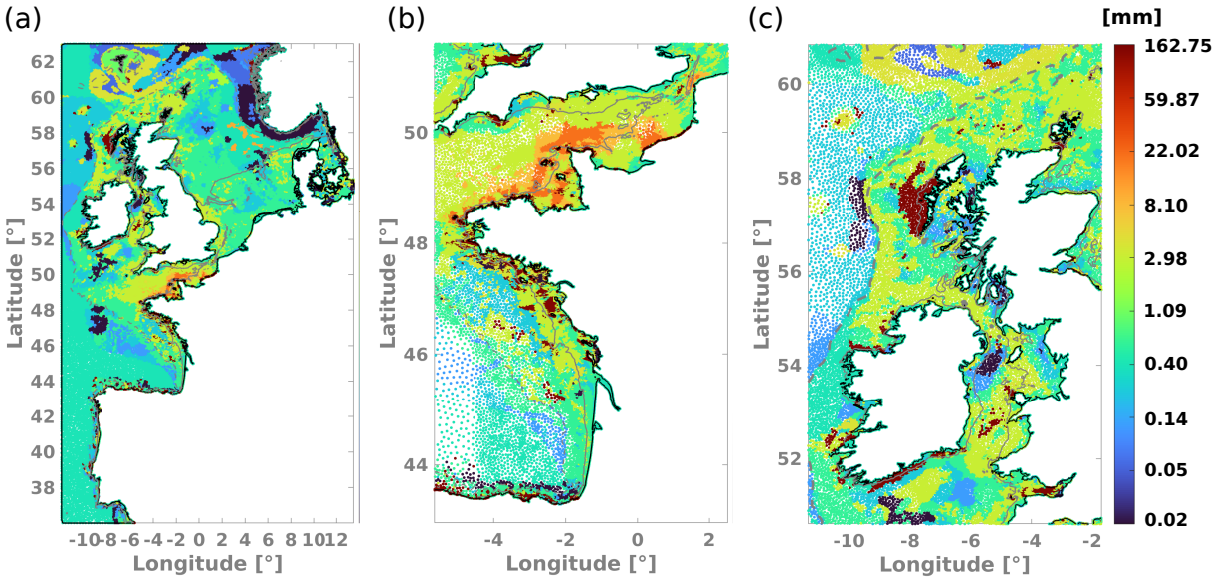

Figure 2.2 – Bottom sediment size map. D_{50} values assigned to each mesh node for: (a) Full domain, (b) Bay of Biscay and the English Channel and (c) UK. Colorbar represents D_{50} in mm. Gray dashed lines represent 200 m depth contours, continuous gray lines represent 50 m depth contours.

2.3.3 Source terms and numerical choices

In WW3 the WAE is solved using a splitting method to treat in different steps temporal depth changes, spatial propagation, intra-spectral propagation and source terms (The WAVEWATCH III® Development Group, 2019; Tolman and Booij, 1998; Yanenko, 1971). Spectral propagation, which includes refraction, is computed with an explicit third order scheme that combines the QUICKEST scheme with the ULTIMATE total variance diminishing limiter (Leonard, 1991), while spatial advection is done with the explicit Narrow-stencil-scheme (N-scheme) (Csík et al., 2002; Roland and Ardhuin, 2014). Nonlinear evolution and wave to wave interactions are represented with the Discrete Interaction Approximation (DIA, Hasselmann et al., 1985). The utilized wind input and wave dissipation source terms are taken from the parameterizations described in Ardhuin

et al. (2010) with adjustments described in Chapter 1 (Alday et al., 2021) consistent with the global model used for our boundary conditions. A constant wave energy reflection of 5% is used at the coastlines, as parameterized by Ardhuin and Roland (2012). A detailed list of the parameters used for the model implementation is given in Appendix B.

2.3.4 Boundary conditions and forcing fields improvements

The accuracy of modelled wave data directly depends on the quality of the forcing fields and the provided boundary conditions (BC) for the case of nested models. This becomes particularly relevant in coastal areas, for accounting wave-current interactions in macro-tidal areas, the assessment of energy resources, port design and operation conditions, or the study of extreme events.

For most test cases and for the final high resolution coastal hindcast, BC are taken from the the wave data set described in Chapter 1. The (directional) spectral BC taken from the global model are prescribed along the southern, western and northern open boundaries of the mesh (Fig. 2.1.b). These are interpolated in space and time into each active node along the open boundaries of the nested mesh.

For the proposed regional model, three main forcing fields were included: wind, tidal levels and tidal currents. As for the global model, ERA5 surface winds were used for wave generation. Similar to what was done in Boudière et al. (2013), tidal levels and currents time series were reconstructed in WW3 with harmonics taken, in this case, from two different sources. The first one, is the output from Ifremer's tidal atlas (Pineau-Guillou, 2013) created with MARS 2D (Lazure and Dumas, 2008), a hydrodynamic model based on the shallow water equations. A total of 5 embedded models with 3 levels of nesting and different spatial resolutions were selected (Table 2.1, Fig. 2.3.a). The second tidal data source was used to cover part of the Atlantic coast of Portugal until the Gulf of Cadiz, which are not included in the tidal atlas. The complement data was taken from the native mesh of the FES2014 model (Carrere et al., 2015) and re-grided to 0.004° (Fig. 2.3.b).

In all simulations, the boundary conditions are updated every three hours, winds every hour, tidal levels and velocities fields are updated each 30 minutes. The output frequency of the nested model is hourly.

Table 2.1 – Selected models from Ifremer's tidal atlas.

Nesting level	Spatial resolution [m]	Model domain limits		Region	Model Name
		Longitude [°]	Latitude [°]		
0	2000	-20.03 to 14.98	39.98 to 64.98	North-East Atlantic	ATLNE2000
1	700	-5.73 to 4.18	43.28 to 52.00	E. Channel and Bay of Biscay	MANGA700
2	250	-5.63 to -3.66	47.34 to 49.03	Iroise Sea	FINIS250
2	250	-4.23 to -1.96	46.78 to 47.93	Southern Brittany	SUDBZH250
2	250	-4.21 to -0.50	48.45 to 50.10	West of English Channel	MANW250

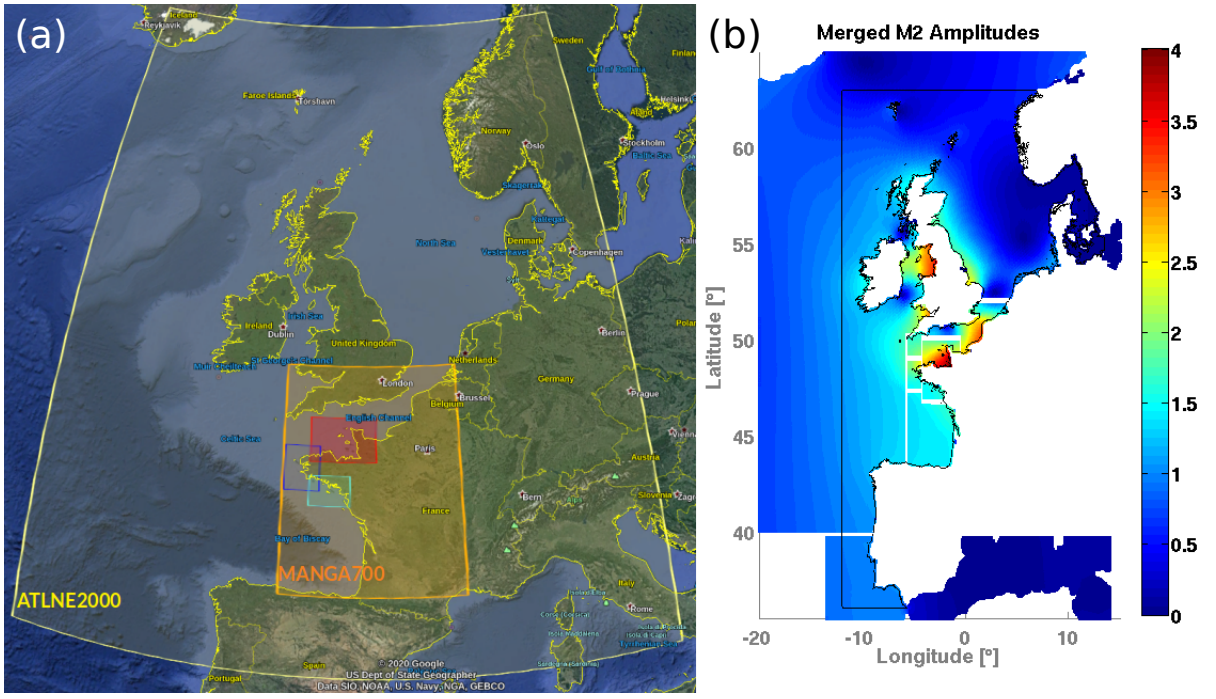

Figure 2.3 – (a) Spatial coverage from selected tidal models. Blue and green rectangles have a 250 m resolution, and the orange and yellow area have resolutions of 700 m and 2000 m respectively. (b)Example of merged tidal harmonics from Ifremer's tidal atlas and FES2014. Colorbar in (b) represents M2 amplitude values in meters; black lines show the boundary and coastline polygons.

2.3.5 Spectral discretization and time steps

The same extended frequency range used in the global grid was employed in the regional mesh to perform all simulations, matching the discretization at the boundary. As previously explained, the extension to higher frequencies is aimed to allow for a better

representation of the variability of the wave spectrum for very low wind speeds or very short fetches. At the other end of the spectrum, the purpose of adding lower frequencies is to let the spectrum develop longer wave components for severe storm cases (e.g. Hanafin et al., 2012). In terms of directional discretization, 36 directions (10° resolution) were used for the full hindcast generation and most of the sensitivity analyses, and tests with 24 and 48 directions were employed to verify the effects of the directional resolution (section 2.5.4).

The source terms are integrated with an adaptative time step that is automatically adjusted in the range 5 to 180 s. The maximum model advection time step was set to 30 s, taking into account the minimum mesh triangle area and the presence of strong currents. The refraction time step was set to 15 s. Sensitivity tests with smaller values (not shown) had very limited impact on the model results.

2.4 Wave data sources

2.4.1 Buoy data

To assess the performance of the model at specific locations, 6 French buoys with spectral data provided by CEREMA, and 2 Belgian buoys from which spectra were not available were selected. The Belgian buoys located within the Flemish banks, besides the usual significant wave height, they provide a low frequency wave height H_{10} (Fig. 2.4). The H_{10} pararameter corresponds to a wave height computed for periods from 10 s and longer (≤ 0.1 Hz).

These sites cover a wide range of depths, current intensities, tidal amplitude levels and proximity to shore, which makes them an appropriate sampling group to evaluate the overall accuracy of the results (Table 2.2). No assessment of potential instruments' replacements, maintenance periods nor deploy position changes have been taken into account for this study.

To match the frequencies discretization of the spectrum and output frequency (hourly) in WW3, spectral data from the in-situ measurements have been first interpolated into the same discrete frequencies used in the model, and then averaged in time to provide hourly output.

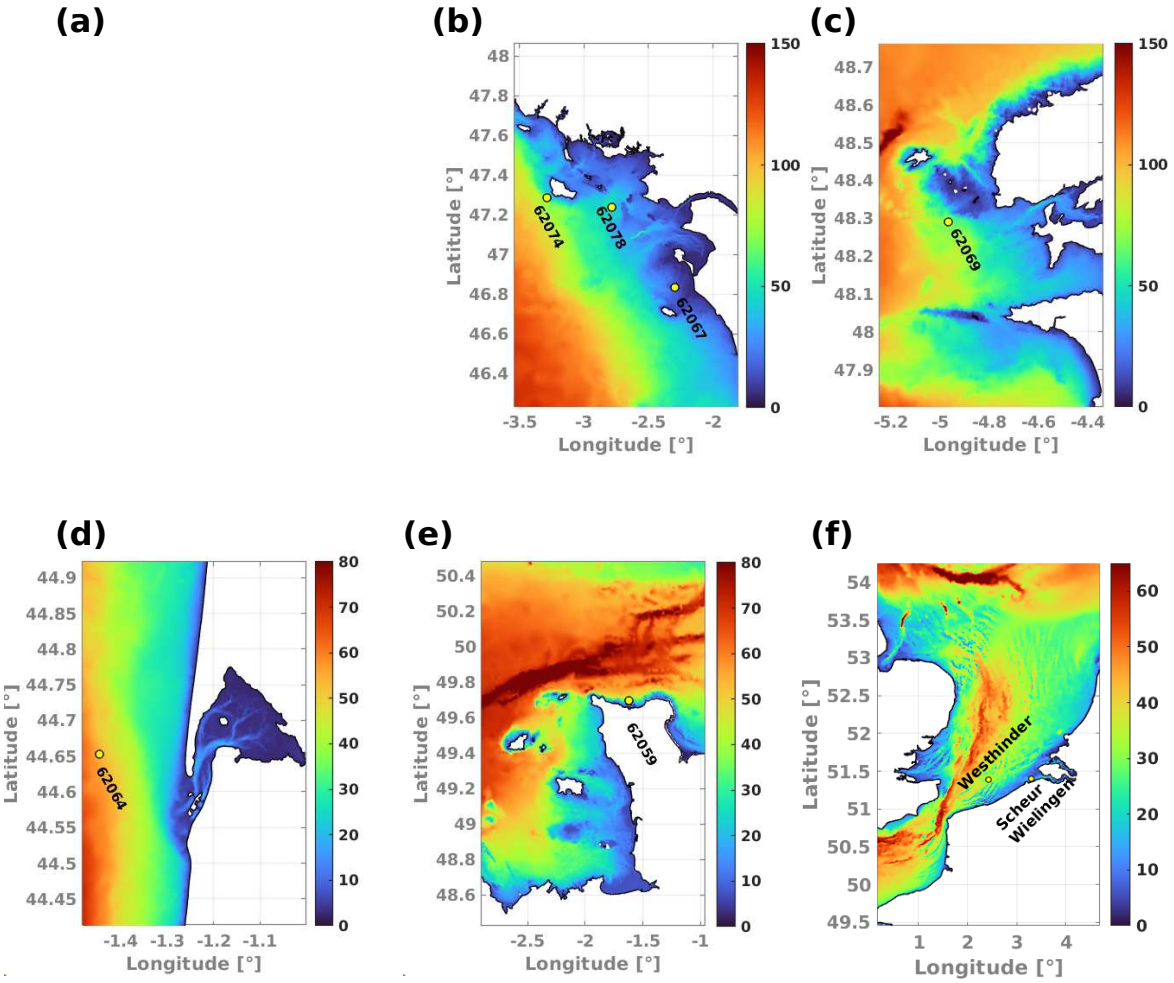

Figure 2.4 – Buoys location and bathymetry features.(a) Buoys along French coast. (b), (c), (d) and (e) details of French buoys locations. (f) detail of Belgian buoys location. Colorbar shows depths in meters with respect to MSL. Maximum depth on each panel has been selected to enhance bathymetry details.

2.4.2 Satellite altimetry data

The general performance evaluation of the model was done by comparing its results with the ESA Sea State CCI V2 altimeter dataset. The "denoised" (Quilfen and Chapron, 2021; Schlembach et al., 2020) significant wave height (SWH) at 1 Hz is used to estimate the performance indicators in an along-track statistical analysis of the wave heights, and for time averaged values over the complete modelled domain. The adjusted denoised SWH has an along track spatial resolution equivalent to approximately 7 km.

Table 2.2 – Spectral buoys ID, location name, position and estimated deploy depth. Distance to coast estimated with respect to continental coast, except for buoy 62074. Deploy depth obtained from model bathymetry interpolated into the buoys' position.

Buoy WMO ID	**Location name**	**Longitude [°]**	**Latitude [°]**	**Distance to coast [km]**	**Depth [m]**	**Data type**
62059	Cherbourg	-1.6200	49.6950	4.0	28.99	spectral
62069	Pierres Noires	-4.96833	48.29033	15.06	67.12	spectral
62074	Belle Ile	-3.2850	47.2850	4.1	56.21	spectral
62078	P. du Four	-2.7870	47.2390	19.0	37.50	spectral
62064	Cap. Ferret	-1.44667	44.65250	14.7	53.45	spectral
62066	Anglet	-1.61500	43.532166	6.7	56.77	spectral
–	Westhinder	2.4358	51.381	32.3	21.90	H_{10}
–	Scheur Wielingen	3.3022	51.401	4.75	7.80	H_{10}

2.5 Model Performance

The modelled domain covers a wide range of bathymetry features, bottom sediment types, fetch and tidal amplitudes. It is thus of interest to analyse how the choices made in the model setup affect the wave fields' characteristics, and to verify when and where those choices introduce relevant changes in the simulated sea states. In the present section, an extended sensitivity analysis is carried out to assess the effects of high spatial resolution, forcing and spectral resolution.

2.5.1 Influence of high spatial resolution

Higher spatial resolution is especially needed in intermediate to shallow depths, where interactions with the sea bottom become dominant in waves' propagation. A more detailed representation of the bathymetric and coastline features allow to better simulate processes like shoaling, refraction and, in some cases, diffraction or depth induced breaking.

A comparison between February 2011 mean significant wave heights (H_s) fields from the global model described in section 2.3.4 and the implemented regional model is presented in Fig. 2.5. To evaluate the differences between models, the output from the 0.5° global grid (Fig. 1.1) was linearly interpolated into the regional mesh nodes before computing the mean H_s and the NMD (between models) for the selected time window.

The most important differences are found on the shelf, often at depths shallower than 400 m, and where complex bathymetry characterization requires higher detail to improve for example wave refraction (NMD in Fig. 2.5). The largest NMD positive

values (> 20%) are commonly found in the regions sheltered from North Atlantic swells. In the low resolution global model, islands and headlands smaller than the grid size are parameterized as obstructions of the wave energy flux (Chawla and Tolman, 2008). Another direct effect of using increased spatial resolution can be seen between the Orkney and the Shetland islands. The regional model shows averaged H_s values of almost 5 m in this area for the analyzed month. On the other hand, the combined effects of the sub-grid obstruction approach and coarse resolution of the global grid, leads to high under-estimation of about -20% with respect to the mesh results.

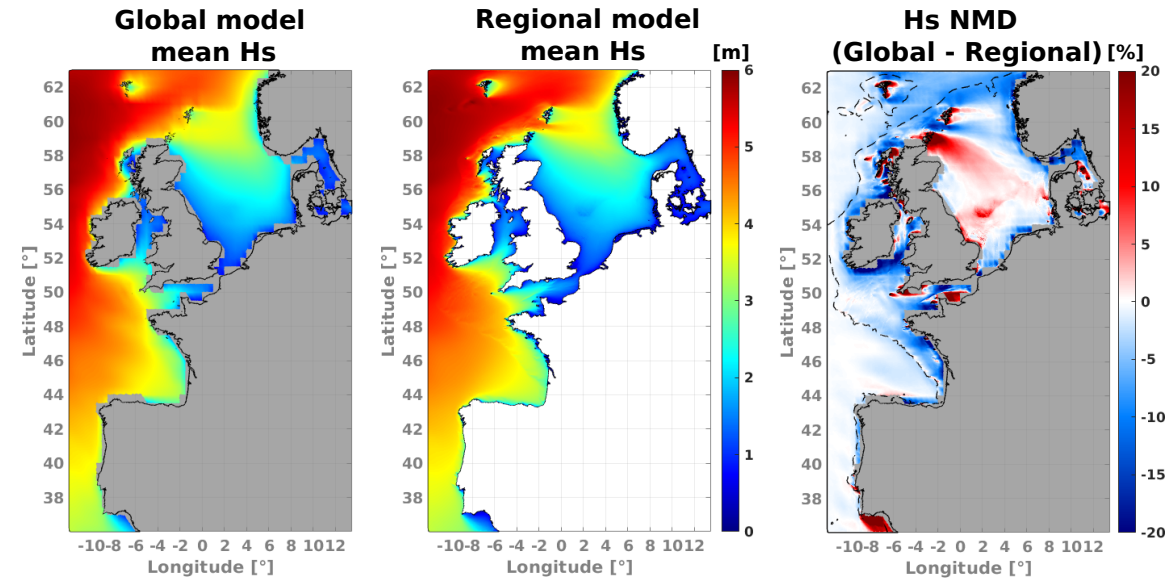

Figure 2.5 – Mean H_s fields from global and regional model, and H_s normalized mean differences (Global - Regional). Dashed black lines represent the 400 m depth contours. Areas where no wave data are available from the global grid are highlighted with a gray background in left and right panels. Results for February 2011.

2.5.2 Adjustments in wind-wave generation and swell dissipation

In Chapter 1 adjustments in the parameterizations of wave generation by the wind and swell dissipation proposed by Ardhuin et al. (2010) and Leckler et al. (2013) were applied to better represent the wave heights measured by altimeters at global scales. Here the impact of these modifications on waves in the coastal domain is further considered, using five different simulations with parameter changes listed in Table 2.3. These changes include an empirical enhancement of the wind speeds above a threshold U_c by the amount $x_c(U_{10} - U_c)$ (see eq. 1.9), and a modification of the swell dissipation with a change in the threshold Reynolds number Re_c that defines the transition from the weak (laminar) to strong (turbulent) swell dissipation and the swell dissipation coefficient s_7 (see eq. 1.7 and 1.8).

Table 2.3 – Tests for wind correction and swell dissipation parameters, in bold, values leading to T475. All parameters not specified here correspond to the T475 parameter adjustment detailed by Alday et al., 2021. Variables Re_c, U_c and x_c correspond to namelist parameters SWELLF7, SWELLF4, WCOR1 and WCOR2 in the WW3 input files (see Appendix B for the full set of parameters). The directional discretization has 24 directions in all of these tests.

Test Name	$\mathbf{s_7}$	$\mathbf{Re_c}$	$\mathbf{U_c}$ (m/s)	$\mathbf{x_c}$
Bm1.75	3.60×10^5	1.50×10^5	-	-
Bm1.75-W02	3.60×10^5	1.50×10^5	21	1.05
Bm1.75-W03	3.60×10^5	1.50×10^5	23	1.08
Bm1.75-W04	3.60×10^5	1.50×10^5	22	1.05
T475	$\mathbf{4.32 \times 10^5}$	$\mathbf{1.15 \times 10^5}$	21	1.05

The model's results were analyzed for two months when extreme sea states have been recorded, February 2011 and January 2014. In February 2011, the extra-tropical storm Quirin generated extreme sea states with peak periods exceeding 20 s over the western coasts of Europe. In January 2014, storm Hercules was one of the many storms from a particularly severe winter. This event caused vast coastal damage in the UK (Masselink et al., 2016), and from the Western coast of France to Portugal (Masselink et al., 2015). H_s values exceeded 10 m and peak periods exceeded 20 s (Castelle et al., 2015; Ponce de León and Guedes Soares, 2015). Given the characteristics of the selected cases, it is considered that they are suitable to study wave energy fluctuations down to frequencies lower than 0.06 Hz. Although analyses were carried out for February 2011 and January

2014, in this section the results for the later period are presented.

Despite the similarities between time series of the wave parameters such as H_s and T_{m02} from one test to another, they noticeably differ for extreme values. Yet, the model runs have systematic differences as a function of wave heights or wave periods, with 5 to 10% deviations for the larger periods and heights that correspond to the most severe storms and associated swells (Fig. 2.6). In these events, and consistent with the global scale results, the wind enhancement is most effective at correcting the low bias in extreme wave heights and mean periods that is typical of the previous hindcasts. Adjustments to the swell dissipation have a negligible impact when acting only over 1000 km of propagation within our coastal domain. As shown in Fig. 2.7, the wind enhancement allows the generation of lower frequency waves. This improves the model accuracy at exposed buoys 62066, 62074 and 62069, and produces realistic energy levels for frequencies below 0.05 Hz during the extreme events of January 2014. Unfortunately, the correction also produces too much low frequency energy at the shallower buoy 62078. It is suspected that dissipative processes in shallow water may be underestimated for these very large periods (Fig. 2.7.e,f).

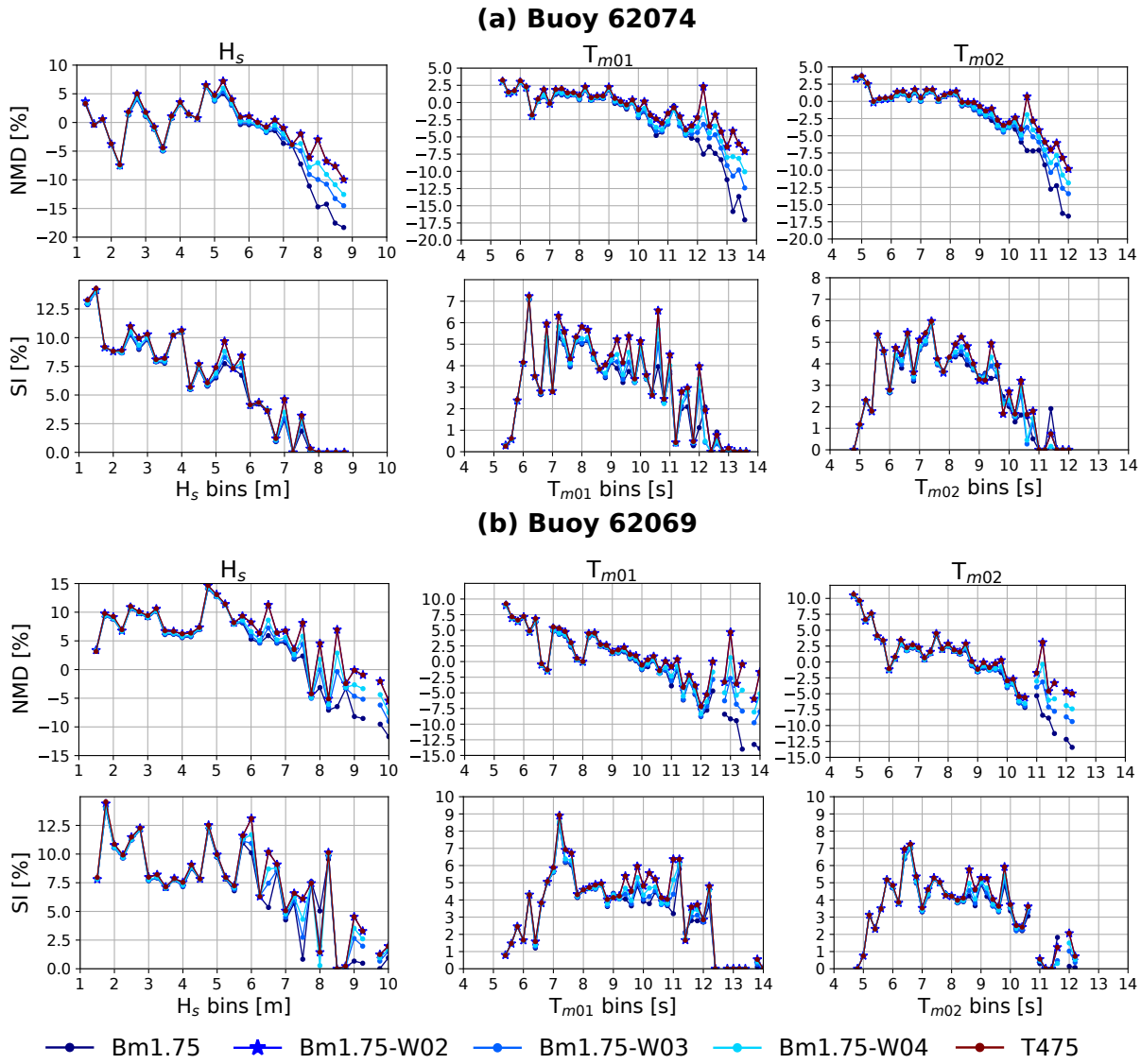

Figure 2.6 – NMD and SI for tests leading to T475 (Table 2.3). Results for January 2014. In (a) and (b) modelled results compared with buoys 62074 and 62069 respectively. H_s bin size is 0.25 m, periods bin size is 0.2 s.

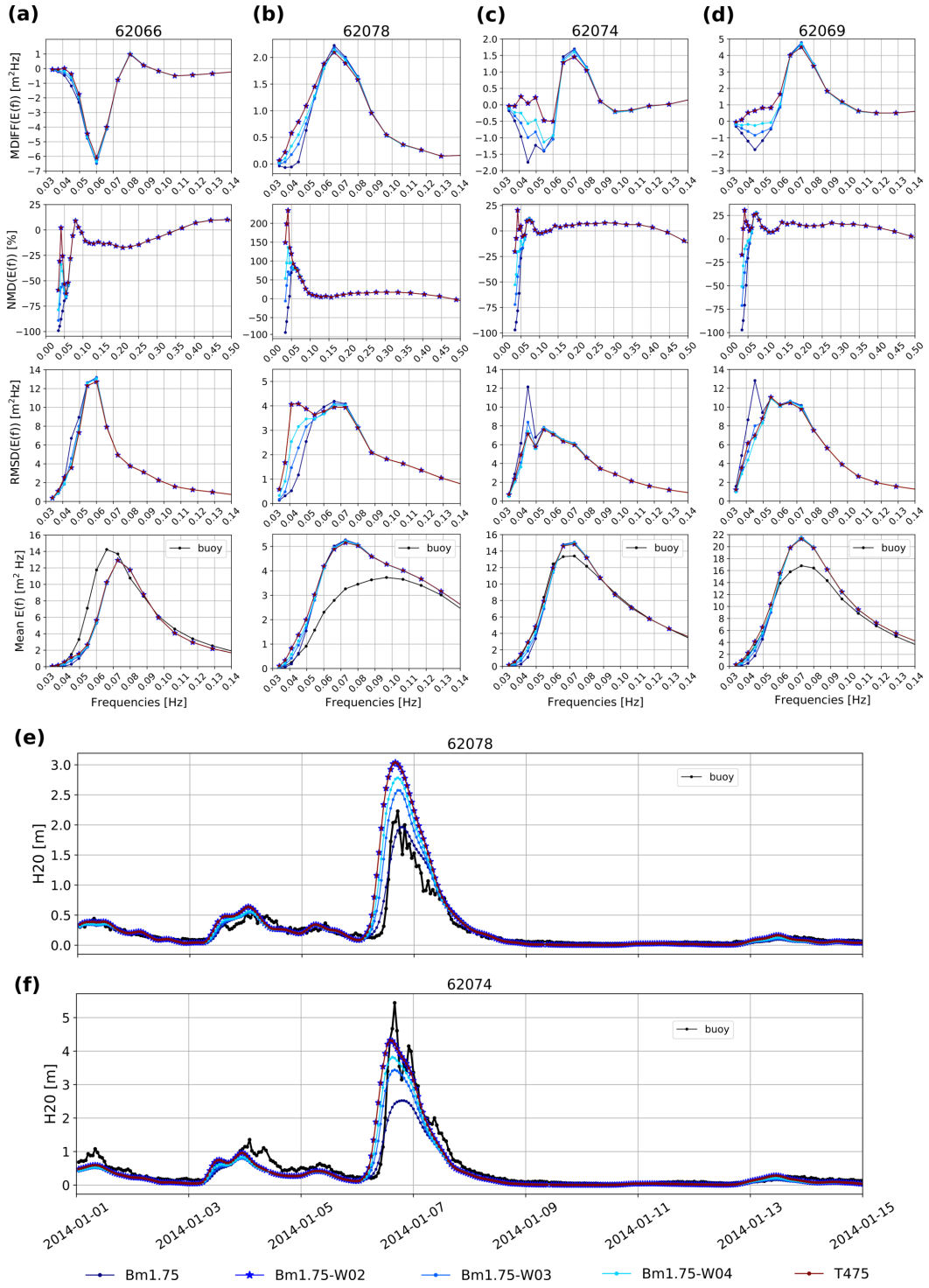

Figure 2.7 – Performance parameters for energy levels at each discrete frequency of the spectrum, for tests leading to T475 (Table 2.3). Results for January 2014 at buoys 62066, 62078, 62074 and 62069. In panels (a) to (d) modelled results compared with buoy data. Time series of modelled and measured H_{20} for buoys 62078 in (e) and 62074 in (f).

2.5.3 Wave-Current Interactions

At global scale, the use of ocean surface currents can improve the accuracy of the simulated sea states (e.g. Chapter 1, Echevarria et al., 2021), although a full effect generally requires relatively high spatial resolution that is generally not achievable by observations and thus models are usually not constrained at the necessary scale (Marechal and Ardhuin, 2021). Adding surface currents in the simulations can have effects on wave generation due to changes on the relative wind, it can modify the advection of waves or induce refraction in regions with large current gradients. At local (smaller) scales, focusing, blocking and induced breaking can occur as waves propagate against strong current jets with increasing velocities (Ardhuin et al., 2012). Given the diverse tidal amplitudes within the modeled domain, it is expected to have different effect levels over the sea states in different areas. An attempt to characterize the changes of the wave field when tidal currents are taken into account in the simulations is done by looking at differences on a set of wave parameters, namely H_s, directional spreading SPR, the peak direction D_p and peak period T_p.

First, the effect of currents at global scale is checked via the boundary conditions, and then the local tidal current effects within the coastal domain. The original $\beta_{\max}$ value was reduced to 1.60 in the global grid when no current forcing is used to define the BC, while maintaining the other parameters' settings from test T475 (Table 1.2). This was done to avoid introducing a high positive energy, and hence H_s bias, through the BC into the mesh domain. In Fig. 2.8 the H_s NMD distribution with respect to the Jason-2 altimeter is presented. Bias estimates are computed with 1-year tests (2011 and 2014) using T475 settings, T475 without currents (T475-NC-*) and our proposed test with $\beta_{\max}$ = 1.60 without global current forcing (NC-Bm1.60-*). Here, it is possible to see the high H_s bias introduced when only global currents are removed without adjusting $\beta_{\max}$ (tests T475-NC-11 and T475-NC-14), and how the reduction of $\beta_{\max}$ helps to improve the global wave heights distribution and NMD almost to the same levels of T475.

To evaluate the effects of global currents on the boundary condition, we analyzed a specific output time with a large Atlantic swell, and differences between 1 month simulations. The most noticeable changes caused by global currents are obtained for H_s, D_p and directional spreading (Fig. 2.9 middle panel), with typical differences of the order of 5 %. These differences vanish when averaged over one month (Fig. 2.9 right panel).

The effects of tidal currents within the model domain are generally more important, with some strong local effects caused by the high spatial currents' variability. In contrast

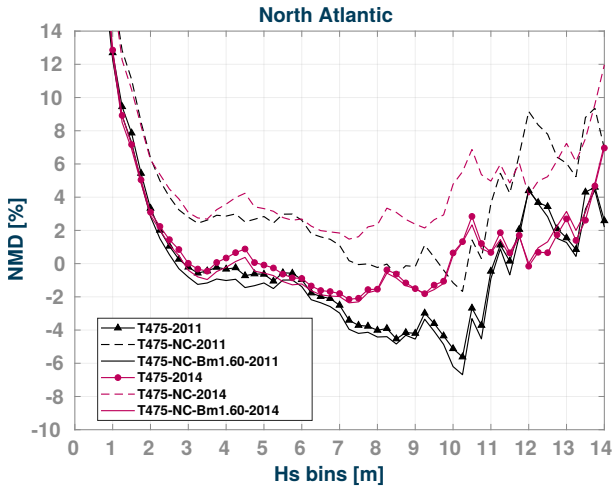

Figure 2.8 – Normalized mean bias of H_s for the North Atlantic (WW3 - altimeter SWH). Wave height bins are 0.25 m. 1-year tests for 2011 and 2014 are identified with black and fuchsia lines respectively. Altimtetry significant wave heights (SWH) from Jason-2.

to the influence of global currents in the BC, there is a clear increase of the wave fields' differences at each temporal output, that can be larger than +/-10 %. Feature mainly seen along the English Channel and the Irish Sea (Fig. 2.10, left panel). Over the entire month, tidal currents induce mean H_s differences of the order of 5 % (Fig. 2.10, right panel). The use of tidal currents also proved to have large impact over the peak period (T_p), up to 15% differences in Normandy and Liverpool bay, for example, and 8 % mean differences over one month (not shown).

There is a noticeable feature of the wave field along the shelf break, starting at the Bay of Biscay and extending northwards up to 49°N, which can be seen more clearly through the D_p and H_s fields from Fig. 2.9.b,c (left panel), and particularly by analyzing the effects of tidal currents over the wave heights in Fig. 2.10.c (left panel). The current intensities generated in WW3 present maximum values of about 0.5 m/s along the aforementioned area, which is consistent with previously recorded in-situ measurements (i.e. Le Cann, 1990). It is thought that the distinct gradients visible in some of the wave parameters are function of the tides' phase and the mean wave direction. Attempts to identify the presence of this signature with altimeter data is an ongoing subject of study.

Results were further compared against in-situ data from January 2014 at buoy 62059 (Fig. 2.12). Including tidal currents helps to reduce the high energy bias at low frequencies, probably due to an overall reduction of the effective wind input for locally generated waves during the tidal cycle (Fig. 2.12.a). In Fig. 2.12.c is possible to observe the mod-

ulation of H_s and T_{m01} caused by the changes in currents intensities and direction (blue line in figure), which in the end helps to reduce the bias of these quantities compared to the measurements (Fig. 2.12.b). Notice that there is a constant shift in the occurrence of peaks and troughs of H_s and T_{m01} in Fig. 2.12.c. This is thought to be mostly attributed to a slight phase shift in the tidal forcing field, which introduces a small increase in the RMSD when tidal currents are included in the simulations (not shown).

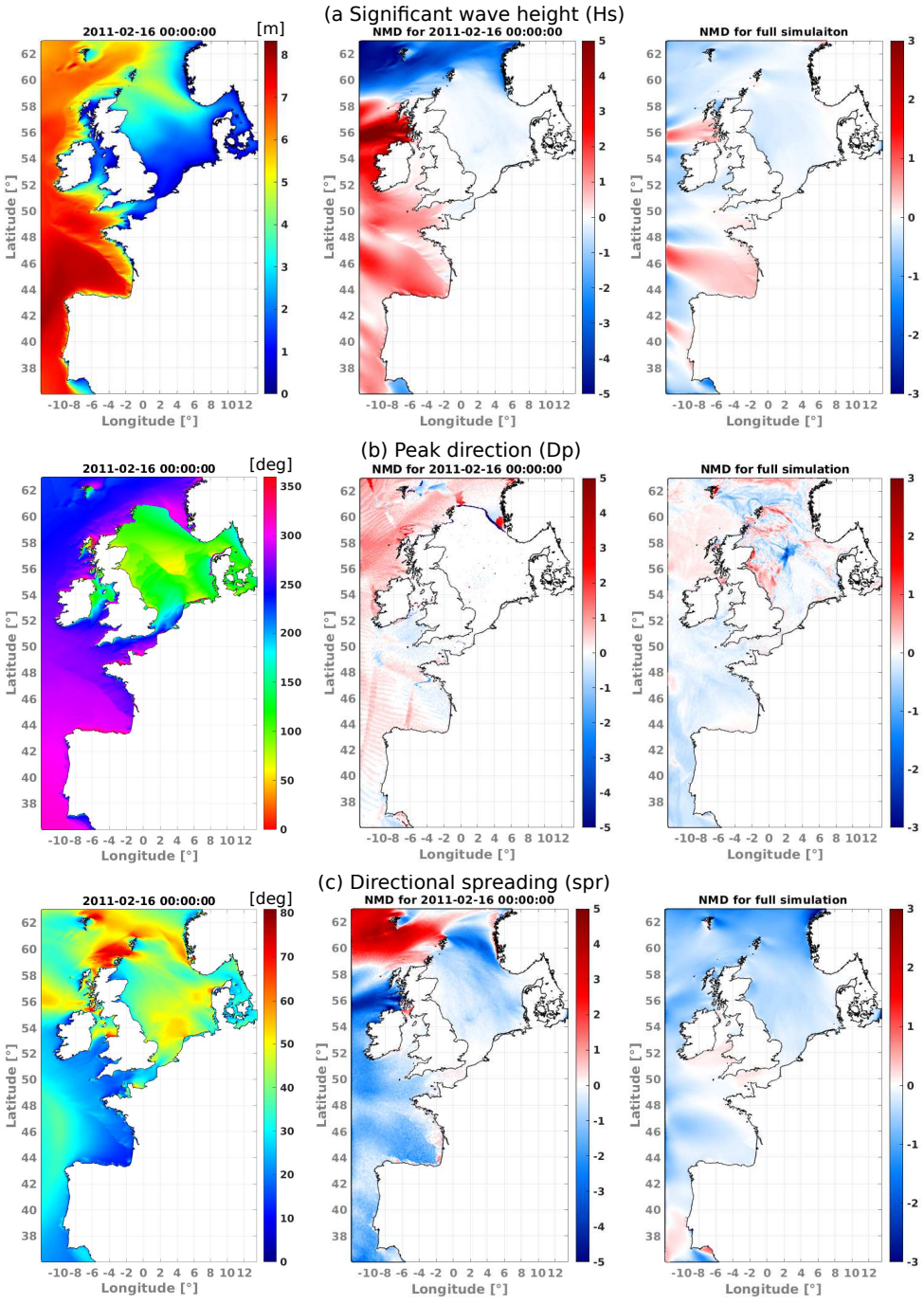

Figure 2.9 – Global currents effects over (a) H_s, (b) D_p and (c) directional spreading. In left panel, model output for test using BC generated with global currents at 2011-02-16 00:00:00 UTM. NMD results in middle and right panels are for test with BC obtained without global surface currents with respect to test with BC from global grid forced with global currents. Colorbars in middle and left panels represent NMD in [%]. Full simulation duration of tests is 1 month.

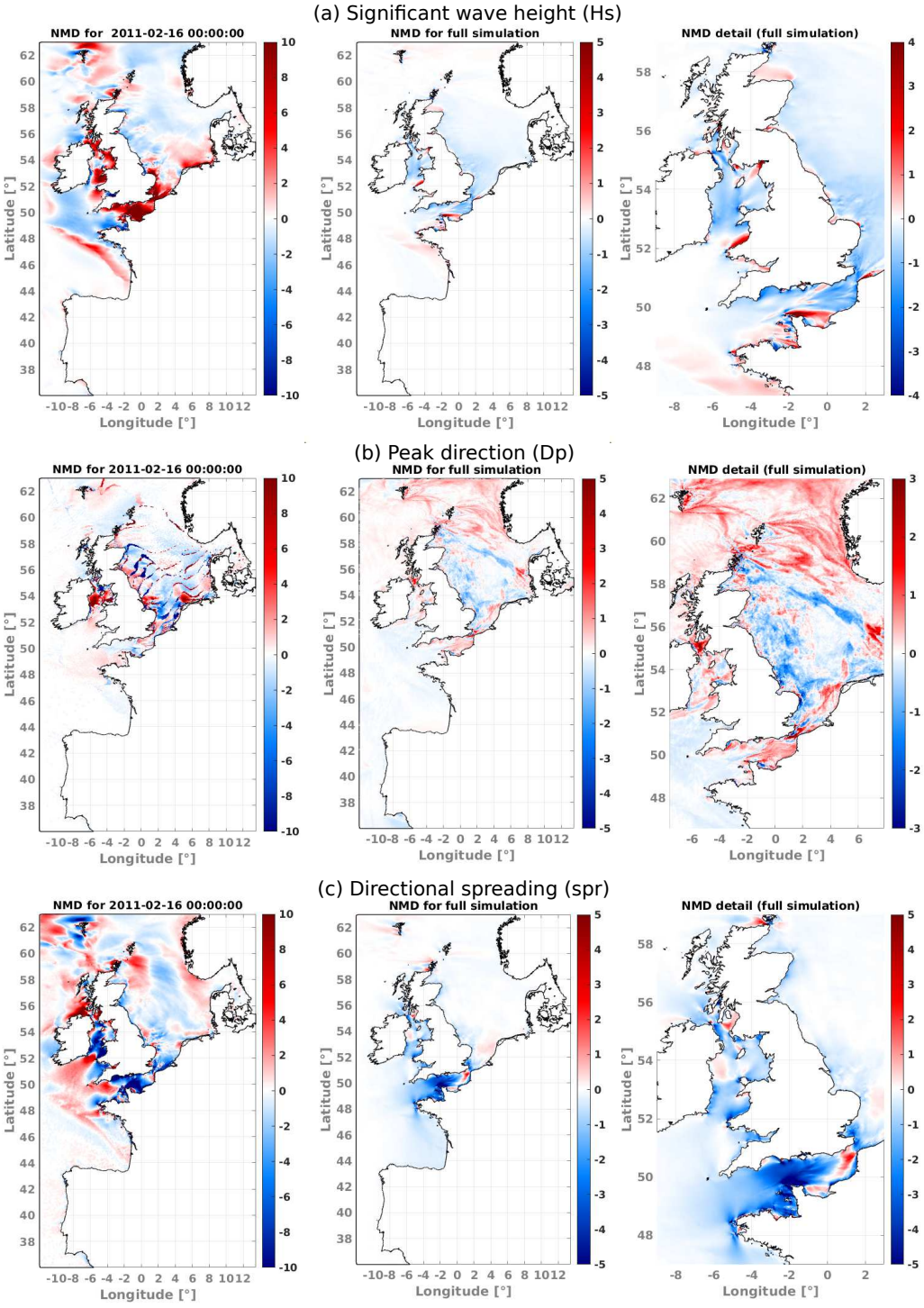

Figure 2.10 – Tidal currents effects over (a) H_s, (b) D_p and (c) directional spreading. NMD results obtained with respect to test using tidal currents. In left panel, NMD with respect to model output at 2011-02-16 00:00:00 UTM presented in left panel of Fig. 2.9. Colorbars represent NMD in [%]. Full simulation duration of tests is 1 month.

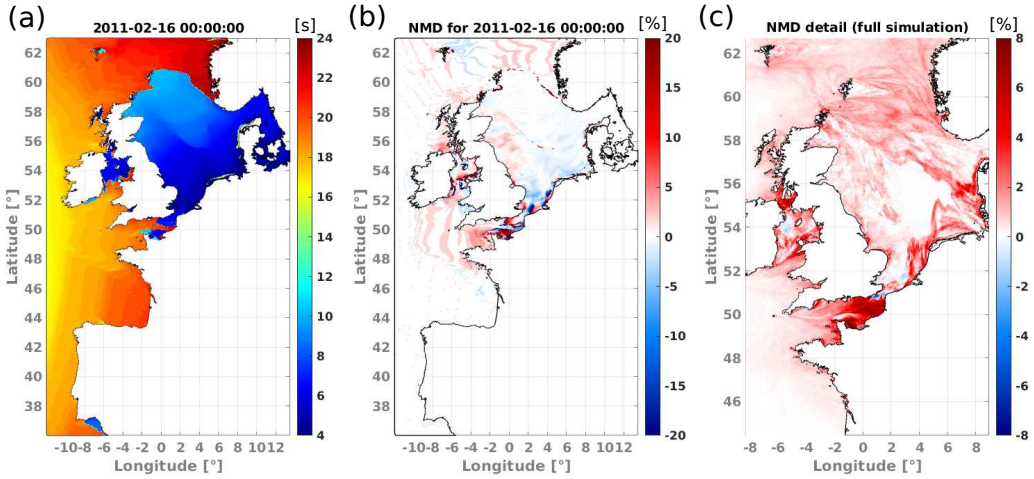

Figure 2.11 – Tidal currents effects over T_p. NMD results obtained with respect to test using tidal currents. (a) T_p field at 2011-02-16 00:00:00 UTM, (b) NMD calculated at 2011-02-16 00:00:00 UTM, (c) NMD detail computed for the full simulation duration. Colorbar in (b) and (C) represent NMD in [%]. Full simulation duration of tests is 1 month.

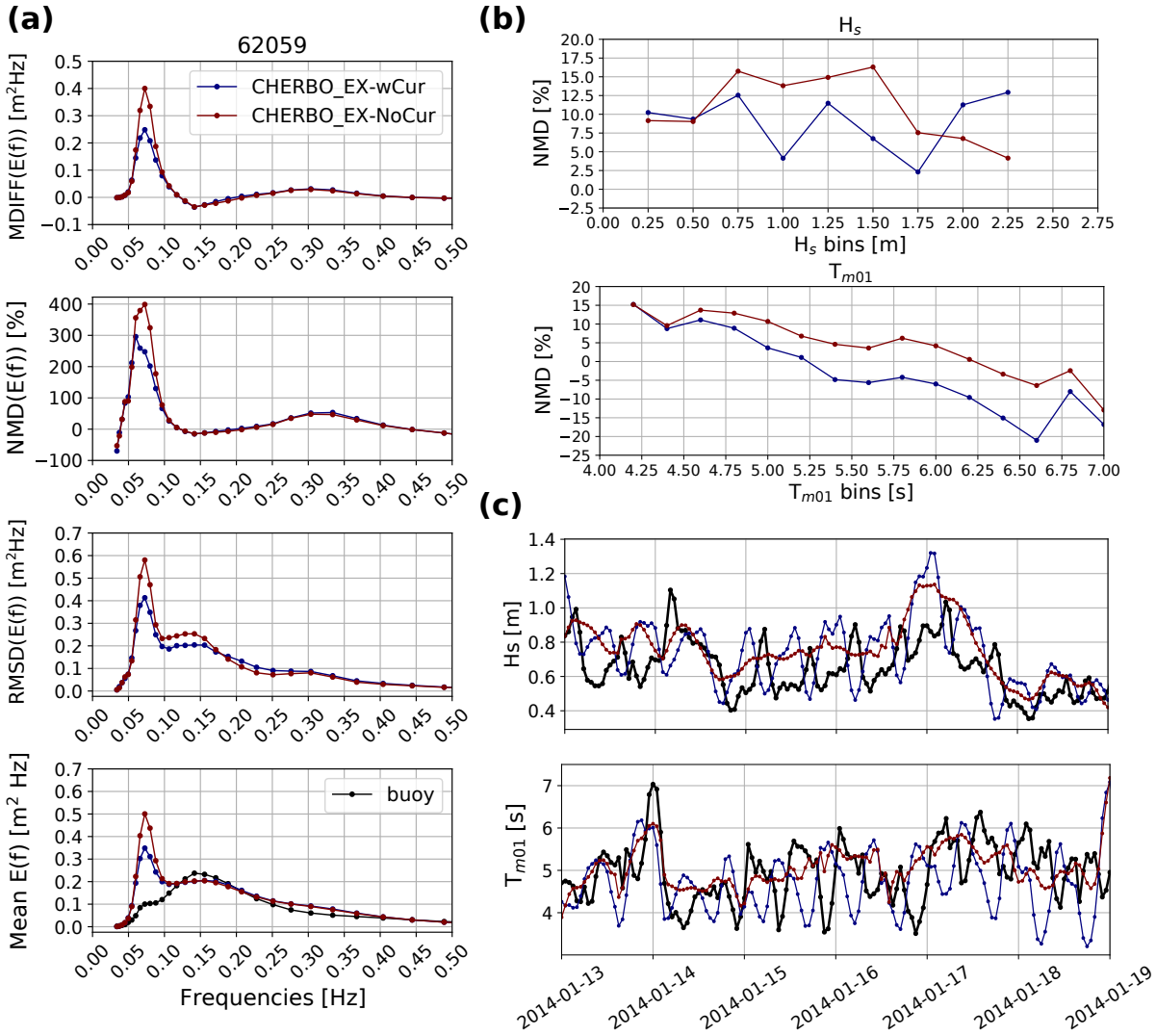

Figure 2.12 – Evaluation of tidal currents effects on wave energy distribution (a) , H_s and T_{m01} at buoy 62059 (Cherbourg Exterieur). Parameteres NMD and time series in (b) and (c) respectively. Results for January 2014. H_s bin size is 0.25 m, T_{m01} bin size is 0.2 s

2.5.4 Effects of spectral directional resolution

The selection of the spectral discretization plays an important role in the characteristics of the simulated sea states obtained through the integration of the WAE (Roland and Ardhuin, 2014; Tolman, 1995a). Normally, in coastal applications like assessments of wave energy or simulation of storm surges, higher time and spatial variability details are desired, and hence, higher spatial and spectral resolution is required (e.g. Accensi et al., 2021; Bertin et al., 2015; Wu et al., 2020). Nevertheless, the quality of the results may be affected by the characteristics of the used BC.

Changes in the energy distribution of the directional spectrum and the wave field evolution due to different directional resolution values in the implemented mesh and in the BC are analyzed. The different BC tests are aimed to identify potential effects when coarser resolution is used at global scale, and then interpolation is applied to match the resolution of the nested mesh (this is done in WW3). Then, to eliminate the potential influence of energy interpolation at the boundary, the effects on wave propagation within the mesh domain keeping consistent resolutions at the BC and the nested model are verified. Tests' specifications are defined in Table 2.4.

Table 2.4 – Tests for spectral directional resolution effects. All parameters not specified here correspond to test T475. When directional resolution of the boundary conditions (BC) is lower than in the mesh, interpolation is applied at the boundary to match the resolution of the nested model.

Test Name	**Number of directions**	**Directional resolution [°]**	**Number of directions in BC**	**Directional resolution in BC [°]**
24D24BC	24	15	24	15
36D24BC	36	10	24	15
36D36BC	36	10	36	10
48D24BC	48	7.5	24	15
48D48BC	48	7.5	48	7.5

Variations in the energy distribution due to lower resolution in the BC are presented in Fig. 2.13, comparing BC with 24 spectral directions with respect to 36. A set of 4 locations were selected: At the boundary (named node W12N56), and along the French coast nodes 62074 (Belle Ile), 62069 (Pierres Noires) and 62059 (Cherbourg). Bathymetry details of these locations presented in Fig. 2.4.

At the boundary, most of the NMD of energy traveling outside the domain is related to very low levels of spectral energy (angles $> 270°$ and $< 360°$, Fig. 2.13.a right panels).

This has negligible effects over of the already analyzed wave parameters (e.g. H_s, D_p, SPR), but it already shows how variations in energy bins are introduced when BC with lower resolution are interpolated to match the directional resolution of the mesh. For waves traveling into the domain , only high NMD ($> +/-10$ %) are observed at lower frequencies (< 0.1 Hz) between directions 20° and 150° (Fig. 2.13.a right panel), which corresponds to the area with higher mean energy at this location for January 2014 (defined by the contours in Mean Energy panel of Fig. 2.13.a). This effect is still present in nearshore areas exposed to the incoming swells from the North Atlantic (nodes 62074 and 62069), although with an overall narrower directional range attributed mostly to the bathymetry induced refraction that tends to "align" the arriving waves (Fig. 2.13.b,c).

No significant changes in energy distribution were found at node 62059, for each output time and for the full simulation NMD (Fig. 2.13.d). This is expected since at Cherbourg the sea state characteristics are mostly driven by the local winds.

To further assess potential changes introduced in wave parameters, differences in fields of H_s, T_p, SPR, D_p, and the mean direction D_m (not shown) are analyzed (Fig. 2.14). Using coarser directional resolution in the BC has minor effects over wave parameters integrated along the complete frequency range (e.g. D_m or H_s; Fig. 2.14.b, top panel). Differences in the results are exacerbated when BC with 24 directions are interpolated into 48 (right panels in Fig. 2.14.a,b) but in general NMD and NRMSD between tests remained below $+/-2.5$ %, with the exception of T_p that presented the largest NRMSD.

Even though the magnitude of these quantities remain fairly consistent, interpolating BC with coarser directional resolution affects the characteristics of the wave fields propagating into the domain. This is attributed to slight changes in the wave celerity ($C=gT/2\pi$ in deep waters) due to frequency shifts in the neighborhood of the energy peak (Fig. 2.13.a,b,c, Energy difference panels).

The analysis of directional resolution of the mesh is mainly focused on the effects of the Garden Sprinkler Effect (GSE) on wave propagation. This phenomenon is observed as a separation or disintegration of continuous swell fields propagated with a discretized spectral wave model (Booij and Holthuijsen, 1987; Tolman, 2002). The generation of the GSE is namely linked to the spectral resolution and the selected numerical scheme to solve the WAE. Currently there are no GSE alleviation methods available for unstructured grids in WW3.

A good example was found during February 1st 2011, where a strong swell from the North Atlantic arrived to the northern coast of Scotland. In Fig. 2.15.a an in-

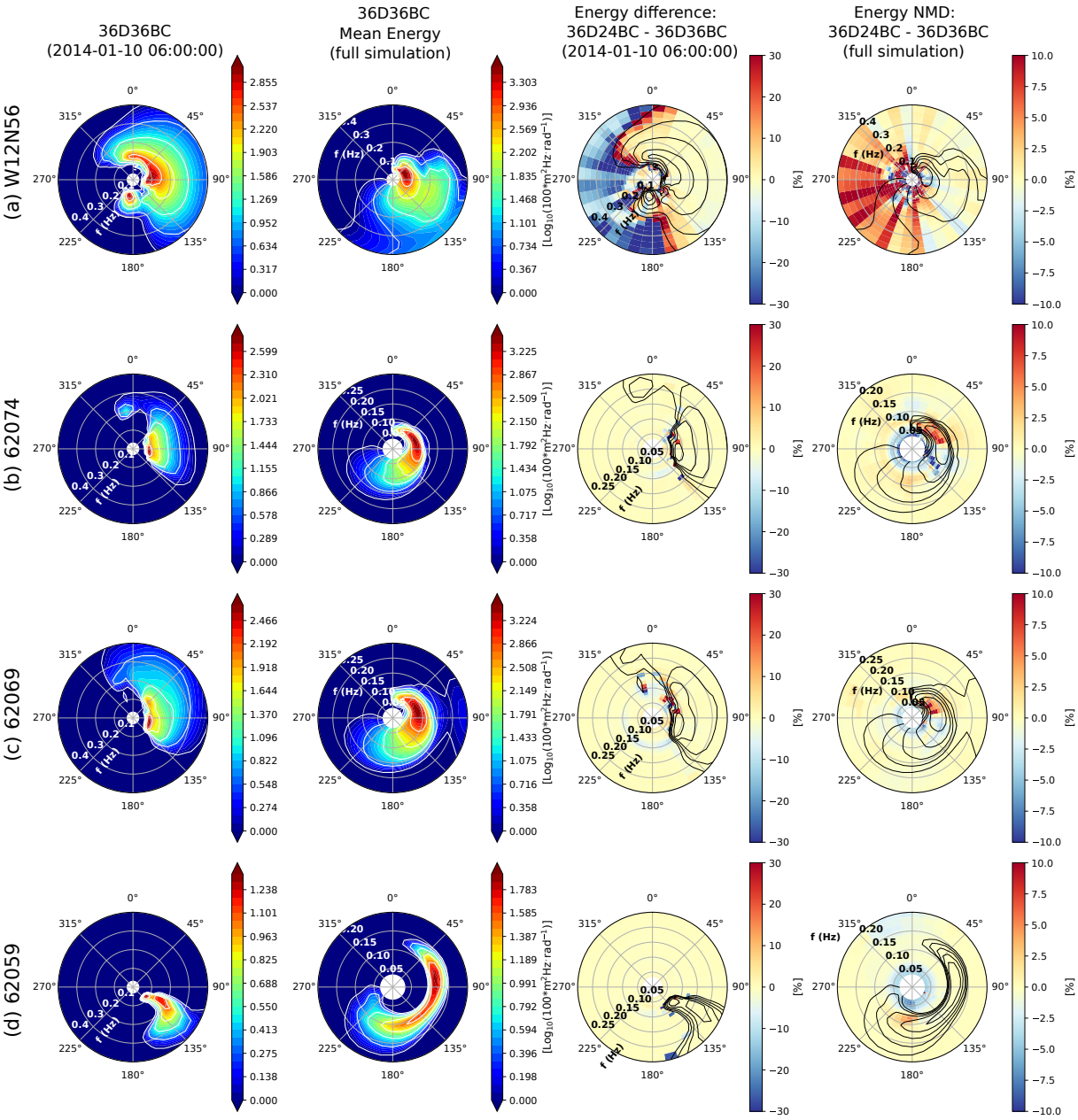

Figure 2.13 – Effects of boundary conditions with lower directional resolution at different output locations. (a) Boundary node W12N56 (Lon.: 12°, Lat.: 56°) (b) 62074 (Belle Ile), (c) 62069 (Pierres Noires), (d) 62059 (Cherbourg). Differences and NMD (36D24BC-36D36BC) computed for January 2014. White contours marking energy levels on left panels are the same plotted in black on the corresponding right panels for energy difference and NMD. Direction convention is towards energy is traveling to.

stant (13:00:00 UTC) of the event is presented using 3 different discretizations from tests 24D24BC, 36D36BC and 48D48BC (Table 2.4). The same number of directions are kept at the BC and the mesh to avoid introducing interpolation effects. The GSE can be observed to the East of the Orkney and Shetland Islands towards the Norwegian Sea (between latitudes 58° and 61°) when 24 directions are employed (Fig. 2.15.a, left panel).

The impact of the GSE was assessed by comparing the results against the output from a model with higher directional resolution. Via a straight forward difference between tests, is possible to visualize changes of the H_s field caused by the spurious wave propagation pattern (Fig. 2.15.b). Comparing tests 24D24BC with 36D36BC, and for this particular scenario, differences in wave height can reach +/-0.2 m (roughly +/-5%) as the swell approaches Norway, between longitudes 2° to 4° (Fig. 2.15.b, left panel). These values are only slightly higher when comparing tests with 24 to 48 directions (Fig. 2.15.b, middle panel). Between 36D36BC and 48D8BC, only minor H_s changes are generated (< 0.05 m; Fig. 2.15.b, right panel).

The mild repercussion of the GSE over the H_s field in the present results shouldn't be generalized, since this phenomenon could be intensified depending on the incoming swell conditions. The obtained results suggest that using a directional resolution of 10° is enough to mitigate the effects of the GSE. It is relevant to point out that, for example, the required computation time in 36D36BC is 40% higher than in 24D24BC, a considerably elevated cost for potential operational (forecasting) applications.

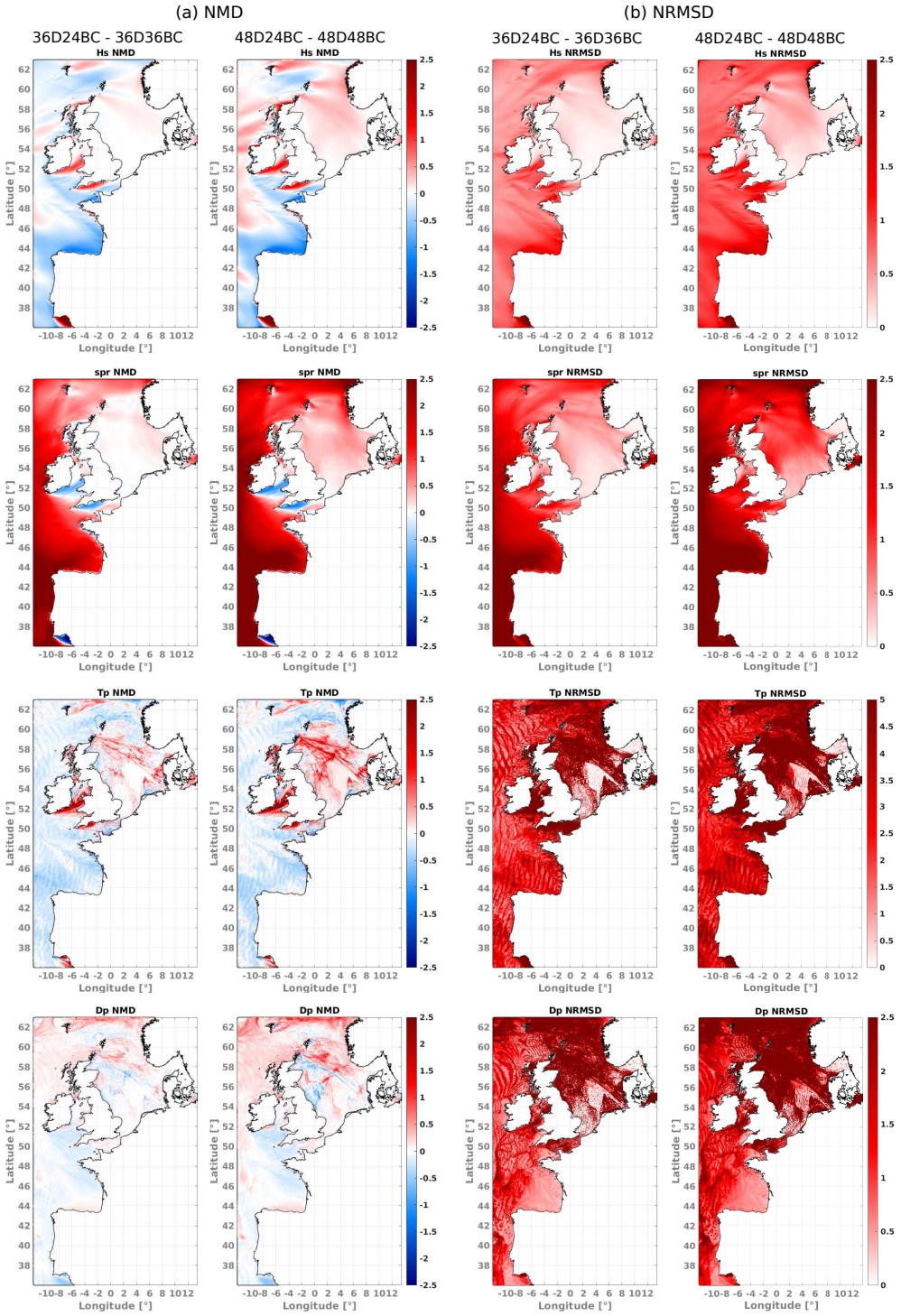

Figure 2.14 – (a) Normalized mean differences (NMD) and (b) normalized root mean squared differences (NRMSD) between tests 36D24BC - 36D36BC and 48D24BC - 48D48BC. Analyzed period : February 2011. Colorbars represent changes in quantities between tests in [%] units.

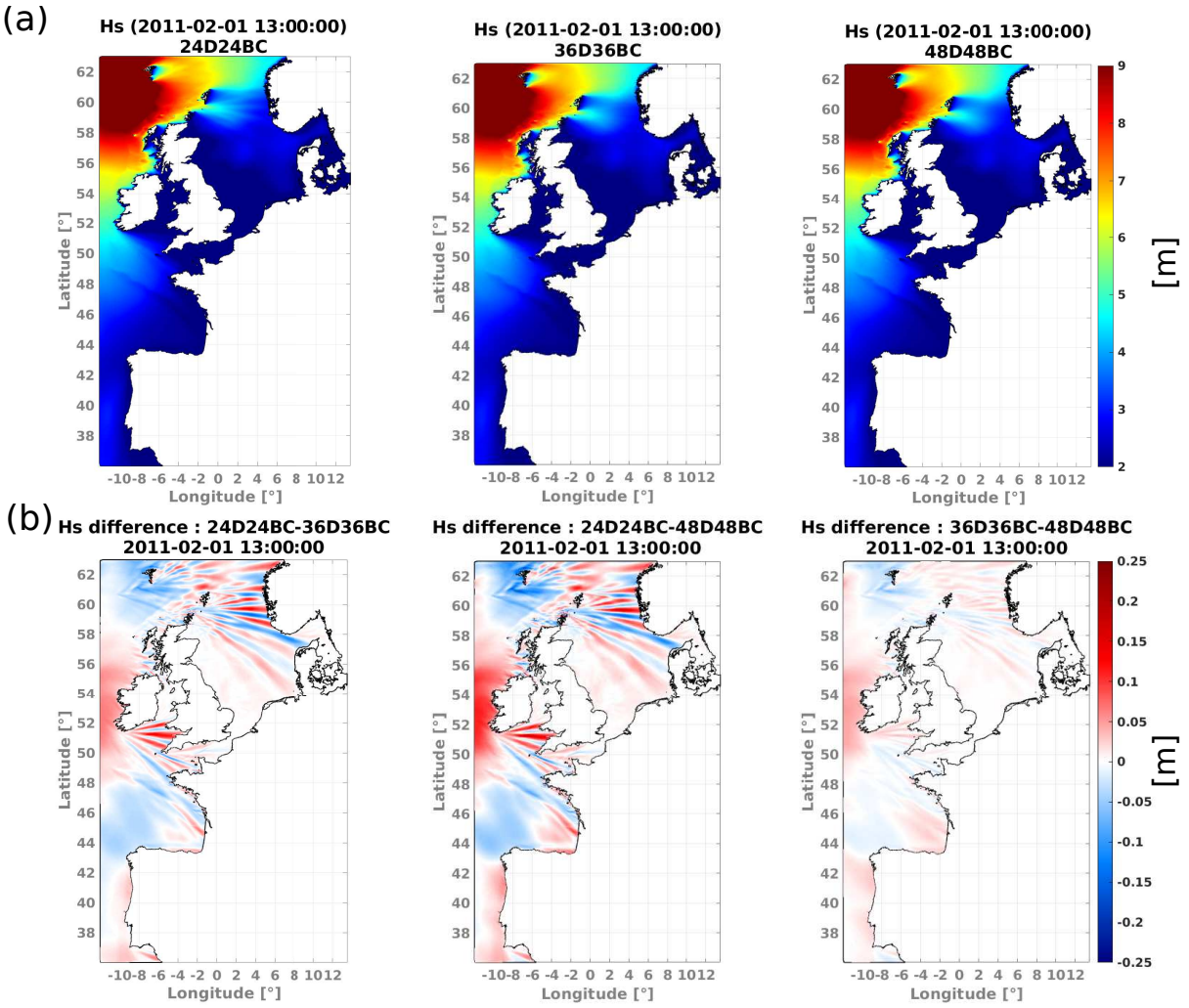

Figure 2.15 – (a) H_s field at 2011-02-01 13:00:00 UTM for different directional resolution tests specified in Table 2.4. (b) Differences in H_s fields presented in (a). Offshore swell conditions at 2011-02-01 13:00:00 UTM (to west of the Orkney and Shetland Islands): T_p = ∼14 s, D_m = ∼260°.

2.5.5 Bottom friction effects

Over the continental shelf, in intermediate to shallow waters, the evolution of the wave fields becomes influenced by the bottom characteristics. In the absence of strong wind seas and outside the surf zone, dissipation of energy is mainly induced by bottom roughness effects. It is thus of interest to quantify the effects of including the bottom friction sink term in the WAE.

To provide a general view, model output from 1-year tests is compared against the 1 Hz altimeter data from the ESA Sea State CCI V2 datset. For this particular analysis 1-year simulations were required in order to have at least a minimum of 5 satellite measurements to compare with the re-gridded WW3 H_s fields at 0.1°. Only altimeter measurements at least 10 km away from the coastline were considered to avoid potential data with high noise to signal ratio.

Bottom friction effects were included through the SHOWEX parameterization proposed in Ardhuin et al. (2003). This expression was initially developed for sandy bottoms based on the eddy viscosity model of Grant and Madsen (1979) and includes a decomposed roughness parameterization for ripple formation and sheet flow. In WW3 it has been implemented including a sub-grid parameterization for water depth variability following Tolman (1995b). The bottom friction source term can be written as follows:

$$S_{\text{bot}} = \quad f_e u_{\text{b,rms}} \frac{\sigma^2}{2g \times \sinh^2(kd)} N(k,\theta) \tag{2.4}$$

with,

$$f_{\text{e}} = \quad \frac{\kappa^2}{2\left(\text{Ker}^2(2\sqrt{z_o/l}) + \text{Kei}^2(2\sqrt{z_o/l})\right)} \tag{2.5}$$

and

$$z_o/l = \quad \sqrt{\frac{2}{f_e}} \frac{k_N}{30\kappa a_{\text{b,rms}}} \tag{2.6}$$

In the following paragraphs, a brief description of the main components of this expression is provided, for further details refer to Ardhuin et al., 2003 and The WAVEWATCH III ® Development Group, 2019.

In eq. 2.4, f_e if the dissipation factor function of the root mean squared (r.m.s.) bottom orbital amplitude ($a_{\text{b,rms}}$), $u_{\text{b,rms}}$ is the bottom r.m.s. orbital velocity, σ the wave frequency, k the wave number, d the local depth and $N(k,\theta)$ the wave action as function of the wave number and the wave direction θ. In eq. 2.5 κ, is the Von Kàrmàn constant,

Ker and Kei are Kelvin functions of zeroth order and z_o/l is a non-dimensional roughness length that is function of $a_{\mathrm{b,rms}}$ and the Nikuradse roughness length k_N.

When the relation between the r.m.s. Shields number and its critical value is $\psi/\psi_c < A_3$, then the Nikuradse roughness k_N is given by a relic roughness length that may weakly increase with $a_{\mathrm{b,rms}}$:

$$k_N = k_{rr} = \quad \max\left(A_5, A_6 D_{50}, A_4 a_{\mathrm{b,rms}}\right) \tag{2.7}$$

when $\psi/\psi_c >= A_3$, then k_N is taken as the sum of the ripple roughness k_r and a sheet flow roughness k_s:

$$k_r = \quad a_{\mathrm{b,rms}} \times A_1 \left(\psi/\psi_c\right)^{A_2} \tag{2.8}$$

$$k_s = \quad 0.57 \frac{u_{\mathrm{b,rms}}^{2.8} a_{\mathrm{b,rms}}^{-0.4}}{[g(s-1)]^{1.4}(2\pi)^2} \tag{2.9}$$

where,

$$\psi = \quad f_w u_{\mathrm{b,rms}}^2 / [g(s-1)D_{50}] \tag{2.10}$$

$$\psi_c = \quad \frac{0.3}{1+1.2D_*} + 0.55[1-\exp(-0.02D_*)] \tag{2.11}$$

with,

$$D_* = \quad D_{50}\left[\frac{g(s-1)}{\nu^2}\right]^{1/3} \tag{2.12}$$

A_1 to A_6 are empirical parameters originally taken from Ardhuin et al., 2003 where particularly A_5 was modified to 0.04. The detailed values are provided in Table 2.5. D_{50} is the median sediment size in meters defined at each node of the unstructured grid (see Fig. 2.2). Finally, in eq. 2.8, s is the sediment specific density (taken as 1.25) and ν is the kinematic viscosity of water.

To assess the effects of the bottom friction parameterization, first 1-year simulations with and without dissipation are compared to verify changes in the wave field. In Fig. 2.16.a the H_s mean bias obtained by comparing with Saral (year 2014) is presented for the full domain. A clear reduction of the wave heights bias is detected in the south of the North Sea. In this area, it is found that H_s mean differences between results with and without bottom friction can be of 0.3 m and higher. Analysis with other altimeters (e.g. Jason-2 and Envisat) for year 2011 show consistent results. The extension of this

Table 2.5 – List of empirical parameters used in SHOWEX bottom friction parameterization. The WW3 variables' names correspond to the keyword used in the model's BT4 namelist.

Parameter	**WW3 variable**	**value**
A_1	RIPFAC1	0.4
A_3	RIPFAC3	1.2
A_4	RIPFAC4	0.05
A_5	BOTROUGHMIN	0.04
A_6	BOTROUGHFAC	1.00

area, highly influenced by bottom friction dissipation, represents and interesting element to take into account for wave modelling in the nearshore. Given the cumulative effect of dissipation in the direction of wave propagation, an adequate parameterization used and/or the proper characterization of the sediment type will be relevant to reduce wave height biases and errors. Furthermore, it becomes evident that in a nesting scheme (e.g. Gautier and Caires, 2015) the limits of each sub-domain and the source of the boundary conditions should be carefully considered.

In general, with altimeter data most relevant changes in wave heights, when bottom friction is included, are detected for depths smaller than 50 m. Special attention is paid to a couple of Envisat tracks passing almost parallel off the coast of La Rochelle and close to Ile de Yeu (Fig. 2.16.b). In both locations the use of the bottom friction parameterization, with the defined D_{50}, helps to reduce the H_s mean bias. These results are consistent with the findings of Roland and Ardhuin, 2014 for this area based on buoy data.

To further quantify the effects of bottom friction, a set of 3 locations were picked to compare the model results with in-situ measurements, buoy 62078 on the Altantic French coast, and buoys Westhinder and Scheur Wielingen deployed in shallower depths along the coast of Belgium (Fig. 2.4).

For buoy 62068, first the full H_s time series of in-situ data is compared against simulations with and without bottom friction effects. Reductions in the wave height's NMD and NRMSD of respectively 4.5 % and 5.0% are obtained when bottom friction and the sediment size map are included (Fig. 2.17.a,c). Nevertheless, most significant changes in the modeled H_s appear at wave heights roughly larger than 3 m. Then, an ad hock H_s threshold of 3.5 m was selected to define "extreme" sea states and analyze the effects of the parameterization over the events on which dissipation due to wave-bottom interactions is dominant. For these events, a wave height bias and RMSD reduction of

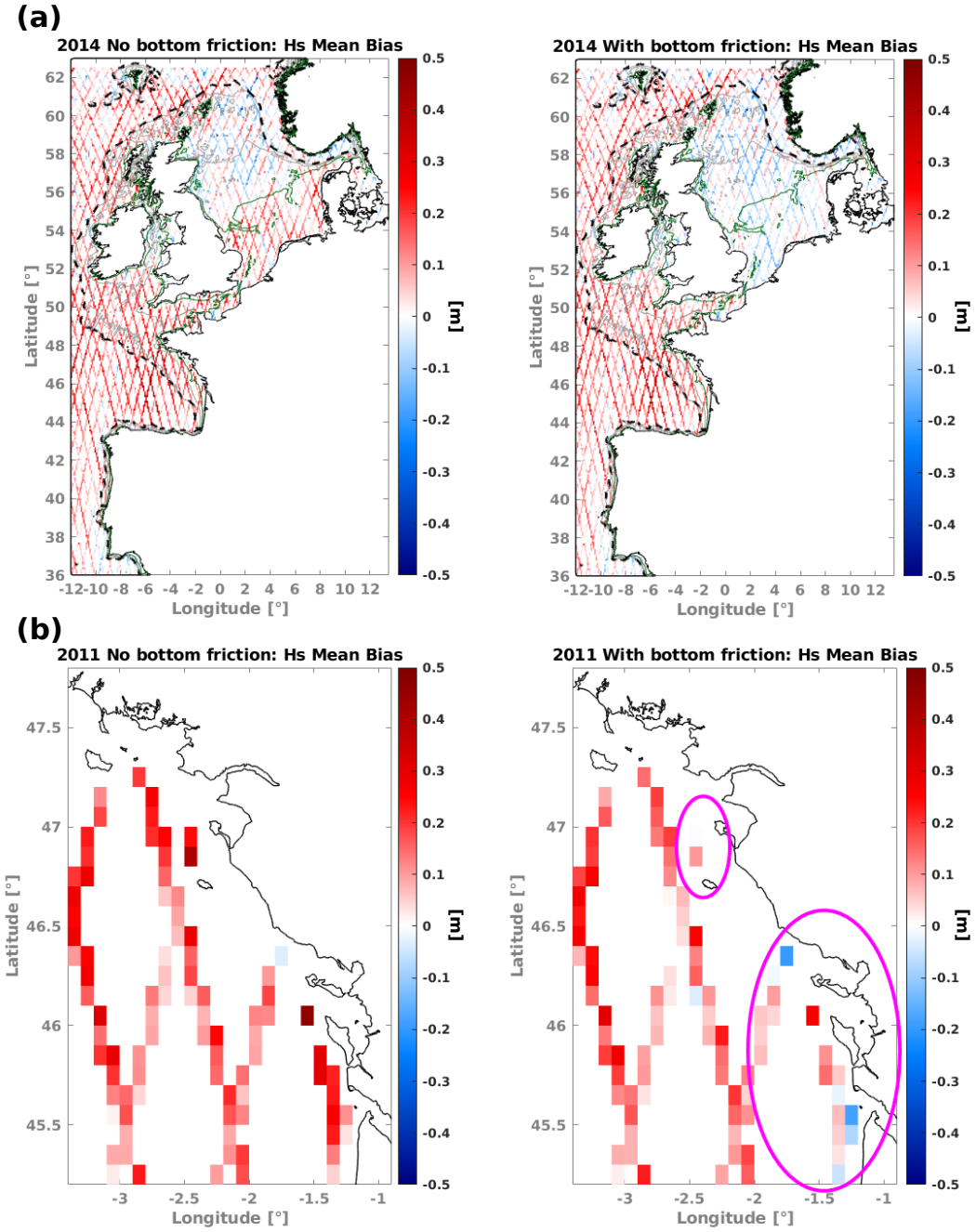

Figure 2.16 – H_s bias (WW3-altimeter) computed with (a) Saral year 2014 and (b) Envisat year 2011. Dashed black lines show 200 m depth contour, green lines the 50 m depth contours, and gray lines depth contours from 100 to 150 m depth. Magenta ovals in (b) highlight areas with mayor bias reduction.

about 0.3 m, with a decrease of about 8% and 5.3% in the NMD and SI is obtained when the SHOWEX dissipation term is used (Fig. 2.17.b). Moreover, good agreement is found between the occurrences of the Shields number ψ exceeding its critical value ψ_c (Fig. 2.17.d) and the occurrences of extreme sea states with $H_s > 3.5$ m (Fig. 2.17.c) especially between January and March 2014. In the model, the evolution time scale due to bottom friction is inversely proportional to $f_e u_{\mathrm{b,rms}}$, which gives a measure of the strength of bottom friction, sharply increasing every time the critical Shields number is exceeded. In this case, the definition of extreme events helps to identify when the effects of bottom friction becomes relevant, since larger H_s are normally related to longer wave lengths, thus wave-bottom interactions start at deeper depths.

At Westhinder and Scheur Wielingen dissipation effects are analyzed over components of the spectrum with periods longer than 10 s comparing H_{10} values. For these locations, measurements are also compared with simulations using the JONSWAP bottom friction parameterization (Hasselmann et al., 1973; Tolman, 1991) with its default values (Fig.2.18). Wave energy for components longer than 10 s is clearly over estimated when no bottom friction is taken into account. The effect is visible at both analyzed depths. At Westhinder both parameterizations have similar effects, but at the shallower buoy location (Scheur Wielingen) the use of SHOWEX and the selected D_{50} introduce a negative bias of $H_{10} > 0.5$ m which could be related to an overestimation of the sediment mean size in this area.

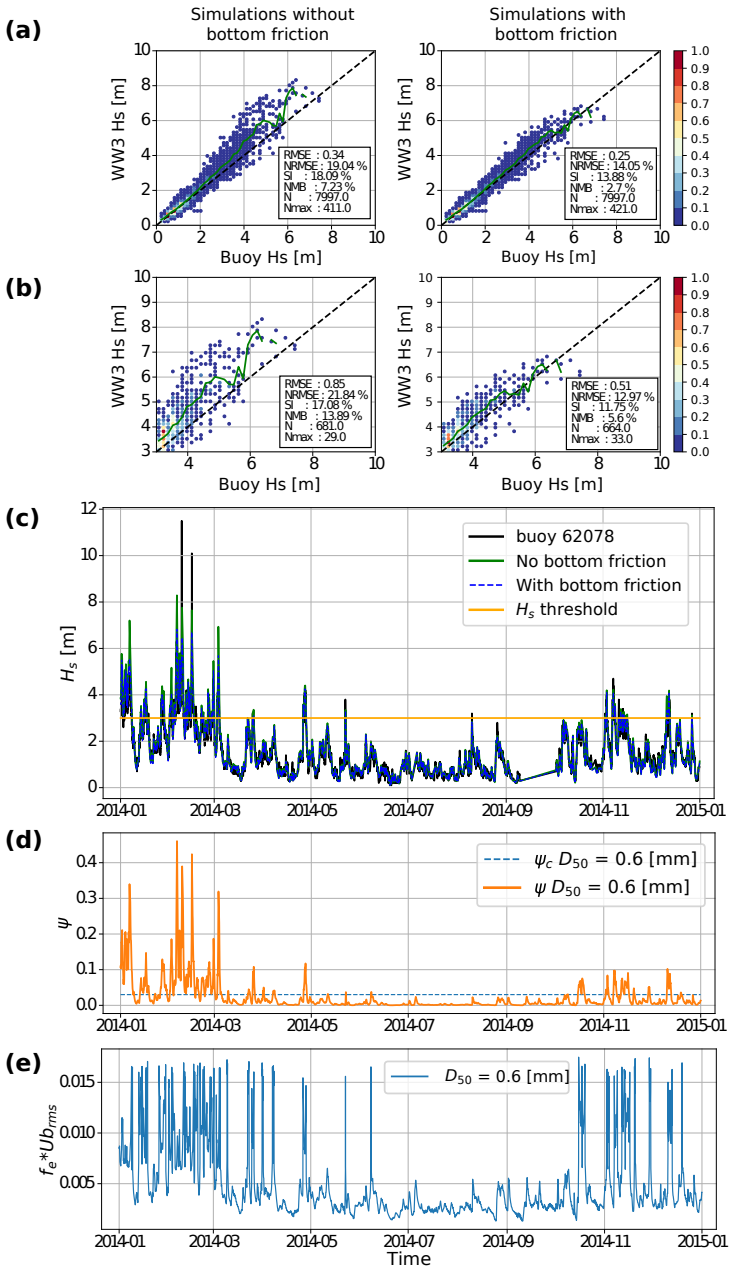

Figure 2.17 – Bottom friction effects at buoy 62078 (year 2014). Performance analysis using (a) complete time series and (b) extreme events ($H_s > 3.5$ m). (c) H_s time series for cases with and without SHOWEX parameterization. Time series of (d) Shields number ψ and (e) dissipation term $f_e u_{\mathrm{b,rms}}$. In (a) and (b) green line shows the modelled averaged values at each 0.15 m wave height bin. Colorbars represent the wave heights frequency of occurrence normalized by the total amount of analyzed data N. Time series in (d) and (e) computed with WW3's frequency spectrum following eq. 2.4 to 2.12. D_{50} taken from bottom sediment map (Fig. 2.2). Blue dashed line in (d) represents the critical Shields number.

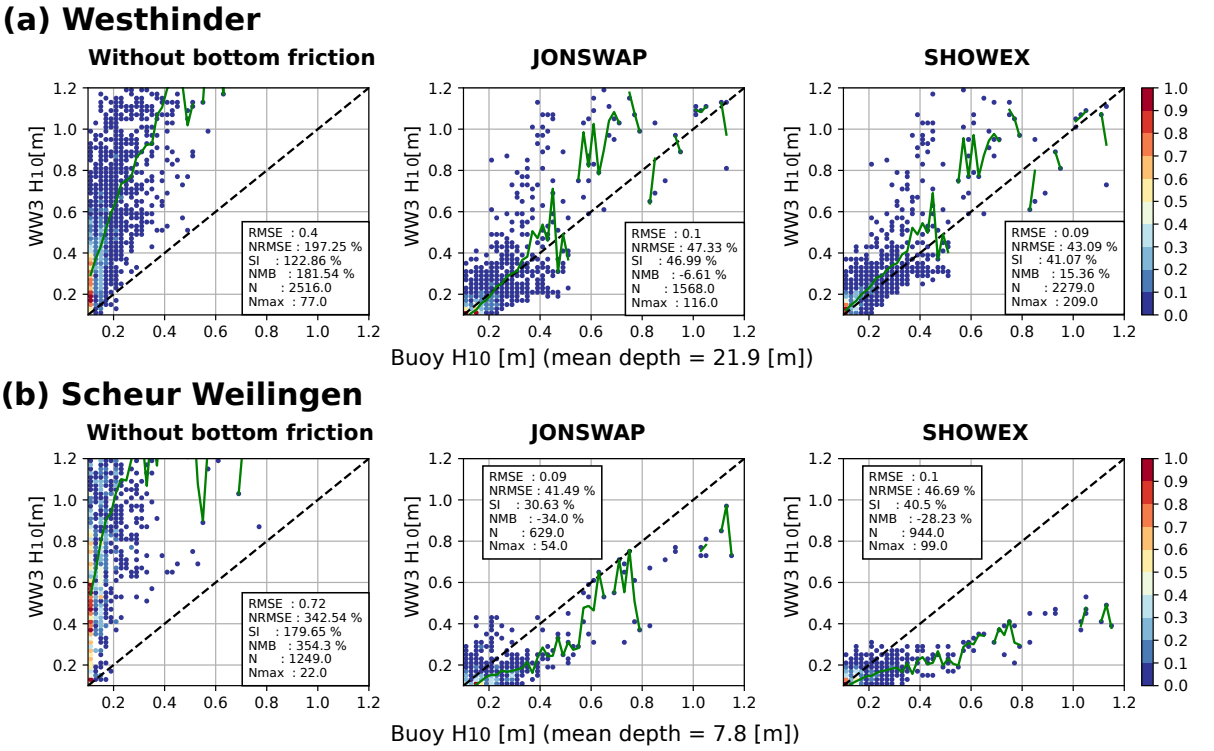

Figure 2.18 – WW3-Buoy H_{10} comparison for tests without bottom friction, using default JONSWAP and with SHOWEX parameterization including the implemented bottom sediment map. Results for (a) Westhinder and (b) Scheur Wielingen buoy location for year 2014. Green line shows the modelled averaged values at each 0.02 m wave height bin. Colorbars represent the wave heights occurrences normalized by the total amount of analyzed data N.

2.6 Model validation with altimetry data

Satellite altimetry provides a unique resource of worldwide wave heights' measurements. The integration and inter-calibration of past and ongoing missions have allowed to continuously extend the coverage of measured data in space and time. As done in Chapter 1, these datasets have been commonly used in open ocean applications to improve our understanding of the sea states globally. On the other hand, their application in coastal (especially nearshore) areas has been very limited due to the "noise" levels in the return signal. What is considered as noise is actually the detection of the non-Gaussian land surface, which makes it difficult to retrieve the waves' geophysical signal in the radar footprint.

The Sea State CCI V2 dataset employs the WHALES waveform retracking algorithm, more effective for reducing the intrinsic noise of the return signal, and suitable for coastal applications (Passaro et al., 2021; Schlembach et al., 2020). The vast amount of measurements available at distances from the coast lines down to 5 km and less implies also a large coverage of measured wave heights in shallower depth areas, providing a broader description than local in-situ records. Making use of the coverage and improvements in this altimeter product, the performance of the regional mesh is analyzed over part of the wave hindcast decribed in Accensi et al. (2021). This hindcast was generated using the T475 parameterization adjustments (Table 2.3) with BC from the global wave dataset described in Chapter 1 (Alday et al., 2021).

The analysis is focused on 3 zones of the modeled area: Bay of Biscay, North Sea and English Channel. The purpose of the defined zones is to assess the performance of the model in different wave generation and propagation conditions. The Bay of Biscay is constantly exposed to swells radiated from the North Atlantic. At the North Sea, wave conditions are dominated by the local winds blowing over a well defined fetch and partially influenced by the swells from the Norwegian Sea. Finally, at the English Channel, most of swells' energy arriving from the North Atlantic is blocked, refracted and dissipated on its western end, local waves are generated over a very short fetch, and it is highly influenced by its tidal regime.

Using an along-track comparison of the modeled H_s with respect to the altimetry derived SWH, the NMD and SI were computed per altimeter mission as function of the distance to the coast, using bins of 1 km and considering SWH $>$ 1 m. To provide an idea of the lower and upper bound values of NMD and SI from distances of 1 km offshore up

to 80 km, the performance parameters were computed over the complete available years of data per mission until 2018: from 2002 to 2012 for Jason-1 and Envisat, 2008 to 2017 for Jason-2, 2013 to 2018 for Saral, and from 2016 to 2018 for Jason-3 (Fig. 2.19).

From distances to the coast of 15 km and more a constant positive NMD is dectected, ranging from 2 to 6% in the Bay of Biscay, and in some cases going up to ∼8% in the English Channel. At the North Sea bias changes are more constrained between +/- 2% (Fig. 2.19.a). The positive NMD in the Bay of Biscay is thought to be related to the BC obtained from the global hindcast using T475, which was calibrated with the altimeter dataset from CCI V1. It was found that there is a small over estimation of SWH in the CCI V1 inter-calibrated missions with respect to offshore buoy measurements (Dodet et al., 2020), which has been corrected in V2. The English Channel stands out as high NMD and SI area which is thought to be caused by the reduced amount of valid altimeter measurements in this area and inaccuracies of the forcing fields. For example, induced wind variability due to inaccuracies of the modelled atmospheric boundary layer development as it transitions from water to land (or the opposite). Finally, less influenced by the BC and with an extended fetch for wave growth, the North Sea presents the lowest NMD values, which along with the more constrained SI (Fig. 2.19.b) shows the good performance of the proposed parameterization and model setup in this area.

An overall NMD decrease is observed for distances to the coast smaller than 15 km reaching negative values, which implies that in general the altimeters' SWH are higher than the modeled H_s. Differences that are particularly more accentuated at the Bay of Biscay at offshore distances < 10 km. Even with the higher uncertainty of modeled/measured wave heights closer to shore, the available altimetry data down to ∼6 km offshore still provides unprecedented access to coastal information that, even at this early stage, allows to evaluate the model performance.

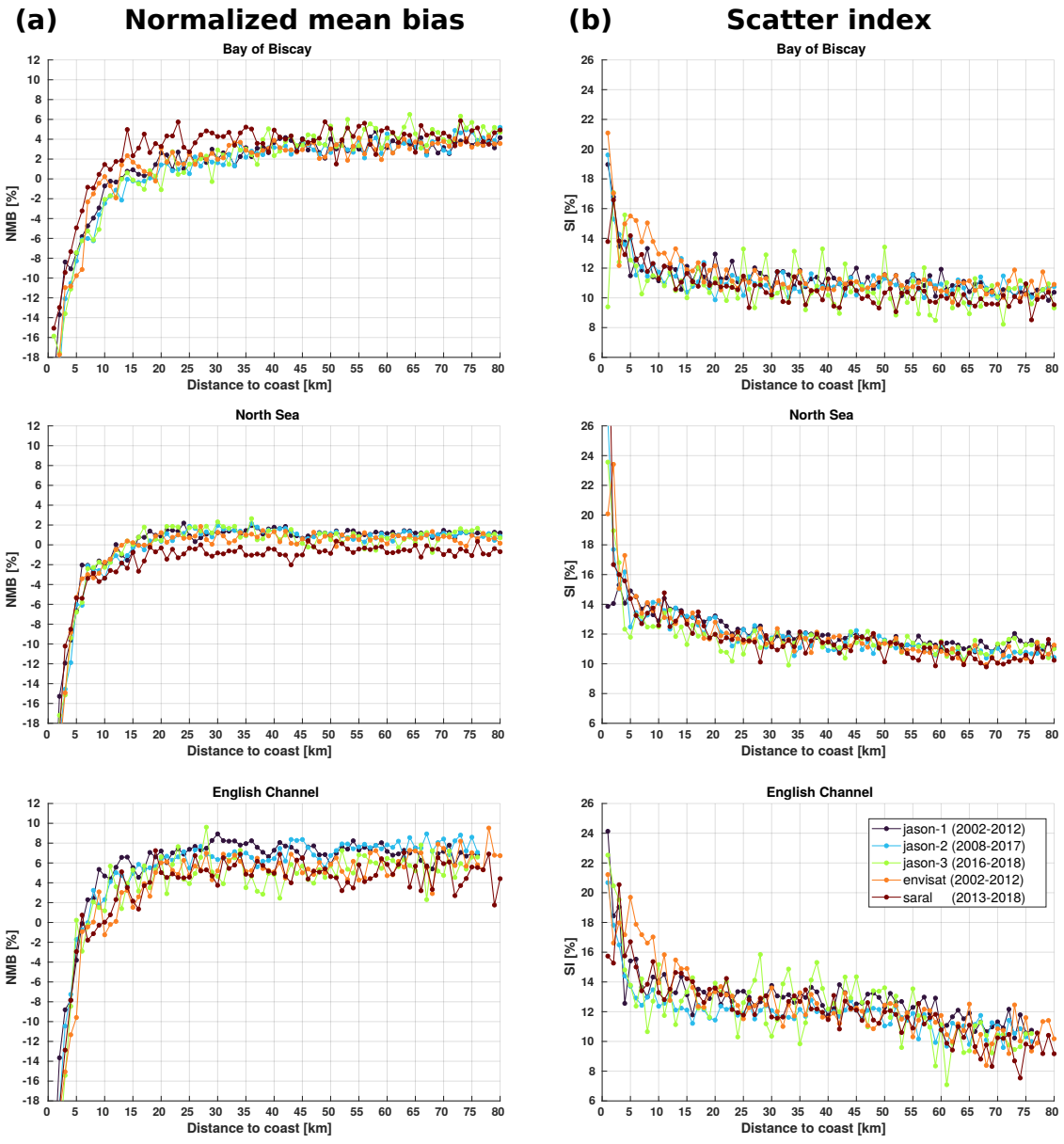

Figure 2.19 – (a) NMD and (b) SI of H_s as function of distance to the coast (WW3-altimeter SWH). Bins' width is 1 km

2.7 Conclusions

The drivers of model errors in coastal areas, and how choices of parameterization, forcing, spectral and spatial resolution, and boundary conditions affect the characteristics of the simulated sea states were investigated in the present section. Extensive sensitivity analyses were carried out with a wave model for European coastal waters using the WAVEWATCH III framework. The performed tests and analyses were aimed to asses when and where the choices in the model setup have a significant effect in regions were waves' interactions with complex bathymetry, tidal currents and bottom roughness become important in wave propagation.

Overall, spatial resolution is one of the most important elements in shallow depth areas. It was found that higher spatial resolution adequate to solve bathymetry features and explicitly solving coastlines can introduce changes in H_s estimations of about 20% when compared to lower resolution models. Differences become more significant below 400 m depth, in areas where refraction and diffraction are dominant, or in regions sheltered from the most frequent swell conditions.

Changes in the energy distribution of the spectrum were analyzed mainly from two points of view, introduced by modifications in the parameterization, and due to changes in directional resolution. Modification of the swell dissipation terms, did not impact significantly the wave energy distribution in the regional domain. Although, their effect become important at global scales (Alday et al., 2021). In general, the applied enhancement to the ERA5 wind fields improves the model accuracy at swell exposed locations, helping to reproduce realistic energy levels for frequencies lower than 0.05 Hz, partially solving their otherwise high under estimation (more than -50% in some cases). These findings suggest that the considerations taken to generate the boundary conditions at global scale, are one of the most important factors on shorelines exposed to waves from the North Atlantic.

For waves traveling into the domain, differences due to directional resolution choices are larger than 10% at frequencies lower than 0.1 Hz. Effect that is visible from the boundary to the nearshore in zones influenced by the BC. Differences in wave parameters (SPR, T_p, D_p) observed between model tests, suggest that the proper selection of directions to define the BC and within the nested model will help to reduce random errors. It was also found that with 10° resolution, the GSE is successfully alleviated in the mesh.

Including tidal forcing (currents and levels) typically change wave parameters by about 10% at each output time, and locally much more (e.g. Ardhuin et al., 2012) in areas with

large tidal amplitudes. These differences are reduced for H_s and D_p for a monthly average, but can still be larger than 5% for the SPR and T_p. These findings imply that even if the average wave heights might be well estimated without tidal forcing, the propagation and evolution of the wave fields will be different. This can be observed in the H_s and T_{m01} time series at buoy 62059 (Fig. 2.12).

Areas influenced by bottom friction dissipation were identified by looking at changes in H_s, comparing with wave heights retrieved from altimeter data with 1-year simulations. It was found that these changes can be observed at depths smaller than 50 m. In shallower areas of the North Sea and some sections of the Atlantic coast of France, including the SHOWEX bottom friction parameterization, helps to reduce the H_s bias. Comparisons between model and in situ measurements of H_{10} revealed an underestimation of the wave energy in the low frequency bands in very shallow areas. This effect could be related to a higher sensitivity of the SHOWEX parameterization in very shallow depths, thus, dissipation induced in longer wave components is over estimated with the proposed model setup.

A validation of the modelled wave height as function of the distance to the coast, was performed using 5 available missions from the Sea State CCI V2 dataset, between years 2002 to 2018. An overall increase of H_s differences with the model is observed for distances to the coast smaller than 10 km that can reach -8% (in average) at 5 km from the coast. These differences are likely due to increased uncertainties in altimeter measurements within the last 10 km from the coast, where coastal features are known to strongly impact radar waveforms (Vignudelli et al., 2019).

It was observed that in many cases averaged differences between model setups or with respect to in-situ data are small, but these differences can be significant at each outputted time, implying that the time evolution of the sea states is in fact different. This could partially explain cases with low bias and still larger random errors (e.g. SI) in some locations, when modelled wave parameters are compared with measurements.

Due to the different characteristics of the modelled domain (e.g. bathymetry features, bottom sediment type, fetch and tidal amplitudes) the elements driving the accuracy of the model cannot be completely generalized. Instead, through the proposed analyses it has been identified where changes in the wave field characteristics are more significant with different choices in forcing, resolution and parameterizations. Yet, it is not straightforward to assess how the combination of these choices can potentially compensate errors in the simulations. Boundary condition effects are most easily evaluated at deep water

or partially sheltered locations (see also Crosby et al., 2017), while separating bottom friction from other effects will require a further analysis of specific swell events.

Chapter 3

Alternative parameterizations and their effect on spectral energy directionality

3.1 Introduction

In Chapter 1 we looked at possible improvements to wave model results updating the forcing fields and discretization of the wave spectrum, and changing the parameterizations of wind-wave growth and swell dissipation. The impact of these model settings was assessed mainly with altimeter data, leading to the adjusted set of parameterizations defined as T475. Then, in Chapter 2 the analysis was extended to coastal areas with more emphasis on the variations of energy levels of the frequency spectrum introduced by T475, including tidal forcing and sediment friction dissipation effects. In this case, the assessment of the changes introduced to the simulated sea states also included several wave parameters besides H_s, mainly the peak period, mean direction and directional spreading.

The directional spread of waves is commonly one of the less accurate characteristics reproduced by the model (Stopa et al., 2016a). In particular the spread at high frequency is often strongly underestimated, because at frequencies above 2 to 3 times the windsea peak frequency, the model energy balance is not correct. For that frequency range, the computed spectrum obtained by the source term integration is replaced by a diagnostic tail shape with the spectral energy level decreasing like f^{-5}. Since it is generally expected that the wind wave growth across the entire spectrum is a function of the roughness determined by the spectral tail, there may be a benefit for the complete spectral energy distribution when parameterizations that better represent the tail of the spectrum are used. Also, remote sensing applications require directional spectra that may give the near-isotropic distribution of surface slopes, especially at low wind speeds (Munk, 2009). Until recently, no parameterization was able to give enough energy in the cross-wind

direction and the observed minimum wave energy in the wind direction for wavelengths around 1 m (Leckler et al., 2015). These deficiencies are also associated to a lack of significant correlation between wave-generated acoustic noise and measured noise level at frequencies around 1 Hz (Peureux and Ardhuin, 2016; Peureux et al., 2018).

New parameterizations have been proposed to better represent the high frequency part of the spectrum, and they may also benefit the estimation of H_s and other parameters. In the present chapter, 3 different parameterizations for wave dissipation that were designed to reduce spectral shape errors are evaluated and adjusted. The first parameterization looked at was proposed by Romero (2019) and was designed to reproduce the shape of the high frequency part of the spectrum that may solve many of the shortcomings of the directional wave spectrum (Romero and Lubana, 2022). This parameterization particularly features a wind-dependent amplification of the number of breaking waves for the short wave part of the spectrum, and a "cumulative dissipation" that is loosely based on the theoretical analysis by Peureux et al. (2021) of short wave modulation by long waves. The second parameterization is the standard of Ardhuin et al. (2010), and the third one is a variation of Ardhuin et al. (2010) with a simplified expression for the cumulative dissipation term. The latter 2 are mainly used to compare directional characteristics of the spectrum with Romero (2019).

Additionally, it is well know that the usual "Discrete Interaction Approximation" (DIA), a parameterization of the 4-wave non-linear interactions that was proposed by Hasselmann and Hasselmann (1985), is a very crude representation of the full interaction and leads to large differences in wave spectra shape (Banner and Young, 1994). Instead, an accurate estimation of the full interaction can be obtained using the Webb-Resio-Tracy method (hereinafter WRT) (Resio and Perrie, 1991; Tracy and Resio, 1982; Webb, 1978) or the Gaussian Quadrature Method (GQM) of Lavrenov (2001), as implemented by Michel Benoit and otpimized by Gagnaire-Renou et al. (2010). Particularly the WRT method requires 10^3 to 10^4 times more computational effort than the DIA. Which is mainly why these calculations are typically made for highly-idealized test cases. Thus, the impact of different dissipation parameterizations will be assessed using either the DIA, WRT or GQM method.

The used forcing fields, frequencies discretization and wind-wave growth parameterization are the same as in the global model described in Chapter 1. Main differences in the model setup are detailed in section 3.2. These differences are related to the formulation of the source terms on the right hand side of the wave action equation (eq. I.26). The

spectral shape of the sum of the source terms $S_{\rm tot} = S_{in} + S_{nl} + S_{ds}$ is the rate of evolution of the spectrum, as illustrated in Fig. 3.1.

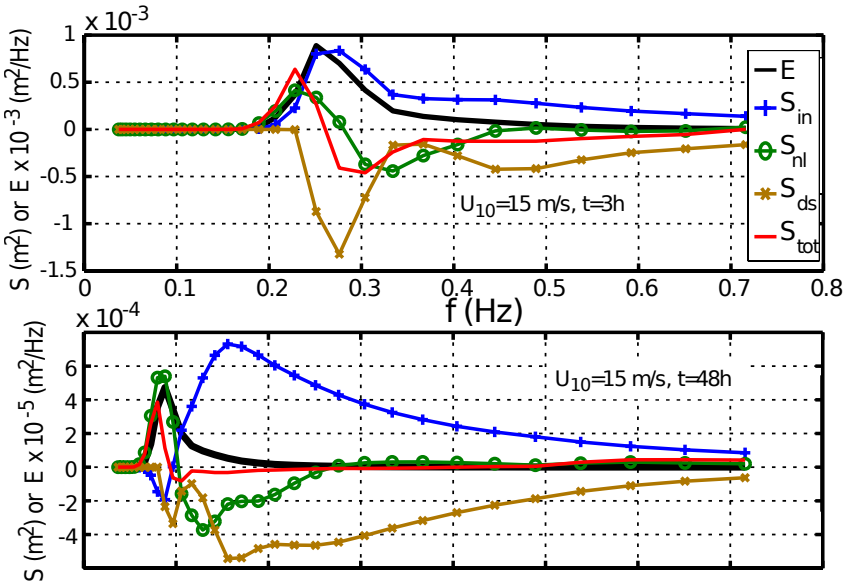

Figure 3.1 – Typical shape of source terms and specturm evolution, both integrated over directions. This simulation is the result of the integration of $dE/dt = S$, which corresponds to spatially uniform sea state, only involving in time, here with a constant wind speed of 15 m/s starting from zero energy at $t = 0$. The similar magnitude of $S_{\rm tot}$ and $E \times 10^{-3}$ in the top panel means that the spectrum evolves on a time scale of 1000 s after 3 hours. This time scale grows to a day after 48 hours, which corresponds to a "fully developed" sea state which does not grow much. Reproduced from Ardhuin (2019).

Note that in the bottom panel (of Fig. 3.1), the total source term (in red), is nearly zero for frequencies 0.2 to 0.5 Hz, meaning that the spectrum is in equilibrium in that range and the source terms balance each other. For $f > 0.5$ Hz, the total source term is slightly positive and the energy level in the tail should be growing, which would not be realistic. For that reason, a "diagnostic tail" is imposed at a factor f_{XFM} times the mean frequency $f_{m-1,0}$ (here $f_{XFM} = 2.5$ is used). Which implies that for frequencies above $f_c = f_{XFM} f_{m-1,0}$, the value of the spectrum at the end of each time step is set to

$$E(f,\theta) = E(f_c,\theta) \times (f_c/f)^5 \quad \text{for} \quad f > f_c. \tag{3.1}$$

One consequence of this tail is that the directional distribution has the same shape $E(f_c,\theta)$ (same mean direction, same directional spread) for all frequencies above f_c. Getting rid of this ad hoc diagnostic tail is one more motivation for updating the model

parameterizations.

One of the main difficulties of wave modelling, is that the model uses a spectral dissipation rate $S_{\mathrm{ds}}(f,\theta)$ that is not measured directly. The impact of the spectral shape of S_{ds} on the shape of the wave spectrum $E(f,\theta)$ is particularly discussed in this chapter. Because full directional measurements are extremely rare (Guimarães et al., 2020), the direction-integrated spectrum is generally used,

$$E(f) = \int_0^{2\pi} E(f,\theta)\mathrm{d}\theta, \tag{3.2}$$

with the directional distribution of wave energy,

$$M(f,\theta) = E(f,\theta)/E(f). \tag{3.3}$$

Wave buoys and other point measurement systems provide reliable estimates of the first five moments $E(f)$, $a_1(f)$, $b_1(f)$, $a_2(f)$, $b_2(f)$ (Ardhuin et al., 2019b; Longuet-Higgins et al., 1963; Swail et al., 2009), with

$$a_n(f) = \int_0^{2\pi} \cos(n\theta)M(f,\theta)\mathrm{d}\theta, \quad b_n(f) = \int_0^{2\pi} \sin(n\theta)M(f,\theta)\mathrm{d}\theta. \tag{3.4}$$

From these moments, several frequency-dependent parameters can be derived from the spectrum to characterize the directional distribution of wave energy. Besides mean directions, the directional spread $\sigma_1(f)$, as defined by Kuik et al. (1988), is reliably measured for frequencies up to 0.4 Hz (O'Reilly et al., 1996). A second spreading parameter $\sigma_{2,E}$ can give additional information and was extensively used by Ewans (1998) to establish that the wave spectrum is generally bimodal at high frequencies, as suggested by model simulations (Banner and Young, 1994). Here the alternative form $\sigma_2 = \sqrt{1-\sigma_{2,E}^2}$ will be used, which is denoted $\sigma^\star$ in Kuik et al. (1988). Hence the two spreads have the following values in radians:

$$\sigma_1(f) = \sqrt{2\left(1-\sqrt{a_1^2+b_1^2}\right)}, \quad \sigma_2(f) = \sqrt{0.5\left(1-\sqrt{a_2^2+b_2^2}\right)}. \tag{3.5}$$

Furthermore, underwater acoustic measurements at frequencies $f_s = 2f$ with f in the range 0.1 to 10 Hz, are expected to be proportional to the value of $E(f)^2 I(f)$ (Ardhuin et al., 2013; Farrell and Munk, 2010), where $I(f)$ is the so-called "overlap integral"

$$I(f) = \int_0^{2\pi} M(f,\theta)M(f,\theta+\pi)\mathrm{d}\theta. \tag{3.6}$$

Which implies that underwater acoustics open a unique window on wave frequencies beyond 0.4 Hz s for which spectral information is very limited.

The general goal of this chapter is to evaluate the effects of implementing the wave breaking term (S_{ds}) proposed by Romero (2019) (from hereon T700) comparing to alternatives based on the commonly used term from Ardhuin et al. (2010). An analysis of the dissipation term form based on idealized cases is given in section 3.4. Then an evaluation of its effect in global conditions is presented in section 3.5. Altimeter and buoy data are used to provide some measure on the dominant wave heights and mean energy conditions. Finally, in section 3.6 underwater acoustic measurements are used to give some control of the directionality in the spectrum tail. Discussions and conclusions follow in section 3.7.

The content of the present chapter can be found in Alday and Ardhuin (2023).

3.2 Model parameterizations

3.2.1 Nonlinear wave interactions

In deep water the dispersion relation of surface gravity waves $\sigma^2 = gk$ is concave and thus there are no possible second order interactions of two wave trains with wavenumber vectors $\mathbf{k}_1$ and $\mathbf{k}_2$, and frequencies f_1 and f_2 that could give rise to resonant interaction, namely it is impossible to have both $\mathbf{k}_3 = \mathbf{k}_1 + \mathbf{k}_2$ and $f_3 = \pm f_1 \pm f_2$ (Phillips, 1960). As result, the lowest-order resonant interactions occur at third order and are such that

$$\begin{aligned} \mathbf{k_1} + \mathbf{k_2} &= \mathbf{k_3} + \mathbf{k_4} \\ \sigma_1 + \sigma_2 &= \sigma_3 + \sigma_4. \end{aligned} \tag{3.7}$$

The existence of such interactions was first demonstrated in the laboratory by McGoldrick et al. (1966) with two wave trains propagating in perpendicular directions with wavenumbers $\mathbf{k}_1$ and $\mathbf{k}_2$ giving rise to an obliquely propagating wave train with wavenumber $2\mathbf{k}_1 - \mathbf{k}_2$, corresponding to the case $\mathbf{k}_3 = \mathbf{k}_1$.

Assuming a quasi-Gaussian sea state, Hasselmann (1962) derived the long-term rate of change of the wave spectral density as sum of the triple products of spectral densities among interacting quadruplets of waves, with an interaction coefficient G that is obtained by Taylor expansion of the Euler equation to fifth order in the wave slope. Therefore, the evolution of the wave spectrum takes the form of a source term on the right hand side of the wave action equation (eq. I.26). Then, the change of wave action density (N) at a

given wavenumber $\mathbf{k_1}$ is given by

$$\frac{\partial N(\mathbf{k_1})}{\partial t} = S_{\mathrm{nl}}(\mathbf{k_1}) = \iiint G(\mathbf{k_1},\mathbf{k_2},\mathbf{k_3},\mathbf{k_4})\delta(\mathbf{k_1}+\mathbf{k_2}-\mathbf{k_3}-\mathbf{k_4})\delta(\sigma_1+\sigma_2-\sigma_3-\sigma_4)\times \Big[N(\mathbf{k})N(\mathbf{k_3})\Big(N(\mathbf{k_4})-N(\mathbf{k_2})\Big)+ N(\mathbf{k_2})N(\mathbf{k_4})\Big(N(\mathbf{k_3})-N(\mathbf{k})\Big)\Big]d\mathbf{k_2}d\mathbf{k_3}d\mathbf{k_4} \tag{3.8}$$

where δ is Dirac's function that is zero for almost all values and gives an integral equal to 1 when integrated in the neighbourhood of 0. The generalization of G to finite water depth is given in Herterich and Hasselmann (1980).

Instead of solving the full integral over 6 dimensions (because each wavenumber is a 2-component vector) the practical calculation can be accelerated by integrating only on the 3-dimensional hyper-surface where the integrand is non-zero (Resio and Perrie, 1991; Webb, 1978). This method was implemented in the WAVEWATCH III code by van Vledder (2006).

The nonlinear 4-wave interaction produces both a direct cascade (transfer of energy towards shorter components in the tail of the wave spectrum) and an inverse cascade (transfer towards longer components). This second transfer is particularly important in the growing phase of the wave field, as demonstrated by Hasselmann et al. (1973). It is important to note that the spectral evolution predicted by eq. (3.8) was verified by deterministic simulations (Annenkov and Shrira, 2018) with some generalizations to strong non-linearity or non-homogeneous conditions.

Because the computational cost of the integral in eq. (3.8) is very high, instead of a full interaction over all resonant components, Hasselmann and Hasselmann (1985) proposed to only take into account neighboring wavenumbers. This parameterization was basically tuned to better represent the evolution of the spectral peak, with view to at least properly account for the magnitude of the inverse cascade, and thus the growth of wave height and peak period when waves develop. As a result, this Discrete Interaction Approximation is applied for each frequency and direction of the spectrum F(f_r,θ). This simplification is based on the fact that interactions between slightly different wavenumbers reproduce the principal features of the nonlinear energy transfer. The nonlinear resonant conditions include 2 identical wavenumber vectors $\mathbf{k_1}$=$\mathbf{k_2}$=$\mathbf{k}$ and 2 wavenumbers $\mathbf{k_3}$ and $\mathbf{k_4}$ of different magnitude and that lie at a different angle from $\mathbf{k}$. The resonant system

for these 4 components is given by

$$\begin{aligned} \mathbf{k_2} + \mathbf{k_1} &= \mathbf{k_3} + \mathbf{k_4}, \\ \sigma_2 &= \sigma_1, \\ \sigma_3 &= (1 + \lambda_{\mathrm{nl}})\sigma_1, \\ \sigma_4 &= (1 - \lambda_{\mathrm{nl}})\sigma_1, \end{aligned} \tag{3.9}$$

where λ_{nl} is a constant.

The wave action increment ($\delta \mathrm{S_{nl}}$) over a time step Δt is given by

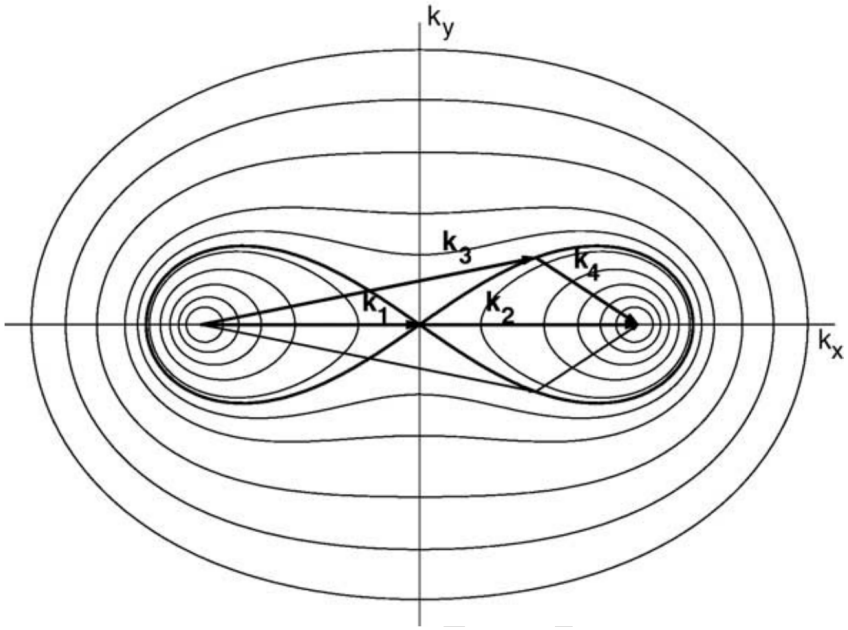

Figure 3.2 – Geometrical arrangement of the wavenumbers that satisfy the 4-wave interaction rule. Each line corresponds to a different value of $f_1 + f_2$.

$$\begin{aligned} \begin{pmatrix} \delta \mathrm{S_{nl}}(\mathrm{f_{r,1}}, \theta_1) \\ \delta \mathrm{S_{nl}}(\mathrm{f_{r,3}}, \theta_3) \\ \delta \mathrm{S_{nl}}(\mathrm{f_{r,4}}, \theta_4) \end{pmatrix} = D \begin{pmatrix} -2 \\ 1 \\ 1 \end{pmatrix} \mathrm{C} \times \mathrm{g}^{-4} \mathrm{f}_{\mathrm{1,r}}^{11} \times \Bigg[\mathrm{F}(\mathrm{f_{r,1}}, \theta_1)^2 \times \\ \left(\frac{\mathrm{F}(\mathrm{f_{r,3}}, \theta_3)}{(1+\lambda)^4} + \frac{\mathrm{F}(\mathrm{f_{r,4}}, \theta_4)}{(1-\lambda)^4} \right) - \frac{\mathrm{F}(\mathrm{f_{r,1}}, \theta_1)\mathrm{F}(\mathrm{f_{r,2}}, \theta_2)\mathrm{F}(\mathrm{f_{r,3}}, \theta_3)}{(1-\lambda^2)^4} \Bigg]. \end{aligned} \tag{3.10}$$

In WW3, the nonlinear interactions computed with eq. 3.10 are done with only one set of parameters λ_{nl} and C. Here, all simulations done with the DIA use λ_{nl}=0.25 and

C=2.5×10^7. The choice $\lambda_{\mathrm{nl}} = 0.25$ gives the ratio of $|k_3|/|k_1|$ and the relative angles of the wavenumbers shown in Fig. 3.2. This value is particularly well suited for a discretized spectrum in which the frequency $f_{n+1} = 1.1 f_n$, corresponding to $k_{n+1} \simeq 1.2 k_n$, as this 20% spacing in wavenumber is comparable to the $|k_3|/|k_1|$ value. When a much finer frequency resolution is used in the spectrum, there is a risk that the DIA will miss the natural smoothing property of the full interaction.

Although widely used, the DIA has many limitations on its representation of the nonlinear wave interactions (Benoit, 2005; van Vledder et al., 2001), and it presents significant differences compared to exact or "quasi-exact" methods such as those proposed in Webb (1978), SWAMP Group et al. (1985), or the GQM from Lavrenov (2001). All of them allowing more accurate representation of the S_{nl} term, the latter one of particular interest given its suitability for operational model applications.

The GQM method employs Gaussian quadratures for different numerical integrations of eq. (3.8). The six dimensions of the integral in eq. (3.8) are reduced to 3 dimensions f_2, θ_2, f_3 by suppressing the 2 Dirac resonance conditions. First the term $\delta(\mathbf{k_1}+\mathbf{k_2}-\mathbf{k_3}-\mathbf{k_4})$, allowing to eliminate 2 dimensions of integration. With these changes and following Lavrenov (2001) working with the directional wave spectrum $E(f,\theta)$, the variable change from $\mathbf{k}$ to (f,θ) leads to an integral over f_2, θ_2, f_3 and θ_3. Integration over θ_3 allows to eliminate the second Dirac. Equation 3.8 can thus be rewritten as follows:

$$\frac{\partial E(f_1,\theta_1)}{\partial t} = \frac{\partial E_1}{\partial t} = \int_{f_2=0}^{+\infty}\int_{\theta_2=0}^{2\pi}\int_{f_3=0}^{f_a/2} \frac{{f_a}^4 G}{f_2 f_3 f_4} \frac{E_3 E_4 (E_1 {f_2}^4 + E_2 {f_1}^4) - E_1 E_2 (E_3 {f_4}^4 + E_4 {f_3}^4)}{\sqrt{\tilde{B}_0(\epsilon_a,\omega_3)\tilde{B}_1(\varepsilon_a,\omega_3)\tilde{B}_2(\varepsilon_a,\omega_3)}} df_2 d\theta_2 df_3 \tag{3.11}$$

where $f_a = f_1 + f_2 = f_3 + f_4$, $\varepsilon_a = 2g\mathbf{k}_a/{f_a}^2$, with $\mathbf{k_a} = \mathbf{k_1} + \mathbf{k_2} = \mathbf{k_3} + \mathbf{k_4}$, $\omega_3 = f_3/f_a$ and $\tilde{B}_0$, $\tilde{B}_1$, and $\tilde{B}_2$ are 3 non-dimensional functions.

Note that the GQM employs adapted quadratures to properly integrate across singularities of eq. (3.11). At the same time, a reduced or extended number of integration points in the quadrature formulas can be used, together with a filter of quadruplets for certain frequencies that may have negligible contribution to the overall integral computation (further details in Gagnaire-Renou, 2010). The effects of the number of integration points and filtering were analyzed by Benoit and Gagnaire-Renou (2007): A "fine" resolution using 26, 12 and 16 points for the integration on f_2, θ_2 and f_3 respectively, a

"medium" resolution using 14,8 and 8 points for integration, and a "coarse" (or rough) resolution using 11, 6 and 6 points to solve the integral (see Fig.3.3).

Results shown here using GQM, employ a coarse integration discretization using 11, 6 and 6 points along the three resonant integration dimensions. It was verified that the finer resolutions only enhanced the peaks in frequency and directional space by about 10%. Following Gagnaire-Renou (2010) quadruplets with coupling coefficients lower than 0.05 times the maximum were also filtered out, and also a filtering out of quadruplets at frequencies for which $f^5E(f) < 5\times10^{-5}$ m^{2}s^{-4} was added. It was noticed that each of these two filtering steps typically reduced the computation time by a factor 2, with no visible impact on the spectral shape. It is important to highlight that this implementation of the GQM is only valid for deep waters conditions, its use on shallower areas might required further analysis and adjustments to eq. (3.11).

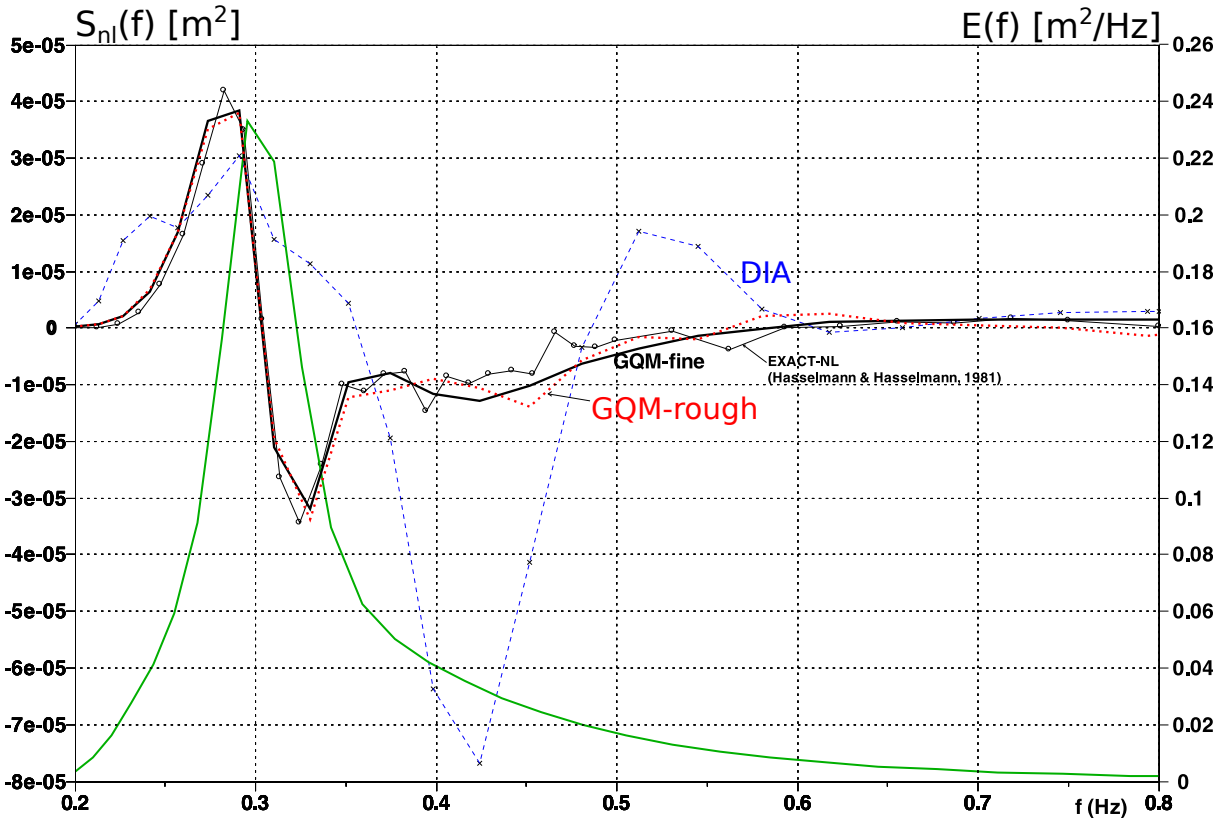

Figure 3.3 – Direction integrated nonlinear transfer terms $S_{\mathrm{nl}}(f)$ computed with various methods: EXACT-NL (SWAMP Group et al., 1985), DIA (blue line), GQM-fine (thick black line), GQM-rough (red dotted line) for the spectrum of case 3 in Hasselmann and Hasselmann (1981). The frequency spectrum E(f) is superimposed (in green). Adapted from Fig. 1 in (Gagnaire-Renou et al., 2010).

3.2.2 Wave breaking parameterizations

At very high frequencies, the dissipation caused by molecular viscosity that scales like the wavenumber squared should be important, together with the straining of turbulence by the Stokes drift shear that scales like the wavenumber to the power 1.5 (Ardhuin and Jenkins, 2006). These are particularly relevant for gravity-capillary waves (Dulov and Kosnik, 2009), and certainly contribute to the shape of the full spectrum (Elfouhaily et al., 1997), with an indirect effect on the dominant waves via the wind stress (Janssen, 1991). However, as this study is limited to a maximum frequency of 1 Hz, these effects are neglected and the dissipation is expected to be controlled by wave breaking (Sutherland and Melville, 2013).

Going back to Miche (1944), it is well understood that waves start to break when crests become unstable, leading to a transfer of energy from waves to the ocean. Crest instability occurs when the orbital velocity approaches the phase speed which, in the case of deep water, may be parameterized as a function of the wave slope (Longuet-Higgins and Cleaver, 1994). The difficulty with random waves is to predict the probability of breaking and the rate of dissipation of wave energy for broken waves.

From tuning knobs to physics-based expressions

For a long time, the dissipation caused by wave breaking was used as an empirical term to close the energy budget, and adjusted to produce realistic wave heights and periods. In that context, the dissipation proposed by Hasselmann (1974) used a scaling of the dissipation with a wave steepness parameter $\varepsilon_r = k_r H_s$ with k_r a mean wavenumber, integrated over the entire spectrum,

$$k_r = \int_0^{2\pi} \int_0^{k_{\max}} k^{-0.5} E(k,\theta) \mathrm{d}k \mathrm{d}\theta, \tag{3.12}$$

giving a dissipation term $S_{\mathrm{ds}}(f,\theta) \propto \sqrt{gk_r}\varepsilon_r^4(k/k_r) \times E(f,\theta)$. That expression was the basis for all parameterizations used in the operational model at ECMWF until June 2019, and thus also used in the recent ERA5 re-analysis. The main defining feature of this parameterization is that the magnitude of dissipation for the entire spectrum is controlled by a single steepness number ε_r. And this steepness takes in all the waves, both windsea and swell. A very undesirable effect is that the same windsea will grow very differently - according to the model - in the presence of swell depending on how they affect ε_r, and in the presence of current gradients that change the steepness (Ardhuin

et al., 2012). Removing this spurious cross-talk of windsea and swell was one of the main reason for improved model results when this was abandoned at ECMWF with the change to Cycle 46r1 of the IFS model in June 2019. Also, it is now generally accepted that the dissipation of the swell is caused by processes different from breaking that possibly involve air-sea friction, as already discussed in Chapter 1.

In trying to provide a sound physical basis for dissipation, Phillips (1985) introduced statistics of wave breaking fronts and their length per unit surface and per vector velocity, with the idea that the dissipation rate of energy in a breaking front is related to its speed, as found in the laboratory by Duncan (1981). A practical difficulty for implementing this approach in wave models is that the occurrence of a breaking front is due to the superposition of different wave trains with the right phases, and not to a single component of the spectrum. How to determine breaking fronts from the spectrum? How to redistribute the dissipation rate to the underlying spectral components? One may think that these wave trains must travel together for some time to lead to breaking waves, hence they have almost the same phase velocity and thus, it could be possible to define a wave steepness from a "region" of the wave spectrum with similar directions and similar phase speeds. That reasoning was followed by Banner et al. (2000) in their analysis of breaking probabilities for dominant waves (waves with frequencies close to the peak frequency).

With very limited information on the distribution of wave energy as a function of wave direction θ, the first discussions of the spectral shape were done in terms of the direction-integrated spectrum $E(f)$. Phillips (1958) proposed that the non-dimensional spectrum

$$\alpha(f) = E(f)(2\pi)^4 f^5/g^2 \tag{3.13}$$

is constant at high frequencies, because in that range all waves are breaking and thus have the same self-similar shape and the energy level "saturates". The idea of saturation was generalized to a two-dimensional spectrum by Phillips (1985) who proposed that the degree of saturation, which is a non-dimensional quantity defined from the spectral density of the surface elevation in wavenumber space,

$$B(\mathbf{k}) = |\mathbf{k}|^3 E(\mathbf{k}) \tag{3.14}$$

or equivalently with (k, θ) spectral coordinates,

$$B(k, \theta) = k^3 E(k, \theta) = \sigma k^3 N(k, \theta.) \tag{3.15}$$

determines the geometry of the surface and the form of the source terms.

It was Phillips who introduced the idea that the dissipation should be related to the length of breaking crests $\Lambda(k,\theta)$. Phillips (1985) proposed that, for a smooth enough spectrum, is possible to use $B(k,\theta)$ as "local steepness", and thus parameterize $S_{\mathrm{ds}}(k,\theta)$ as a function of $B(k,\theta)$. In measurements, it is much more difficult to define breaking probabilities and dissipation rates for different spectral components. Based on the data from Banner et al. (2000), the threshold steepness at which breaking starts to occur could be translated to a threshold B_r in the saturation level. The next step was to extend this to the full spectrum based on observations by Banner et al. (2002).

It has thus come from a "global steepness" proposed by Hasselmann (1974) representative of the entire spectrum, to a local steepness in which each component is completely independent from much larger scales or much smaller scales when it comes to breaking. First attempts with this new approach failed to produce a reasonable energy balance and spectral shape. In particular, the measurements suggested that short waves break more often in the presence of longer waves (Babanin and Young, 2005). This observation is still not fully explained, and in general a full theory for the modulation of wave breaking and associated dissipation rates of short waves is still missing. Many different effects have been proposed to interpret and parameterize that phenomenon, for example the passage of a breaking front may "wipe out" all slower waves (Banner et al., 1989), or the modulation of short waves by long waves making the short wave steeper on the crests of the long waves and thus more likely to break. That second effect was first used by Donelan (2001) who empirically adjusted the following expression

$$S_{\mathrm{ds}}(f,\theta) \propto B(k,\theta)^{2.5}\left[1+500\mathrm{mss}(k)\right]^2 E(f,\theta) \tag{3.16}$$

with the mean square slopes of all waves longer than k defined as

$$\mathrm{mss}(k) = \int_0^{2\pi}\int_0^k k^2 E(k',\theta)\mathrm{d}k'\mathrm{d}\theta. \tag{3.17}$$

Unfortunately there was no theoretical justification for such a large effect of long waves. The short wave modulation theory at the time, due to Longuet-Higgins and Stewart (1960), gave only an amplification of the short waves by a factor $1+4\sqrt{2\mathrm{mss}}$. For a long wave mss of the order of 0.01, the expression given by Donelan (2001) is a factor 30 too large.

The effect of a breaking front with a phase speed vector $\mathbf{C}(\mathbf{k}')$ "wiping out" all slower

waves with a phase speed vector $\mathbf{C}(\mathbf{k})$ (Banner et al., 1989) was parameterized by Ardhuin et al. (2010). In this parameterization it is assumed that any breaking wave instantly dissipates a fraction $|C_{\rm cu}|$ of the energy of all shorter waves provided that the short wave frequency is less than $r_{\rm cu}$ times the long wave frequency, giving a dissipation term

$$S_{\rm ds,cu,-}(k,\theta) = C_{\rm cu} N\,(k,\theta) \int_{k'<r_{\rm cu}^2 k} |\mathbf{C}(\mathbf{k}) - \mathbf{C}(\mathbf{k}')|\,\Lambda(\mathbf{k}')\mathrm{d}\mathbf{k}', \tag{3.18}$$

in which $C_{\rm cu}$ is a tuning factor of order -1, and where the dissipation rate is relatively higher for short waves travelling against the long breaking waves. This expression led to the first successful practical wave model based on a saturation dissipation, that strongly reduced wave model errors. This lead to its implementation in most operational wave forecasting centers starting with Météo-France and NCEP in 2012, followed by Environnement Canada, the UK Met Office, and finally ECMWF as of June 2019.

However, these parameterizations are far from being perfect. First of all, the typical balance of source terms led to a high frequency spectrum tail proportional to $f^{-4.5}$ and thus it still required an imposed parametric tail for the high frequencies. This parametric tail forces the spectrum to decay like f^{-5} from the spectral level at a frequency f_c set to be 2.5 times the windsea mean frequency. In practice the parameterizations based on Ardhuin et al. (2010) produce energy levels at f_c, and thus for the entire tail, that is rather high for young waves and winds over 18 m/s. A high tail level produces a very high drag coefficient via the quasi-linear effect. Still the resulting energy balance produces wave heights that match observed wave heights up to at least 15 m (Alday et al., 2021).

On a practical side, the expression in eq. (3.18) involves a relatively costly integral because the norm of the phase velocity difference varies with the direction of the short and the long waves. This integral was left out in the ECMWF implementation. As an alternative, a good approximation is obtained by using the difference of the norms,

$$S_{\rm ds,cu,+}(k,\theta) = -C_{\rm cu} N\,(k,\theta) \int_{k'<r_{\rm cu}^2 k} (|\mathbf{C}(\mathbf{k})| - |\mathbf{C}(\mathbf{k}')|)\Lambda(\mathbf{k}')\mathrm{d}\mathbf{k}', \tag{3.19}$$

with $C_{\rm cu}$ a tuning factor of order 1.

The T700 dissipation parameterization by Romero (2019)

A more recent analysis of the modulation by Peureux et al. (2021) showed that the modulation could be much stronger than predicted by Longuet-Higgins and Stew-

art (1960), also varying with directions, with a strongest effect when the short and long waves propagate in the same direction. That latter finding motivated Romero (2019) to parameterize that effect as an enhancement of the breaking probability, taking the form,

$$M_L(k,\theta) = \left[1 + 400\sqrt{\mathrm{mss}(k)}\cos^2(\theta - \theta_m)\right]^{1.5}, \tag{3.20}$$

where θ_m is the energy-weighted mean wave direction for the entire wave spectrum, hence close to the direction at the peak frequency. It is a little arguable, or open to discussion, that this mean direction is not weighted by the wave slope. The main idea is that short waves are modulated by long waves, making the short waves steeper on the crests of the long waves and thus more likely to break. Note that M_L in eq. (3.20) is similar to Donelan's dissipation in eq. (3.16) as it uses $\mathrm{mss}(k)$ with an added cosine-squared directional dependency.

With these assumptions, Romero (2019) proposed the first parameterization of the length of breaking crests per unit surface and unit wavenumber $\Lambda(\mathbf{k})$, as a function of the two-dimensional saturation $B(k,\theta)$ without any integration in frequency or direction:

$$\Lambda(\mathbf{k}) = \frac{l}{k}\exp\left(-\frac{B_\mathbf{r}}{B(\mathbf{k})}\right)M_L(\mathbf{k})M_W(\mathbf{k}), \tag{3.21}$$

where $l = 3.5 \times 10^{-5}$ is a dimensionless constant, $B_r = 0.005$ is a threshold for the 2-dimensional saturation spectrum, that is related to the threshold for wave breaking (Banner et al., 2000). $M_W(\mathbf{k})$ is an extra enhancement factor that is a function of the wind speed and was designed to reproduce the transition between the f^{-4} and f^{-5} regions of the wave spectrum, or $k^{-2.5}$ to k^{-3} when considering wavenumber spectra (Lenain and Melville, 2017; Long and Resio, 2007):

$$M_W(k) = \left(1 + D_W \max\{1, k/k_o\}\right)/(1 + D_W) \tag{3.22}$$

with $k_o = g[3/(28u_*)]^2$ corresponding to the scale at which the spectrum was observed to transition from $k^{-2.5}$ to k^{-3}, and D_W is a dimensionless factor with recommended values of 0.9 when the DIA is used and 2 when exact nonlinear wave interactions are computed.

Whereas Duncan (1981) gave a dissipation rate per unit length of breaking wave crest in the form

$$\epsilon_l = b\rho_w c^5/g, \tag{3.23}$$

where c is the wave celerity and with the dimensionless coefficient b varying with the slope of the breaking waves. Later analyses have suggested that b is a function of wave steepness and the rate of energy convergence of wave groups, leading to a parameterization as a function of the direction-integrated saturation in the form (Kleiss and Melville, 2011),

$$b(k) = C_{ds}^{\text{sat}} \left(\sqrt{B(k)} - \sqrt{B_T} \right)^{2.5} / g^2 \tag{3.24}$$

with $B_T = 0.0011$ a direction-integrated saturation threshold.

Combining eqs. (3.21) and (3.24), Romero (2019) gives the following form for the dissipation term:

$$S_{\text{ds}}(k, \theta) = b(k) \frac{\Lambda(k, \theta) c^5}{g^2} \tag{3.25}$$

Romero (2019) only replaced the breaking parameterization (including the cumulative part) of Ardhuin et al. (2010), keeping all other aspects, including the swell dissipation based on Ardhuin et al. (2009) and wind-wave generation that was adapted from Janssen (1991). Additionally, the parameters were set to reproduce the modeled H_s and T_p obtained in fetch-limited academic simulations with the T470 parameterization by Rascle and Ardhuin (2013), which had been adjusted to global scale observations.

Many of the choices that led eqs. (3.21) and (3.24) can be questioned. In building a parameterization there is always a balance to be found between sticking to known processes and simplifying the final expression to represent their effect. One key aspect should always be to make sure that the parameterization does not produce spurious effects, such as the unrealistic cross-talk of swell and windsea in the early parameterizations by Hasselmann (1974) and Komen et al. (1984). In particular, a parameterization should be able to handle all realistic shapes of wave spectra and produce realistic results. The term "realistic" is emphasized here because, for example, a monochromatic wave train of amplitude a will have numerical value of $E(k) = a^2/(2dk)$ that will increase with smaller discretization dk, leading to arbitrarily large values of B and dissipation rates so that waves of very small steepness could be predicted to break. That particular problem was considered by Filipot and Ardhuin (2012) who explicitly framed the breaking probability as a convolution of the spectrum over a spectral neighborhood (not a strictly local effect) and re-distributed the estimated dissipation rate over the underlying spectral component. That extra complexity adds a large cost in the computation of dissipation but may have very limited effect on the practical result. Besides, Filipot and Ardhuin (2012) limited this convolution/deconvolution to the wavenumber magnitude k, and still treated all directions

by using a saturation integrated over directions.

The strong novelty of the parameterization by Romero (2019) is that all directions are treated independently for computing breaking statistics Λ, although they are combined again in the estimation of the dissipation rate parameter $b(k)$. This gives much more freedom to the directional spectrum to develop a wide range of shapes, compared to previous parameterizations. Clearly the the $\cos^2(\theta - \theta_m)$ factor in eq. 3.20 is designed to reduce dissipation away from the dominant wave direction, in order to enhance the magnitude of directional bimodality. The exact form of that expression is very debatable, in particular, it would still be directional even if the dominant waves were isotropic, but since dominant waves are never anywhere near isotropic, this may not represent a real problem.

One last point that should be discussed, is the presence of the wind speed in the parameterization via the parameter k_o (eq. 3.22). Although there is a clear correlation between wave breaking and wind speed, which is the basis of the Beaufort scale for estimating winds at sea, it is not the only factor that determines breaking. Furthermore, introducing the wind in the parameterization goes against the efforts to determine wave breaking from the surface geometry alone. For example, waves will break in an opposing current gradient even if the wind is zero and k_o is infinitely large. Presumably Romero could have retuned this formulation without having to add $M_W(k)$, it could be that this term was introduced first and then kept in later versions. It should be noticed that plugging in the parameterization the observed transition wavenumber k_o, where the spectrum goes from $k^{-2.5}$ to k^{-3}, does not elucidate at all the underlying cause for that transition which requires further studies.

The dissipation prameterization by Ardhuin et al. (2010)

Instead of going directly to the very different use of the saturation for defining Λ and $b(k)$ made by Romero (2019), it is appropriate to revisit previous parameterizations. Here, particular attention is paid to the cumulative dissipation term that was introduced in Ardhuin et al. (2010). As mentioned earlier, this parameterization was not very efficient as it produces spectral tails that are too shallow, with $E(f) \propto f^{-4.5}$ instead of the expected $E(f) \propto f^{-5}$, hence requiring a diagnostic tail for frequencies larger than $f_c = f_{XFM} f_{m-1,0}$, with $f_{XFM} = 2.5$.

Starting from the saturation expressions that were introduced by Ardhuin and Le Boyer (2006) in order to give some possible adjustment to the shape of the directional

wave spectrum,

$$B'(k,\theta) = \int_{\theta-\Delta_\theta}^{\theta+\Delta_\theta} \sigma k^3 \cos^2(\theta-\theta') N(k,\theta') d\theta' \tag{3.26}$$

and

$$B(k) = \max\left\{B'(k,\theta), \theta \in [0, 2\pi]\right\} \tag{3.27}$$

where $N(k,\theta)$ is the wave action, k is the wave number, θ the wave direction, σ the intrinsic wave frequency observed from a frame of reference moving with the mean current. The saturation based dissipation term proposed by Ardhuin et al. (2010) has the following form:

$$\begin{aligned} S_{\mathrm{ds}}(k,\theta) = \sigma \frac{{C_{\mathrm{ds}}}^{sat}}{B_r^2} \Big[\delta_d \max\{B(k) - B_r, 0\}^2 \\ +(1-\delta_d)\max\{B'(k,\theta) - B_r, 0\}^2\Big] N(k,\theta) \\ + S_{\mathrm{ds,cu}}(k,\theta) + S_{\mathrm{turb}}(k,\theta) \end{aligned} \tag{3.28}$$

with

$$S_{\mathrm{turb}}(k,\theta) = -2C_t \sigma \cos(\theta_u - \theta) k \frac{\rho_a {u_*}^2}{g\rho_w} N(k,\theta), \tag{3.29}$$

where $S_{\mathrm{turb}}(k,\theta)$ represents the loss of wave energy caused by Stokes drift vertical shear stretching the near-surface turbulence (Ardhuin and Jenkins, 2006; Kantha, 2006). The C_t coefficient is of order 1 and can be used to adjust for ocean stratification. Here, the cumulative term $S_{\mathrm{ds,cu}}(k,\theta)$ can take 2 forms. The original expression proposed in Ardhuin et al. (2010) given by eq. (3.18) and the approximation given in eq. (3.19).

3.2.3 Model configurations

All model tests analyzed in the present chapter have a spectral discretization of 36 exponentially spaced frequencies from 0.034 to 0.95 Hz, with a 1.1 increment factor from one frequency to the next. The number of spectral directions is normally 36 (10° resolution) with some exceptions with 24 directions (15° resolution) when the GQM is employed (to reduce the required cpu time). Simulations that use the DIA or the GQM for nonlinear wave evolution are done with the same near-global grid described in section 1.3.3, with a spatial resolution of 0.5°, extending from latitude 78° S to 83° N. The time steps used are 900 s for the global time step, 150 s for advection and refraction time steps, and 10 s for the minimum source term time step. Namely the source term integration time step is automatically adjusted between 900 and 10 s.

The importance of the model errors associated with the DIA was the main motivation to perform one of the first global scale analysis of a wave model using the GQM and the Webb-Resio-Tracy method (hereinafter "WRT") for the computation of S_{nl}. Because the cost of WRT simulations is typically 300 times the computing cost of DIA, these simulations were done only for the North Pacific, covering latitudes 4° S to 83° N as shown in Fig. 3.4, and a limited duration of 6 days (following a spin-up of 7 days).

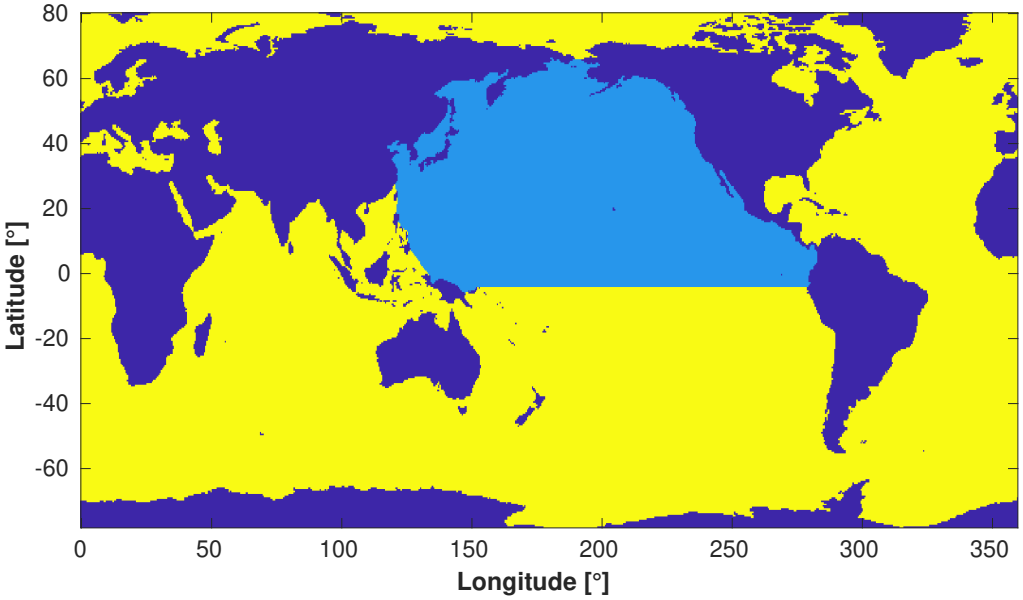

Figure 3.4 – Numerical mask used for North Pacific simulations using the WRT method for nonlinear interactions. Active (wet) grid nodes in light blue, land grid nodes in dark blue and excluded nodes in yellow. Longitudes in plot are presented from 0 to 360° but actual WW3 grid is from -180 to 180°.

3.3 Wave data

To assess global changes related to different used parameterizations, 1-year simulated H_s are compared against the Jason-2 altimeter and the full ESA Sea State Climate Change Initiative merged altimeter data set, using the denoised 1-Hz data for wave heights (Dodet et al., 2020). Additionally, buoy data from CDIP station 166 (or WMO 46246, next to station PAPA) and WMO 51004 close to Hawaii were used to analyze directional characteristics of the spectrum (see Table 1.4). Of particular interest is the data from

buoy 46246, which is a Datawel Waverider buoy maintained by Thomson et al. (2013) that generally provides accurate directional properties (O'Reilly et al., 1996).

3.4 T700 dissipation effects on energy directionality and the tail of the spectrum

Based on an idealized study case with constant wind direction and intensity (10 m/s), an overview of the effects of T700 in the spectral energy is presented for deep water conditions. Tests' parameters specifications are detailed in Table 3.1, where T475 and T700 correspond to the original dissipation parameterizations proposed by Ardhuin et al. (2010) and Romero (2019) respectively.

In some calculations a dissipation term representing wave-turbulence interactions was also included (Ardhuin and Jenkins, 2006), with the coefficient $C_t = 1$ corresponding to a constant momentum flux with depth, while Kantha (2006) argued that typically $C_t \simeq 0.5$. This extra term was found to have no significant impact on the tail part of the spectrum, but $C_t = 1$ may reduce developed wave heights by about 5% as it plays a relatively more important role in the energy balance at frequencies below that of the windsea peak.

Table 3.1 – Choices of parameterizations, methods and parameter adjustments for the different models that use the "ST4" switch in WAVEWATCH III version 7. The choice n_B=1 corresponds to the choice of saturation definition given by Ardhuin et al. (2010), while n_B=3 uses the local saturation defined by Romero (2019). $C_{\rm ds}$ is the first term on the RHS of eq. (3.24). When $C_{\rm cu} < 0$ eq. (3.18) is used, when $C_{\rm cu} > 0$ eq. (3.19). s_u is the sheltering coefficient from Ardhuin et al. (2009) used to tune the stress at high winds.

run:	T475 default	T475b $C_{\rm cu} = 0.3$	700	702	704	700-WRT	702-WRT	702-GQM	707-GQM
$S_{\rm nl}$	DIA	DIA	DIA	DIA	DIA	WRT	WRT	GQM	GQM
n_B	1	1	3	3	3	3	3	3	3
$C_{\rm ds}$			-3.8	-3.8	-3.8	-3.8	-3.8	-3.8	-2.3
$C_{\rm cu}$	-0.4	0.3	0	0.3	0.3	0	0.3	0.3	0.35
$r_{\rm cu}$	0.5	0.5	N.A.	0.5	0.5	N.A.	0.5	0.5	0.5
D_W	N.A.	N.A.	0.9	0	0.9	2.0	0.0	0.0	2.0
C_t	0.0	0.0	0.0	1.0	1.0	0.0	1.0	1.0	1.0
s_u	0.3	0.2	0.3	0.2	0.0	0.3	0.0	0.0	0.0

The overlap integral $I(f)$ (eq. 3.6) is of particular interest for the assessment of directional characteristics of the spectrum. Note that $I(f)$ is non-zero at the wave frequency

f if and only if there are some directions θ for which there is energy in both directions θ and $\theta + \pi$.

Since originally the dissipation in T700 was adjusted to keep the dominant wave behavior (wave height, peak and mean periods), there is little difference in wave heights development, as shown in Fig. 3.5.a. The interesting results brought by the T700 parameterization is that it can produce a shape of the spectrum tail that is close a f^{-5} shape (more exactly a k^{-3} shape that gives f^{-5} when transformed using linear wave theory), namely a nearly flat saturation for frequencies above 0.6 Hz. Still the energy level is higher than the $0.7{\times}10^{-3}\mathrm{m}^2/\mathrm{Hz}^4$ reported by Leckler et al. (2015) for similar wind speeds but for younger waves (see Fig. 3.5.b). In the case of the standard T475 and ST6, the tail shape was imposed above a frequency f_c that is a constant times the mean frequency of the windsea, applying the same directional distribution $M(f, \theta)$ for all f above f_c. This imposed tail is one of the reasons why the ratio of cross-wind (mssc) to down-wind (mssd) mean square slopes is much lower compared to T700 (Fig. 3.5.c). It should be clarified that these slope variances are only integrated up to 1 Hz (1.5 m wavelength), and the contribution of waves with $f > 1$ Hz was added using Elfouhaily et al. (1997). Because 70% of the slope variance is carried by waves shorter than 1.5 m, and the Elfouhaily et al. (1997) spectrum is poorly constrained at wavelengths from 0.2 to 3 m, a direct comparison with observed ratios mssc/mssd is a little premature and will not be pursued here. An alternative validation performed by Romero and Lubana (2022) uses measured slope variance in the presence of oil slicks (Cox and Munk, 1954), but is only qualitative because the effect of the slick on the shape of the wave spectrum is not exactly known.

The most accentuated differences are found for the overlap integral $I(f)$. As noted by Romero and Lubana (2022), $I(f)$ given by T700 can be more than 10 times the value given by any other parameterization, with values around 0.1 for frequencies above 3 times the windsea peak frequency, consistent with stereo-video data (Leckler et al., 2015; Peureux et al., 2018). An interesting property is that the second-order wave field at large wavelengths has a power spectrum density at frequency $f_s = 2f$ that is proportional to $E^2(f)I(f)$. These components generate acoustic-gravity modes (Cox and Jacobs, 1989), seismic modes (Hasselmann, 1963b) and microbaroms (Brekhovskikh et al., 1973), as reviewed by Ardhuin et al. (2019a) and De Carlo et al. (2020). As a result, any underwater acoustic or seismic measurements at frequency $2f$ will be proportional to $E^2(f)I(f)$ (Duennebier et al., 2012; Farrell and Munk, 2008; Peureux et al., 2018), with the proportionality coefficient varying with depth and local sediment properties (Ardhuin

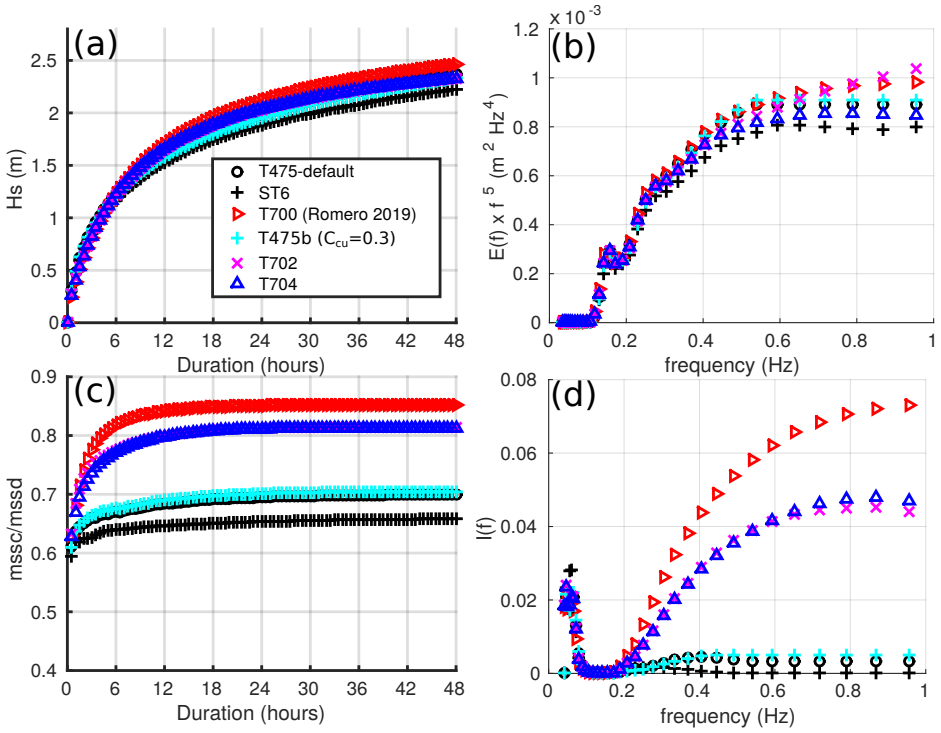

Figure 3.5 – Evolution of (a) wave height (b) cross-wind over down-wind mean square slopes ratio, for a uniform ocean starting from rest with 10 m/s wind, and spectral distribution of (c) saturation level and (d) overlap integral after 30 hours of integration. Results with existing parameterizations based on Ardhuin et al. (2010) (T475, T475b), Rogers et al. (2010) (ST6) are shown for reference, together with Romero (2019) with several proposed adjustments (see Table 3.1).

et al., 2013). A factor 10 difference between modeled seismic response and data can be largely due to uncertainties in the seismic mode generation and dissipation (Ardhuin et al., 2013), but it is expected that these effects are linear and only a function of location and frequency. Therefore, the observed temporal variation of underwater acoustic data should clearly discriminate between different parameterizations. This is further developed in section 3.6.

In order to further improve on the parameterizations it is interesting to expose the features that give this spectrum behavior, namely the proper levelling of the direction-integrated saturation level $f^5E(f)$ and the directional broadening that gives these high $I(f)$ values. A distinctive feature of Romero (2019)'s parameterization is that both the dissipation term and the cumulative effect are highly directional. Thus, for directions more than 90 degrees away from the wind, if the value of $B(k,\theta)$ is not high enough

there is no dissipation at all, and since the wind input is zero (or weakly negative) the only source of energy for these very oblique waves is the non-linear energy flux. This implies that whatever little flux of energy comes from $S_{\rm nl}$ can accumulate to a significant energy level. Figure 3.6 shows the inverse dissipation time scales $S_{\rm ds}/E$ and the resulting directional spectra distribution at frequencies 0.5 Hz and 1 Hz.

The first striking difference is that the previous parameterizations (T475, and ST6) have a nearly isotropic dissipation time scale $S_{\rm ds}/E$. The use of a partial directional integration of $B(k,\theta)$ in the (default) expression of Ardhuin et al. (2010) gives a slightly larger dissipation in the wind direction compared to 30° away from the wind, but the dissipation remains relatively high for waves against the wind. In contrast, the relative dissipation $S_{\rm ds}/E$ from Romero (2019) goes to zero for wave directions 180 to 360°, allowing the spectrum to grow "broad shoulders" with high energy levels for directions 60-120 away from the wind, and still zero in the direction opposite to the wind (Fig. 3.6.b,d). Namely, whatever little energy is pumped in these directions by the non-linear wave-wave interactions, stays there with very little dissipation. Note that a minor change of the cumulative term in T475b, using eq. (3.19) with $S_{\rm cu} = 0.3$ instead of eq. (3.18) slightly increases the width of the spectra (cyan '+' symbols in Fig. 3.5.c,d and 3.6). But this effect is weak, and the dissipation rate is still high for the large oblique angles relative to the wind. One may combine this cumulative effect with the one used by Romero (2019) to get some control over the magnitude of the "broad shoulders".

As seen in Table 3.1, two versions of the T700 parameterization are proposed: T702 and T704. In T702 Romero's cumulative term is simplified by removing the wind dependent part ($D_W = 0$), and the isotropic cumulative term of eq. (3.19) is added with $S_{\rm cu} = 0.3$. This gives almost the same direction-integrated spectrum at high frequencies, as shown in Fig. 3.5.b, but a much lower overlap due to the finite dissipation time scales (5000 s at 0.5 Hz, 1000 s at 1 Hz; see Fig. 3.6). Alternatively, the T704 parameterization combines both cumulative effects, in which case the wind sheltering can be removed ($s_u = 0$) and a good high frequency tail level can be obtained, very similar to the default Ardhuin et al. (2010) parameterization and the typical observed saturation level (Leckler et al., 2015).

Because the DIA is a poor approximation of the full non-linear interaction, it is interesting to check on the effect of using the full interaction which is computed here using two approaches. Either the method of Webb (1978) and Tracy and Resio (1982) as implemented by van Vledder (2006) (WRT), or the Gaussian Quadrature Method (GQM) of

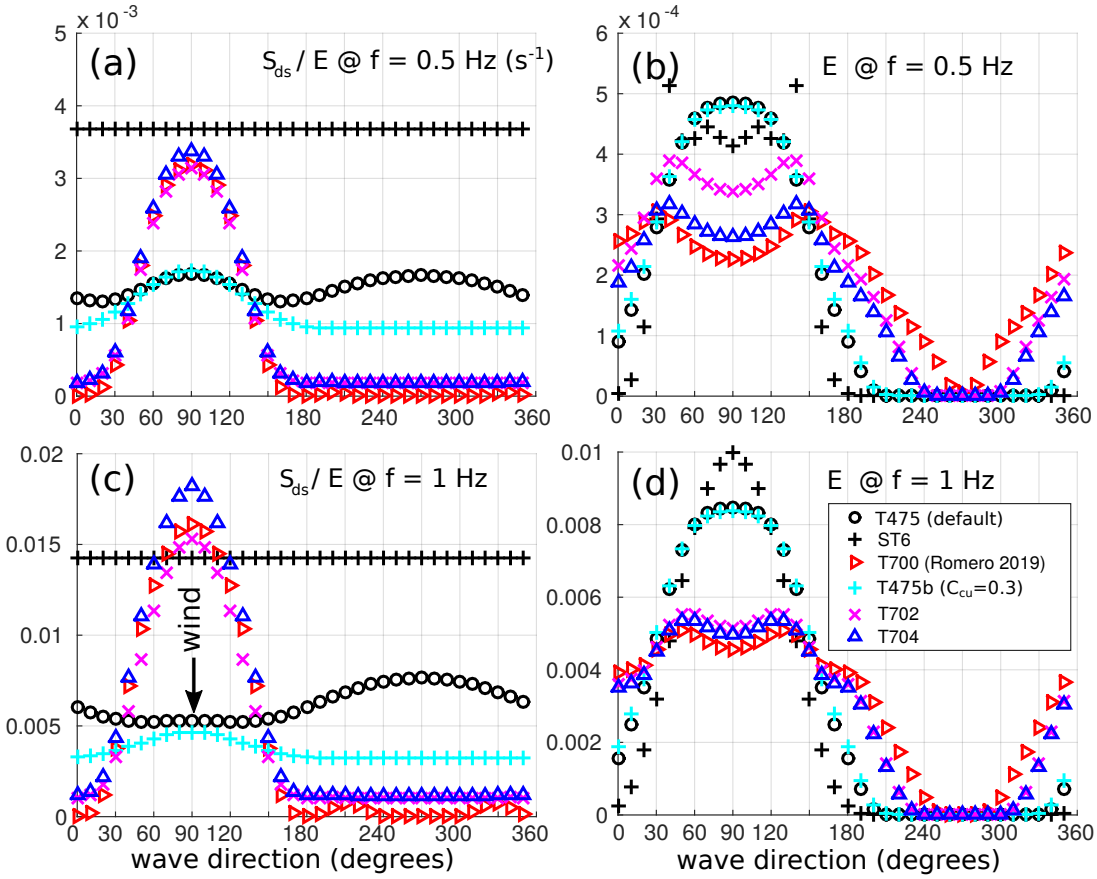

Figure 3.6 – Inverse dissipation time scale S_{ds}/E and directional spectrum shape $E(f,\theta)$ for frequencies 0.5 Hz (in top panels) and 1 Hz (bottom panels). These are obtained after 100 hours of simulation for a uniform ocean with a constant wind speed of 10 m/s blowing in direction 90°.

Lavrenov (2001) (Fig. 3.7 and 3.8). The only adjustment made to the other parameters, when GQM or WRT are employed, follow the recommendation of Romero (2019) with the wind modulation coefficient D_w in eq. (3.22) changed from 0.9 to 2. This increased value of D_w was not sufficient to obtain a correct energy balance at high frequency, hence the T707 adjustments are proposed with a reduced dissipation coefficient C_{ds} in eq. (3.24), similar to what is usually done when replacing the DIA method with exact interactions (Banner and Young, 1994). Additionally the wind sheltering coefficient was kept at zero, as in the T704 adjustment with the DIA. It was also noticed that model results with directional discretizations using 36 directions or 24 directions give very similar result, which is interesting for practical applications since the GQM, and the model in general, is faster when using 24 directions.

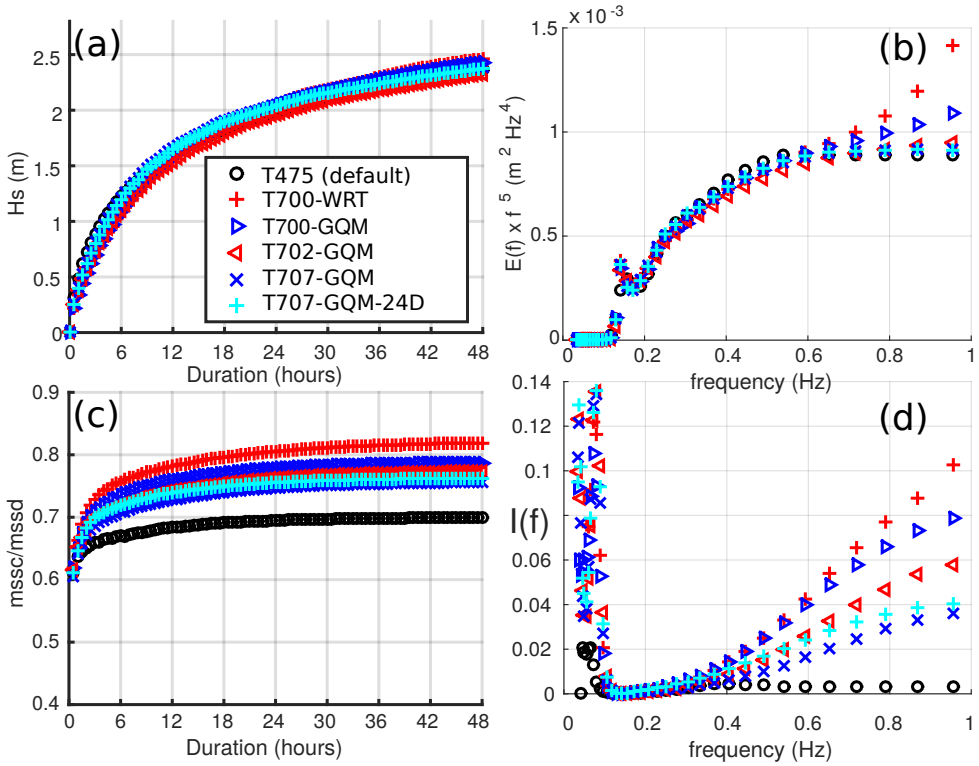

Figure 3.7 – Same as Fig. 3.5, for simulations using exact methods for the non-linear 4-wave interactions.

Among all the runs done with exact interaction methods the only one that stands out with large cross-wind slopes and overlap integrals is T700-WRT, the one obtained without the isotropic cumulative effect of long wave breaking wiping out the shorter waves. Whereas T700-GQM is supposed to compute the exact same thing, it is noticed that the higher frequencies differ slightly with a higher energy level and larger cross-wind energy when the WRT method is used. By changing the number of model frequencies, and changing the maximum model discrete frequency $f_{\max}$ it was found that the WRT method, as implemented, often develops a spurious tail level for $f > 0.7 f_{\max}$. This effect is much less pronounced with the GQM implementation.

To understand the qualitative difference between DIA and exact calculations, it is useful to look at the energy balance as a function of direction, and in particular the relative dissipation rate S_{ds}/E, shown in Fig. 3.8. Contrary to the case with the DIA, the full interactions are able to fill all directions with some energy, including directions opposite to the wind, in particular at high frequencies, a phenomenon that has long been observed with High-Frequency (HF) coastal radars (Crombie et al., 1978). This effect was first

modelled by Lavrenov and Ocampo-Torres (1999) in simulations without dissipation. The 17 dB difference between upwind and downwind energy levels for 0.5 Hz is compatible with the typical 20 dB difference in energy levels for wave upwind and downwind as recorded by 25 MHz HF radars (Kirincich, 2016). At 1 Hz, corresponding to $k = 4$ rad/m, the smaller difference with the T700-WRT simulation between upwind and downwind energy levels is a little surprising but no coastal radar data is available to probe these frequencies. The stereo-video data reported by Peureux et al. (2018) in similar conditions is not conclusive due to a noise level of $E(k, \theta)$ that is probably obscuring the low energy level of waves opposing the wind. Other parameters like the lobe separation and lobe ratio (ratio energy in peak direction to energy in the wind direction) are overestimated at 1 Hz by T700-WRT, and associated with the spurious tail level (the lobe ratio at 1 Hz is identical to T700-GQM when WRT is used with a maximum model frequency of 1.5 Hz, not shown). The overlap integral is probably underestimated by the T707 parameterization, compared to the stereo-video data reported by Peureux et al. (2018). It is also noticed that the high level of upwind energy at 1 Hz obtained with T700-GQM is reduced by a factor 2 with T702-GQM which has a dissipation time scale of 600 s for upwind waves compared to 50 s for downwind waves (Fig. 3.8.c,d). One way to keep some of the general behaviour of the source terms when also using a cumulative dissipation term given by eq. (3.19) is to make sure that it only acts at high enough frequencies, for example with $r_{cu} > 2.5$. Further investigation of measured spectra in steady or turning winds can probably be used for additional testing of the parameterizations.

Note that the two directional spreads that can be measured by directional buoys have different behaviors, from narrow bimodal spectra to broad bimodal spectra as shown in Fig. 3.8.e,f. Indeed the σ_1 spread is defined from the a_1 and b_1 directional moments, and is maximum when the same amount of energy is found in opposite directions (i.e. when both a_1 and b_1 are zero. In contrast, σ_2 -which is called $\sigma^\star$ by Kuik et al. (1988)- is maximum when both a_2 and b_2 are zero, which happens when the same amount of energy is found in perpendicular directions. Hence σ_2 peaks at frequencies around 0.5 Hz where the two lobes are almost perpendicular and decreases as they spread further apart, so that σ_1 keeps increasing towards higher frequency when σ_2 decreases. This behavior is very well described by Ewans (1998). Remember that Ewans (1998) uses $\sigma_{2,E} = \sqrt{1 - \sigma_2^2}$, so that $\sigma_{2,E}$ and σ_2 are anti-correlated. For $f = 0.6$ Hz=$4f_p$ in Fig. 3.8, the typical values given by Ewans (1998) correspond to $\sigma_1 = 60°$ and $\sigma_2 = 37°$, which is closer to the behavior obtained with T700-WRT and T700-GQM simulations.

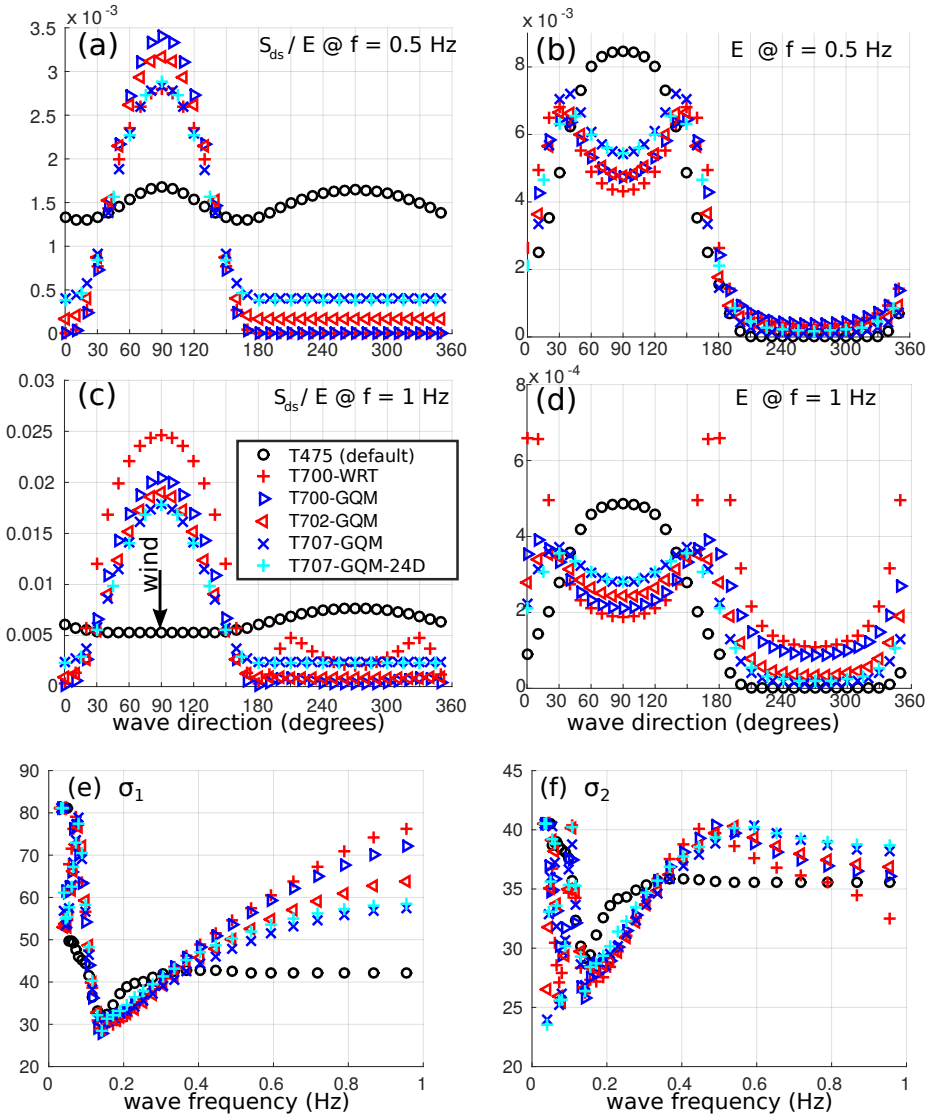

Figure 3.8 – Same as Fig. 3.6, for simulations using exact methods for the non-linear 4-wave interactions, with the addition of directional spreads σ_1, defined from a_1 and b_1 directional moments, and σ_2, defined from a_2 and b_2 directional moments following (Kuik et al., 1988).

3.5 Global impact of alternative dissipation parameterizations

The parameters' adjustment process that lead to T475 allowed to improve the bias and H_s distributions globally. Although, no further changes in wave directional properties were introduced compared to previous hindcasts (e.g. Rascle and Ardhuin, 2013). As seen in section 3.4 with idealized cases, introducing the T700 parameterization affect's directional properties of the simulated sea states and introduces minor changes in the H_s development. It is thus necessary to analyze these differences and evaluate the performance levels of the model when T475 or adjusted T700 parameterizations are used together with the DIA or the GQM in the context of realistic simulations.

3.5.1 Wave heights

As demonstrated by Ardhuin et al. (2010) and showed in detail in Chapter 1, wave heights from global-scale models are most sensitive to parameters defining the swell dissipation. Any change to the wave breaking dissipation can have an impact on the wind-sea to swell transition and thus on the energy radiated into swell which makes it necessary to re-adjust the swell dissipation values. The parameter adjustment procedure defined in Chapter 1 is thus repeated, using the distribution of wave heights measured by Jason-2 for the year 2011, as provided in the ESA Sea State Climate Change Initiative version 1 dataset (Dodet et al., 2020). The model was run with either T702 and the DIA or T707 and the GQM method (details in Table 3.2 and 3.1). The value of s_7 was reduced from 432000 for T475 and T702, to 360000 for T707-GQM, and the swell dissipation factor was reduced from 0.66 for T475 and T707-GQM to 0.6 for T702. Additionally, T702 use a wind-wave growth parameter $\beta_{\max} = 1.7$ while T707-GQM uses $\beta_{\max} = 1.6$, which is consistent with the general reduction of other source terms when replacing the DIA with an exact method (Banner and Young, 1994). Additionally the wind correction factor proposed for T475 using ERA5 winds was reduced to $x_c = 0.5$ for T707-GQM and T702-Bm1.7b (see eq. 1.9). Table 3.2 gives the different sets of wave growth and swell dissipation parameters from the 1-year global runs presented in this section.

This is possibly the first study discussing a global-scale 1-year long simulation using an exact calculation of 4-wave interactions. The "coarse" GQM integration settings proposed in Gagnaire-Renou (2010) and used in Beyramzadeh and Siadatmousavi (2022)

Table 3.2 – Wind-wave generation and swell dissipation adjustments to models with alternative dissipation parameterizations. Variables $\beta_{\max}$, s_7 Re_c, U_c and x_c correspond to namelist parameters BETAMAX, SWELLF7, SWELLF4, WCOR1 and WCOR2 in the WW3 input files (see Appendix C for the full set of parameters). Only T707 employs the GQM method, in all other tests the DIA is used for nonlinear interactions.

Test name	$\beta_{\max}$	$\mathbf{s_7}$	$\mathbf{Re_c}$	$\mathbf{U_c}$ (m/s)	$\mathbf{x_c}$
T475	1.75	4.32×10^5	1.15×10^5	21	1.05
T702-Bm1.7	1.70	4.32×10^5	1.15×10^5	21	1.05
T702-Bm1.7b	1.70	4.32×10^5	1.15×10^5	21	0.5
T700-GQM-Bm1.6	1.60	3.60×10^5	1.50×10^5	21	0.5

are implemented here, with the same filtering details described in section 3.2.1: a first filtering on the coupling coefficient that removes half of the quadruplets (leaving around 800 quadruplets for each spectral component, compared to 2 for the DIA) and a second filtering based on the value of $E(f)f^5$, so that on average the S_{nl} term is not computed for half of the spectral components, typically for the low frequency swells. Verifying with a few buoy locations in the Pacific, this second filtering showed minor impact on the low frequency energy levels, which was typically reduced by under 5% for frequencies under 0.06 Hz (not shown). The CPU usage was 7.5 times longer for the full model using GQM with 24 directions' discretization compared to the DIA with 36 directions, taking 45 hours of run time for one year of simulation, using 432 computational cores. Note that a typical 6-day global forecast would typically take only one hour with the same set-up.

Wave heights in simulations with the implementation of the T700 dissipation parameterization are very close to those obtained with T475. Model runs with T702 and T707-GQM have a reduced bias compared to T475 for wave heights in the range 1-3 m, but present a higher scatter around the observed values. Most of these differences may be associated to swell dissipation. Note that the reduction of x_c in the wind correction term is more effective in combination with T707-GQM, while for T702-Bm1.7b further adjustments could be done to reduce the negative bias for $H_s > 11$ m (Fig. 3.9).

Further verification on H_s values is done using the CCI V1 merged altimeter product for 2011, this includes Cryosat-2, Envisat, Jason-1 and Jason-2. For wave heights, the mean difference is within $\pm 2\%$ locally (Fig. 3.10.c,d), with some stronger negative biases in the tropical west Pacific when using the new parameterizations. Random differences are similar in general. Particularly with T702 the scatter index increases from 5% in the trade wind areas (in T475) to 15% (clearer in the Southern hemisphere), and more along

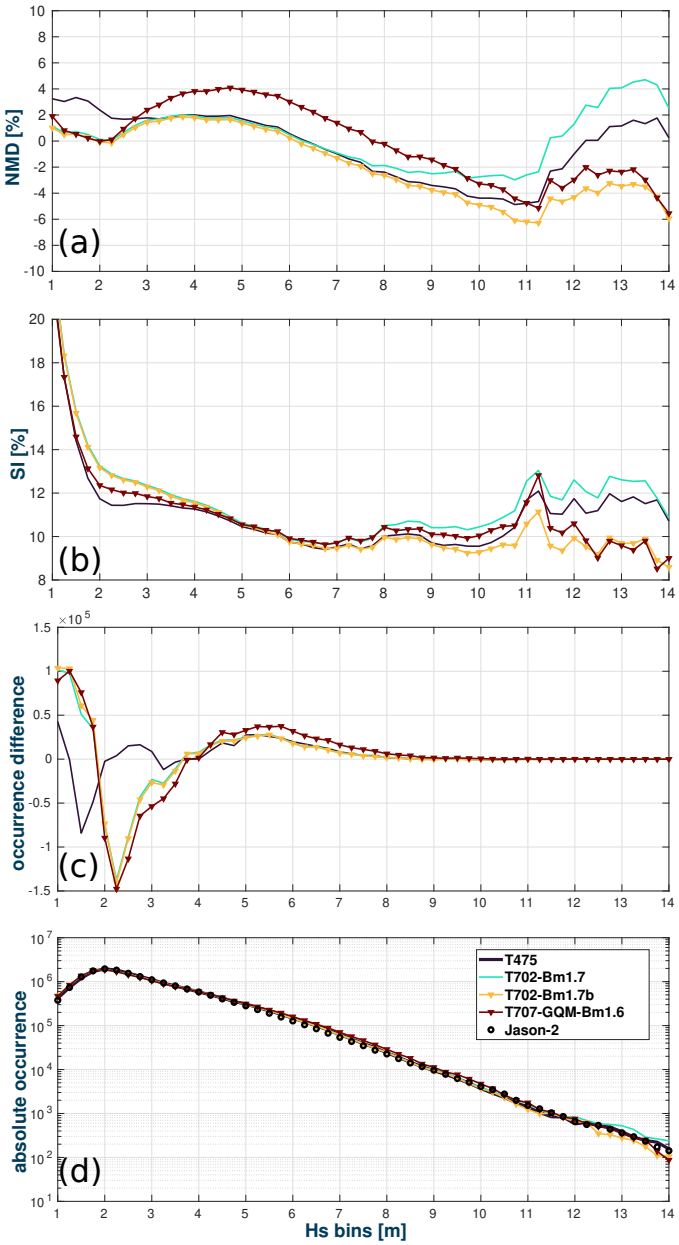

Figure 3.9 – Model global performance with different parameterizations as a function of the wave height: T475, T702-Bm1.7, T702-Bm1.7b and T707-GQM. Wave heights performance parameters for year 2011 (WW3 - Jason-2). (a) H_s NMD, (b) scatter index, (c) H_s occurrences differences (to better observe changes for wave heights < 5 m) and (d) H_s occurrences in log scale.

East coasts and in enclosed seas (Fig. 3.10.b,c, right panel). It should be noted that the random error of denoised 1 Hz altimeter measurements is of the order of 7% for the data

used here (Dodet et al., 2022). It is thus expected that in the trade wind areas most of the difference between model and satellite data is caused by random errors in satellite data. Typically the T707-GQM run gives a lower random differences than T475 in the Pacific, but larger values in the South Atlantic, and they have similar area-weighted averaged index of 10.4% for T475 and 10.3% for T707-GQM, compared to 10.6% for T702.

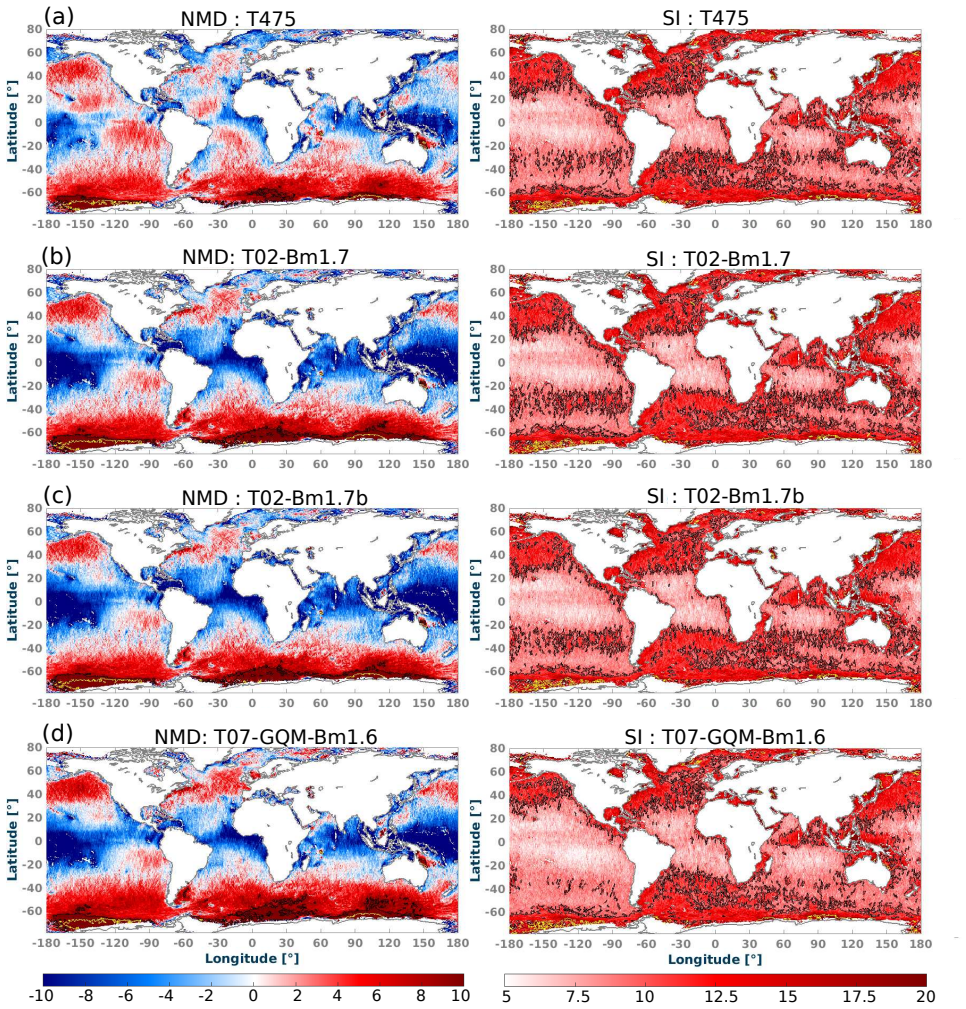

Figure 3.10 – Normalized mean differences (NMD on left panel) and scatter index (SI on right panel) for H_s. Black and yellow lines represent the 10% and 20% contours respectively. Colorbars represent NMD and SI in % points.

For very large wave heights altimeters are usually most accurate, and they are consistent with other data up to 20 m wave height (Hanafin et al., 2012). Wave heights over 10 m account for 0.06% of the full altimeter record, but they are hugely important in defining extremes both locally and remotely through the radiation of swells (Hoeke et al.,

2013). In that range of wave heights, the "out of the box" T700-GQM with the proposed parameter values from Romero (2019) gave low biases from -10 to -15%. This led to the series of adjustment defined for T707-GQM. Although the increase of the bias for wave heights in the range of 4 to 6 m is still not fully solved.

Examination of a few cases suggest that the T475 and T702 runs give tail levels much higher than T700-GQM for the high winds found in these cases, contrary to what was shown for 10 m/s winds in the previous section. It is somewhat "lucky" to have the T475 and T702 runs with probably wrong spectral level and wind-wave growth term that leads to a correct growth of wave heights for $H_s > 10$ m. Efforts to resolve this are underway, and various observations of the spectral tail level and its variability (Yurovskaya et al., 2013) associated with remote sensing data (Ryabkova et al., 2019) and recent findings by Janssen and Bidlot (2023) may lead to more realistic spectra and wind stress. In this context, characterized by very few detailed spectral wave measurements, underwater acoustic data may provide interesting constraints on the source terms. This is done here in section 3.6 with data acquired in the deep ocean north of Hawaii by Duennebier et al. (2012), which covers wind speeds up to 17 m/s.

3.5.2 Spectral shapes

Further analysis of the Romero (2019) parameterization is done by studying its effect on the spectral shape evolution, including the directional characteristics. The influence of the model parameterization on directional wave spectra may be more easily interpreted with the more familiar kind of data obtained from buoys. Although buoy data may not be reliable at frequencies above 0.4 Hz, they provide separate measurements of the energy level and some measure of the directional spreading. The variation of these quantities for one wave event in January 2011 is illustrated here. The selected event has initial low winds veering from North-westerly to an Easterly directions in the early hours of 27 January, and increasing to 13 m/s (these are uncorrected winds measured at 5 m height) with a steady Easterly direction, as shown in Fig. 3.11.a. The resulting sea state is thus relatively complex on 27 January with the northwesterly waves accounting for most of the wave energy and the easterly windsea progressively growing from high frequencies down to 0.15 Hz. The sea state is a more simple windsea dominated condition on January 28. A more general view of the sea state development can be seen in Fig. 3.12.

Model results for different source term settings are shown in Fig. 3.13. The analysis is focused on 3 spectral quantities, that are the saturation level of the spectrum, proportional to $f^5E(f)$, the first directional spread $\sigma_1(f)$ and the second directional spread $\sigma_2(f)$ as defined by Kuik et al. (1988) and already discussed in Section 3.1 and Ewans (1998).

Starting from the saturation levels comes from the idea that it might be possible to examine data beyond the equilibrium range in which the energy levels decrease like f^{-4}. As the transition from f^{-4} to f^{-5} is expected to occur at a frequency of the order of $f_n = 0.0225g/u_\star$ (Lenain and Melville, 2017), this would be around 2 Hz for a 3 m/s wind and around 0.4 Hz for 14 m/s. In the analyzed event this could be visible in the buoy record on 28 January, but surprisingly the spectral tail shoots up at high frequencies (black lines with dots in Fig. 3.13, panels in top row). The highest values of the measured tail level happen to coincide with times when the current follows the wind with speeds around 20 cm/s, and when the ratio of horizontal to vertical motion (also known as the "check ratio") drops around 0.8 for frequencies above 0.4 Hz. It is thus assumed that the buoy is somewhat hampered by its mooring and may not be reliable for frequencies above 0.4 Hz. Nevertheless, it is still interesting to examine the behaviour of the different model tests. First of all, the energy level in T475 runs are dictated by the imposed f^{-5} tail, which here limit the value of $f^5E(f)$ to about 0.001 m^2 Hz^4, i.e. a saturation level of 0.0005 $(2\pi)^4/g^2 = 0.008$, which is rather high. Computations without the imposed tail

and using the WRT method for the exact non-linear interactions also produce sharply increasing saturation levels. This anomalous tail level is reduced when using GQM, and the tail can be adjusted to any level when a cumulative breaking term is added in T702 and T707 simulations, based on eq. (3.19).

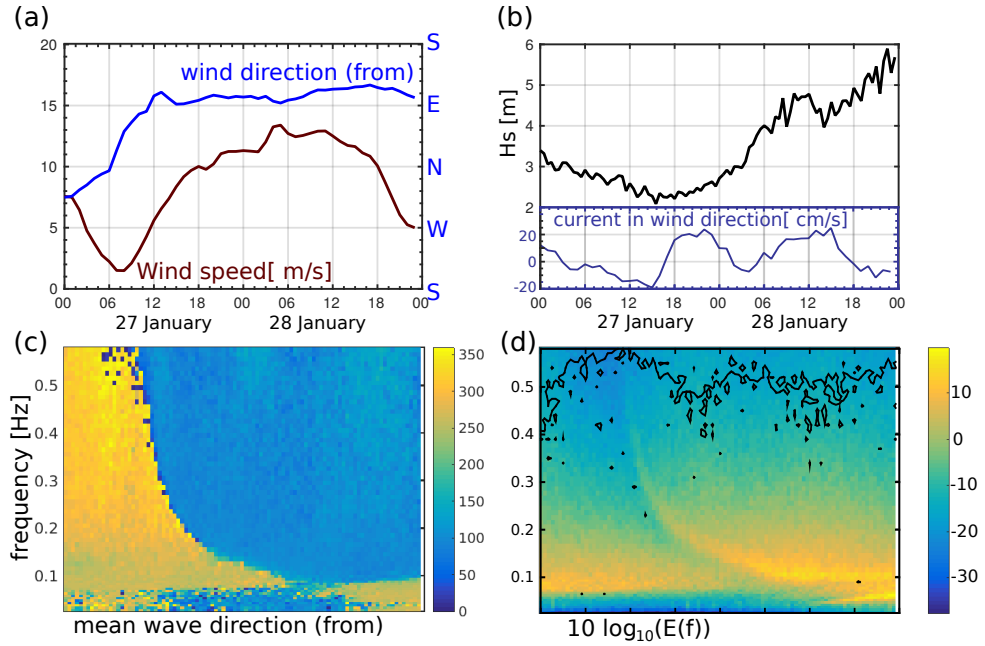

Figure 3.11 – Oceanographic parameters at buoy 46246 and Ocean Station Papa for 27 to 28 January 2011: (a) Wind speed, wind direction, (b) significant wave height over a wind event recorded at Ocean Station Papa and current at 15 m depth (projected on the wind direction) nearby buoy 46246 (CDIP station 166), (d) evolution of the mean wave direction and (e) the evolution of the wave spectrum $E(f)$, with contours for the check ratio equal to 0.8 overlaid in black.

Now looking at directional spread σ_1 (middle row in Fig. 3.12) and σ_2 (bottom row), it is observed that T700 an T702 have a tendency to overestimate the directional spread when using the DIA, specially between 0.2 and 0.4 Hz, while T700-WRT has a general very good reproduction of the variations of both σ_1 and σ_2. Note that on 28 January all parameterizations based on Romero (2019) are able to reproduce the monotonic rise in σ_1 towards higher frequencies and a maximum of σ_2 at intermediate frequencies that are typical of an increasing angular lobe separation towards higher frequencies. The T700 calculation in blue develops the σ_2 peak at lower frequencies than the buoy data due to the much broader lobes produced by the DIA compared to exact non-linear calculations. We also find that T702 and T707-GQM directional spread σ_1 is lower than measured by

the buoy as the wind speed increases between January 27 and 28, suggesting that the added cumulative term is too strong and that the energy level against the wind direction may be more realistic with the original T700.

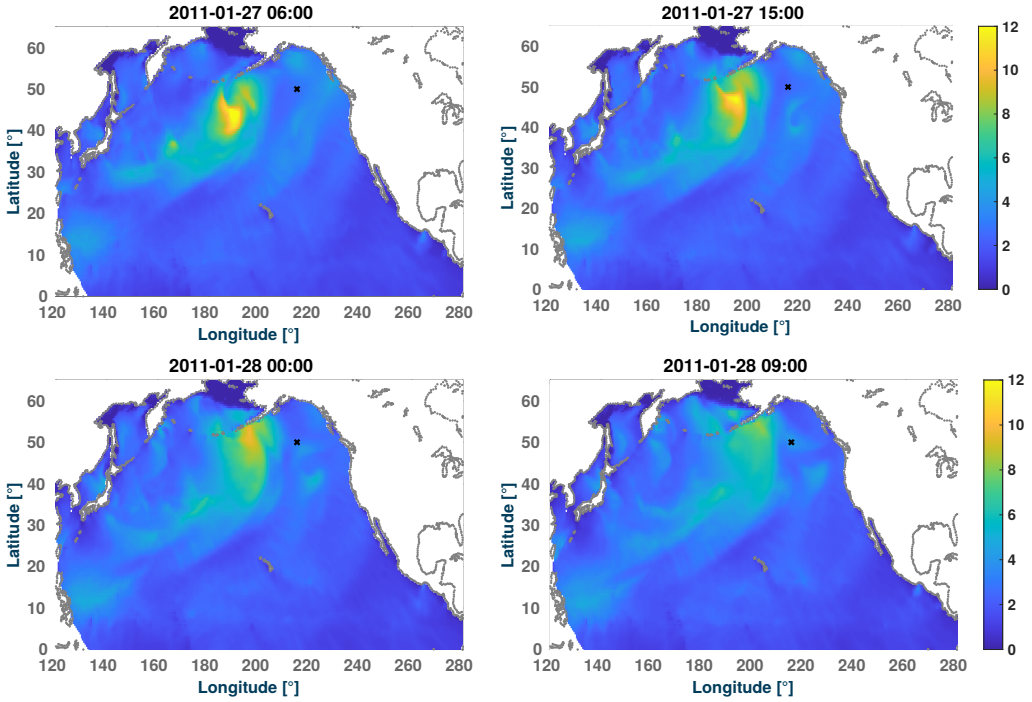

Figure 3.12 – H_s field evolution between 27 and 28 of January 2011. Colorbars indicate H_s values in meters, and the cross indicates the location of buoy 46246. Longitude coordinates are from 0 to 360° in these plots.

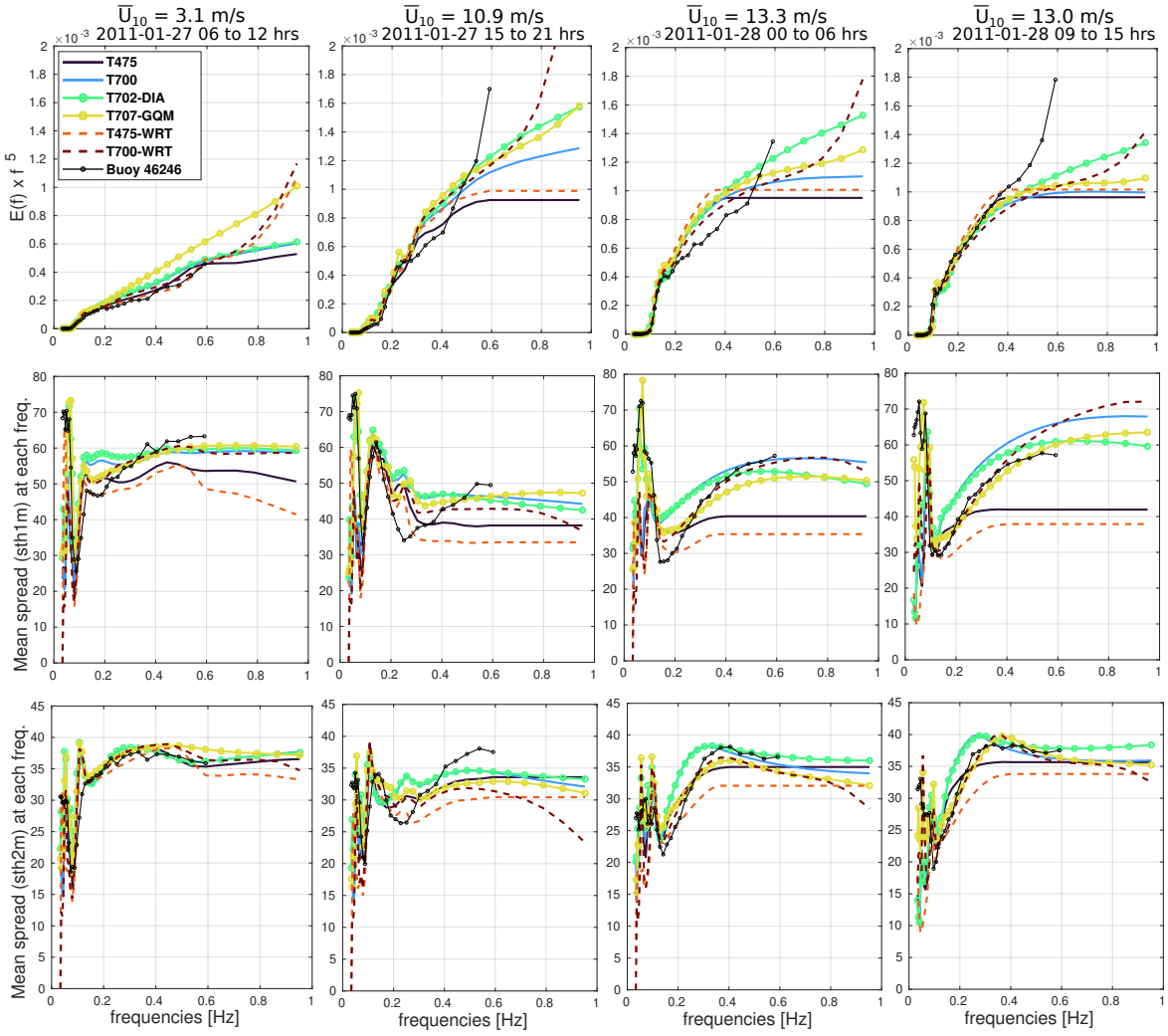

Figure 3.13 – Modeled and measured spectrum, multiplied by f^5 (top panels), first mean spread $\sigma_1(f)$ (middle panels), and second mean spread $\sigma_2(f)$ (bottom panels).

3.6 Underwater acoustic data and directional spectral tail properties

Further information on the wave spectrum shape is provided by underwater acoustic data and seismic records. Ocean waves give a signature in seismic and acoustic fields because of the 3-wave interaction that radiates acoustic or seismic waves of frequency f_s and wavenumber vector $\mathbf{K}$ from any pair of waves with nearly the same frequency f and f' and nearly opposing directions with wavenumbers $\mathbf{k}$ and $\mathbf{k}'$ such that $\mathbf{K} = \mathbf{k} + \mathbf{k}'$ and $f_s = f + f'$. The theory for random waves was derived by Hasselmann (1963a), and it

gives a local source of acoustic or seismic power that is isotropic (the same amount of energy is radiated along all azimuths), and proportional to,

$$S(f_s) = \int_0^{2\pi} E(f_s/2,\theta)E(f_s/2,\theta+\pi)\mathrm{d}\theta = [E(f_s/2)]^2 I(f_s/2) \tag{3.30}$$

where $I(f_s/2)$ is the overlap integral (eq. 3.6).

As a result, microseism and acoustic power can give some indication on the width of the windsea spectrum, the magnitude of reflection at the shoreline and the presence of swells of the same frequency in opposite directions (Ardhuin and Roland, 2012; Ardhuin et al., 2011).

Recent model developments show that one could predict the variability of the seismic or acoustic wave energy at acoustic frequencies f_s in the range 0.08 to 0.4 Hz using a wave model like WW3. However, underwater acoustic data show that wave-induced signal extend all the way to 60 Hz (Duennebier et al., 2012; Farrell and Munk, 2010). Ardhuin et al. (2013) suspected that the poor acoustic model performance for $f_s > 0.4$ Hz was caused by an unrealistic directional wave spectra shape. This question was also discussed by Peureux and Ardhuin (2016) who proposed parameterizations of the directional distribution that could explain the observed acoustic levels.

One general difficulty of using seismic or acoustic data generated by the double-frequency mechanism of Longuet-Higgins (1950) and Hasselmann (1963b) is that the absolute magnitude of the signal is influenced by bottom properties, as already noted by Abramovici (1968). Also, at the lower frequencies typically $f_s < 0.3$ Hz, the signal can propagate over thousands of kilometers along the wave guide that is constituted by the water layer and the upper crust and sediment layers. Hence, it is not straightforward to link the local wave properties and the local acoustic field. However, for the higher frequencies, as the scale over which the signal is attenuated becomes shorter than the scale at which we can consider the sea state to be homogeneous, there should be a linear relation between the local value of $E^2(f)I(f)$ and the local seismic or acoustic power.

Farrell and Munk (2010) analyzed ocean bottom hydrophone data in 5000 m depth and showed that the acoustic level for frequencies 1 to 6 Hz transitions from a saturated level when the wind is above 5-6 m/s to a "bust" very low level when the wind drops below this value. This is expected to be caused by a narrowing of the spectrum as the windsea peak frequency goes up closer to 0.2 - 0.5 Hz, and thus a very strong reduction of the overlap integral $I(f_s)$, by a factor at least 10. Because most parameterizations (including

T475) use a diagnostic tail that made $M(f,\theta)$ constant above some frequency f_c, the value of $I(f)$ is frequency-independent above f_c and has a narrow range of variation. Romero and Lubana (2022) showed that T700 gave a much higher value of the overlap integral but did not directly compare predicted acoustic or seismic data to measurements.

Here we use from the ALOHA cabled observatory provided by Duennebier et al. (2012) to compare the relative variation of local predicted seismo-acoustic source proportional to $E^2(f)I(f)$ with the ocean bottom acoustic power. The employed data corresponds to acoustic power spectra from 26 February to 31 December 2007. From the original spectra computed every 5 minutes, the lowest spectral density in a 3 hours window is taken and compared to the time-centered model snapshot computed from the local wave spectrum. Choosing the minimum instead of a median mitigates the contribution of non-continuous noise sources, and generally gives a better correlation with the model.

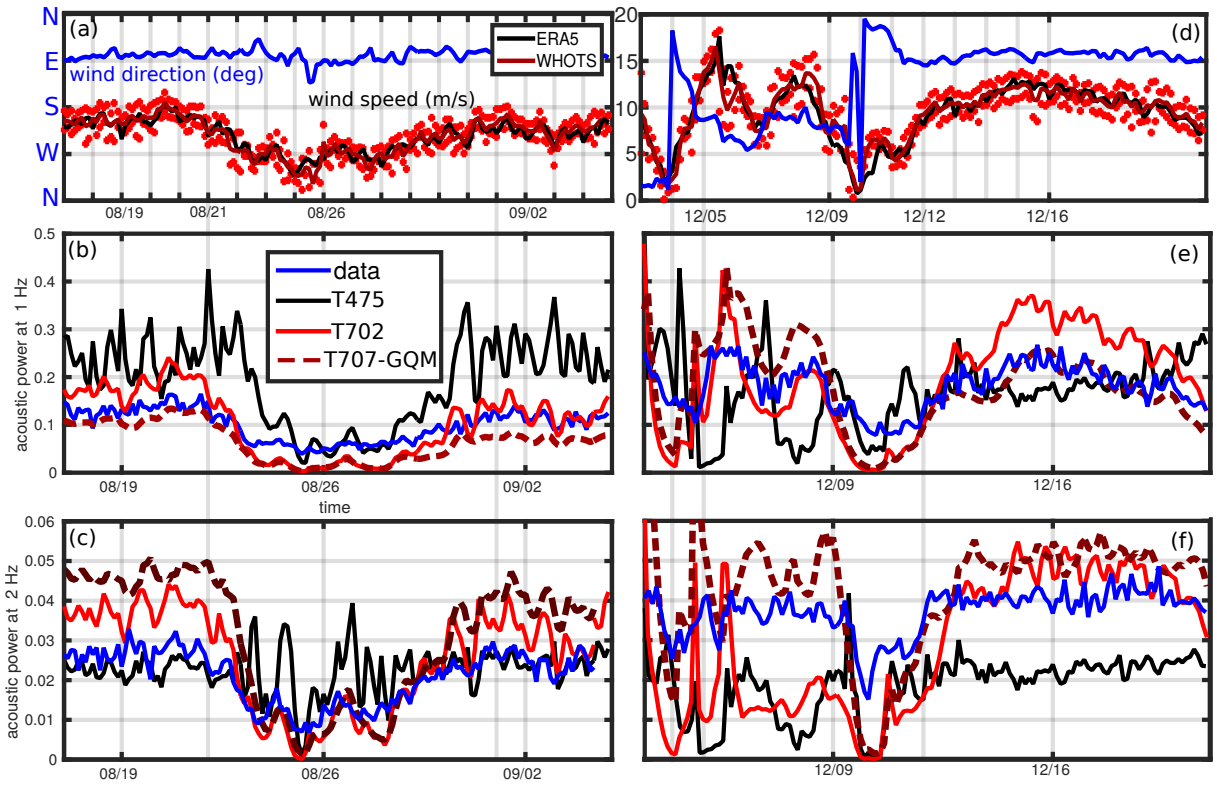

Figure 3.14 – Time series of 3-hourly wind speed and direction and 10-minute averaged measurements (panels a,d) and noise level over a few weeks of summer (a,b,c) and winter (d,e,f) in 2007 at the ALOHA Cabled Observatory, north of Ohahu Hawaii, using data provided by Duennebier et al. (2012) and model runs T475, T702 and T700-GQM. In order to give results comparable to T700, results for T475 are multiplied by 10 for 1 Hz and 15 for 20 Hz.

Fig. 3.14 shows time series of modeled seismic source and observed acoustic power for two typical time intervals with moderate (Easterly) trade winds in the summer, and a winter Southerly storm followed by intense trade winds. Note that the modeled acoustic noise was re-scaled because of the poorly known bottom amplification effect, with a larger re-scaling coefficient for T475.

Farrell and Munk (2010) showed that the 2 Hz acoustic signal has a fairly constant level, here around 0.04 Pa^2/Hz (Fig. 3.14.c,f), with some occasional drops, which they called "busts". Such busts occur in the record when the wind speed decreases below 8 m/s, from 21 August to 1st of September and from 9 December to 12 December. This behaviour is associated with 1 Hz surface gravity waves and is generally well reproduced by T702 and T707-GQM but not by T475, which has too narrow a range of variation of the seismo-acoustic source. The rise in modeled acoustic level is delayed with T707-GQM with a saturation that is only reached when the wind speed rises to 10 m/s and the general sensitivity of the modeled acoustic level is larger with T702 and T707-GQM, with an amplification by a factor 40 from a wind speed increase of 2 m/s to 10 m/s. While it is possible that background noise may obscure low noise levels, the analysis of Duennebier et al. (2012) suggests only a factor 10 increase for such a wind speed increase, while Farrell and Munk (2013) give a factor up to 30 (15 dB).

The behaviour at 1 Hz is more complex, and there is no simple saturation of the acoustic energy in that case but rather a general increase of acoustic power with increasing wind speed, which in this case is exaggerated by the proposed adjustments to T700 and not well followed by T475 when the wind speed exceeds 10 m/s. The model with T702 and T707-GQM parameterizations produces spurious peaks on December 4 in both 1 Hz and 2 Hz time series. That day has a rapidly turning wind, and at some point the wind direction is 220° while the mean wave direction (energy-weighted) is around 330°. That mean direction is the same parameter θ_m in eq. (3.20) that defines the direction around which a strong dissipation is added by the cumulative effect. Two additional model runs were performed to test the impact of the definition of the direction θ_m in eq. (3.20); T700-GQM uses an energy-weighted mean direction, and T701-GQM is the exact same run with a mean direction weighted by the orbital velocity variance. The time series shown in 3.15.a demonstrate that the peak in modeled acoustic noise was indeed associated to the large mismatch between the wind direction and the direction θ_m.

Correlations between model output and measured acoustic levels over the full time series are shown in Fig. 3.15.b as a function of frequency, an where it is possible to

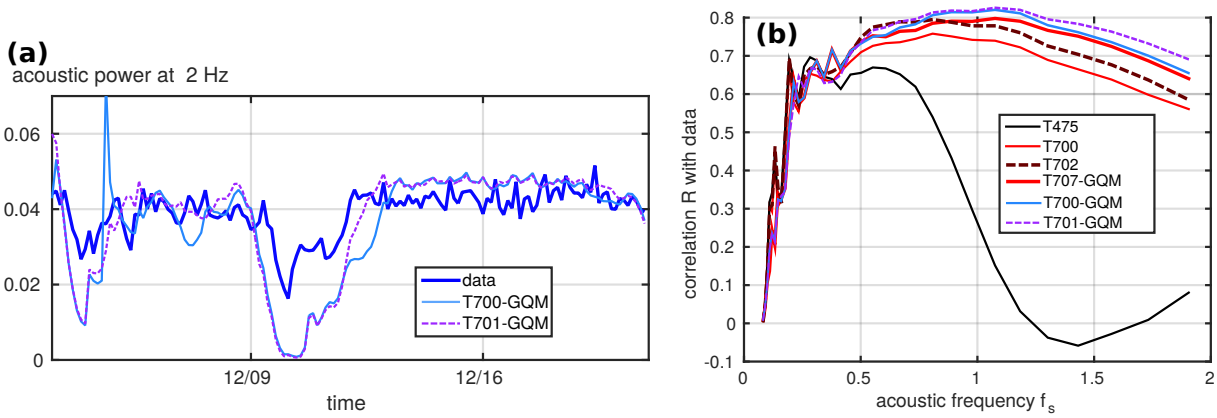

Figure 3.15 – Correlation of modeled acoustic noise at the ALOHA observatory, north of Ohahu Hawaii, for the year 2007 using data provided by Duennebier et al., 2012 and model runs T475, T700, T702 and T700-GQM.

see the general better performance of a direction θ_m using a stronger weighting by the higher frequency waves (here using orbital velocities instead of surface elevation). It is evident T475 has very little skill for acoustic frequencies above 0.8 Hz (wave frequencies above 0.4 Hz), and parameterizations by Tolman and Chalikov (1996) and Bidlot et al. (2005) were previously shown to be even worse (Ardhuin et al., 2013). T700 is a clear improvement, even more so when the exact non-linear calculation with GQM replaces the DIA parameterization. It would be interesting to explore higher frequencies, but this is beyond the scope of the present study.

It is observed that for wave frequencies in the range 0.3 to 1 Hz, the good correlation between modeled and measured acoustic noise levels (with frequencies 0.6 to 2 Hz) supports the idea that noise is mostly driven by waves propagating at angles 80 degrees or more relative to the wind direction. Having a significant energy level in those directions requires a much larger dissipation time scale for compared to the time scale in the mean wave direction allowing the appropriate balance with the nonlinear 4-wave flux of energy (to those directions $>$ 80 degrees relative to the wind direction). In the T707-GQM parameterization an isotropic cumulative term was re-introduced, this helped in getting more accurate wave heights but it degraded the fit to the acoustic data compared to T700. Hence it is concluded that if there is any isotropic dissipation effect it should have a weaker effect than the term introduced in T707-GQM.

3.7 Conclusions

The effects of 2 different wave dissipation parameterizations have been studied, Romero (2019)'s T700, and the wave dissipation parameterization of Ardhuin et al. (2010) as modified by Leckler et al. (2013). Two variations of the latter one were used to compare with T700. The analysis was done with idealized cases and global scale models, comparing the generated results with altimeter, buoy and underwater acoustic data in an attempt to provide a degree of control over main wave parameters and spectral energy distribution, specially the tail of the spectrum.

The most profound difference introduced by Romero (2019) is a practically "directionally decoupled dissipation": the Λ's are decoupled but the dissipation rates are not. This idea of decoupling was already used to justify the variation in wave energy with wind direction for slanting fetches (Donelan et al., 1985; Pettersson et al., 2010). This parameterization is the first that can give a very weak (close to zero) dissipation rate for waves travelling at 90° from the wind, and a strong dissipation rate for waves in the wind direction. This feature is capable of producing directional bimodal spectra, first reported by Young et al. (1995), with realistic shapes, which was a an important objective of Romero (2019). As expected by Romero and Lubana (2022), it was demonstrated that one particular benefit is the capability to reproduce the variability in microseism sources at high frequencies, without compromising the accuracy of wave heights. It was observed that the most accurate results are obtained with exact non-linear calculations that are now affordable thanks to the Gaussian Quadrature Method (GQM) proposed by Lavrenov (2001), and which were used extensively here for idealized cases and for global simulations. These calculations support the conclusion that the energy level in cross-wind and up-wind directions that is found at frequencies higher than 3 times the wind sea peak, is the result of a balance between the 4-wave interactions and a relatively very weak dissipation, compared to the dissipation in the main wave direction, thereby providing a constraint on this relative strength of the dissipation in different directions.

The different possible adjustments to Romero (2019) that have been proposed were motivated by curiosity, which led to challenge some of the ad hoc choices that were made, not based on first principles. In particular the choices in the cumulative term of a cosine squared factor and a reference direction in the energy-weighted mean direction θ_m is associated to spurious directional spectral shapes in the presence of swell and in turning wind conditions. A mean direction weighted by orbital-velocity performed better, but

one could also try other directions related to the waves that are taken into account in the cumulative term. It was shown that a wind parameter in the dissipation term is not necessary and $D_W = 0$ in the T702 runs gave satisfactory results. Although wind may directly impact wave breaking at high wind speeds (Soloviev et al., 2014) or in shoaling waves (Feddersen and Veron, 2005) there is no generally established mechanism for such an effect.

Proposed alternatives using T702 and T707-GQM showed similar results compared to T475 with global scale simulations, but still some further adjustments are required to reduce the higher SI and underestimation of H_s occurrences in the neighborhood of the most frequent wave heights (2 m). It is thought that these differences are due to swell dissipation effects since changes in the wave breaking dissipation affect the transition from wind-sea to swell. Even with these slight differences, all tests done with T700, especially those with the GQM or WRT method closely follow the mean spread values recorded by buoy 46246 for frequencies > 0.3 Hz.

Even though no attempt was done to adjust the spectral tail level to a particular value, it was observed that this level may vary widely depending on the choice of cumulative terms. However, if the cumulative term include a significant near-isotropic contribution as given by eqs. (3.18) or (3.19) it will reduce the directional spread to a level that is lower than observed.

Clearly much more work is needed on understanding the possible physical processes that may justify the detailed parameterization choices of Romero (2019) or any future evolution on it, and in particular much more research is required to understand the "cumulative effect". Without this understanding, we are left to grope in the dark. As we have shown we can constrain plausible parameterizations of source terms using both directional spreads σ_1 and σ_2 from buoy data, as done by Ewans (1998), up to 0.4-0.6 Hz, and underwater acoustic data for a winder range of frequencies. Further constraints on spectral shapes and source terms can be given by HF and VHF radars (Kirincich, 2016; Tyler et al., 1974) up to 0.5 Hz, and microwave radar backscatter for waves with frequencies from 2 Hz (with L-band radar) to 40 Hz (with Ka-band radars) (Kudryavtsev et al., 2003; Ryabkova et al., 2019). One will probably have to distinguish homogeneous conditions from more complex situations, including current gradients (Phillips, 1984; Romero, 2019).

Chapter 4

Conclusion

4.1 Reminder of the main scientific questions and objectives

The main subject of this document evolved around 3 questions related to the choices affecting spectral models' results:

— What is the effect of combined improved forcing fields and increased resolution in the model setup and how do they affect the simulated sea states?
— How sensitive are the wave parameters and the spectral shape to different parameterizations and to their adjustments?
— What are the main drivers of errors?

Based on these questions, the main objective of this thesis was to analyze and improve the characteristics of the simulated sea states by studying the effects on wave generation, propagation and dissipation, introduced by changes/adjustments in physical parameterizations, spectral and spatial resolution, and the forcing fields considered. Additionally, from this main objective, 3 related specific objectives were defined:

— Improve the model performance at global scale mainly in terms of wave heights distributions and reduction of differences with respect to altimeter data.
— Verify in coastal regions (Atlantic coast of Europe) the effects of the model adjustments done at global scale , and identify other potential sources of errors in intermediate to shallow water depth environments using both in situ and altimeter measurements.
— Analyze changes in the energy directional distribution of the wave spectrum, due to the implementation of different wave dissipation parameterizations and methods to account for nonlinear wave interactions.

4.2 Main outcomes of the study

In the present thesis extensive analyses were carried out to assess the characteristics of simulated sea states in terms of wave parameters such as H_s, D_m or T_{m01} and in terms of the spectral energy distribution of the spectrum. Considering that the quality of models' output is a function of mainly the accuracy of forcing fields, the realism of physical parameterizations to represent wave evolution and numerical choices made to integrate the WAE, the overall focus of this study was directed to analyze and quantify how these choices influence the simulated sea states. At the same time, the evaluation of the wave fields characteristics and model performance was done in two distinct environments, involving different dominant forcing and processes: Global open ocean and coastal (regional).

In Chapter 1 the discussion is centered on the effects, at global scales, of improved spectral discretization and forcing fields (namely winds, surface current and sea ice concentration), and the adjustments of the wind-wave generation and swell damping parameterization from Ardhuin et al. (2010). Most of the model performance analyses in this chapter were done comparing with SWH from altimetry data. One of the main findings here is related to the adequate adjustment of the model parameterizations of air-sea interactions and the use of the H_s global PDF. It was shown that the distribution of H_s around the neighborhood of the most frequent wave heights (2 m), could be used to adjust the transition from a laminar to a turbulent boundary layer above the waves, which is very important for the attenuation of swells, and is probably the most sensitive part of the model parameterizations. For the forcing, it was found that the applied correction of the low bias of high speeds (> 21 m/s) in the ERA5 winds, has a direct effect on the partial reduction of the global underestimation of $H_s > 7$ m.

In Chapter 2 the analysis was extended to coastal areas were waves interact with a wide range of bathymetric features, tidal amplitudes and bottom sediment types. In this case a high resolution regional model was implemented, and the assessment of the sea states' characteristics was done using wave parameters and the wave spectrum from buoys, and the latest Sea State CCI altimeter data set. On this latter point, this study provided robust results regarding the application of altimeter data to quantify the accuracy of the simulated wave heights at distances to the coast smaller than 10 km. Due to the different characteristics of the modelled domain, the factors driving the accuracy of the model cannot be completely generalized. Instead, it was possible to identify when and where changes in the wave field characteristics are more significant with different choices

in forcing, resolution, parameterizations and boundary conditions (BC). Overall, spatial resolution is one of the most important elements in shallow depth areas, while the effects of changes in the BC are most easily evaluated at areas exposed to the open ocean (North Atlantic in this case). It was found that including the bottom friction parameterization helps to reduce errors in the simulation of "extreme" events during the development of longer wave components of the spectrum. Nevertheless, further analysis is required to assess its effect in very shallow water depths (< 10 m) where the dissipation effects at lower frequencies might be over estimated without proper tuning.

Finally, Chapter 3 focuses on wave dissipation and wave nonlinear interactions parameterizations, and their effect on spectral energy distribution, with special attention to energy directionality at high frequencies (> 0.5 Hz). Changes introduced by the tested parameterizations were evaluated first with idealized cases, then at global scale with altimeter and buoy data, and then with underwater acoustic data. It was found that the dissipation formulation from Romero (2019) (T700) is the first to give a very weak dissipation rate for waves travelling at 90° from the wind and a strong dissipation rate for waves in the wind direction and thus producing spectra with a realistic strong bimodality. One particular benefit is the capability to reproduce the variability in microseism sources at high frequencies, without compromising the accuracy of wave heights (compared for example to T475). It was observed that the most accurate results are obtained with exact non-linear calculations using Gaussian Quadrature Method (GQM). I believe that the observed differences in global H_s biases and distributions between runs using T700 (T02, T707-GQM) and T475 are due to swell dissipation effects since changes in the wave breaking dissipation affect the transition from wind-sea to swell. Still, all tests done including the T700 wave dissipation term, especially those with the GQM or WRT method closely follow the mean spread values recorded by buoy 46246 for frequencies > 0.3 Hz.

4.3 Findings

Throughout the different sections of this document, it was possible to verify how improved forcing fields and the adequate incorporation of different forcing fields (e.g. wind and currents) have a direct effect on the simulated sea states. Corrections of the ERA5 winds and including surface currents helped to effectively reduce wave height bias and errors at global scale. It was also verified that the proposed correction to reduce the low intensities bias in ERA5 winds helped to reproduce realistic energy levels for

frequencies lower than 0.05 Hz. Although this represents a real improvement in terms of the accuracy of the simulated spectra, the correction of the small energy levels at lower frequencies do not introduce significant changes in the wave parameters.

It was found that modifications of the forcing fields and/or spectral discretization requires a simultaneous verification of the physical parameterizations included in the model. A clear example of this effect is presented in Chapter 1 and 3. As soon as a different wave dissipation parameterization is incorporated, the overall balance of the WAE is modified, hence, the simulated wave fields will be affected by these changes.

In the absence of a global buoy data network, representative of the sea state conditions in different ocean basins, the use of altimetry data was key to verify changes of the simulated wave heights world wide. The SWH distributions from altimeters served as a reference point to adjust the transition from a laminar to a turbulent boundary layer above the waves and thus improve the estimation of swells attenuation.

Identifying the drivers of errors at global scale in open ocean conditions, is probably more straight forward than in coastal environments. In deep waters most wave processes are related to ocean surface-wind interactions: generation, wave growth, propagation and dissipation with currents playing a secondary role at larger scales (but they can be very important locally). These elements are directly related to the accuracy of the forcing fields and the processes represented in the physical parameterizations, relation that is verified in Chapter 1 and 3.

As seen in Chapter 2, in coastal environments, progressively higher spatial resolution in shallower depths is key to improve the representation of wave interactions with complex bathymetry features and to represent wave-current interactions in areas with strong intensity gradients. In the latter cases, higher directional resolution is also required to improve the representation of current induced refraction. Additionally, the overall characteristics of the boundary conditions, including their spectral resolution, are one of the most important factors on shorelines exposed to waves from the North Atlantic. This is a key point to consider when down scaling is required. The quality of the results from the nested model will be bounded to the accuracy of the used boundary conditions.

In particular, for areas with strong tidal regimes, including this forcing can help to reduce random errors of the H_s as wave heights modulation is taken into account. Including currents will also affect the energy levels in the neighborhood of the peak of the wave spectrum, which helps to reduce errors on the mean wave periods. This improvement of the energy levels of the spectrum is thought to be caused by changes of the effective wind.

It should be noticed that if there is a phase shift of the forcing tides, including them could potentially increase the random errors of the simulated wave fields (with respect to measurements).

The use of altimeter data in coastal areas helped to detect and quantify the average effects of the bottom friction parameterization for depths < 50 m. This represents an interesting tool to assess the influence of bottom friction dissipation in areas where in situ measurements are not available, and can give a good first approach for the tuning of the employed parameterization.

In terms of spectral energy diretionallity, it was found that the balance between the wave dissipation and the nonlinear interactions parameterization play a key role to obtain a broader directional distribution at frequencies higher than 3 times the wind sea peak. This requires a relatively very weak dissipation away from the downwind or main wave direction, allowing the build-up of energy "leaking" from the the 4-wave interactions and thus allowing the development of energy bi-modality at high frequencies.

4.4 Perspectives

Within a defined time window for the development of this study, it was not possible to assess every aspect of the model regarding numerical choices or physical parameterizations. Instead special attention was paid to those elements that are thought to have the largest impact on the simulated sea states. It is expected that the methods followed to test and optimize the results will help as reference for future work in this subject.

Many of the model performance analyses were based on comparisons with altimeter data. These datasets are traditionally used to compare with simulations in open ocean conditions and several kilometers away from the coast (e.g. > 50 km) as done in Chapter 1. Using the latest Sea State CCI V2 dataset which is suitable for coastal studies (Passaro et al., 2021), the preset work also includes a complete assessment of the model performance as function of the distance to the coast. The analysis was done with 5 different alimeter missions covering a time span of 16 years. Since the application of altimeter data to coastal environments is relatively new, the use of different missions instead of a "merged" SWH product was intentionally done in order to have an idea of the model-altimeter differences variability range (NMD, SI) at each distance to the coast bin. This information gives more insights on the model performance specially when comparing at distances to the coast smaller than 10 km.

One aspect that wasn't considered in the present study was the effect of the output frequency of the global model (here set to 3 hours). This could have implications in two main elements: The time matching with altimeter data to compare results, and the update of the boundary conditions used in the regional mesh. The reduction of the time interpolation of the model data to compare with the altimeters SWH could influence the computation of the used performance parameters (e.g NMD, NRMSD, SI). Regarding the boundary conditions of the mesh, it should be verified if a more frequent update of the spectral energy can introduce changes on the wave fields evolution.

Throughout the study, and particularly for the coastal implementation of WW3, many tests and adjustments of the model setup did not introduce large changes in the average values of the analyzed wave parameters. Instead, the clear differences observed at each time step between different model configurations point to changes that are related to the evolution and propagation of the simulated wave fields. Moreover, it was proved that even if the overall energy levels of the frequency spectra are similar, directional characteristics may largely differ. In this sense, it might be necessary to define the scopes of the generated data usage in order to fully evaluate the importance of these differences. For example when downscaling to higher resolution models the following question must be asked: What is the main objective and what are the potential uses?. This should immediately make us think about how the boundary conditions were generated. While traditionally the concept of nesting considers going from coarser to higher spectral and spatial resolution, it was shown that directional interpolation of the spectrum (when creating BC) can introduce shifts on the energy distribution of the spectrum, which effects should be further analyzed.

Probably one of the most interesting results presented in this thesis are the effects of the wave dissipation parameterizations on the spectral shape (energy spreading) presented in Chapter 3. Nevertheless, the present work was limited by the availability of large datasets with detailed directional wave measurements and reliable measurements of the short wave energy level. In particular there was no attempt to tune the spectral level to an elusive reference and only stereo-photo and stereo-video measurements were used as a weak guideline for average wind conditions (Banner et al., 1989; Leckler et al., 2013; Peureux et al., 2018). It is expected that video data in a wider range of conditions (including non-bimodal cases), and also drifting buoy data that may be able to accurately resolve shorter waves, will be key in the detail examination of source term behavior in a wider range of conditions, including turning winds. These data will be very useful for further validation of the direction-integrated energy level at different frequencies.

Particularly after the work done in Chapter 3, the parameters' adjustments to correct for a low wave height bias become very questionable. In order to increase wave heights one may increase the wind-wave generation, decrease the dissipation, or even enhance the non-linear 4-wave interactions as proposed by Lavrenov (2001) with the aim to represent fluctuations in the wave field. Ardhuin et al. (2007) have shown that one may use slanting fetch conditions to adjust the magnitude of the input while wave growth with fetch is controlled by the difference between input and dissipation. Another test of the model realism is given by the wind stress, or equivalently the drag coefficient C_d that is the ratio of the friction velocity ($u_\star$) squared and the wind speed squared. Recall that the wind input is generally proportional to $u_\star^2$ and $u_\star$ is a function of the wind input. As a result, the feedback of the spectrum tail on wind wave growth via the quasi-linear effect is important (Fabrikant, 1976; Janssen et al., 1992). The difficulty is that $u_\star$ is generally highly dependent on the part of the wave spectrum that is at frequencies higher than highest resolved frequency (in this study 1 Hz), including the shape of the spectrum in the gravity-capillary range. This aspect of the parameterization was never analysed with the ST4 parameterizations implemented in WW3. Now that the forced tail shape from the resolved part of the spectrum has been removed, it is interesting to look at the impact on C_d. Figure 4.1 shows the variability of C_d produced by different source term parameterizations and justifies that future adjustments will be needed, in particular if the wave model is to be used in a coupled ocean-atmosphere context. First of all it is noticed that the viscous part of the wind stress is not included in the default ST4 calculation of $u_\star$, this part gives the shape of the C_d variation for wind speeds under 5 m/s in the COARE3.5 parameterization by Edson et al. (2013). Second, all variants of the ST4 parameterization overestimate C_d for wind speeds 4 to 15 m/s. This is the result of adjustments of the wind-wave growth parameters to large values. Note that the 707-GQM parameterization (without any imposed tail shape) behaves very much like T475 (with the imposed f^{-5} tail above 2.5 times the mean frequency). T702 gives even higher values of C_d and future adjustment should probably reduce both generation and dissipation terms. For wind speeds over 25 m/s, C_d is artificially reduced by the use of a pre-computed table that limits its value under 0.003, although that may be a desirable feature (Donelan et al., 2012), it was not intended as such, and probably does not behave like it should.

Another particular aspect that is flawed in the WAVEWATCH III - ST4 implementation of the $u_\star$ calculation is the iteration loop between the source term computation that

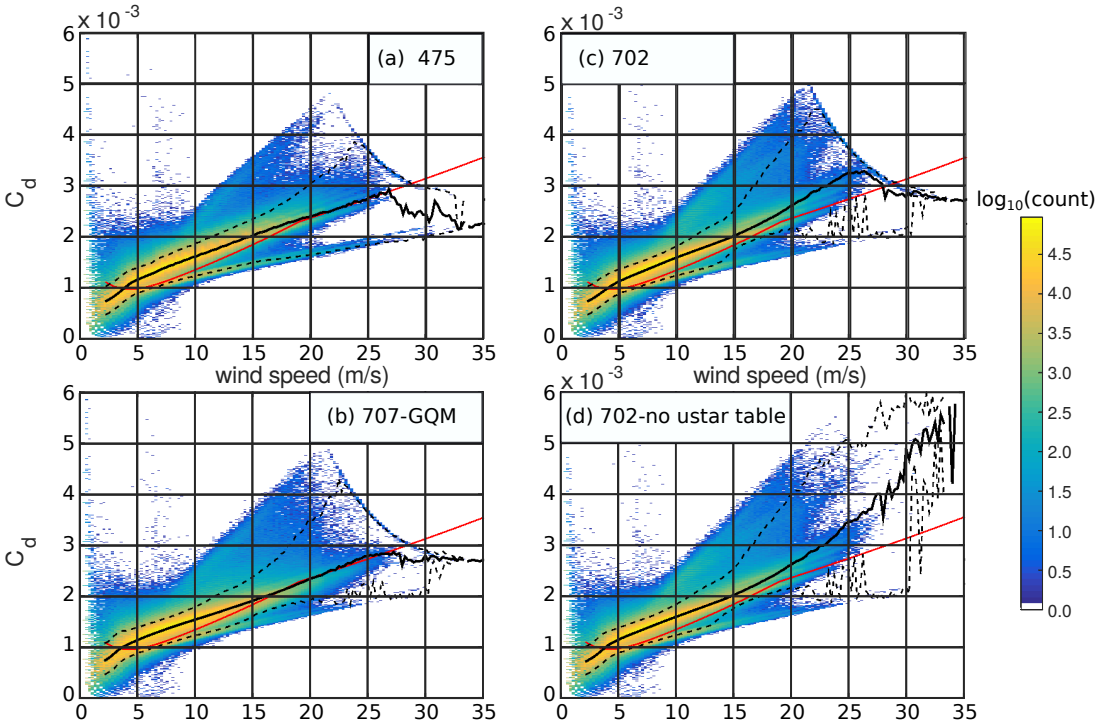

Figure 4.1 – Distribution of drag coefficients for 4 different model runs over the month of January 2007, taking all model output every 3 hours. In each panel the red line is the Edson et al. (2013) COARE3.5 value of C_d in neutral conditions, the solid black line is the mean value for each wind speed and the dashed lines bracket 95% of the values.

uses an estimate of $u_\star$ and produces a wave-supported stress τ_w, and the calculation of $u_\star$ that uses τ_w. At present this is limited to 3 iterations and $u_\star$ can be as much as 50% below its converged value: this explains why rather high values of the wind-wave growth parameter were used ($\beta_{\max} = 1.6$ with GQM and $\beta_{\max} = 1.7$ with DIA) compared to WAM model implementations. As a result, correcting these numerical issues and using lower values of $\beta_{\max}$ may lead to more realistic drag coefficients. It remains to be seen how we may use realistic shapes of the spectrum for the unresolved part of the spectrum (Elfouhaily et al., 1997; Yurovskaya et al., 2013) so that the model may produce realistic mean square slopes and drag coefficients in particular for high wind speeds (Janssen and Bidlot, 2022).

4.5 Future work

In the context of analyzing and improving the simulation of sea states and as continuation of the preset study, the following subjects for future work are of interest:

— Analysis of the effects of T475 and T700 on the evolution of extreme events, and a full in depth analysis on the effect of different wind forcing sources on the energy distribution of the spectrum and not only based on time series of wave parameters. In this sense, it seems logical to extend the global performance analysis with spectral data derived from SAR or retrieved from SWIM (Morrow et al., 2019).

— Study the possibility of using machine learning techniques to improve the adjustments of the atmosphere-wave interactions parameterization, namely the wave growth and swell dissipation terms. This might represent a good approach to improve the sea states characteristics in different regions.

— Extend the analysis of the changes introduced in the spectral tail level and wave directionality at high frequencies with T700 (Romero, 2019) (probably the energy levels should be analyzed first). This would require the use of stereo video measurements to analyze the saturation levels of the tail and adequate buoy data to study the directional energy distribution at higher frequencies.

— A particular aspect not discussed in this work, is the high H_s bias obtained for the Southern Ocean. None of the adjustments in parameterizations directed to reduce the large model-altimeter differences in this region were effective. The lower accuracy of the modelled results in this area could be attributed to inaccuracies of the wind and currents forcing fields, which I think is partly related to the lack of measurements in the area. The improvement of the sea states characterization in high southern latitudes represent an interesting research subject that can help to improve the estimations of ice-wave interactions in the area.

APPENDIX

A Global model implementation

The wave model hindcast and tests presented in Chapter 1 use version 7.0 of WAVEWATCH III (regular grid). The hindcast uses a list of switches, which appears in all NetCDF file products outputted from the model,

- physical parameterizations : LN1 ST4 STAB0 NL1 BT4 DB1 MLIM TR0 BS0 IC2 IS2 REF1 RWND WCOR
- advection and GSE correction: PR3 UQ
- other numerical aspects: F90 NOGRB NC4 SCRIP SCRIPNC DIST MPI FLX0 XX0 WNT2 WNX1 CRT1 CRX1 TIDE TRKNC O0 O1 O2 O2a O2b O2c O3 O4 O5 O6 O7

The model parameters are adjusted with the same parameters for all model grids in the multi-grid configuration. Except for default parameter values specified in the WW3 user manual, test T475 uses the following adjusted values:

- Air-sea interaction parameters (SIN4 namelist) BETAMAX = 1.75, SWELLF = 0.66, TAUWSHELTER = 0.3, SWELLF3 = 0.022, SWELLF4 = 115000.0, SWELLF7 = 432000.00
- wave-ice dissipation parameters (SIC2 namelist) IC2DISPER = F, IC2TURB = 1.0, IC2ROUGH = 0.001, IC2DMAX = 0.3, IC2REYNOLDS = 150000, IC2SMOOTH = 200000., IC2VISC = 2.
- wave-ice scattering and floe size effects including break-up and inelastic dissipation (SIS2 namelist): ISC1 = 0.2, IS2C2 = 0., IS2C3 = 0., IS2BACKSCAT = 1., IS2BREAK = T, IS2DUPDATE = F, IS2CREEPB = 0.2E8, IS2CREEPD = 0.5, IS2CREEPN = 3.0, IS2BREAKF = 3.6, IS2WIM1 = 1.0, IS2FLEXSTR = 2.7414E+05, IS2CREEPC = 0.4, IS2ANDISE = 0.55
- reflexion parameters (REF1 namelist): REFCOAST = 0.05, REFCOSP_STRAIGHT = 4, REFFREQ = 1., REFICEBERG = 0.2, REFMAP = 0., REFSLOPE=0., REFSUBGRID = 0.1, REFRMAX = 0.5
- other parameterizations (MISC namelist) ICEHINIT = 1., ICEHMIN = 0.1, CICE0

= 0.25, CICEN = 2.00, LICE = 40000., FLAGTR = 4, FACBERG = 0.2, NOSW = 6, WCOR1 = 21., WCOR2 = 1.05 /

— activation of 3D output fields (full spectra and seismic sources, OUTS namelist) P2SF = 1, E3D = 1, I1P2SF = 3, I2P2SF = 24

B Regional model implementation

All simulations' results presented in Chapter 2 were generated using the unstructured grid WAVEWATCH III model version 7.0. The following compilation switches were included:

— Physical parameterizations: LN1 ST4 STAB0 NL1 BT4 DB1 MLIM TR0 BS0 REF1 WCOR RWND TIDE
— Advection scheme: UQ
— Numerical choices: F90 NOGRB NC4 SCRIP SCRIPNC SHRD TRKNC O0 O1 O2 O2a O2b O2c O3 O4 O5 O6 O7

In the presented tests, a few different combinations of the swell dissipation terms were used for SWELLF7 and SWELLF4 of the ST4 parameterization. Here the model namelist with its final values as defined in T475 is presented:

— Wave growth and swell dissipation (SIN4 namelist): BETAMAX = 1.75, SWELLF = 0.66, TAUWSHELTER = 0.3, SWELLF3 = 0.022, SWELLF4 = 115000.0, SWELLF7 = 432000.00
— Wave reflexion parameters (REF1 namelist): REFCOAST = 0.05, REFCOSP_STRAIGHT = 4, REFFREQ = 1.0, REFMAP = 0.0, REFSLOPE = 0.03, REFSUBGRID = 0.1, REFRMAX = 0.5
— SHOWEX parameterization (SBT4 namelist): SEDMAPD50 = T, BOTROUGHMIN = 0.0400, BOTROUGHFAC = 1.0
— Unstructured grid options (UNST namelist): UGBCCFL = F, UGOBCAUTO = T, UGOBCDEPTH = -15.0, EXPFSN = T
— Wind correction and others (MISC namelist): NOSW = 6, WCOR1= 21., WCOR2=1.05

C Parameters used with T700 implementations

As described in Chapter 3, a set of different tests with parameterization T700 were employed in the analysis of alternative dissipation formulations. Here, details on the WW3 variables' namelist for tests T702 and T707-GQM are provided. All variables not specified in this section should be considered equal to those in Appendix A.

C.1 Namelist details for T707-QGM

— Air-sea interaction parameters (SIN4 namelist): BETAMAX = 1.60, SWELLF = 0.66, TAUWSHELTER = 0.0, SWELLF3 = 0.022, SWELLF4 = 150000.0, SWELLF7 = 360000.00

— Dissipation parameters (SDS4 namelist): SDSBCHOICE=3, SDSC2 = -2.3, SDSBR = 0.005, CUMSIGP =0.0, SDSSTRAIN =0., SDSSTRAIN2 = 0., FXFM3 = 20, SDSFACMTF = 400., SDSMWD = 2., SDSCUM = 0.35, SDSNUW =0, SDSC5=1., SDSBRF1=0.5

— Nonlinear interactions (GQM) parameters (SNL2 namelist): IQTYPE = -2, GQMNF1 = 11, GQMNT1 = 6, GQMNQ_OM2 = 6, TAILNL=-5.0, GQMTHRSAT=5E-5, GQMTHRCOU = 0.05, GQAMP1=1., GQAMP2=0.0022, GQAMP3=1., GQAMP4=1.0

— Wind correction and others (MISC namelist): NOSW = 6, WCOR1= 21., WCOR2=0.5

C.2 Namelist details for T702

— Air-sea interaction parameters (SIN4 namelist): BETAMAX = 1.70, SWELLF = 0.60, TAUWSHELTER = 0.2, SWELLF3 = 0.022, SWELLF4 = 115000.0, SWELLF7 = 432000.00

— Dissipation parameters (SDS4 namelist): SSDSBCHOICE = 3, SDSC2 = -3.80, FXFM3 = 20.00, SDSSTRAINA = 0.00, SDSSTRAIN = 0.00, SDSSTRAIN2 = 0.00, SDSBR = 0.005, SDSBT = 0.0011, SDSCUM = 0.300, SDSC5 = 1.0, SDSMWD = 0.00, SDSFACMTF = 400

— Wind correction and others (MISC namelist): NOSW = 6, WCOR1= 21., WCOR2=1.05

BIBLIOGRAPHY

Aarnes, O. J., Abdalla, S., Bidlot, J.-R., & Breivik, Ø., (2015), Marine wind and wave height trends at different ERA-Interim forecast ranges, *Journal of Climate*, *28 1*, 819–837, https://doi.org/10.1175/JCLI-D-14-00470.1

Abercromby, R., (1887), Observations on the height, length, and velocity of ocean waves, *Proceedings of the Physical Society of London (1874-1925)*, *9 1*, 150.

Abramovici, F., (1968), Diagnostic diagrams and transfer functions for oceanic waveguides, *Bulletin of the Seismological Society of America*, *58 1*, 426–456.

Accensi, M., Alday, M., Maisondieu, C., Raillard, N., Darbynian, D., Old, C., Sellar, B., Thilleul, O., Perignon, Y., Payne, G., O'Boyle, L., Fernandez, L., Dias, F., Chumbinho, R., & Guitton, G., (2021), ResourceCODE framework: a high-resolution wave parameter dataset for the european shelf and analysis toolbox, https://archimer.ifremer.fr/doc/00736/84812/

Airy, G. B., (1845), *Tides and waves*, B. Fellowes.

Alday, M., Accensi, M., Ardhuin, F., & Dodet, G., (2021), A global wave parameter database for geophysical applications. part 3: improved forcing and spectral resolution, *Ocean Modelling*, *166*, 101848, https://doi.org/https://doi.org/10.1016/j.ocemod.2021.101848

Alday, M., & Ardhuin, F., (2023), On consistent parameterizations for both dominant wind-waves and spectral tail directionality [e2022JC019581 2022JC019581], *Journal of Geophysical Research: Oceans*, *128 4*, e2022JC019581, https://doi.org/https://doi.org/10.1029/2022JC019581

Alday, M., Ardhuin, F., Dodet, G., & Accensi, M., (2022), Accuracy of numerical wave model results: application to the atlantic coasts of europe, *Ocean Science*, *18 6*, 1665–1689.

Alves, J. G. M., Wittmann, P., Sestak, M., Schauer, J., Stripling, S., Bernier, N. B., McLean, J., Chao, Y., Chawla, A., Tolman, H. L., Nelson, G., & Klotz, S., (2013), The NCEP-FNMOC combined wave ensemble product: expanding benefits of interagency probabilistic forecasts to the oceanic environment, *Bulletin of American*

Meteorological Society, *94 12*, 1893–1905, https://doi.org/http://dx.doi.org/10.1175/BAMS-D-12-00032.1

Annenkov, S. Y., & Shrira, V. I., (2018), Spectral evolution of weakly nonlinear random waves: kinetic description vs direct numerical simulations, *Journal of Fluid Mechanics*, *844*, 766–795, https://doi.org/10.1017/jfm.2018.185

Ardhuin, F., (2019), *Ocean waves in geosciences*, https://doi.org/10.13140/RG.2.2.16019.78888/9

Ardhuin, F., Chapron, B., & Collard, F., (2009), Observation of swell dissipation across oceans, *Geophysical Research Letters*, *36*, L06607, https://doi.org/10.1029/2008GL037030

Ardhuin, F., Dumas, F., Bennis, A.-C., Roland, A., Sentchev, A., Forget, P., Wolf, J., Girard, F., Osuna, P., & Benoit, M., (2012), Numerical wave modeling in conditions with strong currents: dissipation, refraction and relative wind, *Journal of Physical Oceanography*, *42*, 2101–2120.

Ardhuin, F., Gualtieri, L., & Stutzmann, E., (2019a), Physics of ambient noise generation by ocean waves, *In* N. Nakata, L. Gualtieri, & A. Fichtner (Eds.), *Ambient seismic noise* (pp. 69–107), Cambridge University Press.

Ardhuin, F., Herbers, T. H. C., Watts, K. P., van Vledder, G. P., Jensen, R., & Graber, H., (2007), Swell and slanting fetch effects on wind wave growth, *Journal of Physical Oceanography*, *374*, 908–931, https://doi.org/10.1175/JPO3039.1

Ardhuin, F., & Herbers, T. H. C., (2005), Numerical and physical diffusion: can wave prediction models resolve directional spread?, *Journal of Atmospheric and Oceanic Technology*, *227*, 886–895, https://doi.org/http://journals.ametsoc.org/doi/pdf/10.1175/JTECH1723.1

Ardhuin, F., & Jenkins, A. D., (2006), On the interaction of surface waves and upper ocean turbulence, *Journal of Physical Oceanography*, *363*, 551–557, https://doi.org/10.1175/JPO2862.1

Ardhuin, F., Lavanant, T., Obrebski, M., Marié, L., Royer, J.-Y., d'Eu, J.-F., Howe, B. M., Lukas, R., & Aucan, J., (2013), A numerical model for ocean ultra low frequency noise: wave-generated acoustic-gravity and Rayleigh modes, *J. Acoust. Soc. Amer.*, *1344*, 3242–3259.

Ardhuin, F., & Le Boyer, A., (2006), Numerical modelling of sea states: validation of spectral shapes (in French), *Navigation*, *54 216*, 55–71.

Ardhuin, F., O'Reilly, W. C., Herbers, T. H. C., & Jessen, P. F., (2003), Swell transformation across the continental shelf. part I: attenuation and directional broadening, *Journal of Physical Oceanography*, *33*, 1921–1939, https://doi.org/doi/pdf/10.1175/1520-0485%282003%29033%3C1921%3ASTATCS%3E2.0.CO%3B2

Ardhuin, F., Otero, M., Merrifield, S., Grouazel, A., & Terrill, E., (2020), Ice breakup controls dissipation of wind waves across southern ocean sea ice, *Geophysical Research Letters*, *47*, e2020GL087699, https://doi.org/10.1029/2020GL087699

Ardhuin, F., Rascle, N., Chapron, B., Gula, J., Molemaker, J., Gille, S. T., Menemenlis, D., & Rocha, C., (2017a), Small scale currents have large effects on wind wave heights, *Journal of Geophysical Research*, *122 C6*, 4500–4517, https://doi.org/10.1002/2016JC012413

Ardhuin, F., Rawat, A., & Aucan, J., (2014), A numerical model for free infragravity waves: definition and validation at regional and global scales, *Odean Modelling*, *77*, 20–32, https://doi.org/10.1016/j.ocemod.2014.02.006

Ardhuin, F., Rogers, E., Babanin, A., Filipot, J.-F., Magne, R., Roland, A., van der Westhuysen, A., Queffeulou, P., Lefevre, J.-M., Aouf, L., & Collard, F., (2010), Semi-empirical dissipation source functions for wind-wave models: part I, definition, calibration and validation, *Journal of Physical Oceanography*, *40 9*, 1917–1941, https://doi.org/10.1175/2010JPO4324.1

Ardhuin, F., & Roland, A., (2012), Coastal wave reflection, directional spreading, and seismo-acoustic noise sources, *Journal of Geophysical Research*, *117*, C00J20, https://doi.org/10.1029/2011JC007832

Ardhuin, F., Stopa, J. E., Chapron, B., Collard, F., Husson, R., Jensen, R. E., Johannessen, J., Mouche, A., Passaro, M., Quartly, G. D., Swail, V., & Young, I., (2019b), Observing sea states, *Frontiers in Marine Science*, *6*, 124, https://doi.org/10.3389/fmars.2019.00124

Ardhuin, F., Suzuki, N., McWilliams, J. C., & Aiki, N., (2017b), Comments on "a combined derivation of the integrated and vertically resolved, coupled wave-current equations", *Journal of Physical Oceanography*, *47 9*, 2377–2385, https://doi.org/10.1175/JPO-D-17-0065.1

Ardhuin, F., Tournadre, J., Queffelou, P., & Girard-Ardhuin, F., (2011), Observation and parameterization of small icebergs: drifting breakwaters in the southern ocean, *Ocean Modelling*, *39*, 405–410, https://doi.org/10.1016/j.ocemod.2011.03.004

Babanin, A. V., & Young, I. R., (2005), Two-phase behaviour of the spectral dissipation of wind waves [paper number 51], *Proceedings of the 5th International Symposium Ocean Wave Measurement and Analysis, Madrid, june 2005.*

Bai, Y., & Jin, W.-L., (2016), Chapter 5 - wave loads for ship design and classification, *In* Y. Bai & W.-L. Jin (Eds.), *Marine structural design (second edition)* (Second Edition, pp. 73–93), Butterworth-Heinemann, https://doi.org/https://doi.org/10.1016/B978-0-08-099997-5.00005-8

Baldock, T., Manoonvoravong, P., & Pham, K. S., (2010), Sediment transport and beach morphodynamics induced by free long waves, bound long waves and wave groups, *Coastal Engineering*, *57 10*, 898–916.

Ballarotta, M., Ubelmann, C., Pujol, M.-I., Taburet, G., Fournier, F., Legeais, J.-F., Faugère, Y., Delepoulle, A., Chelton, D., Dibarboure, G. et al., (2019), On the resolutions of ocean altimetry maps, *Ocean Science*, *15 4*, 1091–1109.

Banner, M. L., Jones, I. S. F., & Trinder, J. C., (1989), Wavenumber spectra of short gravity waves, *Journal of Fluid Mechanics*, *198*, 321–344.

Banner, M. L., Babanin, A. V., & Young, I. R., (2000), Breaking probability for dominant waves on the sea surface, *Journal of Physical Oceanography*, *30*, 3145–3160, https://doi.org/10.1175/1520-0485(2000)030<3145:BPFDWO>2.0.CO;2

Banner, M. L., Gemmrich, J. R., & Farmer, D. M., (2002), Multiscale measurement of ocean wave breaking probability, *Journal of Physical Oceanography*, *32*, 3364–3374, http://ams.allenpress.com/archive/1520-0485/32/12/pdf/i1520-0485-32-12-3364.pdf

Banner, M. L., & Morison, R. P., (2006), On modeling spectral dissipation due to wave breaking for ocean wind waves, *Proc. Ninth Int. Workshop on Wave Hindcasting and Forecasting*, 1–12.

Banner, M. L., & Young, I. R., (1994), Modeling spectral dissipation in the evolution of wind waves. part i: assessment of existing model performance, *Journal of Physical Oceanography*, *24 7*, 1550–1571.

Barrick, D. E., Headrick, J. M., Bogle, R. W., & Crombie, D. D., (1974), Sea backscatter at HF: interpretation and utilization of the echo, *Proceedings of the IEEE*, *62*, 673–680, https://doi.org/10.1109/PROC.1974.9507

Benoit, M., (2005), Evaluation of methods to compute the non-linear quadruplet interactions for deep-water wave spectra, *Proc. 5th Int. Symp. on Ocean Wave Measurement and Analysis (WAVES'2005)*, 3–7.

Benoit, M., & Gagnaire-Renou, E., (2007), Interactions vague-vague non-linéaires et spectre d'équilibre pour les vagues de gravité en grande profondeur d'eau, *CFM 2007-18ème Congrès Français de Mécanique*.

Benoit, M., Marcos, F., & Becq, F., (1996), Development of a third generation shallow-water wave model with unstructured spatial meshing, *Proceedings of the 25th International Conference on Coastal Engineering, Orlando*, 465–478.

Bentamy, A., Grodsky, S. A., Carton, J. A., Croizé-Fillon, D., & Chapron, B., (2012), The ERA-interim reanalysis: configuration and performance of the data assimilation system, *Journal of Geophysical Research*, *117*, C02011, https://doi.org/10.1029/2011JC007479

Bentamy, A., Grodsky, S. A., Chapron, B., & Carton, J. A., (2013), Compatibility of C- and Ku-band scatterometer winds: ERS-2 and QuikSCAT, *Journal of Marine Systems*, *117–118*, 72–80, https://doi.org/10.1016/j.jmarsys.2013.02.008

Bentamy, A., Piollé, J. F., & Prevost, C., (2018), *Product user manual for wind product WIND_GLO_WIND_L4_REP_OBSERVATIONS_012_006* (tech. rep. CMEMS-WIND-PUM-012-006), EU Copernicus Marine Service.

Bertin, X., Li, K., Roland, A., & Bidlot, J.-R., (2015), The contribution of short-waves in storm surges: two case studies in the bay of biscay, *Continental Shelf Research*, *96*, 1–15, https://doi.org/https://doi.org/10.1016/j.csr.2015.01.005

Beyramzadeh, M., & Siadatmousavi, S. M., (2022), Skill assessment of different quadruplet wave-wave interaction formulations in the wavewatch-iii model with application to the gulf of mexico, *Applied Ocean Research*, *127*, 103316, https://doi.org//10.1016/j.apor.2022.103316

Bidlot, J., (2005), *Use of Mercator surface currents in the ECMWF forecasting system* (tech. rep. Memorandum R60.9/JB/10104), Research Department, ECMWF, Reading, U. K.

Bidlot, J., Janssen, P. A. E. M., & Abdalla, S., (2005), *A revised formulation for ocean wave dissipation in CY25R1* (tech. rep. Memorandum R60.9/JB/0516), Research Department, ECMWF, Reading, U. K.

Bidlot, J., Janssen, P. A. E. M., & Abdalla, S., (2007), *A revised formulation of ocean wave dissipation and its model impact* (tech. rep. Memorandum 509), ECMWF, Reading, U. K.

Booij, N., & Holthuijsen, L. H., (1987), Propagation of ocean waves in discrete spectral wave models, *Journal of Computational Physics*, *68*, 307–326.

Booij, N., Ris, R. C., & Holthuijsen, L. H., (1999), A third-generation wave model for coastal regions. 1. model description and validation, *Journal of Geophysical Research*, *10 C4*, 7, 649–7, 666.

Boudière, E., Maisondieu, C., Ardhuin, F., Accensi, M., Pineau-Guillou, L., & Lepesqueur, J., (2013), A suitable metocean hindcast database for the design of marine energy converters, *International Journal of Marine Energy*, *28 3–4*, e40–e52.

Boussinesq, J., (1872), Théorie des ondes et des remous qui se propagent le long d'un canal rectangulaire horizontal, en communiquant au liquide contenu dans ce canal des vitesses sensiblement pareilles de la surface au fond., *Journal de mathématiques pures et appliquées*, 55–108.

Boutin, G., Ardhuin, F., Dumont, D., Sévigny, C., & Girard-Ardhuin, F., (2018), Floe size effects on wave-ice interactions: theoretical background, implementation and applications, *Journal of Geophysical Research*, *123*, 4779–4805, https://doi.org/doi.org/10.1029/2017JC013622

Brekhovskikh, L. M., Goncharov, V. V., Kurtepov, V. M., & Naugolnykh, K. A., (1973), The radiation of infrasound into the atmosphere by surface waves in the ocean, *Izvestiya, Atmospheric and Oceanic Physics*, *9*, 899–907 (In the English translation, 511–515.)

Bretherton, F. P., & Garret, C., (1970), Wavetrains in inhomogeneous moving media. *Hyperbolic equations and waves* (pp. 211–236), Springer.

Bretschneider, C. L., (1952), The generation and decay of wind waves in deep water, *Transactions American Geophysical Union*, *33 3*, 381–389.

Bretschneider, C. L., (1965), *Generation of waves by wind. state of the art* (tech. rep.), NATIONAL ENGINEERING SCIENCE CO WASHINGTON DC.

Bretschneider, C., & Reid, R., (1954), Changes in wave height due to bottom firction, percolation and refraction, *34 th Annual Meeting of American Geophisical union.*

Brown, G. 9., (1977), The average impulse response of a rough surface and its applications, *IEEE transactions on antennas and propagation*, *25 1*, 67–74.

Caldwell, J., & Williams, L., (1961), The beach erosion board's wave spectrum analyzer and its purpose, *Spectra of Ocean Waves*, 259–266.

Carrere, L., Lyard, F., Cancet, M., & Guillot, A., (2015), FES 2014, a new tidal model on the global ocean with enhanced accuracy in shallow seas and in the arctic region, *EGUGA*, 5481.

Castelle, B., Marieu, V., Bujan, S., Splinter, K. D., Robinet, A., Sénéchal, N., & Ferreira, S., (2015), Impact of the winter 2013–2014 series of severe western europe storms on a double-barred sandy coast: beach and dune erosion and megacusp embayments, *Geomorphology*, *238*, 135–148.

Cavaleri, L., Fox-Kemper, B., & Hemer, M., (2012), Wind waves in the coupled climate system, *Bulletin of the American Meteorological Society*, *78*, 1651–1661.

Cavaleri, L., & Bertotti, L., (1997), In search of the correct wind and wave fields in a minor basin, *Monthly Weather Review*, *125 8*, 1964–1975, http://ams.allenpress.com/archive/1520-0493/125/11/pdf/i1520-0493-125-8-1964.pdf

Chawla, A., & Tolman, H. L., (2008), Obstruction grids for spectral wave models, *Ocean Modelling*, *22*, 12–25.

Chawla, A., Tolman, H. L., Gerald, V., Spindler, D., Spindler, T., Alves, J.-H. G. M., Cao, D., Hanson, J. L., & Devaliere, E.-M., (2013), A multigrid wave forecasting model: a new paradigm in operational wave forecasting, *Weather and Forecasting*, *28*, 1057–1078, https://doi.org/10.1175/waf-d-12-00007.1

Chelton, D. B., Ries, J. C., Haines, B. J., Fu, L.-L., & Callahan, P. S., (2001), Satellite altimetry. *International geophysics* (pp. 1–ii), Elsevier.

Chen, G., & Belcher, S. E., (2000), Effects of long waves on wind-generated waves, *Journal of Physical Oceanography*, *30*, 2246–2256.

Chen, G., Chapron, B., Ezraty, R., & Vandemark, D., (2002), A global view of swell and wind sea climate in the ocean by satellite altimeter and scatterometer, *Journal of Atmospheric and Oceanic Technology*, *19*, 1849–1859.

Cornish, V., (1904), On the dimensions of deep-sea waves, and their relation to meteorological and geographical conditions, *Geographical Journal*, 623–645.

Cornish, V., (1910), Waves of the sea, and other water waves. with 50 photographs taken by the author.

Cox, C., & Munk, W., (1954), Measurement of the roughness of the sea surface from photographs of the sun's glitter, *Journal of the optical Society of America*, *44 11*, 838–850, https://doi.org/10.1364/josa.44.000838

Cox, C. S., & Jacobs, D. C., (1989), Cartesian diver observations of double frequency pressure fluctuations in the upper levels of the ocean, *Geophysical Research Letters*, *16 8*, 807–810.

Crombie, D. D., Hasselmann, K., & Sell, W., (1978), High-frequency radar observations of sea waves travelling in opposition to the wind, *Boundary Layer Meteorology*, *13*, 45–54.

Crosby, S. C., Cornuelle, B. D., O'Reilly, W. C., & Guza, R. T., (2017), Assimilating global wave model predictions and deep-water wave observations in nearshore swell predictions, *Journal of Atmospheric and Oceanic Technology*, *34*, 1823–1836, https://doi.org/10.1175/JTECH-D-17-0003.1

Csík, Á., Ricchiuto, M., & Deconinck, H., (2002), A conservative formulation of the multidimensional upwind residual distribution schemes for general nonlinear conservation laws, *Journal of Computational Physics*, *172 2*, 286–312.

Datawell, (2014), *Datawell - high frequency heave resonance* (tech. rep.), https://www.youtube.com/watch?v=OlrCKTnrhbQ

De Carlo, M., Ardhuin, F., & Le Pichon, A., (2020), Atmospheric infrasound radiation from ocean waves in finite depth: a unified generation theory and application to radiation patterns, *Geophysical Journal International*, *221*, 569–585, https://doi.org/10.1093/gji/ggaa015

De Carlo, M., Hupe, P., Le Pichon, A., Ceranna, L., & Ardhuin, F., (2021), Global microbarom patterns: a first confirmation of the theory for source and propagation, *Geophysical Research Letters*, *48 3*, e2020GL090163, https://doi.org/10.1029/2020GL090163

Dean, R. G., & Dalrymple, R. A., (1991), *Water wave mechanics for engineers and scientists* (second) [353 pp.], World Scientific.

Dee, D. P., Uppala, S. M., Simmons, A. J., Berrisford, P., Poli, P., Kobayashi, S., Andrae, U., Balmaseda, M. A., Balsamo, G., Bauer, P., Bechtold, P., Beljaars, A. C. M., van de Berg, L., Bidlot, J., Bormann, N., Delsol, C., Dragani, R., Fuentes, M., Geer, A. J., ... Vitart, F., (2011), The era-interim reanalysis: configuration and performance of the data assimilation system, *Quarterly Journal of the Royal Meteorological Society*, *137*, 553–597, https://doi.org/10.1002/qj.828

Delpey, M., (2012), *Etude de la dispersion horizontale en zone littorale sous l'effet de la circulation tridimensionnelle forcée par les vagues* (Doctoral dissertation), Université Européenne de Bretagne, Ecole doctorale des Sciences de la Mer, Brest, France.

Dietrich, J. C., Westerink, J. J., Kennedy, A. B., Smith, J. M., Jensen, R. E., Zijlema, M., Holthuijsen, L. H., Dawson, C., Luettich, R. A., Powell, M. D., Cardone, V. J., Cox,

A. T., Stone, G. W., Pourtaheri, H., Hope, M. E., Tanaka, S., Westerink, L. G., Westerink, H. J., & Cobell, Z., (2011), Hurricane gustav (2008) waves and storm surge: hindcast, synoptic analysis, and validation in southern louisiana, *Monthly Weather Review*, *139*, 2488–2522.

Doble, M. J., & Bidlot, J.-R., (2013), Wave buoy measurements at the Antarctic sea ice edge compared with an enhanced ECMWF WAM: progress towards global waves-in-ice modelling, *Ocean Modelling*, *70*, 166–173, https://doi.org/10.1016/j.ocemod.2013.05.012

Doble, M. J., Coon, M. D., & Wadhams, P., (2003), Pancake ice formation in the weddell sea, *Journal of Geophysical Research*, *108 C7*, 3209, https://doi.org/doi.org/10.1029/2002JC001373

Dobler, D., Huck, T., Maes, C., Grima, N., Blanke, B., Martinez, E., & Ardhuin, F., (2019), Large impact of stokes drift on the fate of surface floating debris in the south indian basin, *Marine Pollution Bulletin*, *148*, 202–209, https://doi.org/j.marpolbul.2019.07.057

Dodet, G., Abdalla, S., Alday, M., Accensi, M., Bidlot, J., & Ardhuin, F., (2022), Error characterization of significant wave heights in multidecadal satellite altimeter product, model hindcast, and in situ measurements using the triple collocation technique [Dataset], *Journal of Atmospheric and Oceanic Technology*, *39*, 887–901, https://doi.org/10.1175/JTECH-D-21-0179.1

Dodet, G., Piolle, J.-F., Quilfen, Y., Abdalla, S., Accensi, M., Ardhuin, F., Ash, E., Bidlot, J.-R., Gommenginger, C., Marechal, G., Passaro, M., Quartly, G., Stopa, J., Timmermans, B., Young, I., Cipollini, P., & Donlon, C., (2020), The sea state cci dataset v1: towards a sea state climate data record based on satellite observations, *Earth System Science Data*, *12*, 1929–1951, https://doi.org/10.5194/essd-12-1929-2020

Donelan, M. A., Curcic, M., Chen, S. S., & Magnusson, A. K., (2012), Modeling waves and wind stress, *Journal of Geophysical Research*, *117*, C00J23, https://doi.org/10.1029/2011JC007787

Donelan, M. A., Hamilton, J., & Hui, W. H., (1985), Directional spectra of wind-generated waves, *Philosophical Transactions of the Royal Society of London A*, *315*, 509–562.

Donelan, M. A., (2001), A nonlinear dissipation function due to wave breaking, *Proceedings of ECMWF workshop on ocean wave forecasting, 2–4 July*, 87–94.

Duennebier, F. K., Lukas, R., Nosal, E.-M., Aucan, J., & Weller, R. A., (2012), Wind, waves, and acoustic background levels at station ALOHA, *Journal of Geophysical Research*, *117*, C03017, https://doi.org/10.1029/2011JC007267

Dulov, V. A., & Kosnik, M. V., (2009), Effects of three-wave interactions in the gravity-capillary range of wind waves, *Izvestiya, Atmospheric and Oceanic Physics*, *45 3*, 380–391.

Duncan, J. H., (1981), An experimental investigation of breaking waves produced by a towed hydrofoil, *Proceedings of the Royal Society of London. Series A*, *377*, 331–348.

Echevarria, E. R., Hemer, M. A., & Holbrook, N. J., (2021), Global implications of surface current modulation of the wind-wave field, *Ocean Modelling*, *161*, 101792.

ECMWF, (2019), *IFS documentation cy46r1. part vii: ecmwf wave model* (Tech. Note No. 333), https://www.ecmwf.int/node/19311

Edson, J. B., Jampana, V., Weller, R. A., Bigorre, S. P., Plueddemann, A. J., Fairall, C. W., Miller, S. D., Mahrt, L., Vickers, D., & Hersbach, H., (2013), On the exchange of momentum over the open ocean, *Journal of Physical Oceanography*, *43*, 1589–1610, https://doi.org/10.1175/JPO-D-12-0173.1

Elfouhaily, T., Chapron, B., Katsaros, K., & Vandemark, D., (1997), A unified directional spectrum for long and short wind-driven waves, *Journal of Geophysical Research*, *102 C7*, 15781–15796, https://doi.org/10.1029/97jc00467

Elipot, S., Lumpkin, R., Perez, R. C., Lilly, J. M., Early, J. J., & Sykulski, A. M., (2016), A global surface drifter data set at hourly resolution, *Journal of Geophysical Research*, *121*, 2937–2966, https://doi.org/10.1002/2016JC011716

ESA, (2019), *Report for mission selection: SKIM* (tech. rep. ESA-EOPSM-SKIM-RP-3550), European Space Agency, Noordwijk, The Netherlands, https://doi.org/10.13140/RG.2.2.22907.98081/3

Ewans, K. C., (1998), Observations of the directional spectrum of fetch-limited waves, *Journal of Physical Oceanography*, *28*, 495–512, http://ams.allenpress.com/archive/1520-0485/28/3/pdf/i1520-0485-28-4-495.pdf

Fabrikant, A. L., (1976), Quasilinear theory of wind-wave generation, *Izvestiya, Atmospheric and Oceanic Physics*, *12*, 524–526.

Farrell, W. E., & Munk, W., (2008), What do deep sea pressure fluctuations tell about short surface waves?, *Geophysical Research Letters*, *35 7*, L19605, https://doi.org/10.1029/2008GL035008

Farrell, W. E., & Munk, W., (2010), Booms and busts in the deep, *Journal of Physical Oceanography*, *40 9*, 2159–2169.

Farrell, W. E., & Munk, W., (2013), Surface gravity waves and their acoustic signatures, 1-30 hz, on the mid-Pacific sea floor, *J. Acoust. Soc. Amer.*, *134 4*, 3161–3173.

Feddersen, F., & Veron, F., (2005), Wind effects on shoaling wave shape, *Journal of Physical Oceanography*, *35*, 1223–1228.

Filipot, J.-F., & Ardhuin, F., (2012), A unified spectral parameterization for wave breaking: from the deep ocean to the surf zone, *Journal of Geophysical Research*, *117*, C00J08, https://doi.org/10.1029/2011JC007784

Franz, G., Delpey, M. T., Brito, D., Pinto, L., Leitão, P., & Neves, R., (2017), Modelling of sediment transport and morphological evolution under the combined action of waves and currents, *Ocean Science*, *13 5*, 673–690.

Frappart, F., Blumstein, D., Cazenave, A., Ramillien, G., Birol, F., Morrow, R., & Rémy, F., (1999), Satellite altimetry: principles and applications in earth sciences, *Wiley Encyclopedia of Electrical and Electronics Engineering*, 1–25.

Fraser, C. I., Morrison, A. K., Hogg, A. M., Macaya, E. C., van Sebille, E., Ryan, P. G., Padovan, A., Jack, C., Valdivia, N., & Waters, J. M., (2018), Antarctica's ecological isolation will be broken by storm-driven dispersal and warming, *Nature Climate Change*, *8*, 704–708, https://doi.org/10.1038/s41558-018-0209-7

Gagnaire-Renou, E., Benoit, M., & Forget, P., (2010), Ocean wave spectrum properties as derived from quasi-exact computations of nonlinear wave-wave interactions, *Journal of Geophysical Research*, *115*, C12058, https://doi.org/10.1029/2009JC005665

Gagnaire-Renou, E., (2010), *Amelioration de la modelisation spectrale des etats de mer par un calcul quasi-exact des interactions non-lineaires vague-vague* (Doctoral dissertation), Université du Sud Toulon Var.

García-Medina, G., Yang, Z., Wu, W.-C., & Wang, T., (2021), Wave resource characterization at regional and nearshore scales for the us alaska coast based on a 32-year high-resolution hindcast, *Renewable Energy*, *170*, 595–612.

Gautier, C., & Caires, S., (2015), Operational wave forecasts in the southern north sea, *36th IAHR World Congress, 28th June–3 July*, *1*, 5.

Gelaro, R., McCarty, W., Suárez, M. J., Todling, R., Molod, A., Takacs, L., Randles, C. A., Darmenov, A., Bosilovich, M. G., Reichle, R. et al., (2017), The modern-era retrospective analysis for research and applications, version 2 (merra-2), *Journal of climate*, *30 14*, 5419–5454.

Gelci, R., (1957), Prévision de la houle. la méthode des densités spectroangulaires, *Bull. Inform. Comité Central Oceanogr. d'Etude Côtes*, *9*, 416–435.

Girard-Ardhuin, F., & Ezraty, R., (2012), Enhanced arctic sea ice drift estimation merging radiometer and scatterometer data, *IEEE Transactions on Geoscience and Remote Sensing*, *50*, 2639–2648.

Grant, W. D., & Madsen, O. S., (1979), Combined wave and current interaction with a rough bottom, *Journal of Geophysical Research*, *84*, 1797–1808.

Guimarães, P. V., Ardhuin, F., Bergamasco, F., Leckler, F., Filipot, J.-F., Shim, J.-S., Dulov, V., & Benetazzo, A., (2020), A data set of sea surface stereo images to resolve space-time wave fields, *Scientific Data*, *7*, 145, https://doi.org/10.1038/s41597-020-0492-95

Hanafin, J., Quilfen, Y., Ardhuin, F., Sienkiewicz, J., Queffeulou, P., Obrebski, M., Chapron, B., Reul, N., Collard, F., Corman, D., de Azevedo, E. B., Vandemark, D., & Stutzmann, E., (2012), Phenomenal sea states and swell radiation: a comprehensive analysis of the 12-16 February 2011 North Atlantic storms, *Bulletin of the American Meteorological Society*, *93*, 1825–1832, https://doi.org/10.1175/BAMS-D-11-00128.1

Hasselmann, K., (1962), On the non-linear energy transfer in a gravity wave spectrum, part 1: general theory, *Journal of Fluid Mechanics*, *12*, 481–501.

Hasselmann, K., Barnett, T. P., Bouws, E., Carlson, H., Cartwright, D. E., Enke, K., Ewing, J. A., Gienapp, H., Hasselmann, D. E., Kruseman, P., Meerburg, A., Müller, P., Olbers, D. J., Richter, K., Sell, W., & Walden, H., (1973), Measurements of wind-wave growth and swell decay during the Joint North Sea Wave Project [Suppl. A], *Deutsche Hydrographische Zeitschrift*, *8 12*, 1–95.

Hasselmann, K., (1963a), On the non-linear energy transfer in a gravity-wave spectrum. part 3. evaluation of the energy flux and swell-sea interaction for a neumann spectrum, *Journal of Fluid Mechanics*, *15 3*, 385–398.

Hasselmann, K., (1963b), A statistical analysis of the generation of microseisms, *Reviews of Geophysics*, *1 2*, 177–210.

Hasselmann, K., (1974), On the spectral dissipation of ocean waves due to white capping, *Boundary Layer Meteorology*, *6*, 107–127.

Hasselmann, S., & Hasselmann, K., (1981), A symmetrical method of computing the nonlinear transfer in a gravity wave spectrum.

Hasselmann, S., Hasselmann, K., Allender, J. H., & Barnett, T. P., (1985), Computation and parameterizations of the nonlinear energy transfer in a gravity-wave spectrum. Part II: Parameterizations of the nonlinear energy transfer for application in wave models, *Journal of Physical Oceanography*, *15*, 1378–1391, https://doi.org/https://doi.org/10.1175/1520-0485(1985)015<1378:CAPOTN>2.0.CO;2

Hasselmann, S., & Hasselmann, K., (1985), Computations and parameterizations of the nonlinear energy transfer in a gravity-wave spectrum. part i: a new method for efficient computations of the exact nonlinear transfer integral, *Journal of Physical Oceanography*, *15 11*, 1369–1377.

Hersbach, H., Bell, B., Berrisford, P., Hirahara, S., Horányi, A., Muñoz-Sabater, J., Nicolas, J., Peubey, C., Radu, R., Schepers, D., Simmons, A., Soci, C., Abdalla, S., Abellan, X., Balsamo, G., Bechtold, P., Biavati, G., Bidlot, J., Bonavita, M., ... Thépaut, J.-N., (2020), The ERA5 global reanalysis, *Quarterly Journal of the Royal Meteorological Society*, *146*, 1999–2049, https://doi.org/10.1002/qj.3803

Hersbach, H., & Bidlot, J.-R., (2008), The relevance of ocean surface current in the ecmwf analysis and forecast system, *Proc. ECMWF Workshop on Atmosphere-Ocean Interaction*, *6173*.

Herterich, K., & Hasselmann, K., (1980), A similarity relation for the non-linear energy transfer in a finite-depth gravity-wave spectrum, *Journal of Fluid Mechanics*, *97*, 215–224.

Hoeke, R. K., McInnesa, K. L., Kruger, J. C., McNaught, R. J., Hunter, J. R., & Smithers, S. G., (2013), Widespread inundation of Pacific islands triggered by distant-source wind-waves, *Global and Planetary Change*, *108*, 128–138, https://doi.org/10.1016/j.gloplacha.2013.06.006

Huber, P. J., (2004), Robust statistics. vol. 523.

Janssen, P. A. E. M., (1991), Quasi-linear theory of wind wave generation applied to wave forecasting, *Journal of Physical Oceanography*, *21*, 1631–1642, https://doi.org/http://journals.ametsoc.org/doi/pdf/10.1175/1520-0485%281991%29021%3C1631%3AQLTOWW%3E2.0.CO%3B2

Janssen, P. A. E. M., & Bidlot, J.-R., (2022), Wind-wave interaction for strong winds, *Journal of Physical Oceanography*, https://doi.org/https://doi.org/10.1175/JPO-D-21-0293.1

Janssen, P. A. E. M., & Bidlot, J.-R., (2023), Wind–wave interaction for strong winds, *Journal of Physical Oceanography*, *53 3*, 779–804, https://doi.org/https://doi.org/10.1175/JPO-D-21-0293.1

Janssen, P. A. E. M., Lionello, P., Feistad, M., & Hollingsworth, A., (1992), Hindcasts and data assimilation studies with the wam model during the seasat period, *Journal of Geophysical Research*, *94*, 973–993.

Kantha, L., (2006), A note on the decay rate of swell, *Ocean Modelling*, *11*, 67–173.

Kirincich, A., (2016), Remote sensing of the surface wind field over the coastal ocean via direct calibration of HF radar backscatter power, *Journal of Atmospheric and Oceanic Technology*, *33 7*, 1377–1392, https://doi.org/10.1175//JTECH-D-15-0242.1

Kleiss, J. M., & Melville, W. K., (2011), The analysis of sea surface imagery for whitecap kinematics, *Journal of Atmospheric and Oceanic Technology*, *28*, 219–243.

Komen, G. J., Hasselmann, K., & Hasselmann, S., (1984), On the existence of a fully developed windsea spectrum, *Journal of Physical Oceanography*, *14*, 1271–1285, http://ams.allenpress.com/archive/1520-0485/14/8/pdf/i1520-0485-14-8-1271.pdf

Kudryavtsev, V., Hauser, D., Caudal, G., & Chapron, B., (2003), A semiempirical model of the normalized radar cross-section of the sea surface 2. radar modulation transfer function, *Journal of Geophysical Research*, *108 C3*, 8055, https://doi.org/10.1029/2001JCOO1004

Kuik, A. J., van Vledder, G. P., & Holthuijsen, L. H., (1988), A method for the routine analysis of pitch-and-roll buoy wave data, *Journal of physical oceanography*, *18*, 1020–1034, https://doi.org/https://doi.org/10.1175/1520-0485(1987)017<0845:TROWDT>2.0.CO;2

Lamb, H., (1945), Hydrodynamics, ed. 6-th, *NY Dover publ*, *194 5*.

Lavrenov, I. V., (2001), Effect of wind wave parameter fluctuation on the nonlinear spectrum evolution, *Journal of Physical Oceanography*, *31*, 861–873, http://ams.allenpress.com/archive/1520-0485/31/4/pdf/i1520-0485-31-4-861

Lavrenov, I. V., & Ocampo-Torres, F. J., (1999), Angular distribution effect on weakly nonlinear energy transfer in the spectrum of wind waves, *Izvestiya, Atmospheric and Oceanic Physics*, *35*, 278–290.

Lazure, P., & Dumas, F., (2008), An external-internal mode cou- pling for a 3d hydrodynamical model for applications at regional scale (MARS)., *Advances in Water Resources*, *31*, 233–250.

Le Cann, B., (1990), Barotropic tidal dynamics of the bay of biscay shelf: observations, numerical modelling and physical interpretation, *Continental Shelf Research*, *10 8*, 723–758, https://doi.org/https://doi.org/10.1016/0278-4343(90)90008-A

Leckler, F., (2013), *Observation et modélisation du déferlement des vagues* (Doctoral dissertation), Université Européenne de Bretagne, Ecole doctorale des Sciences de la Mer, Brest, France, http://tinyurl.com/leckler-thesis

Leckler, F., Ardhuin, F., Filipot, J.-F., & Mironov, A., (2013), Dissipation source terms and whitecap statistics, *Ocean Modelling*, *70 9*, 62–74.

Leckler, F., Ardhuin, F., Peureux, C., Benetazzo, A., Bergamasco, F., & Dulov, V., (2015), Analysis and interpretation of frequency-wavenumber spectra of young wind waves, *Journal of Physical Oceanography*, *45*, 2484–2496, https://doi.org/10.1175/JPO-D-14-0237.1

Lecocq, T., Ardhuin, F., Collin, F., & Camelbeeck, T., (2019), On the extraction of microseismic groundmotion from analog seismograms for the validation of ocean-climate models, *Seismol. Res. Lett.*, *91*, 1518–1530, https://doi.org/10.1785/0220190276

Lenain, L., & Melville, W. K., (2017), Measurements of the directional spectrum across the equilibrium saturation ranges of wind-generated surface waves, *Journal of Physical Oceanography*, *47*, 2123–2138, https://doi.org/10.1175/jpo-d-17-0017.1

Leonard, B. P., (1991), The ULTIMATE conservative difference scheme applied to unsteady one-dimensional advection, *Computational Methods in Applied Mechanical Engineering*, *88*, 17–74.

Long, C. E., & Resio, D. T., (2007), Wind wave spectral observations in Currituck Sound, North Carolina, *Journal of Geophysical Research*, *112*, C05001, https://doi.org/10.1029/2006JC003835

Longuet-Higgins, M. S., (1950), A theory of the origin of microseisms, *Philosophical Transactions of the Royal Society of London A*, *243*, 1–35.

Longuet-Higgins, M. S., (1952), On the statistical distributions of sea waves, *Journal of Marine Research*, *11 3*, 245–265.

Longuet-Higgins, M. S., Cartwright, D. E., & Smith, N. D., (1963), Observations of the directional spectrum of sea waves using the motions of a floating buoy, *Ocean Wave Spectra, proceedings of a conference, Easton, Maryland*, 111–136.

Longuet-Higgins, M. S., & Cleaver, R. P., (1994), Crest instabilities of gravity waves. Part 1. The almost-highest wave, *Journal of Fluid Mechanics*, *258*, 115–129.

Longuet-Higgins, M. S., & Stewart, R. W., (1960), Changes in the form of short gravity waves on long waves and tidal currents, *Journal of Fluid Mechanics*, *8*, 565–583.

Lumpkin, R., Özgökmen, T., & Centurioni, L., (2017), Advances in the application of surface drifters, *Annual Review of Marine Science*, *9*, 6.1–6.23, https://doi.org/10.1146/annurev-marine-010816-060641

Marechal, G., & Ardhuin, F., (2021), Surface currents and significant wave height gradients: matching numerical models and high-resolution altimeter wave heights in the agulhas current region, *Journal of Geophysical Research: Oceans*, *126 2*, e2020JC016564, https://doi.org/10.1002/essoar.10505343.1

Masselink, G., Castelle, B., Dodet, T. S. G., Suanez, S., Jackson, D., & Floc'h, F., (2015), Extreme wave activity during 2013/2014 winter and morphological impacts along the Atlantic coast of Europe, *Geophysical Research Letters*, *93*, 2135–2143, https://doi.org/10.1002/2015GL067492

Masselink, G., Scott, T., Poate, T., Russell, P., Davidson, M., & Conley, D., (2016), The extreme 2013/2014 winter storms: hydrodynamic forcing and coastal response along the southwest coast of england, *Earth Surface Processes and Landforms*, *41 3*, 378–391.

McConathy, D. R., & Kilgus, C. C., (1987), The navy geosat mission: an overview, *Johns Hopkins APL technical digest*, *8 2*, 170–175.

McGoldrick, L. F., Phillips, O. M., Huang, N. E., & Hodgson, T. H., (1966), Measurements of third-order wave interactions, *Journal of Fluid Mechanics*, *25*, 437–456.

Mentaschi, L., Besio, G., Cassola, F., & Mazzino, A., (2015), Performance evaluation of WAVEWATCH III in the mediterranean sea, *Ocean Modelling*, *90*, 82–94, https://doi.org/10.1016/j.ocemod.2015.04.003

Miche, A., (1944), Mouvements ondulatoires de la mer en profondeur croissante ou décroissante. forme limite de la houle lors de son déferlement. application aux digues maritimes. deuxième partie. mouvements ondulatoires périodiques en profondeur régulièrement décroissante, *Annales des Ponts et Chaussées*, *Tome 114*, 131–164,

270–292, http://patrimoine.enpc.fr/document/ENPC02_PER_P_277_1944?find_page=369

Morrow, R., Fu, L.-L., Ardhuin, F., Benkiran, M., Chapron, B., Cosme, E., d'Ovidio, F., Farrar, J. T., Gille, S. T., Lapeyre, G. et al., (2019), Global observations of fine-scale ocean surface topography with the surface water and ocean topography (swot) mission, *Frontiers in Marine Science*, *6*, 232.

Mulet, S., Rio, M.-H., Etienne, H., Artana, C., Cancet, M., Dibarboure, G., Feng, H., Husson, R., Picot, N., Provost, C. et al., (2021), The new CNES-CLS18 global mean dynamic topography, *Ocean Science*, *173*, 789–808, https://doi.org/10.5194/os-2020-117

Munk, W., (1949), Surf beat, *Eos Transactions American Geophysical Union*, *30*, 849–854.

Munk, W., (2009), An inconvenient sea truth: spread, steepness, and skewness of surface slopes, *Annual Review of Marine Science*, *1*, 377–415, https://doi.org/n10.1146/annurev.marine.010908.163940

Nishida, K., & Takagi, R., (2016), Teleseismic S wave microseisms, *Science*, *353*, 919–921, https://doi.org/10.1126/science.aaf7573

Nouguier, F., Mouche, A., Rascle, N., Chapron, B., & Vandemark, D., (2016), Analysis of dual-frequency ocean backscatter measurements at Ku- and Ka-bands using near-nadir incidence GPM radar data, *IEEE Geoscience And Remote Sensing Letters*, *31*, 2023–2245, https://doi.org/10.1109/LGRS.2016.2583198

Onink, V., Wichmann, D., Delandmeter, P., & van Sebille, E., (2019), The role of ekman currents, geostrophy and stokes drift in the accumulation of floating microplastic, *Journal of Geophysical Research*, *124*, 1474–1490, https://doi.org/10.1029/2018JC014547

O'Reilly, W. C., Herbers, T. H. C., Seymour, R. J., & Guza, R. T., (1996), A comparison of directional buoy and fixed platform measurements of Pacific swell, *Journal of Atmospheric and Oceanic Technology*, *13*, 231–238.

Passaro, M., Hemer, M. A., Quartly, G. D., Schwatke, C., Dettmering, D., & Seitz, F., (2021), Global coastal attenuation of wind-waves observed with radar altimetry, *Nature Communications*, *121*, 1–13.

Perignon, Y., Ardhuin, F., Cathelain, M., & Robert, M., (2014), Swell dissipation by induced atmospheric shear stress, *Journal of Geophysical Research*, *119*, 6622–6630, https://doi.org/10.1002/2014JC009896

Pettersson, H., Kahma, K. K., & Tuomi, L., (2010), Wave directions in a narrow bay, *Journal of Physical Oceanography*, *40*, 155–169, http://journals.ametsoc.org/doi/pdf/10.1175/2009JPO4220.1

Peureux, C., & Ardhuin, F., (2016), Ocean bottom pressure records from the cascadia array and short surface gravity waves, *Journal of Geophysical Research*, *121*, 2862–2873, https://doi.org/10.1002/2015JC011580

Peureux, C., Ardhuin, F., & Veras Guimarães, P., (2021), On the unsteady steepening of short gravity waves near the crests of longer waves in the absence of generation or dissipation, *Journal of Geophysical Research: Oceans*, *126 1*, e2020JC016735, https://doi.org/doi/abs/10.1029/2020JC016735

Peureux, C., Benetazzo, A., & Ardhuin, F., (2018), Note on the directional properties of meter-scale gravity waves, *Ocean Science*, *14*, 41–52, https://doi.org/10.5194/os-14-41-2018

Phillips, O. M., (1958), The equilibrium range in the spectrum of wind-generated waves, *Journal of Fluid Mechanics*, *4*, 426–433.

Phillips, O. M., (1960), On the dynamics of unsteady gravity waves of finite amplitude, *Journal of Fluid Mechanics*, *9*, 193–217.

Phillips, O. M., (1984), On the response of short ocean wave components at a fixed wavenumber to ocean current variations, *Journal of Physical Oceanography*, *14*, 1425–1433, https://doi.org/10.1175/1520-0485(1984)014<1425:OTROSO>2.0.CO;2

Phillips, O. M., (1985), Spectral and statistical properties of the equilibrium range in wind-generated gravity waves, *Journal of Fluid Mechanics*, *156*, 505–531.

Pierson, W. J., Neumann, G., & James, R., (1955a), Observing and forecasting ocean waves by means of wave spectra and statistics, hydrog, *O/rice Publ*, *603*, 180.

Pierson, W. J., Neumann, G., & James, R. W., (1955b), Practical methods for observing and forecasting ocean waves by means of wave spectra and statistics, U. S. Hydrographic Office.

Pineau-Guillou, L., Ardhuin, F., Bouin, M.-N., Redelsperger, J.-L., Chapron, B., Bidlot, J., & Quilfen, Y., (2018), Strong winds in a coupled wave-atmosphere model during a north Atlantic storm event: evaluation against observations, *Quarterly Journal of the Royal Meteorological Society*, *144*, 317–332, https://doi.org/10.1002/qj.3205

Pineau-Guillou, L., (2013), *PREVIMER. validation des atlas de composantes harmoniques de hauteurs et courants de marée* (tech. rep.).

Piollé, J., Dodet, G., Quilfen, Y., Initiative, E. S. S. C. C. et al., (2020), Global remote sensing multi-mission along-track significant wave height, l2p product, version 1.1, centre for environmental data analysis.

Ponce de León, S., & Guedes Soares, C., (2015), Hindcast of the hércules winter storm in the North Atlantic, *Natural Hazards*, *78 3*, 1883–1897.

Quilfen, Y., & Chapron, B., (2019), Ocean surface wave-current signatures from satellite altimeter measurements, *Geophysical Research Letters*, *216*, 253–261, https://doi.org/10.1029/2018GL081029

Quilfen, Y., & Chapron, B., (2021), On denoising satellite altimeter measurements for high-resolution geophysical signal analysis [25 Years of Progress in Radar Altimetry], *Advances in Space Research*, *68 2*, 875–891, https://doi.org/https://doi.org/10.1016/j.asr.2020.01.005

Quilfen, Y., Chapron, B., & Vandemark, D., (2004), The ERS scatterometer wind measurement accuracy: evidence of seasonal and regional biases, *Journal of Atmospheric and Oceanic Technology*, *18*, 1684–1697.

Rapizo, H., Durrant, T. H., & Babanin, A. V., (2018), Current-induced dissipation in spectral wave models, *Ocean Dynamics*, *68*, 939–955, https://doi.org/10.1007/s10236-018-1171-7

Rascle, N., & Ardhuin, F., (2013), A global wave parameter database for geophysical applications. part 2: model validation with improved source term parameterization, *Ocean Modelling*, *70*, 174–188, https://doi.org/10.1016/j.ocemod.2012.12.001

Rascle, N., Ardhuin, F., Queffeulou, P., & Croizé-Fillon, D., (2008), A global wave parameter database for geophysical applications. part 1: wave-current-turbulence interaction parameters for the open ocean based on traditional parameterizations, *Ocean Modelling*, *25*, 154–171, https://doi.org/10.1016/j.ocemod.2008.07.006

Renault, L., Molemaker, M. J., McWilliams, J. C., Shchepetkin, A. F., Lemarié, F., Chelton, D., Illig, S., & Hall, A., (2016), Modulation of wind work by oceanic current interaction with the atmosphere, *Journal of Physical Oceanography*, *46*, 1685–1704, https://doi.org/10.1175/JPO-D-15-0232.1

Resio, D. T., & Perrie, W., (1991), A numerical study of nonlinear energy fluxes due to wave-wave interactions part 1. methodology and basic results, *Journal of Fluid Mechanics*, *223*, 603–629.

Resio, D. T., Vincent, L., & Ardag, D., (2016), Characteristics of directional wave spectra and implications for detailed-balance wave modeling, *Ocean Modelling*, *103*, 38–52.

Retailleau, L., Boué, P., Stehly, L., & Campillo, M., (2017), Locating microseism sources using spurious arrivals in intercontinental noise correlations, *Journal of Geophysical Research*, *122*, 8107–8120, https://doi.org/10.1002/2017JB014593

Rio, M.-H., Mulet, S., & Picot, N., (2014), Beyond GOCE for the ocean circulation estimate: synergetic use of altimetry, gravimetry, and in situ data provides new insight into geostrophic and Ekman currents, *Geophysical Research Letters*, *41*, 8918–8925, https://doi.org/10.1002/2014GL061773

Rivas, M. B., & Stoffelen, A., (2019), Characterizing ERA-Interim and ERA5 surface wind biases using ASCAT, *Ocean Science*, *15*, 831–852, https://doi.org/10.5194/os-15-831-2019

Roarty, H., Cook, T., Hazard, L., George, D., Harlan, J., Cosoli, S., Wyatt, L., Fanjul, E. A., Terrill, E., Otero, M., Largier, J., Glenn, S., Ebuchi, N., Whitehouse, B., Bartlett, K., Mader, J., Rubio, A., Corgnati, L., Mantovani, C., ... Grilli, S., (2019), The global high frequency radar network, *Frontiers in Marine Science*, *6*, 164:1–164:23, https://doi.org/10.3389/fmars.2019.00164

Rogers, W. E., Babanin, A. V., & Wang, D. W., (2010), Observation-consistent input and whitecapping dissipation in a model for wind-generated surface waves: description and simple calculations, *Journal of Atmospheric and Oceanic Technology*, *29*, 1329–1346.

Roland, A., (2008), *Development of WWM II: spectral wave modelling on unstructured meshes* (Doctoral dissertation), Technische Universität Darmstadt, Institute of Hydraulic and Water Resources Engineering.

Roland, A., & Ardhuin, F., (2014), On the developments of spectral wave models: numerics and parameterizations for the coastal ocean, *Ocean Dynamics*, *64 6*, 833–846, https://doi.org/10.1007/s10236-014-0711-z

Romero, L., (2019), Distribution of surface wave breaking fronts, *Geophysical Research Letters*, *46*, 10463–10474, https://doi.org//10.1029/2019GL083408

Romero, L., Lenain, L., & Melville, W. K., (2017), Observations of surface wave–current interaction, *Journal of Physical Oceanography*, *47*, 615–632, https://doi.org/10.1175/JPO-D-16-0108.1

Romero, L., & Lubana, K., (2022), On the bimodality of the wind-wave spectrum: mean-squared-slopes and azimuthal overlap integral, *Journal of Physical Oceanography*, *52*, 1549–1562, https://doi.org/10.1175/JPO-D-21-0299.1.8

Ryabkova, M., Karaev, V., Guo, J., & Titchenko, Y., (2019), A review of wave spectrum models as applied to the problem of radar probing of the sea surface, *Journal of Geophysical Research*, *124*, 71047134, https://doi.org/10.1029/2018JC014804

Saha, S., Moorthi, S., Pan, H.-L., Wu, X., Wang, J., Nadiga, S., Tripp, P., Kistler, R., Woollen, J., Behringer, D., Liu, H., Stokes, D., Grumbine, R., Gayno, G., Wang, J., Hou, Y.-T., Chuang, H.-y., Juang, H.-M. H. a. J. S., Iredell, M., ... Goldberg, M., (2010), The NCEP Climate Forecast System Reanalysis, *Bulletin of the American Meteorological Society*, *91*, 1015–1057.

Salmon, J. E., Holthuijsen, L. H., Zijlema, M., van Vledder, G. P., & Pietrzak, J. D., (2015), Scaling depth-induced wave-breaking in two-dimensional spectral wave models, *Ocean Modelling*, *87*, 30–47, https://doi.org/10.1016/j.ocemod.2014.12.011

Samaras, A. G., Gaeta, M. G., Miquel, A. M., & Archetti, R., (2016), High-resolution wave and hydrodynamics modelling in coastal areas: operational applications for coastal planning, decision support and assessment, *Natural hazards and earth system sciences*, *16 6*, 1499–1518.

Schlembach, F., Passaro, M., Quartly, G. D., Kurekin, A., Nencioli, F., Dodet, G., Piollé, J.-F., Ardhuin, F., Bidlot, J., Schwatke, C., Seitz, F., Cipollini, P., & Donlon, C., (2020), Round robin assessment of radar altimeter low resolution mode and delay-doppler retracking algorithms for significant wave height, *Remote Sensing*, *12 8*, https://doi.org/10.3390/rs12081254

Schott, G., (1893), *Wissenschaftliche ergebnisse einer forschungsreise zur see, ausgeführt in den jahren 1891 und 1892*, J. Perthes.

Shapiro, B., (1988), The geosat orbit adjust, *Journal of the Astronautical Sciences*, *36*, 407–424.

Sharmar, V., Markina, M. Y., & Gulev, S., (2021), Global ocean wind-wave model hindcasts forced by different reanalyzes: a comparative assessment, *Journal of Geophysical Research: Oceans*, *126*, https://doi.org/10.1029/2020JC01671

Smith, W. H. F., & Scharroo, R., (2015), Waveform aliasing in satellite radar altimetry, *IEEE Transactions on Geoscience and Remote Sensing*, *53*, 1671–1682, https://doi.org/10.1109/TGRS.2014.2331193

Soloviev, A. V., Lukas, R., Donelan, M. A., Haus, B. K., & Ginis, I., (2014), The air-sea interface and surface stress under tropical cyclones, *Scientific Reports*, *4*, 5306, https://doi.org/10.1038/srep05306

Stokes, G. G., (1847), On the theory of oscillatory waves, *Trans. Camb. Phil. Soc.*, *8*, 411–455.

Stopa, J. E., Ardhuin, F., Bababin, A., & Zieger, S., (2016a), Comparison and validation of physical wave parameterizations in spectral wave models, *Ocean Modelling*, *103*, 2–17, https://doi.org/10.1016/j.ocemod.2015.09.003

Stopa, J. E., Ardhuin, F., & Girard-Ardhuin, F., (2016b), Wave climate in the Arctic 1992-2014: seasonality and trends, *The Cryosphere*, *10*, 1605–1629, https://doi.org/10.5194/tc-10-1605-2016

Stopa, J. E., Ardhuin, F., Stutzmann, E., & Lecocq, T., (2019), Sea state trends and variability: consistency between models, altimeters, buoys, and seismic data (1979-2016), *Journal of Geophysical Research*, *124*, 3923–3940, https://doi.org/10.1029/2018JC014607

Stutzmann, E., Schimmel, M., & Ardhuin, F., (2012), Modeling long-term seismic noise in various environments, *Geophysical Journal International*, *191*, 707–722, https://doi.org/10.1111/j.1365-246X.2012.05638.x

Sutherland, P., & Melville, W. K., (2013), Field measurements and scaling of ocean surface wave-breaking statistics, *Geophysical Research Letters*, *40*, 3074–3079, https://doi.org/10.1002/grl.50584

Suthons, C., (1945), *The forecasting of sea and swell waves*, Naval Meteorological Branch, Hydrographic Department.

Sverdrup, H. U., & Munk, W., (1946), Empirical and theoretical relations between wind, sea, and swell, *Eos, Transactions American Geophysical Union*, *276*, 823–827.

Sverdrup, H. U., & Munk, W., (1947), *Wind, sea, and swell: theory of relations for forecasting* (tech. rep. No. 601), U. S. Hydrographic Office.

Swail, V., Jensen, R., Lee, B., Turton, J., Thomas, J., Gulev, S., Yelland, M., Etala, P., Meldrum, D., Birkemeier, W., Burnett, W., & Warren, G., (2009), Wave measurements, needs and developments for the next decade, *Proceedings of Oceanbs'09, Sustained Ocean Observations and Information for Society, Venice, Italy, 21-25 September 2009*, https://doi.org/10.5270/OceanObs09

SWAMP Group, Hasselmann, S., & Hasselmann, K., (1985), The wave model exact-nl, *Ocean wave modeling*, 249–251.

The WAVEWATCH III ® Development Group, (2019), *User manual and system documentation of WAVEWATCH III ® version 6.07* (Tech. Note No. 333) [465 pp. + Appendices], NOAA/NWS/NCEP/MMAB, C.

Thomson, J., D'Asaro, E. A., Cronin, M. F., Rogers, W. E., Harcourt, R. R., & Shcherbina, A., (2013), Waves and the equilibrium range at ocean weather station P, *Journal of Geophysical Research*, *118*, 595–5962, https://doi.org/10.1002/2013JC008837

Thomson, J., Ackley, S., Girard-Ardhuin, F., Ardhuin, F., Babanin, A., Boutin, G., Brozena, J., Cheng, S., Collins, C., Doble, M., Fairall, C., Guest, P., Gebhardt, C., Gemmrich, J., Graber, H. C., Holt, B., Lehner, S., Lund, B., Meylan, M. H., ... Wadhams, P., (2018), Overview of the arctic sea state and boundary layer physics program, *Journal of Geophysical Research*, *123*, 8674–8687, https://doi.org/doi.org/10.1002/2018JC013766

Tolman, H. L., (1991), A third generation model for wind on slowly varying, unsteady and inhomogeneous depth and currents, *Journal of Physical Oceanography*, *21*, 766–781, https://doi.org/https://doi.org/10.1175/1520-0485(1991)021<0782:ATGMFW>2.0.CO;2

Tolman, H. L., (1992), Effects of numerics on the physics in a third-generation wind-wave model, *Journal of Physical Oceanography*, *22*, 1095–1111.

Tolman, H. L., (1995a), *On the selection of propagation schemes for a spectral wind wave model* (Office Note No. 411) [30 pp + figures], NWS/NCEP.

Tolman, H. L., (1995b), Subgrid modeling of moveable-bed bottom friction in wind wave models, *Coastal Engineering*, *26*, 57–75.

Tolman, H. L., (2002), Alleviating the garden sprinkler effect in wind wave models, *Ocean Modelling*, *4*, 269–289.

Tolman, H. L., (2008), A mosaic approach to wind wave modeling, *Ocean Modelling*, *25*, 35–47, https://doi.org/10.1016/j.ocemod.2008.06.005

Tolman, H. L., & Booij, N., (1998), Modeling wind waves using wavenumber-direction spectra and a variable wavenumber grid, *The Global Atmosphere and Ocean System*, *6*, 295–309.

Tolman, H. L., & Chalikov, D., (1996), Source terms in a third-generation wind wave model, *Journal of Physical Oceanography*, *26*, 2497–2518, http://journals.ametsoc.org/doi/pdf/10.1175/1520-0485%281996%29026%3C2497%3ASTIATG%3E2.0.CO%3B2

Tournadre, J., Bouhier, N., Girard-Ardhuin, F., & Rémy, F., (2016), Antarctic iceberg distributions 2002–2010, *Journal of Geophysical Research*, *121*, 327–349, https://doi.org/10.1002/2015JC011178

Tournadre, J., Poisson, J. C., Steunou, N., & Picard, B., (2015), Validation of AltiKa matching pursuit rain flag, *Marine Geodesy*, *38*, 107–1023, https://doi.org/10.1080/01490419.2014.1001048

Tracy, B. A., & Resio, D. T., (1982), *Theory and calculation of the nonlinear energy transfer between sea waves in deep water* (tech. rep. No. 11), U.S.

Tyler, G. L., Teague, C. C., Stewart, R. H., Peterson, A. M., Munk, W. H., & Joy, J. W., (1974), Wave directional spectra from synthetic aperture observations of radio scatter, *Deep Sea Research*, *21*, 989–1016.

van Vledder, G. P., (2006), The WRT method for the computation of non-linear four-wave interactions in discrete spectral wave models, *Coastal Engineering*, *53*, 223–242.

van Vledder, G. P., Herbers, T. H., Jensen, R. J., Resio, D. T., & Tracy, B., (2001), Modelling of non-linear quadruplet wave-wave interactions in operational wave models. *Coastal engineering 2000* (pp. 797–811).

Vignudelli, S., Birol, F., Benveniste, J., Fu, L.-L., Picot, N., Raynal, M., & Roinard, H., (2019), Satellite altimetry measurements of sea level in the coastal zone, *Surveys in geophysics*, *406*, 1319–1349.

WAMDI, G., (1988), The WAM model - a third generation ocean wave prediction model, *Journal of Physical Oceanography*, *18*, 1775–1810, https://doi.org/10.1175/1520-0485(1988)018%3C1775:TWMTGO%3E2.0.CO;2

Webb, D., (1978), Non-linear transfers between sea waves, *Deep Sea Research*, *253*, 279–298.

Williams, G., Maksym, T., Wilkinson, J., Kunz, C., Murphy, C., Kimball, P., & Singh, H., (2014), Thick and deformed antarctic sea ice mapped with autonomous underwater vehicles, *Nature Geoscience*, *8*, 61–67, https://doi.org/doi.org/10.1038/ngeo2299

Wu, W.-C., Wang, T., Yang, Z., & García-Medina, G., (2020), Development and validation of a high-resolution regional wave hindcast model for u.s. west coast wave resource characterization, *Renewable Energy*, *152*, 736–753, https://doi.org/https://doi.org/10.1016/j.renene.2020.01.077

Wunsch, C., & Ferrari, R., (2009), Ocean circulation kinetic energy:reservoirs, sources, and sinks., *Annual Review of Fluid Mechanics*, *41*, 253–282, https://doi.org/10.1146/annurev.fluid.40.111406.1021

Yanenko, N. N., (1971), *The method of fractional steps*, Springer-Verlag.

Young, I. R., Verhagen, L. A., & Banner, M. L., (1995), A note on the bimodal directional spreading of fetch-limited wind waves, *Journal of Geophysical Research*, *100 C1*, 773–778.

Young, I. R., Zieger, S., & Babanin, A. V., (2011), Global trends in wind speed and wave height, *Science*, *332 6028*, 451–455.

Yurovskaya, M. V., Dulov, V. A., Chapron, B., & Kudryavtsev, V. N., (2013), Directional short wind wave spectra derived from the sea surface photography, *Journal of Geophysical Research*, *113*, C12024, https://doi.org/10.1002/jgrc.20296

COLLEGE DOCTORAL BRETAGNE SCIENCES DE LA MER ET DU LITTORAL

Université de Bretagne Occidentale

Titre : Améliorations de la modélisation spectrale des états de mer : Aspects numériques et physiques et apports de la télédétection spatiale

Mots clés : Modèle des vagues, WAVEWATCH III, États de la mer, Paramétrisations, Altimétrie spatiale

Résumé : La présente thèse vise à identifier les éléments des modèles de vagues susceptibles d'améliorer différents aspects de la simulation des états de mer. Une attention particulière est accordée à l'influence des champs de forçage utilisés, des paramétrisations physiques et de la discrétisation du spectre de vagues. L'évaluation des caractéristiques des états de mer est dans un premier temps effectuée avec une implémentation globale du modèle WAVEWATCH III, puis étendue aux régions côtières avec une grille non structurée à haute résolution pour les eaux européennes. Une analyse approfondie des principaux processus physiques impactant les champs de vagues simulés est réalisée d'abord en haute mer, puis dans des environnements côtiers. Cette approche permet d'identifier où et quand les paramètres du modèle ont un effet significatif sur les champs de vagues simulés : depuis la génération de vagues en eaux profondes jusqu'à leur propagation dans des profondeurs plus faibles avec des caractéristiques bathymétriques complexes, des effets de frottement sur le fond et des forts gradients de courants de marée. À l'échelle mondiale, l'évaluation des performances des simulations est principalement réalisée à partir de données altimétriques. Les résultats du modèle régional sont quant à eux, comparés aux données de bouées spectrales et d'altimétrie. Les résultats obtenus suggèrent qu'à l'échelle mondiale, la partie la plus sensible du modèle pour l'obtention de distributions réalistes de hauteurs de vagues est liée aux ajustements de l'atténuation de la houle à partir de la paramétrisation des interactions air-mer d'Ardhuin et al. (2010). En termes de forme spectrale, l'utilisation de la paramétrisation de la dissipation de vague de Romero (2019) permet de développer une plus large gamme de formes de spectres directionnels par rapport aux paramétrisations précédentes, ce qui conduit à des valeurs d'élargissement qui suivent de près les mesures de bouées pour les fréquences > 0.3 Hz.

Title : Improvements in spectral modeling of sea states : Numerical and physical aspects and contributions of space remote sensing

Keywords : Wave model, WAVEWATCH III, Sea states, Parameterizations, Satellite Altimetry

Abstract : The present thesis aims to find the elements in wave models that can help to improve different aspects of sea states simulations. Special attention is paid to the influence of the used forcing fields, physical parameterizations and the discretization of the wave spectrum. The assessment of the sea states characteristics is done first with a global implementation of the WAVEWATCH III model and then extended to coastal regions with a high-resolution unstructured grid for European waters. Extensive analysis of the main physical processes affecting the simulated wave fields is done first in open ocean condition and then in coastal environments. This approach allows to identify when and where the choices made in the model setup have a significant effect on the modelled wave fields; from waves generation in deep waters to their propagation into shallower depths with complex bathymetry features, bottom friction effects and strong tidal current gradients. Performance evaluation of the simulations is done mainly with altimeter data at global scale. Results from the regional model are compared with spectral buoys and altimeter data. The obtained results suggest that at global scale the adjustments of the swell attenuation from the Ardhuin et al. (2010) air-sea interactions parameterization is the most sensitive part of the model to obtain realistic wave heights distributions. In terms of the spectral shape, using the Romero (2019) wave dissipation parameterization gives more freedom to the directional spectrum to develop a wide range of shapes compared to previous parameterizations, resulting in spreading values that closely follow buoy measurements for frequencies > 0.3 Hz. In coastal environments the use of the ESA Sea State CCI V2 altimeter dataset was employed to assess bottom friction effects within the modelled domain and the modelled wave heights accuracy as function of the distance to the coast. Reduction of the mean wave heights due to the bottom friction parmeterization were identified up to depths of 50 m, suggesting that in the absence of in situ measurements altimetry data could be used to adjust the bottom fiction parameterization. Additionally, the use of the CCI V2 dataset helped to estimate overall mesh performance down to distances of about 10 km from the coast with estimated model-altimeter difference ranges similar to those obtained further offshore.